Electrochemical-Thermal Modeling and Microscale Phase Change for Passive Internal Thermal Management of Lithium Ion Batteries

A Dissertation
Presented to
The Academic Faculty

By

Todd Matthew Bandhauer

In Partial Fulfillment
Of the Requirements for the Degree
Doctor of Philosophy in the
School of Mechanical Engineering

Georgia Institute of Technology
December 2011

Electrochemical-Thermal Modeling and Microscale Phase Change for Passive Internal Thermal Management of Lithium Ion Batteries

Approved By**:**

Dr. Srinivas Garimella, Co-Chair
G. W. Woodruff School of Mechanical Engineering
Georgia Institute of Technology

Dr. Samuel Graham
G. W. Woodruff School of Mechanical Engineering
Georgia Institute of Technology

Dr. Thomas F. Fuller, Co-Chair
School of Chemical and Bio-Molecular Engineering
Georgia Institute of Technology

Dr. Paul Kohl
School of Chemical and Bio-Molecular Engineering
Georgia Institute of Technology

Dr. S. Mostafa Ghiaasiaan
G. W. Woodruff School of Mechanical Engineering
Georgia Institute of Technology

Date Approved:

DEDICATION

To Karen, Morgan, and Mason

ACKNOWLEDGEMENTS

I would like to thank my advisor, Dr. Srinivas Garimella, for encouraging and giving me an opportunity to pursue intellectual growth on a problem of practical importance. I am most grateful for the personal and professional flexibility he has given me throughout my time at STSL. I also appreciate the many hours he spent preparing me for professional life after graduation, which has been a rewarding experience.

Many past and present STSL members deserve my gratitude for support during my experiments, reviewing my dissertation, fabricating test facilities, and other miscellaneous tasks that have enabled me to conduct this research. I want to specifically acknowledge Brian Fronk, Brendon Keinath, Jeff Milkie, Jared Delahanty, Alex Rattner, John Bustamante, Adrienne Little, Thomas Robbins, Dr. Matt Determan, Anand Nagavarapu, Chris Keinath, Malcolm MacDonald, Jesse Killion, Dave Hickman, Alex Raymond, Chris Goodman, Dan Golden, and Mark Meacham for their assistance in myriad ways.

I am also thankful to my co-advisor, Dr. Tom Fuller, for guiding my research as I ventured into the field of electrochemistry. I would not have been able to do this work without his valuable insights, especially those into electrochemical modeling. I also acknowledge the help I received from past and present members of his research group, specifically Raji Chandrasekaran, Gary Gray, Eric Ping, Kevin Gallagher, Cheng Chen, Normitsu Takeuchi, Erin Redmond, Vyran George, Kara Evanoff, and Brian Setzler.

I also want to thank Ben Hertzberg and Dr. Gleb Yushin for letting me use their glove box when cutting open batteries.

The people at the ME and GTRI sample shops were also of great help in fabricating various components, especially John Graham, Louis Boulanger, Dennis Brown, and Dennis Denney.

I am also thankful for the financial support and flexibility Sandia National Laboratories has given for me to conduct my research. The fellowship I received from them is paying great dividends for my ongoing professional career too.

Finally, I am grateful to my dissertation reading committee for providing valuable insight and asking challenging questions that have improved the quality of my work.

TABLE OF CONTENTS

LIST OF TABLES

LIST OF FIGURES

NOMENCLATURE

a	calibration slope
A	surface area [m^2]
b	calibration intercept
C	battery C-rate [A], two phase frictional pressure drop variable
C_p	specific heat [J kg^{-1} K^{-1}]
C_d	drag coefficient
Cap_{after}	battery capacity after testing [Ah]
Cap_{before}	battery capacity after testing [Ah]
Cap_{nom}	normalized battery capacity [Ah]
CF	compactness factor
Co	confinement number
b	curve fit intercept
B	bias uncertainty
B'	correlated bias error
c	salt concentration in the electrolyte [mol m^{-3}]
$c_{i,j}$	concentration of species i in phase j [mol m^{-3}]
D	diameter [m]
D_h	hydraulic diameter [m]
c_{Li}	concentration of lithium in the solid insertion electrode [mol m^{-3}]
D_{Li}	diffusion coefficient of lithium in an insertion electrode [m^2 s^{-1}]
DOD	depth of discharge [Ah], normalized depth of discharge
dP/dz	pressure gradient [kPa m^{-1}]
$\partial U/\partial T$	entropic heat coefficient [V K^{-1}]
E_1	void fraction parameter
E_2	void fraction parameter

E'''	energy extraction density [Wh L^{-1}]
E_{FR}	Friedel correlation variable
F	convective boiling enhancement factor
f	Darcy friction factor
Fr	Froude number
FT	void fraction parameter
$func$	function
G	mass flux [kg m^{-2} s^{-1}]
g	gravitational constant, 9.81 [m s^{-2}]
gap	argon gap in center of battery [m]
gap_{cool}	battery pack cooling channel gap width [m]
H	height [m]
h	heat transfer coefficient [W m^{-2} K^{-1}]
H_{FR}	Friedel correlation variable
h_{lv}	enthalpy of vaporization [J g^{-1}]
h_r	refrigerant enthalpy [J g^{-1}]
HEV	hybrid electric vehicle
ΔH	height from condenser outlet to evaporator channel inlet [m]
ΔH_s	enthalpy change per unit separator area [J mol^{-1} m^{-2}]
$\Delta H°_{i,j\rightarrow m}$	molar enthalpy phase change of species i from phase j to m [J mol^{-1}]
$\overline{H}_{Li}$	partial molar enthalpy of lithium [J mol^{-1}]
I	total cell current [A]
i'''	current per unit cell volume [A m^{-3}]
i''	current flux [A m^{-2}]
i	channel number from inlet
j	superficial velocity [m s^{-1}]
K	minor loss coefficient
K_{Armand}	Armand void fraction coefficient
k	thermal conductivity [W m^{-1} K^{-1}]
L	length [m]
l	length [m]

L_{stack}	thickness of cell stack [m]
M	molecular weight [J mol^{-1}]
$\dot{m}$	mass flow rate [kg s^{-1}]
m	critical Reynolds number constant
N	total number of quantity
$N_{balance}$	non-dimensional number for thermal gradient induced charge balancing
N_{pitch}	test section channel spacing [m]
n	critical Reynolds number constant
$n_{i,j}$	moles of species i in phase j [mol]
Nu	Nusselt number
P	pressure [kPa], precision
P_r	reduced pressure
$Power$	total power of cell within a pack [W]
R^2	correlation coefficient
R''_{cont}	specific contact resistance
Ra	Rayleigh number
Re	Reynolds number
RMS_{error}	root mean square error
Q	heat generation [J]
$\dot{Q}$	heat generation rate [W]
$\dot{Q}'''$	heat generation rate per unit cell volume [W m^{-3}]
$\dot{Q}''$	heat flux [W m^{-2}]
Pr	Prandtl number
R	universal gas constant, 8.314 [J mol^{-1} K^{-1}]
$R_{particle}$	radius of particle [m]
S	sample standard deviation
SEE	standard error of estimate
T	temperature [K, °C]
T_C	temperature [°C]
$\bar{T}$	average temperature [K, °C]

t	time [s], thickness [m], *t*-distribution value
$\bar{U}$	average open circuit potential [V]
U	open circuit potential [V]
UN	uncertainty
V	overall cell potential [V], velocity [m s^{-1}]
$\bar{V}$	average voltage [V]
$\dot{V}$	volume flow rate [m^3 s^{-1}]
VF	void fraction
W	width [m]
We	Weber number
v	volume [m^3]
$X_{\text{Martinelli}}$	Martinelli parameter
x	quality
X	sample variable
$\bar{X}$	sample mean
Y	measured quantity
y	void fraction parameter

Symbols

α	aspect ratio
β	homogeneous void fraction
Δ	difference
δ	Kronecker delta function
ε	volume fraction, emissivity, surface roughness [m]
ϕ	local potential in stack [V], two phase friction multiplier
$\gamma_{i,j}$	activity coefficient of species i in phase j
η	overpotential, V
η_{fin}	fin efficiency
λ	entropic heat coefficient [V K^{-1}]
μ	viscosity [kg m^{-1} s^{-1}]

ρ	density [kg m^{-3}]
σ	electrical conductivity [S m^{-1}], or Stefan-Boltzman constant, 5.67×10^{-8} [W m^{-2} K^{-4}]
θ	half angle subtended by thermocouple from blocking circular channel [rad]
ψ	surface tension parameter
ζ	two phase frictional pressure drop parameter
∞	bulk property or volume average value

Subscripts and Superscripts

1	covered portion of environmental chamber
2	uncovered portion of environmental chamber
a	ambient air
Al	aluminum
alt	alternative
air	ambient air
amb	ambient
avg	average
back	back surface
bot	down-facing horizontal side, top thermocouple row of test section
br	branch
bubble	vapor core in annular flow
byp	bypass
c	maximum quantity in tee line, environmental chamber, cross section
calc	calculated quantity
cell	individual battery within a pack
cc	current collector
ch	channel
cha	charge
Churchill	Churchill friction factor or Nusselt number
cs	calibration standard

Cu	copper
cumulative	total time integrated value
con	contraction
cool	coolant
conv	convective
crit	critical
dis	discharge
ECM	electrochemical
eff	effective
ent	entropic
exp	expansion
f-b	film-bubble region
f	friction
film	average film property
fin	final
front	front surface
gap	coolant gap
head	gravity head
header	test section header
HG	homogeneous
high	higher transition boundary
hr	hours
htr	heater
i	summation index, inside, inlet
i/o	inlet and outlet
ih/oh	inlet header and outlet header
insertion	insertion electrode
init	initial
ins	insulation
interface	bubble-film interface
IR	irreversible

j	phase index, radiation surface index
k	reaction number index, summation index
L	characteristic length, left
l	liquid
line	line segment of tee
lo	liquid only
low	low rates, lower transition boundary
M	middle
matrix	insertion material matrix
meas	measured
mid	middle thermocouple row of test section
min	minimum
minor	minor losses
n	normal direction
NB	nucleate boiling
NC	natural convection
neg	negative
nom	nominal
norm	normalized
o	outside, outlet
other	additional major losses
pack	battery pack
par	parallel modules
pos	positive
PVC	polyvinylchloride
R	right
r	refrigerant, ratio
rev	reversible
rs	rise
s	surface, test section surface
sat	saturation

SB	Shah and Bhatti friction factor
SF	separated flow
shell	battery casing
side	vertical side
sp	single phase
st	minimum quantity in tee line
straight	straight portion of battery unit cell
t/c	thermocouple
tab	cell tab
tee	line flow through a tee
test	test section
top	up-facing horizontal side, top thermocouple row of test section
tp	two phase
trans	transition
tt	turbulent liquid and vapor
tube	connecting tube
turb	turbulent
unit cell	battery active material
v	vapor
vert	vertical
vo	vapor only
vv	laminar liquid and vapor
wall	outer surface of cell
wind	battery unit cell winding
+	positive current collector
-	negative current collector
$\parallel$	parallel to wound stack direction
$\perp$	perpendicular to wound stack direction

SUMMARY

Energy-storing electrochemical batteries are the most critical components of high energy density storage systems for stationary and mobile applications. Lithium-ion batteries have received considerable interest for hybrid electric vehicles (HEV) because of their high specific energy, but face inherent thermal management challenges that have not been adequately addressed. Most previous modeling efforts for these batteries have focused either exclusively on particle electrochemistry or bulk thermal transport, and no investigation has successfully integrated all the relevant physics into one self-consistent model that is capable of simulating dynamic performance. Moreover, existing thermal management systems for large HEV packs are all external to the batteries, causing either unwanted temperature rise or imposed internal thermal gradients due to the low thermal conductivity and large thermal pathway from the heat source to the cooling fluid.

In the current investigation, a fully coupled electrochemical and thermal model for lithium-ion batteries is developed to investigate the effects of different thermal management strategies on battery performance. This work represents the first ever study of these coupled electrochemical-thermal phenomena in batteries from the electrochemical heat generation all the way to the dynamic heat removal in actual HEV drive cycles. In addition, a novel, passive internal cooling system that uses heat removal through liquid-vapor phase change is developed. The proposed cooling system passively removes heat almost isothermally with negligible thermal resistances between the heat

source and cooling fluid, thereby allowing battery performance to improve unimpeded by thermal limitations.

For the battery model, local electrochemical reaction rates are predicted using temperature-dependent data on a commercially available battery designed for high rates ($C/LiFePO_4$) in a computationally efficient manner. Data were collected on this small battery (~1 Ah) over a wide range of temperatures (10°C to 60°C), depths of discharge (0.15 Ah < *DOD* < 0.95 Ah), and rates (-5 A to 5 A) using two separate test facilities to maintain sufficient temperature fidelity and to discern the relative influence of reversible and irreversible heating. The results show that total volumetric heat generation is a primarily a function of current and *DOD*, and secondarily a function of temperature. The results also show that reversible heating is significant compared to irreversible heating, with a minimum of 7.5% of the total heat generation attributable to reversible heating at 5 A and 15°C. Additional tests show that these constant current data can be used to simulate the response of the battery to dynamic loading, which serves as the basis for the electrochemical-thermal model development. This model is then used to compare the effects of external and internal cooling on battery performance.

The proposed internal cooling system utilizes microchannels inserted into the interior of the cell that contain a liquid-vapor phase change fluid for heat removal at the source of heat generation. Although there have been prior investigations of phase change at the microscales, fluid flow for pure refrigerants at low mass fluxes ($G < 120$ kg m^{-2} s^{-1}) experienced in the passive internal cooling system is not well understood. Therefore, passive, thermally driven refrigerant (R134a) flow in a representative test section geometry (3.175 mm × 160 mm) is investigated using a surrogate heat source. Heat

inputs were varied over a wide range of values representative of battery operating conditions ($120 < \dot{Q}''' < 6500$ W L^{-1}). The measured mass flow rate and test section outlet quality from these experiments are utilized to accurately calculate the two-phase frictional pressure drop in the test section, which is the dominant flow loss in the passive system in most cases. Because prior research poorly predicts the data, a new correlation is developed based on adaptations of the work of Saisorn and Wongwises (2009), which predicts 83% of the data to within ±22%.

The two-phase frictional pressure drop model is used to predict the performance of a simplified passive internal cooling system. This thermal-hydraulic performance model is coupled to the electrochemical-thermal model for performance assessment of two-scaled up HEV battery packs (9.6 kWh based on 8 Ah and 20 Ah cells) subjected to an aggressive highway dynamic simulation. This assessment is used to compare the impact of air, liquid, and edge external cooling on battery performance. The results show that edge cooling causes large thermal gradients inside the cells, leading to non-uniform cycling. Air cooling also causes unacceptable temperature rise, while liquid cooling is sufficient only for the pack based on the thinner 8 Ah cell. In contrast, internally cooled cells reduce peak temperature without imposing significant thermal gradients. As a result, packs with internal cooling can be cycled more aggressively, leading to higher charge and discharge energy extraction densities in spite of the volume increase due to 160 μm channels inserted into the 284.5 μm unit cell. Furthermore, the saturation temperature of the phase change fluid can be optimized to balance capacity fade and energy extraction at elevated temperatures. At a saturation temperature of 34°C, the energy extraction density was 80.2% and 66.7% greater than for the best externally

cooled system (liquid) even when the pack volume increased due to incorporation of the channels.

This research moves the state of the art towards a more fully integrated understanding of thermal management of large lithium-ion battery packs intended for HEV applications. Internally cooling batteries can lead to improvements in battery performance, safety, and longevity that are unencumbered by thermal limitations.

CHAPTER 1. INTRODUCTION

Electric and hybrid electric vehicles (EV and HEV) may present the best near-term solution for the transportation sector to reduce dependence on petroleum and to reduce emissions of greenhouse gases and criteria pollutants. Rechargeable lithium-ion batteries are well suited for these vehicles because they have, among other things, high specific energy and energy density relative to other cell chemistries. For example, practical nickel-metal hydride (NiMH) batteries, which have dominated the HEV market, have a nominal specific energy and energy density of 75 Wh kg^{-1} and 240 Wh L^{-1}, respectively. In contrast, lithium-ion batteries can achieve 150 Wh kg^{-1} and 400 Wh L^{-1} (Linden, 2002), *i.e.*, nearly two times the specific energy and energy density of NiMH batteries.

Although lithium ion batteries are rapidly displacing NiMH and nickel-cadmium secondary batteries for portable and hand-held devices, they have not yet been widely introduced in automotive products. The main barriers to the deployment of large fleets of vehicles on public roads equipped with lithium-ion batteries continue to be safety and cost (related to cycle and calendar life) (Conte, 2006) - *both challenges that are coupled to thermal effects in the battery*. Since the recent introduction of HEV fleets, the industry trend is toward larger batteries required for plug-in hybrids, extended-range hybrids, and all-electric vehicles. These larger battery designs impose greater pressure on the need to lower costs and improve safety.

As detailed in a recent review (Bandhauer *et al.*, 2011), lithium-ion battery performance characteristics are sensitive to the cell-operating temperature. The recoverable power and capacity can be reduced significantly when these batteries are operated or stored at temperatures above ~50°C, especially at high states of charge (SOC), due to multiple factors, including lithium loss from increased growth of the solid electrolyte interphase (SEI) on the negative electrode from it reacting with the electrolyte. This also leads to increases in Ohmic resistances that reduce deliverable power. At these low temperatures, the extractable energy is also significantly reduced. Furthermore, if temperature differences exist among cells within a pack, the hotter cells will be capable of discharging or charging faster than colder cells. Hence, electrical and temperature balance are linked together. Finally, at temperatures near 100°C, deleterious heat-producing side-reactions inside the battery can lead to even further increases in battery temperature, which can be caused by multiple factors, including overcharging or internal short-circuiting. This can lead to rapid temperature rises in an individual cell, and the temperature increase in one cell can propagate to other nearby cells, thus causing them to rapidly self-heat too.

To predict battery temperature during operation, thermal modeling has been previously used to simulate the performance of lithium-ion batteries in multiple investigations (Al Hallaj *et al.*, 1999; Botte *et al.*, 1999; Chen *et al.*, 2006; Chen *et al.*, 2005; Chen and Evans, 1993; Chen and Evans, 1994a; Chen and Evans, 1994b; Chen and Evans, 1996; Gomadam *et al.*, 2002; Kim *et al.*, 2008; Kim *et al.*, 2009; Kumaresan *et al.*, 2008; Pals and Newman, 1995a; Pals and Newman, 1995b; Song and Evans, 2000; Srinivasan and Wang, 2003; Thomas and Newman, 2003b; Verbrugge, 1995). However,

all of these studies have been limited in some way, and there has not been an investigation that correctly accounts for both temperature dependent local heat generation and current production for varying power profiles observed in HEV applications. In addition, although essential in developing accurate thermal models, there have been few investigations (Al Hallaj *et al.*, 2000a; Song and Evans, 2000; Thomas and Newman, 2003a) that measure total heat generation for discharge rates > 1*C*[1], and none > 2*C*, which routinely occur in HEV applications. The majority of these studies have also been conducted at one temperature (near nominal ambient: 20°C to 25°C), and few studies have investigated the impact of temperature on heat generation. For those that have investigated temperature influences, the range of temperatures is typically small and/or the rates are low. Thus, there is a significant opportunity to improve the fidelity and accuracy of battery performance prediction through an improved understanding of the electrochemical heat rates and integrating this into fully coupled models that can be used to assess the performance of batteries in realistic applications.

The essential thermal problem for batteries is the poor thermal conductivity that creates a large thermal resistance between the heat generation locations and the cooling medium. Air is the most common fluid used to cool battery packs, but air cooling may not be the best method for maintaining cell-to-cell temperature uniformity or limiting undesirable temperature rise (Bandhauer *et al.*, 2011). Liquids have a higher thermal conductivity and heat capacity than air, and, as a result, can lower temperature rise of individual cells and the difference among multiple cells in a pack. However, this strategy is limited because the cooling medium is external to the batteries themselves, and the

[1] The 1*C* rate is defined as the discharge current that would discharge the battery in one hour. Hence, the 2*C* rate corresponds to the 1*C* rate multiplied by 2, i.e., would achieve complete discharge in 30 minutes.

increased surface convection leads to large internal thermal gradients within individual cells. Constant temperature heat rejection (*e.g.*, to a phase change material) can also reduce cell-to-cell temperature uniformity, but at the expense of adding an additional significant thermal resistance between the cell surface and the ultimate cold temperature sink. Therefore, because all existing thermal management strategies are fundamentally limited to the external surface of the battery, the packs utilized in HEV applications are typically oversized to compensate for the unwanted temperature rise induced from poor thermal management.

In the current study, the electrochemical heat generation on a small (OD = 18 mm, and H = 65 mm) commercially available battery (C/$LiFePO_4$) was measured over a wide range of charge and discharge rates (up to 5C) and temperatures (10°C to 60°C). These data were used to develop a simplified, but temperature and rate dependent, electrochemical model that substantially reduced computational effort when simulating battery performance. This model was then fully coupled to both thermal and current collection fields in a scaled-up battery intended for HEV applications, and was used to simulate its performance under dynamic loads. Such fully coupled, realistic operating scenario simulations have not been reported in the literature. The impacts of several different thermal management strategies on battery performance were investigated using this model, including an innovative passive internal cooling system that utilizes microscale liquid-vapor phase change that results in near-isothermal heat removal through low thermal resistances between the heat generation site and the heat sink. Due to poor understanding of liquid-vapor phase change at the small dimensions necessary to integrate the channels within the battery, a thermal-hydraulic model was developed for a

representative internal cooling system. The performance of this system was validated experimentally over a range of saturation temperatures (24°C to 33°C) using a test section with small multiple parallel passages (3.175 mm × 160 μm, effective) for low heat fluxes typically observed for lithium-ion batteries in normal operation (*i.e.*, below 0.04 W/cm^2). A simplified version of the thermal-hydraulic model was then coupled to the battery model to demonstrate the pack size reduction achievable from improved thermal management.

1.1. Dissertation Organization

The dissertation is organized as follows. In Chapter Two, a critical review of the available literature on electrochemical heat generation, thermal modeling, and thermal management for lithium-ion batteries is presented, and the need for the present work is identified. The details of the two experimental methods used to measure electrochemical heat generation rates for the small battery along with a discussion of the results are given in Chapter Three. In Chapter Four, the experimental approach used to validate the performance of the thermal-hydraulic model for the representative passive internal cooling system is presented. This chapter also includes a new frictional pressure drop model for flow inside the small channels used in the passive cooling system evaporator. The development of the fully coupled electrochemical-thermal model is detailed in Chapter Five, including the simplifications needed to couple the thermal-hydraulic performance of the internal cooling system to scaled-up batteries. The simulation results are also discussed in this chapter, which includes the effect of thermal management on performance, localized cycling, and power density improvements. The conclusions from this study are presented in Chapter Six. Recommendations for future research on a broad

range of topics including microchannel liquid-vapor phase-change fluid flow, battery thermal management, and battery modeling are also included in this chapter.

CHAPTER 2. LITERATURE REVIEW

Heat generation inside batteries is a complex process that requires understanding of how the electrochemical reaction rates change with time and temperature and how current is distributed within larger batteries. Many investigators have studied heat dissipation characteristics inside both single-cell batteries and multi-cell battery packs using a variety of assumptions applied to models ranging from simple 1-D analyses with uniform heat generation to detailed 3-D investigations of coupled electrochemical-thermal models. Some investigators have attempted to measure battery heat generation rates using both commercially available and custom-built calorimeters. The use of measured data is critical to the understanding of the magnitude and pattern of the variety of mechanisms that cause batteries to generate heat. However, as discussed below, all of the prior work in these areas is insufficient for understanding the impact of thermal management on battery performance when the battery is charged and discharged dynamically and at high rates. Furthermore, existing thermal management strategies are all external to the batteries and thus cause a significant thermal resistance between the cell interior and the cooling fluid. Thus, there is a critical need to develop improved battery models that appropriately capture all the relevant coupled physics (*i.e.*, electrochemistry, heat transfer, and current collection) so that their performance can be assessed in practical operating conditions. In addition, a thermal management strategy that significantly improves heat transport from the interior of the cell to the outside is

needed.

A review of the literature on lithium batteries is presented here in three sections: heat generation, thermal modeling, and thermal management. In addition to discussing the theoretical basis for heat generation in batteries, the various techniques used to measure battery heat generation are also discussed. Thus, this review elucidates the deficiencies in understanding of battery heat generation, in existing coupled electrochemical-thermal battery models, and in thermal management strategies, which underscoring the need for the present study.

2.1. Heat Generation

Heat is produced in batteries from three fundamental sources: activation (interfacial kinetics), concentration (species transport), and ohmic (joule heating from the movement of charged particles) losses. For small cells, the heat loss from the movement of electrons in the current collectors is usually negligible. However, as the battery increases in size, the distance from the current source to the tab and the concentration of current near the tabs may cause significant heat generation (Figure 2.1). In this section, the fundamental expressions for localized electrochemical heat generation are discussed first, followed by a discussion of the modifications needed for application to larger batteries. This section also describes the various techniques used to measure the heat generation rate in lithium-based batteries. This information is used to assess the ranges of temperature and discharge/charge rates addressed by previous researchers, to understand the magnitudes of overpotential and entropic heat generation rates, and to evaluate the methods used to measure the heat rates.

2.1.1. Electrochemical Process Heat Generation

Bernardi *et al.* (1985) derived an expression for battery heat using a thermodynamic energy balance on a complete cell. Discrete phases inside the battery interact with each other by means of electrochemical reaction, phase changes, and mixing. By applying the first law of thermodynamics around the cell control volume (not including current collectors) and making numerous simplifications, they determined the following expression for heat generation inside the battery:

$$q = -IV - \sum_{k} I_k T^2 \frac{d\frac{U_{k,avg}}{T}}{dT} + \sum_{j} \frac{d}{dt}\left(\int_{v_j} \sum_{i} c_{ij} R T^2 \frac{\partial}{\partial T} \ln\left(\frac{\gamma_{i,j}}{\gamma_{i,j}^{avg}} \right) dv_j \right) + \sum_{j,j\neq m} \sum_{i} \left[\left(\Delta H^{\circ}_{i,j\rightarrow m} - RT^2 \frac{d}{dT} \ln \frac{\gamma_{i,m}^{avg}}{\gamma_{i,j}^{avg}} \right) \frac{dn_{i,j}}{dt} \right] \tag{2.1}$$

Here, the first term is the electrical power produced by the battery. The second term is the sum of available work and entropic heating from the reaction, and is summed over all simultaneously occurring reactions. The third term is heat produced from mixing. Since the reaction rates are not uniform, concentration variations across the battery develop as the reaction proceeds. When the current is interrupted, the concentration gradients developed inside the battery relax, causing heat to be released or absorbed. Hence, as the concentration profile inside the battery is developed during operation, an apparent relaxation heat will occur and be opposite in sign but equal in magnitude to the heat observed when the current is cut off. This term may be significant if the enthalpy of the mixture as a function of concentration is non-linear. The final term in the energy balance is heat from material phase changes. The equation proposed by Bernardi *et al.* is cited frequently in the literature in its simplified form (Gu and Wang, 2000):

$$\dot{Q} = I\left(U - V\right) - I\left(T\frac{\partial U}{\partial T}\right) \tag{2.2}$$

This form has been reported previously (*e.g.,* Sherfey and Brenner (1958)); some key features are as follows. The first term on the right-hand side is the overpotential heat due to Ohmic losses in the cell, charge-transfer overpotentials at the interface, and mass transfer limitations. The electrode potential is determined at the average composition. The second term is the entropic heat, and the potential derivative with respect to temperature is often referred to as the entropic heat coefficient. Phase change and mixing effects are neglected in this expression, and this equation assumes that there is only one electrochemical reaction in the cell. Phase change does not occur in lithium-ion batteries during normal operation, and only one electrochemical reaction occurs in these batteries during normal operation. However, mixing effects can be significant in some cases.

Recently, Thomas and Newman (2003b) studied the heat of mixing effect inside a battery containing a porous insertion electrode. They noted that there are four possible ways mixing effects occur inside the cell. The first is heat of mixing inside the bulk electrode through variation in local current density on the effective electrode open-circuit potential, which was previously modeled by Rao and Newman (1997). The remaining modes of mixing heat are from concentration gradients inside the spherical particles, bulk electrolyte, and inside the electrolyte pores of the insertion electrode. Thomas and Newman illustrated the relative magnitudes of these terms using representative calculations on data collected for a $Li/LiAl_{0.2}Mn_{1.8}O_{4-\delta}F_{0.2}$ battery discharged at the 2*C* and *C*/3 rates for 5 minutes and 3 hours, respectively. In both cases, the mixing heat from the cylindrical electrolyte pores was negligible due to small concentration gradients. The

mixing heat across the bulk electrodes and electrolyte was more significant, but small compared to the irreversible and reversible heat. This was a different conclusion than that of Rao and Newman because the ionic conductivity used in this study was an order of magnitude higher, which is more representative of commercial organic solvent-based electrolyte batteries. Although the heat of mixing in the spherical particle at the lower discharge rate was small at *C*/3, the mixing heat across the spherical particles was significant compared to the sum of irreversible and reversible heats at the higher discharge rate.

To calculate the enthalpy of mixing in each case, Thomas and Newman determined expressions for the difference in enthalpy from the operating state to the relaxed state using a Taylor-series expansion for the molar enthalpy of each species, while neglecting density and temperature changes and concentration dependence on the second derivative of partial molar volume with respect to partial molar enthalpy. For the solid spherical particles, they assumed that the rate of reaction is approximately constant with time (pseudo-steady-state) and the particles had uniform current distribution on the surface. For a constant diffusivity, the enthalpy of mixing for the particle per unit separator area is calculated as follows:

$$\Delta H_{\mathrm{s}} = \frac{1}{c_{\mathrm{matrix},\infty} v_{\mathrm{matrix},\infty}} \frac{\partial \overline{H}_{\mathrm{Li}}}{\partial c_{\mathrm{Li}}}\bigg|_{\infty} \left(\frac{I}{F \cdot D_{\mathrm{Li}}} \right)^2 \frac{R_{\mathrm{particle}}^4}{\varepsilon_{\mathrm{insertion}} L_{\mathrm{stack}}} \frac{1}{1050} \tag{2.3}$$

The relaxed state is denoted by ∞. This expression determines the energy per unit separator area released/absorbed when the concentration gradients inside the particles are allowed to relax. The constant 1050 arises from integration of species concentration. Thomas and Newman pointed out that their tested battery design will have higher heat of

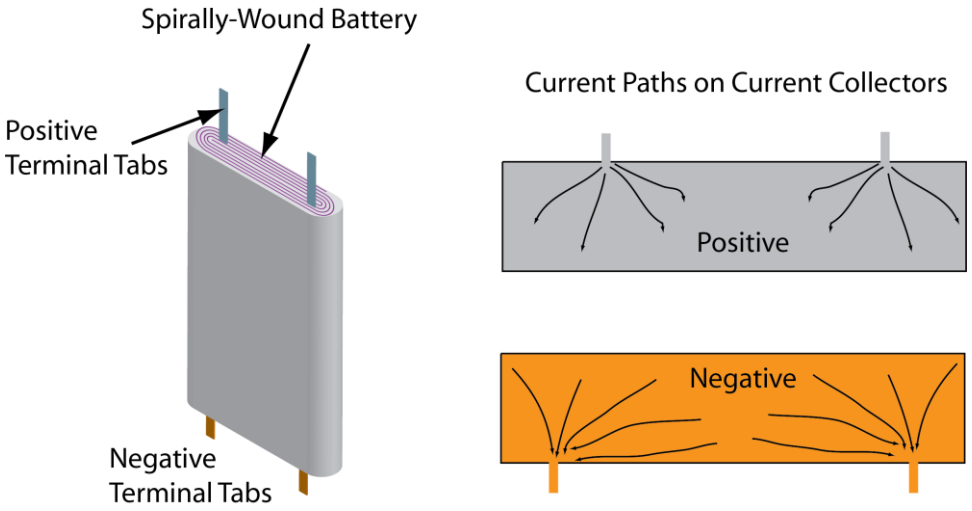

Figure 2.1: Schematic of Spirally-Wound Battery and Electron Flow Paths in the Current Collectors

mixing than for commercially made batteries due to their large particle size (20 μm). Thus, it is generally safe to neglect heat of mixing when estimating volumetric heat generation in commercial battery technology. However, one can use the above expression to determine whether heat of mixing in the solid particle is important for a particular electrode design.

2.1.2. Current Collection Heat in Large Batteries

In addition to electrochemical heat generation, joule heating is produced from bulk electron movement in the current collectors (Figure 2.1). In small cells, this term may be insignificant. However, increased attention is now being paid to larger cells used in HEVs and EVs, where the electrical distribution in the current collectors may have a large impact on the overall heat generation rate. For example, Kim *et al.* (2008; 2009) have investigated the impact of current distribution on several different electrode configurations for a C/LiNiCoMnO$_2$ polymer electrolyte battery. The 2-D model (variation in the thickness was neglected) consisted of two electrode current collectors

coupled via a temperature-independent parameterized electrochemical model, which uses local overpotential to estimate local current production. The current fields in each collector are determined using Ohm's law, and the local volumetric heat generation rate is determined as follows:

$$\dot{Q}''' = i'''\left(U - V - T\frac{\partial U}{\partial T}\right) + \left(\sigma\left|\nabla\phi\right|^2\right)_{\text{cc,pos}} + \left(\sigma\left|\nabla\phi\right|^2\right)_{\text{cc,neg}} \tag{2.4}$$

The first term on the right-hand side is the electrochemical heat generation (per unit volume), which was discussed in detail above. The last two terms are the resistive heating due to current movement in the positive and negative metal current collectors, respectively. If the tab locations are designed appropriately, the distribution of local current generation from the electrochemical reaction may be minimally impacted. However, even though current production and overpotential may be similar, increased current is passed through the battery locally, which increases resistive heating in the current collectors. For example, in the first study by Kim *et al.* (2008), a ~87 mm wide and ~150 mm tall cell with 35 mm wide current collector tabs placed on the top end of the current collectors caused less than 0.5% maldistribution in current when discharged at the 1*C* rate for 30 minutes. However, both the simulation and experiments show a more than 17°C temperature variation, with the hottest portions of the battery near the current collection tabs. The recent work at NREL that includes solving electrochemical transport locally has also shown similar results (Kim and Smith, 2008; Kim and Smith, 2009).

In summary, the heat generation estimated by Bernardi *et al.* (Equation 2.2) is the most commonly used equation to estimate battery heat generation. This equation may be readily applied to estimate the amount of electrochemical heat generation in small

lithium-ion batteries if there is no heat from mixing or phase change, no spatial variation in temperature or SOC, only one electrochemical reaction occurring at each electrode, and negligible joule heating in the current collectors. In lithium-ion batteries without side reactions, there is only one reaction occurring at each electrode, and no phase change effects exist. Neglecting the heat of mixing terms is acceptable for low discharge rates, and will be for high discharge rates when the particle size is sufficiently small, which is representative of commercial battery designs. In larger batteries, the electrochemical reactions may be sufficiently non-uniform for poorly placed current collection tabs, which result in both SOC and temperature non-uniformities. However, resistive heating in the current collectors of large batteries may be significant compared to the electrochemical heat generation rate for even well designed batteries that have uniform current production and working potential across the cell throughout the battery. In these cases, discretization of the battery into smaller cells and accounting for current collector joule heating through Equation 2.2 is imperative.

2.1.3. Prior Experimental Investigations

There have been multiple attempts to experimentally determine the irreversible electrochemical heat generation rate for lithium-ion batteries. The primary experimental methods are accelerated-rate calorimetry (ARC) (Al Hallaj *et al.*, 2000a; Al Hallaj *et al.*, 2000b; Hong *et al.*, 1998) and isothermal heat conduction calorimetry (IHC) (Bang *et al.*, 2005; Kim *et al.*, 2001; Kobayashi *et al.*, 1999; Kobayashi *et al.*, 2002; Lu *et al.*, 2007; Lu *et al.*, 2006a; Lu and Prakash, 2003; Lu *et al.*, 2006b; Onda *et al.*, 2003; Saito *et al.*, 1997; Saito *et al.*, 2001; Song and Evans, 2000; Thomas and Newman, 2003a; Yang and Prakash, 2004). The ARC method consists of measuring the heat rejected by the battery during operation while encapsulated in either air or solid material (*e.g.*, Styrofoam). In

this method, the temperature of the battery is allowed to rise as heat is transferred through the medium to a constant temperature sink. The heat generation rate is estimated using an energy balance on the battery. For IHC, the battery remains at one temperature throughout operation using an isothermal well in close contact with the surface of the battery (*e.g.*, liquid or a metal heat sink). High-accuracy thermopiles either embedded inside the heat sink or placed near the surface of the battery are used to measure the heat rate. As in all calorimetric methods, special data processing or experimental procedures are usually required due to the long instrument time constants (*i.e.*, time elapsed from heat generation to measurement).

The reversible heat has been estimated using multiple techniques. Several methods are used to estimate the entropic heat coefficient (*i.e.*, $\partial U/\partial T$). The most common method is to measure the open-circuit potential (OCP) variation with temperature at a fixed SOC (Al Hallaj *et al.*, 2000a; Al Hallaj *et al.*, 2000b; Bang *et al.*, 2005; Hong *et al.*, 1998; Lu *et al.*, 2006a; Lu and Prakash, 2003; Onda *et al.*, 2003; Onda *et al.*, 2006; Thomas and Newman, 2003a; Yang and Prakash, 2004). The other methods are calorimeter-based. First, several authors assumed that irreversible heat remained constant upon charge and discharge. Hence, they subtracted the charge calorimeter data from the discharge data, which cancels the overpotential heat, and allows for the entropic heat to be determined as follows:

$$\dot{Q}_{\text{ent}} = \frac{\dot{Q}_{\text{dis}} - \dot{Q}_{\text{cha}}}{2} \tag{2.5}$$

Thomas *et al.* (2001) showed that this method provided results to those obtained using their SOC cycling method. Onda *et al.* (2003) also showed that this method produced

Table 2-1: Gap Analysis of Battery Heat Generation Test Methods

Collection Method	Charge or Discharge	$< C/10$	$C/10 \leq I \leq C/1$	$> C/1$
ARC	Charge			
	Discharge			
IHC	Charge		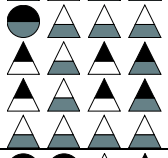	
	Discharge	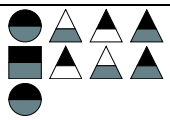	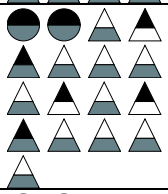	
RAD	Charge			
	Discharge			

Legend:
Square = prismatic cell; Circle = cylindrical cell; Triangle = coin cell
Bottom half = positive electrode; Top half = negative electrode
Materials:
carbon insertion compound (black), lithium metal (white), lithiated metal oxide (gray)

results similar to those of the direct measurement of OCP versus temperature. However, Hong *et al.* (1998) observed that this method produced entropic heat coefficients that were a function of rate, which may be attributable to inaccuracies in their measurement technique. Another calorimetric method is to subtract an estimated irreversible heat from the total heat. The overpotential heat is typically (and most accurately) estimated by direct calculation of the overpotential using OCP and operating voltage data (Lu *et al.*, 2007; Lu *et al.*, 2006a; Lu and Prakash, 2003; Lu *et al.*, 2006b).

A detailed discussion of the results gleaned from the relevant techniques for measuring total and reversible heat generation rate is available elsewhere (Bandhauer *et al.*, 2011). A few significant conclusions are discussed here. First, there are relatively few investigations (Al Hallaj *et al.*, 2000a; Song and Evans, 2000; Thomas and Newman,

2003a) that measure total heat generation for currents greater than 1*C*, and none higher than 2*C* (Table 2-1). In addition, the majority of studies have been conducted at one temperature (near nominal ambient: 20°C to 25°C), and few studies have investigated the impact of temperature on heat generation. For those that have investigated temperature influences, the range of temperatures is typically small. The studies of Saito *et al.* (1997) and Kobayashi *et al.* (1999) have the largest temperature ranges (20°C to 60°C and 25°C to 60°C, respectively), but they only tested batteries discharged at low current (*C*/10). Thomas and Newman (2003b) and Hong *et al.* (1998) tested higher rates, but with a more narrow temperature spread (15°C to 30°C and 35°C to 55°C, respectively). In both of these studies, no appreciable difference in heat generation was observed for the temperatures tested. Moreover, the measured overall heat generation for these batteries is not large (at most a peak of 84.5 W L^{-1} for the 0.92*C* rate at the end of discharge (Onda *et al.*, 2003)). Thus, small temperature changes inside the battery can lead to significant heat accumulation, which, in some cases, can be larger than the heat rejected by the device (Hong *et al.*, 1998). Thus, accurate measurement of the battery temperature and heat capacity is required for these techniques. In addition, as the rate increases, maintaining constant temperature may not be achievable with the IHC method, which was implied by Lu and Prakash (2003).

2.2. Thermal Modeling

Simulations studies can be subdivided into two main categories based on the overpotential calculation method: measurements-based, and detailed electrochemical models. Table 2-2 summarizes the simulation studies on lithium-based batteries based on experimental studies. For the majority of the previous investigations, overpotential and

entropic heat coefficient measurements gathered from experiments are used to predict the volumetric heat generation rate using the simplified expression in Equation 2.2 (Kim e*t al.* (2008; 2009) also included current collection resistance heat), which is inserted into the heat equation on a per unit volume basis as follows:

$$. \rho C_{\mathrm{p}} \frac{\partial T}{\partial t} = \nabla \cdot \left(k \nabla T \right) + \dot{Q}''' . \tag{2.6}$$

The first term is the heat stored by the battery, followed by the heat conduction and generation terms. Using appropriate boundary and initial conditions, the heat equation is applied to these cells and solved to determine the temperature distribution throughout the battery. For most of these studies, the only means of coupling the thermal field to the electrochemical heat generation is through the entropic heat, which is the product of temperature and the entropic heat coefficient. In contrast, Onda *et al.* (2006) presented a

Table 2-2: Summary of Experimental Thermal Simulation Studies

Investigation	Negative/Positive Electrode Material	Heat Generation	
		Equation	Temperature Dependency
Al Hallaj *et al.* (1999)	C/$LiCoO_2$	Equation 2.2	entropic only
Chen *et al.* (2006)	C/$LiCoO_2$		entropic only
Onda *et al.* (2006)	C/$LiCoO_2$		entropic heat and current distribution
Chen and Evans (1993)	Li/LiV_6O_{13}		entropic only
Chen and Evans (1994a)	Li/LiV_6O_{13} Li/$LiTiS_2$		entropic only
Chen and Evans (1994b)	Li/$LiTiS_2$		entropic only
Chen and Evans (1996)	C/$LiCoO_2$		entropic only
Chen *et al.* (2005)	C/$LiCoO_2$		entropic only
Kim *et al.* (2008; 2009)	C/ $LiNiCoMnO_2$	Equation 2.4	entropic only

simplified electrochemical model to predict current distribution along their spirally-wound cylindrical cell (OD = 18 mm, length = 65 mm). They assumed current flows only perpendicular to the wind direction, and that heat is transported in the radial direction only. Yet, no evidence of current (or state of charge) maldistribution was presented. Furthermore, in nearly all of these studies, except for Chen and Evans (1994b), who simulated a dynamic power profile, the battery was operated constant current.

The simulations studies that use detailed electrochemical models to predict cell performance and heat generation rate are summarized in Table 2-3. By and large, the electrochemical model of Doyle *et al.* (1993), and subsequent developments (Doyle *et al.*, 1996; Fuller *et al.*, 1994; Smith and Wang, 2006) have been adopted. In each of these models, lithium ion transport through the electrolyte is modeled using concentrated solution theory in which the driving force for mass transport is the gradient in electrochemical potential (Fuller *et al.*, 1994). Furthermore, the porous insertion electrodes consist of spherical particles with diffusion of lithium ions in the solid. The primary equations in these models are species and charge balances in the electrolyte and solid particles. In addition, Butler-Volmer expressions are used to represent the charge-transfer kinetics at the solid-electrolyte interface. These models are one-dimensional and applied across the thickness of the battery. The expressions for heat generation rate vary between studies, but are generally just local expressions of Equation 2.2 (*e.g.*, Gu and Wang (2000)) or corrections for non-uniform reaction rate across the thickness of the battery and side reactions (*e.g.*, Botte *et al.* (1999)). The operation of the cell can be sensitive to temperature variations due to its influence on various transport properties in

the battery. As shown in Table 2-3, the primary temperature-dependent transport properties used in these studies are ionic conductivity of the electrolyte, diffusion coefficient of the salt, and electronic conductivity and diffusion coefficient of lithium in the solid. Furthermore, it can be seen that only a few studies attempt to capture the effects of temperature on cell performance (Gomadam *et al.*, 2002; Srinivasan and Wang, 2003; Verbrugge, 1995), and most of these studies (except Smith and Wang (2006), who simulate battery performance in a dynamic power profile) are conducted at either constant current or voltage, which are not observed in EV and HEV applications.

A detailed analysis of battery thermal modeling studies is available elsewhere (Bandhauer *et al.*, 2011). It is clear that thermal management affects the performance of the battery in several ways. For low surface convection, high thermal resistance results in increased overall temperatures at the interior portions of the battery. Increasing the surface convection can mitigate the peak temperature rise, but does so at the expense of producing a substantial thermal gradient (Al Hallaj *et al.*, 1999; Chen and Evans, 1994a; Chen and Evans, 1996). Increasing the cell operating temperature also improves the electrochemical performance of the cell due to reduce mass transfer and kinetic overpotentials. Parts of batteries in closer thermal proximity to the cooling environment will generate more heat than the interior parts of the battery when current is uniformly distributed across the battery. As a result, the colder cells that generate more heat flatten the temperature gradient inside the battery (Pals and Newman, 1995b; Song and Evans, 2000). However, improved mass transport and kinetics allow additional current to pass through hotter sections of the battery, thus counteracting increased polarization for colder cells. This is clear from the work of Verbrugge (1995), who showed that the center

Table 2-3: Summary of Thermal Simulations Studies using Electrochemical Models to Predict Heat Generation

Investigation	Negative/Positive Electrode Material	Electrochemical Model	Heat Generation Equation	Operation Type	Temperature dependent parameters	*I-T* feedback simulated?
Pals and Newman (1995a; 1995b)	$Li/LiTiS_2$	Doyle *et al.* (1993)	Equation 2.2	constant *I*	electrolyte ionic conductivity and diffusion coefficient	No - although transport properties are T-dependent, feedback is on the potential only
Botte *et al.* (1999)	$C/LiNiO_2$	Fuller *et al.* (1994)	Rao and Newman (1997) plus side reaction	constant *I*	ion diffusion coefficients in the solvent, transference number, solid diffusion coefficients, ionic conductivity of electrolyte	No - transport properties are evaluated at 25°C only
Thomas and Newman (2003b)	$Li/ LiAl_{0.2}Mn_{1.8}O_{4-d}F_{0.2}$	Doyle *et al.* (1993)	given formulation	constant *I*	none given	No - simulation was isothermal
Srinivasan and Wang (2003)	$C/LiMn_2O_4$	Doyle *et al.* (1996)	Gu and Wang (2000)	constant *I*	all diffusion coefficients and conductivities	Yes - galvanostatic, but reaction distribution is temperature dependent
Smith and Wang (2006)	$C/Li(NiCoAl)O_2$ (2010)	1-D model in paper	given formula	constant *I*, Dynamic Power	solid and electrolyte diffusion coefficients, electrolyte conductivity	No - simulations are isothermal

Table 2-3: Continued…

Investigation	Negative/Positive Electrode Material	Electrochemical Model	Heat Generation Equation	Operation Type	Temperature dependent parameters	*I-T* feedback simulated?
Gomadam *et al.* (2002)	unknown	Doyle *et al.* (1993)	Gu and Wang (2000)	constant *I*	same as Pals and Newman (1995a)	Yes - galvanostatic, but reaction distribution is temperature dependent
Kumaresan *et al.* (2008)	C/$LiCoO_2$	Doyle *et al.* (1993)	Gu and Wang (2000)	constant *I*	solid-phase diffusion coefficient for negative electrode, mean molar activity coefficient of the salt, ionic conductivity and salt-diffusion coefficient of the electrolyte	No - temperature dependent properties cause voltage changes, not current distribution
Verbrugge (1995)	Li/Vanadium Oxide	Applied voltage use to solve for *I* and *T* fields	Equation 2.2	constant *V*	interfacial exchange current density coefficient, ionic conductivity of the electrolyte, thermal conductivity of the electrodes and electrolyte, heat capacity of electrodes	Yes

Table 2-3: Continued…

Investigation	Negative/Positive Electrode Material	Electrochemical Model	Heat Generation Equation	Operation Type	Temperature dependent parameters	*I-T* feedback simulated?
Song and Evans (2000)	Li/$LiMn_2O_4$	Doyle *et al.* (1993)	given formula	constant *I*	ionic conductivity and diffusion coefficient of electrolyte	No - voltage profile was modified for fixed current density

portions of the lithium vanadium oxide polymer electrolyte battery simulated using a 3-D model can produce twice the current as colder edge cells. In another study, Gomadam *et al.* (2002) summarized a previous investigation on lithium-ion 18650 cells and noted that for a cell cooled preferentially at the surface opposite the cell terminals, more current passes through the top of the cell because the colder cells have become more resistive. Several investigations have also shown that as the rate of discharge rate increases, the cell temperature at the end of discharge reaches a maximum, followed by a subsequent decrease. Botte *et al.* (1999) and Srinivasan and Wang (2003) showed that the discharge time decreases faster than the heat generation rate as the applied current increases. Therefore, as the rate was increased, the peak temperature achieved by the cell can decrease despite an increase in heating rate. However, if a battery is cycled repeatedly, as in an HEV application, without adequately removing the accumulated heat, the cell temperature can continue to rise (see, for example, Chen and Evans (1996)).

Very few investigators have conducted thermal modeling studies for batteries operating in HEV applications. Furthermore, in even these few studies, the performance of the battery is not adequately characterized. For example, in the study by Chen and Evans (1994b), the cell performance (*i.e.,* current and potential) for the Simplified Federal Urban Driving Cycle (SFUDS) was predicted from galvanostatic data previously collected on a $Li/LiTiS_2$ battery at one temperature using the Shepherd equation (Shepherd, 1965) to account for the effect of discharge rate. Thus, temperature feedback on the local current and heat generation rates was not incorporated. Smith and Wang (2006) simulated a 1.65 kWh lithium-ion battery pack operating in three different HEV driving cycles using their detailed electrochemical model. However, their simulations

assumed isothermal battery packs, which may not be realistic. Thus, although thermal modeling that correctly couples local current and heat generation is necessary to evaluate different thermal management strategies, there has been no model proposed that captures theses effects in HEV applications.

2.3. Thermal Management

Although obviously an important topic for various battery applications, there are very few studies conducting detailed investigations of battery thermal management strategies. This section reviews some of the thermal management techniques used in commercial HEVs and reported elsewhere in the literature.

The 2000 Honda Insight and 2001 Toyota Prius were the first commercially available hybrid electric vehicles, and the National Renewable Energy Laboratory (NREL) has conducted a series of thermal performance tests on these battery packs both inside (Kelly *et al.*, 2002) and outside (Zolot *et al.*, 2002; Zolot *et al.*, 2001) the vehicle. Both vehicles use multiple nickel-metal hydride batteries to recover and supply energy from and to the vehicle drivetrain. Both battery packs also contain multiple 7.2 V modules of six batteries, connected in series. The Prius pack is larger (38 modules, 273.6 V, 1.78 kWh) and the batteries are prismatic, while the Insight pack (20 modules, 144 V, 0.94 kWh) uses cylindrical D-sized batteries. The battery packs are both cooled using conditioned air taken from the cabin and exhausted to the ambient, and each pack contains special features to mitigate temperature maldistribution among cells. In the Prius pack, air flow is divided in parallel between each of the modules, each arranged with decreasing space between each module from the air inlet. This is an attempt to distribute the air more evenly across the pack. For the Insight pack, the six batteries in a

module are stacked onto one another, making a single column. The 20 modules are arranged in three rows of six, seven, and seven modules similar to an aligned tube-bank. Air is drawn through the aligned bank across the three rows in parallel. Special baffles designed to decrease airflow maldistribution hold the batteries in place and direct the air over the tubes. The first modules in each row are covered with a plastic sleeve, which is designed to increase the thermal resistance between these batteries and the cold air inlet stream to minimize the temperature difference between cells.

In general, the results from these studies show that air cooling of the battery packs can produce temperature differences within the packs. For example, in the out of vehicle tests on the Insight pack, Zolot *et al.* (2001) found that, generally, the temperature differential across the pack approached 3°C to 4°C when subjected to the US06 standard driving cycle (which reaches a ±5.34*C* rate about 20 times), with the hottest cells located near the air inlet, which is caused by insulating the first column of modules. Similarly, a 4°C to 5°C temperature difference was observed across the Prius pack when subjected to twelve consecutive 20-minute US06 power profile cycles (Zolot *et al.*, 2002). In addition, in the same study, the temperature in the Prius pack reached unsafe limits (55°C) during the second cycle of an aggressive SUV 25-minute test even when the battery was initially at 25°C.

In the tests conducted on the Insight and Prius battery packs, the true maximum temperature differential is not known. However, it is clear that to maintain fine temperature uniformity for lithium-ion battery packs (which have more inherent safety risks than nickel metal hydride packs), air may not be the best heat transfer medium. Due to their larger specific heats and densities, liquids may mitigate problems with both the

cell-to-cell temperature differences and maximum temperature rise. Using simple order of magnitude estimates, Bandhauer *et al.* (2011) recently showed that the maximum temperature difference is significantly larger for air cooling than water cooling due to the poorer thermal properties of air (*i.e.*, specific heat, density, and thermal conductivity). For example, at steady-state, thirty 50 mm OD and 100 mm tall cells arranged five by six generating a mere 30 W L^{-1} and cooled by either air or liquid moving at 288.9 m^3 hr^{-1} and 2.68 lpm, respectively, cause a maximum temperature differential of 8.19°C and 3.04°C, respectively. If maldistribution occurs and the flow rate is halved, the maximum temperature differentials increase to 11.65°C and 3.83°C, respectively. The difference in temperature rise between the two methods exists in spite of the Reynolds number and pumping power being several orders of magnitude lower for water than for air.

As an alternative to direct liquid or air-cooling, researchers at Illinois Institute of Technology (Al Hallaj and Selman, 2000; Khateeb *et al.*, 2005; Khateeb *et al.*, 2004; Sabbah *et al.*, 2008) have proposed placing the battery module in a liquid/solid phase-change material (PCM) to promote cell-to-cell temperature uniformity. The PCM studied was a paraffin wax, which has a low thermal conductivity. To reduce the temperature difference inside the battery pack, they propose inserting an expanded metal foam matrix inside the PCM, which increases the effective thermal conductivity to 3 W m^{-1} K^{-1} (Khateeb *et al.*, 2004). (Graphite flakes increase the thermal conductivity to 16 W m^{-1} K^{-1} (Sabbah *et al.*, 2008).) Sabbah *et al.* (2008) simulated and compared PCM and direct forced-air cooling of a large lithium-ion battery pack (7.34 kWh) intended for HEV applications. For direct-air cooling, the temperature differences are approximately 2°C and 4°C for 2*C* and 6.67*C* discharge, respectively, while they are only 0.03°C and 0.07°C

for the PCM. Similar results are obtained for the low rate discharge at 45°C. However, for the high-rate discharge, the PCM begins to melt substantially, thus its temperature rise is only 10°C with a temperature difference less than 0.5°C. In contrast, the temperature of the directly air-cooled batteries rose by more than 15°C, with temperature differences approaching 5°C. They also noted that increased surface convection increased the temperature difference.

Although it effectively minimizes the thermal gradient inside the battery pack, the PCM concept has some disadvantages. For example, the PCM increases the volume and weight of the overall battery pack. In the design by Khateeb *et al.* (2004), the weight and volume of the cells in each module are 746 g and 297 cm^3, respectively, while the combined weight and volume of the PCM/metal matrix are 466 g and 237 cm^3. Furthermore, complete melting of the PCM matrix is possible during multiple charge/discharge cycles. If the PCM completely melts, the low thermal conductivity of even the PCM/metal matrix creates an additional large thermal resistance between the cooling fluid and the batteries, thus causing the battery temperatures to rise further; *i.e.*, resulting in a worse situation than direct air cooling. Finally, since the melting range is tuned for cooling the batteries, warming in cold environments is difficult, and, due to the low thermal conductivity of the PCM/metal matrix, a temperature difference among the cells would be established if externally warmed.

In all the above strategies, the thermal management system is external to the batteries. Because of the low thermal conductivity of the battery, heat builds up, and the battery temperature rises. As an alternative, internal cooling of the batteries can be considered. This allows heat to be removed directly from the source without having to be

rejected through the surface of the battery. Parise (2000) proposed integrating thermoelectric coolers into the assembly of plate-type lead–acid batteries. In addition, Choi and Yao (1979) showed that forced circulation of the electrolyte in lead acid batteries can lead to improved heat removal and cell-temperature uniformity. Although the latter is not practical in lithium-ion batteries due to the high-reactivity of lithium, internal-cooling strategies for lithium-ion batteries should be explored further due to the potential for more uniform cooling both within an individual cell and among many cells within a pack. In addition, internal cooling strategies can dramatically increase the cooling surface area at the heat generation sites, which may significantly reduce the effective thermal resistance between the heat generation locations and the cooling fluid. This should reduce the temperature rise for the batteries, and allow the pack to withstand abusive thermal events. In addition, this may also limit SOC maldistribution created by temperature-induced current maldistribution.

2.4. Research Needs in Battery Coupled Physics Modeling and Thermal Management

The modeling efforts utilized thus far have not simultaneously accounted for the relevant physical fields present inside a lithium-ion battery: current-temperature feedback, state of charge tracking, current collection, and dynamic loading. As a result, the extent to which thermal management affects performance is not yet fully understood. In addition, the few investigations that do attempt to simulate dynamic performance are all limited either to isothermal operation or to data collected at a single temperature. Furthermore, although frequently encountered in HEV drive cycles, the electrochemical heat generation rate has yet to be measured and understood at rates greater than ~2C over

a wide range of ambient temperatures. This information is crucial to document the feedback between local current generation and temperature when subjected to different cooling strategies, especially as the battery is operated. Thus, there is a significant need to understand high rate heat generation and to improve electrochemical-thermal modeling of these batteries so that the impact of thermal management can be assessed in realistic applications.

It is also clear that existing thermal management strategies that rely upon external air cooling are insufficient to maintain minimal temperature rise and difference of the battery pack during operation. Liquid cooling is an improvement over air cooling, but its impact on performance has yet to be systematically assessed. Furthermore, these types of thermal management strategies are all external, and are thus limited by the low thermal conductivity of the battery (~1 W m^{-1} K^{-1}). This will cause thermal gradients to develop inside the battery, which may lead to non-uniform cycling of the battery during dynamic operation. In contrast, internally cooled batteries may substantially reduce this imposed thermal gradient while maintaining a small temperature rise, and, thus, merit further investigation.

Most of the research on lithium-ion batteries has been focused on improving the energy density of the battery materials. However, it is possible that when these materials are scaled up to a large pack for an HEV application, the packs are oversized to compensate for unwanted temperature induced capacity fade. For example, in an HEV application, the battery is repeatedly charged and discharged around a nominal SOC (*e.g.*, between 0.4 and 0.6) using a combination of brake energy, drive energy, and excess energy from the internal combustion engine. If the batteries themselves were cycled

more aggressively (*e.g.*, between a wider SOC from 0.1 to 0.9), the packs themselves could become smaller at the expense of increasing heat generation. It is not known if any external cooling strategy can be used to keep the pack below a specific threshold temperature when this is the case. However, it is possible that internally cooled batteries can overcome this thermal limitation to successfully reduce pack size further for a specific application, but further investigation is warranted.

2.5. Objectives of Current Investigation

One goal of the two-fold focus of the present study is to develop an experimentally validated, fully coupled electrochemical-thermal model that accounts for all the relevant physical mechanisms in a battery subjected to a dynamic load to assess the impact of thermal management on performance. The other goal is to develop an experimentally validated thermal-hydraulic model for an internal cooling system that removes heat from the interior of the battery to a passively circulating liquid vapor phase change fluid. This model is then coupled to the battery model to determine the pack size reduction possible for internal cooling relative to other external cooling techniques. Some intermediate steps are needed to accomplish these goals. First, electrochemical heat and current generation is characterized on a small, commercially available battery at high charge and discharge rates. This information is then used as the boundary condition for the characterization of the passive internal cooling system, and as a building block to drive the development of a parameterized electrochemical-thermal model that substantially reduces computational intensity. The specific objectives of this study are summarized as follows:

- Measure temperature dependent heat generation on a commercially available

C/$LiFePO_4$ battery (~1 Ah capacity) over a wide range of applied currents (-5*C* to 5*C*) and temperatures (10°C to 60°C) not previously characterized in the literature.

- Measure performance of passive internal cooling thermal management system that utilizes liquid-vapor phase change in microchannels (3.175 mm × 160 μm) over a range of heat inputs (120 to 6,500 W L^{-1}) and saturation temperatures (24°C to 33°C), and utilize performance information to develop a thermal-hydraulic model for this system.
- Develop a self-consistent, fully coupled battery model using the electrochemical thermal performance information gathered from the commercially battery tests.
- Determine the possible pack size reduction for three external cooling strategies (air, liquid, and edge cooling) and the passive internal cooling system on a scaled-up battery pack (9.8 kWh) that utilizes two different individual cell sizes (8 Ah and 20 Ah) using the battery and thermal-hydraulic models.

CHAPTER 3. ELECTROCHEMICAL HEAT GENERATION

As discussed Chapter Two and shown in Equation 2.2, the two most important quantities needed to determine the electrochemical heat generation rate are the cell overpotential (η) and the entropic heat coefficient (λ), which are calculated as follows:

$$\eta = \left(U - V\right) \tag{3.1}$$

$$\lambda = \frac{\partial U}{\partial T} \tag{3.2}$$

The entropic heat coefficient is typically calculated as the slope of the open circuit potential versus temperature at a fixed SOC, which, as described in Section 3.2.1, was determined on a sample battery placed in a temperature-controlled environmental chamber. In the chamber, heat is rejected from the battery primarily through natural convection, with some minimal forced convection. Thus, when the battery is subjected to high rates of discharge or charge for measurement of the overpotential, significant temperature rise of the battery can occur due to heat generated during operation. Assuming a lumped capacitance analysis, the temperature rise of the cell under consideration can be calculated as follows:

$$\Delta T_{\mathrm{rs}} = \frac{\dot{Q}}{hA_{\mathrm{s}}}\left[1 - \exp\left(-\frac{hA_{\mathrm{s}}}{\rho C_{\mathrm{p}}}t\right)\right] \tag{3.3}$$

For example, a small cylindrical cell (18 mm OD and 65 mm height) with a heat capacity

of 41.62 J K^{-1} can generate up to ~0.6 W at the 1*C* rate (Hong *et al.*, 1998). Assuming that heat is removed with a surface convection coefficient of 10 W m^{-2} K^{-1}, the temperature rise after 18 minutes is 10°C. The temperature rise will be larger at higher discharge and charge rates, which makes discerning the effect of temperature during normal operation (10°C to 60°C in the present study) on electrochemical heat generation prohibitive. Furthermore, it is expected that because the overpotential is not constant throughout discharge, the battery heat generation rate will be transient, with high rates expected near the end of charge or discharge. Hence, as described below, a test facility that specifically enables sufficiently high heat removal was developed and fabricated to ensure that the battery was kept at an approximately constant surface temperature throughout its transient operation.

In the present investigation, the impact of thermal management on the performance of a large lithium-ion battery was assessed during normal operation. The overpotential and entropic heat coefficients shown in Equations 3.1 and 3.2, respectively, are the critical parameters needed to model the heat generation inside the battery. As shown in Chapter Five, the overpotential measurements as a function of rate, temperature, and *DOD* can also be used to develop a simplified temperature dependent electrochemical model that substantially reduces computational effort and enables assessment of different thermal management strategies for lithium-ion batteries when subjected to dynamic loads for the first time. However, this information is not readily available in the literature and, thus, was measured in the present study. To measure the entropic heat coefficient, the dependence of open circuit potential on temperature is needed over a wide range of *DOD*. The battery is at rest during these measurements,

which enables utilization of the environmental chamber with a surface heat removal environment. However, as outlined above, distinguishing the overpotential over a wide range of temperatures at high rates requires better heat removal from the battery. In addition, because the overpotential is a strong function of *DOD*, the heat generation rate changes with time during operation. Thus, a second test facility that directs high velocity, temperature controlled air over the battery for forced convective heat removal while maintaining a constant battery surface temperature was designed and fabricated.

In this chapter, details of the selected commercially available C/$LiFePO_4$ lithium-ion battery designed for high rate applications are provided first. Next, the experimental facilities, procedures, data reduction, and associated uncertainties for calculating reversible heat are discussed. Subsequently, the second set of experiments conducted to measure irreversible heat over a wide range of charge and discharge rates (-5 A to 5 A) for a wide range of controlled surface temperatures (15°C to 55°C) is described. Finally, data collected on a battery sample tested subjected to an HEV simulation power profile are reported and compared to heat generation rate and performance data gathered for galvanostatic discharge and charge. Ultimately, the results presented here are used to:

1. Discern the effects of temperature on the total electrochemical heat generation rate
2. Aid the development of the corresponding thermal-hydraulic and parameterized electrochemical-thermal models.
3. Serve as inputs to the passive internal cooling experiments

3.1. Description of Tested Commercial Battery

Two samples of an 18650 commercially available battery from K2 Energy Systems (model LFP18650P) were tested in this investigation. The battery contained a carbonaceous negative electrode and $LiFePO_4$ positive electrode, separated by a porous plastic separator. The electrolyte consisted of 10 percent by weight of $LiPF_6$ salt and 30/30/30 percent by weight EC/DMC/EC aqueous solvent (Hodge, 2009). A sample battery was sectioned and the thicknesses of the composite electrodes (including current collectors) and separator were measured, with the results provided in Table 3-1. Figure 3.1 shows the sample unit cell for this battery, which consists of negative and positive composite electrodes and two porous separators. The composite electrodes are metal

Table 3-1: Summary of Commercial Battery Unit Cell Thicknesses

Component	Thickness [mm]
Composite Negative Electrode	**0.102**
Cu Current Collector	0.036
Electrode material (1-side)	0.033
Composite Positive Electrode	**0.132**
Al Current Collector	0.036
Electrode material (1-side)	0.048
Separator	**0.025**
Total Unit Cell	**0.284**

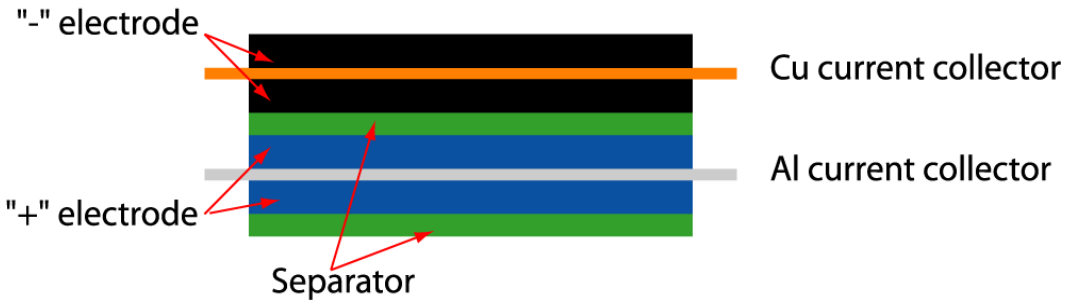

Figure 3.1: Battery Unit Cell Schematic

current collectors (copper for the negative and aluminum for the positive) coated on both sides with the porous electrode material. Thus, the unit cell thickness is 284 μm. Using the width of the jelly roll[2] (58.74 mm) and length of the smallest (positive) electrode (782.6 mm), the approximate heat generation volume is 13.08 mL. The estimated heat rates were divided by this volume to obtain the local volumetric heat generation rate. The published capacity for this battery is 1.25 Ah; however, as shown in Section 3.3.2, this was higher than the value measured at a 1 A discharge rate.

3.2. Reversible Heating

3.2.1. Experimental Facility and Procedure

The reversible heat generation was calculated using the entropic heat coefficient, which, in this investigation, was determined from the slope of OCP versus temperature at a specified SOC for both samples. The equipment used in this experiment is listed in Table 3-2, and a picture of the test fixture is shown in Figure 3.2. The OCP was measured using an Arbin BT-2000 battery cycling unit with a calibrated uncertainty

Table 3-2: Major Components in the Reversible Heat Generation Test Facility

Item	Description	Supplier	Part Number
Battery Charger with built-in DAQ	4 I/V channels: 25 A to 25 A and 0 to 10 VDC per channel; 8 type K thermocouple channels	Arbin Instruments, Inc.	BT-2000
Environmental Chamber	0.61 × 0.61 × 0.61 m interior space, -37°C to +177°C, 20% to 98% ±2% RH	Associated Environmental Systems	BHD-508
Thermocouples	Type K surface mount thermocouple probes with 1.83 m connecting wire	Omega	SA1-K-72-SC

[2] The jelly roll is the wound cylindrical portion of the battery that contains only the current collectors, electrode materials, and separators

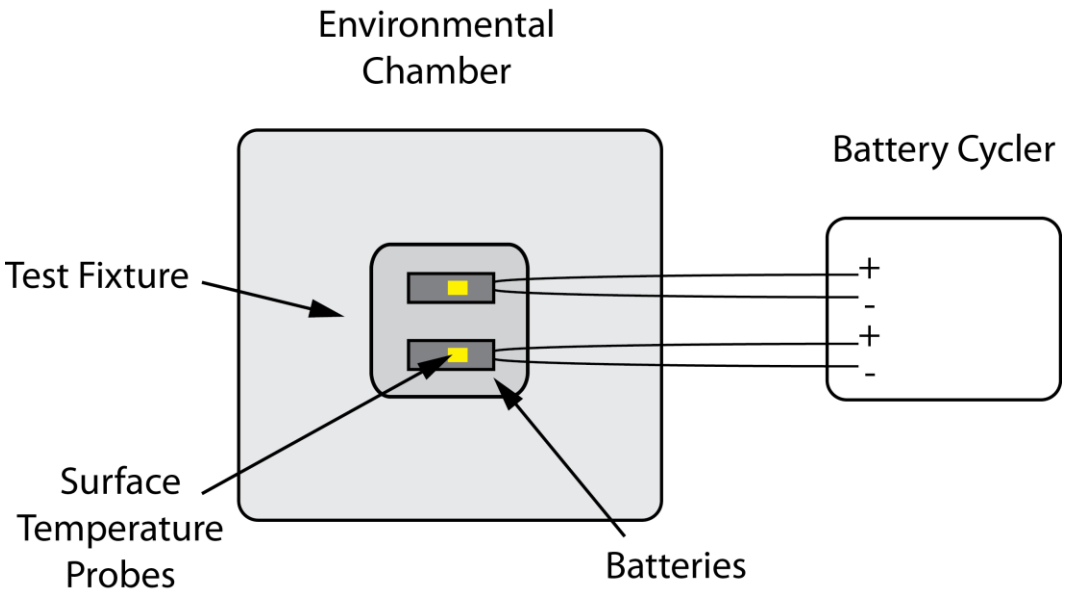

(a)

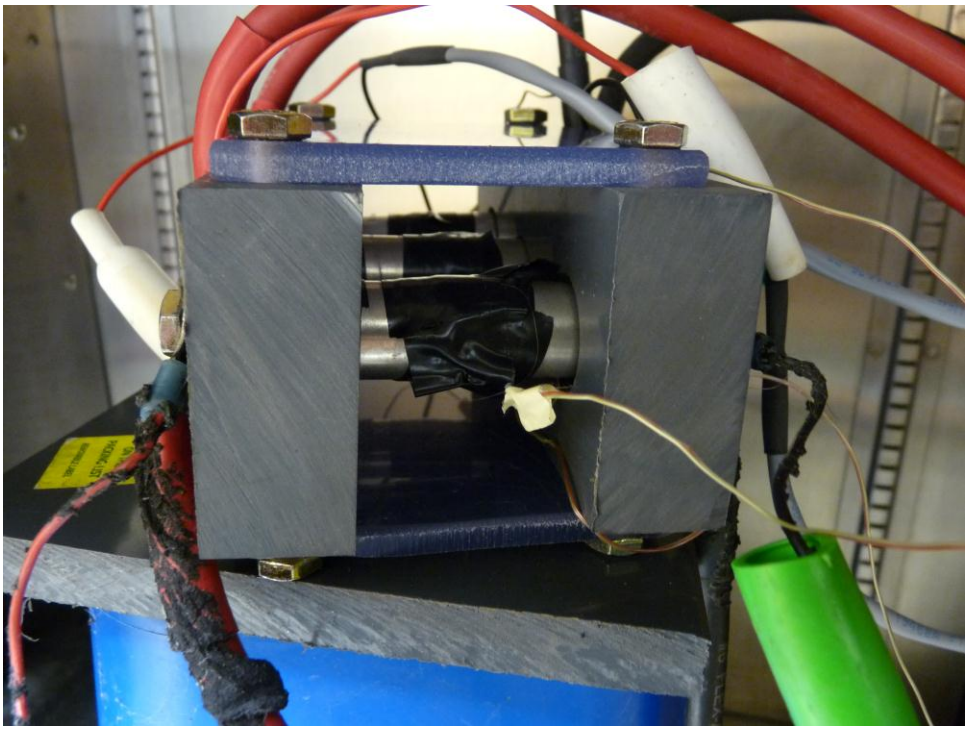

(b)

Figure 3.2: Reversible Heat Test Facilty: (a) Schematic and (b) Picture of Test Fixture

Table 3-3: Open Circuit Potential Test Procedure

Step	Description	Duration [hr]	Set Temperature(s) [°C]
1	Constant current at 0.5 A to 3.65 V	varies	30
2	Constant voltage at 3.65 V to 50 mA	varies	
3	Rest	1 (cumulative)	
4	Discharge at 50 mA to 0.15 Ah	3	
5	Rest	4	
6	Rest - take measurement	2	10
7		2	20
8		2	30
9		2	40
10		2	50
11		2	60
12		1	30
13	Discharge at 50 mA in 0.05 Ah increment	1	
14	Repeat Steps 6-13 13 times	18	10 to 60

summarized in Section 3.2.2 and detailed in Appendix A. Two cells were tested simultaneously, and two Type K surface mount temperature probes were affixed to the surface of each battery during operation (Figure 3.2). The fixture was placed in a programmable environmental chamber to ensure constant battery temperature over a wide range.

The testing procedure to obtain the open circuit potential versus temperature at specific SOCs is shown in Table 3-3 and Figure 3.3. To ensure that the battery begins at the same SOC for all tests, the battery was first charged at a constant rate of 0.5 A to a voltage of 3.65 V. Thereafter, the battery was held at 3.65 V and taper-charged to 50 mA. This charging procedure was conducted at a 30°C nominal ambient temperature to minimize any temperature-related effects. At this stage, the battery *DOD* was assumed to be 0 Ah. After charging, the battery was discharged at 50 mA for three hours to a *DOD*

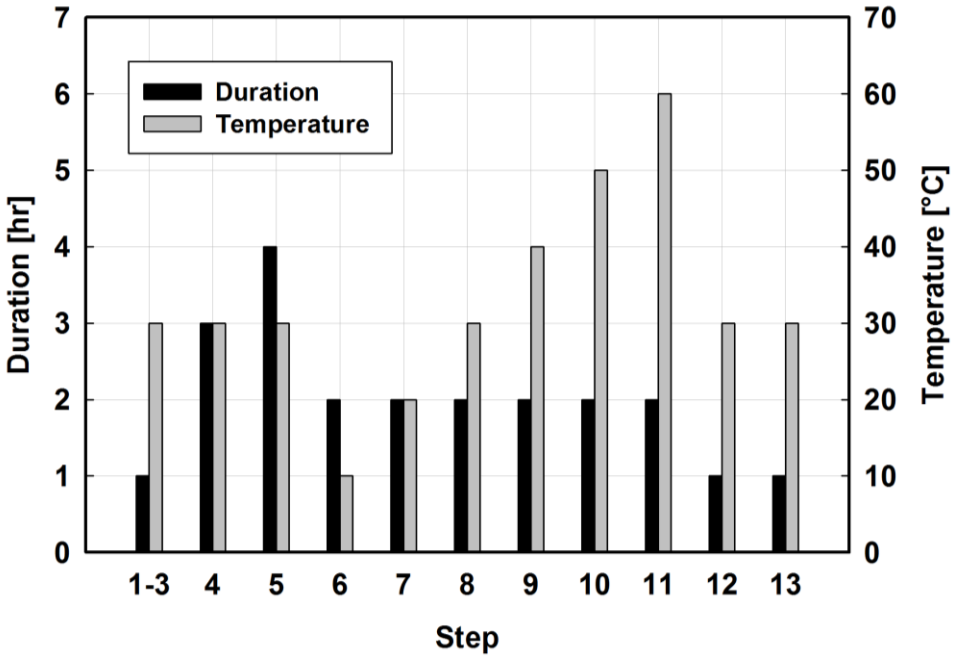

Figure 3.3: Open Circuit Potential Test Procedure: Step Duration and Temperature at each Step

of 0.15 Ah while maintaining a 30°C battery temperature. The battery was then allowed to rest for four hours at 30°C. Thereafter, the environmental chamber temperature was decreased to 10°C and held for two hours. The subsequent soak temperatures increased in 10°C increments up to 60°C, with each held for two hours. Data points were collected at each soak temperature beginning at 10°C once every minute. After the soak at 60°C, the soak temperature was decreased to 30°C, and held for 1 hour. Thereafter, the battery was discharged in 0.05 Ah increments at 50 mA up to a *DOD* of 0.95 Ah. A sample data set at a *DOD* of 0.55 Ah for Sample 1 is given graphically in Figure 3.4, which shows that both the cell potential and temperature easily reached steady state by the end of each two-hour soak period. For all tests, the slope of the last 20 data points (*i.e.*, 20 minutes) was never greater than 0.046°C min^{-1} or 0.080 mV min^{-1} for the average test temperature and potential, respectively.

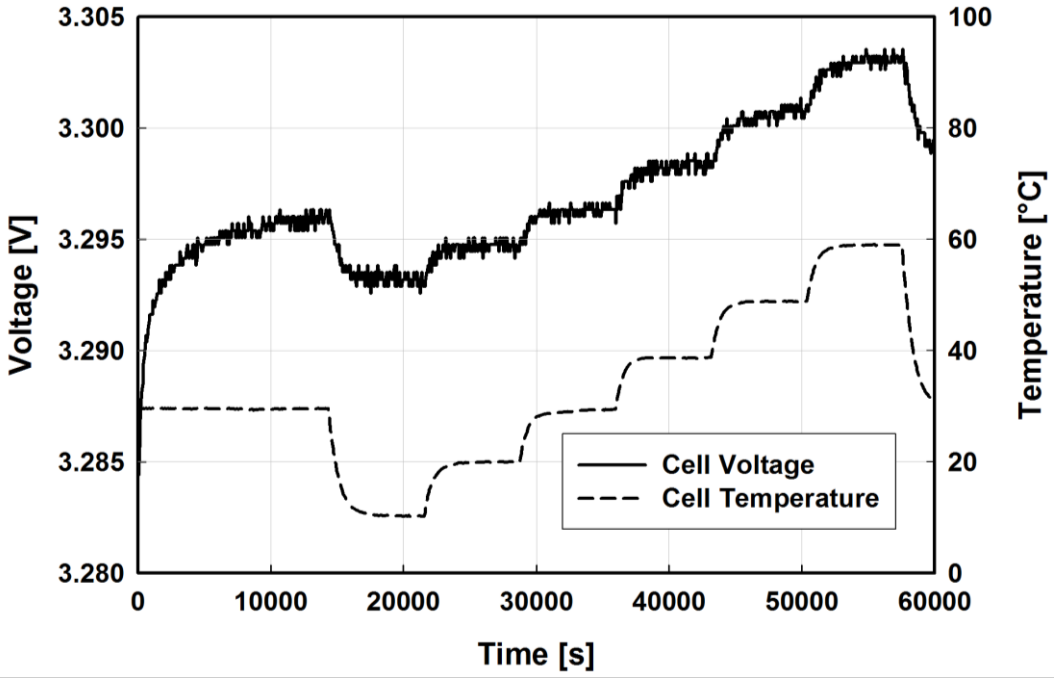

Figure 3.4: Voltage and Temperature Traces for Sample 1 at *DOD* = 0.55 Ah

3.2.2. Entropic Heat Coefficient and Associated Uncertainty

The dependence of OCP on temperature is shown in Figure 3.5 for Sample 1. This relationship appears to be linear over most of the range of *DOD* considered here, which has also been shown for other chemistries (*e.g.*, Hong *et al.* (1998) and Thomas *et al.* (2001)). The entropic heat coefficients and correlation coefficients (R^2) for Samples 1 and 2 are plotted as a function of normalized *DOD* in Figure 3.6. The entropic heat coefficient at a given *DOD* was determined from the slope of the OCP versus temperature graph using the method of least squares for a linear curve fit as follows:

$$\frac{\partial U}{\partial T} = \frac{\sum_{i=1}^{N}\left(T_i - \bar{T}\right)\left(U_i - \bar{U}\right)}{\sum_{i=1}^{N}\left(T_i - \bar{T}\right)^2} \tag{3.4}$$

For example, at a normalized *DOD* (Section 3.3.2) of 0.532, the OCP at 10.25°C,

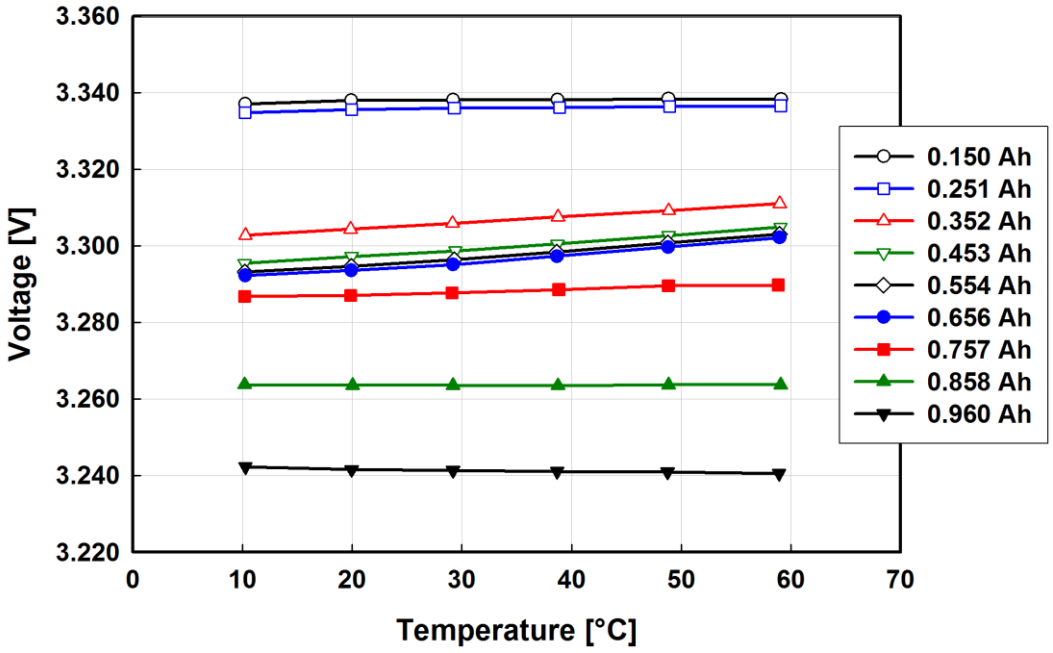

Figure 3.5: OCP versus Temperature for Sample 1

19.95°C, 29.35°C, 38.68°C, 48.81°C, and 58.98°C are 3.2932 V, 3.2947 V, 3.2964 V, 3.2984 V, 3.3008 V, and 3.3031 V, respectively. Therefore, the average OCP and temperature were 3.2977 V and 34.33°C and the entropic heat coefficient was 0.206 mV K^{-1}. As shown in Figure 3.6, there was little variation in both the magnitude and trend of entropic heat coefficient over the tested normalized *DOD* between the two samples. The entropic heat coefficient was generally positive, with a maximum near 0.2 mV K^{-1} for normalized *DOD*s between 0.35 and 0.7. The positive value indicated an endothermic heat effect upon discharge, and, because this heat was reversible, an exothermic heat release upon charging. (A detailed comparison between the reversible and irreversible heat generations is provided in Section 3.4.1.) The correlation coefficients in this range were near 1, suggesting a substantially linear relationship between OCP and temperature. When the state of charge was near zero or one, the correlation coefficients deviated significantly from unity, suggesting that the relationship was not linear. However, the

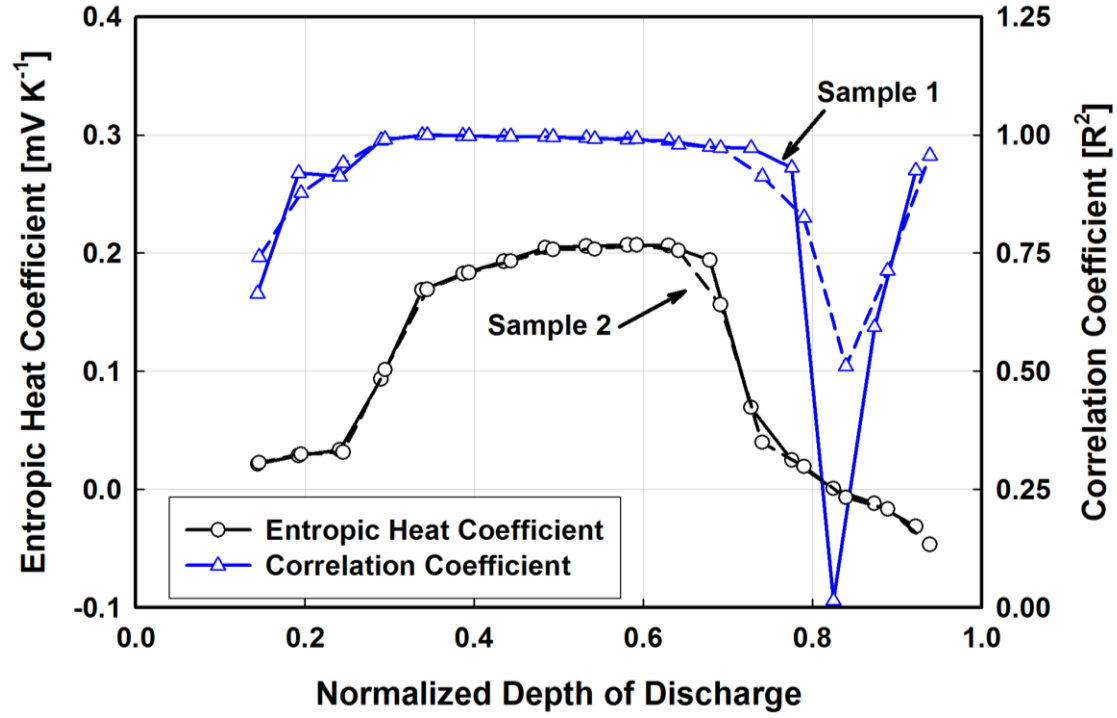

Figure 3.6: Entropic Heat Coefficient and Correlation Coefficient for Samples 1 and 2

non-linearity was most likely due to the uncertainty in measured voltage (maximum of ±0.428 mV for Sample 1; Table 3-4). For example, at the lowest normalized *DOD* (Section 3.3.2) for Sample 1, the difference in OCP between 10°C and 60°C was only 1.29 mV. Conversely, at a normalized *DOD* of 0.532, the difference in OCP between the same two temperatures was 9.91 mV. Thus, better accuracy on the measured voltage is required to improve the accuracy of the entropic heat coefficient when it is near zero.

The estimation of uncertainties in the measurements and results is shown in detail in Appendix A. Table 3-4 summarizes the bias and precision uncertainties for the measured voltage, temperature, and current assuming a 95% confidence interval. Using the procedure documented in Appendix A, the entropic heat coefficients were known to within ±9.93 μV K^{-1} and ±13.43 μV K^{-1} for Samples 1 and 2, respectively.

Table 3-4: Maximum Precision and Bias Uncertainties for the Reversible and Irreversible Heat Tests

Item	Detail	Value
Precision - OCP Tests		
Voltage		0.035 mV
Temperature		0.016°C
Precision - Operation Tests		
Voltage		0.729 mV
Temperature		1.29°C
Current		1.71 mA
$\partial U/\partial T$		3.44 μV K^{-1}
Bias		
Voltage	Channel 1	0.427 mV
	Channel 2	0.559 mV
Temperature	t/c 1	0.156°C
	t/c 2	0.156°C*
	t/c 3	0.170°C
	t/c 4	0.167°C
Current	0.25 A and 0.5 A	2 mA
	1 A to 5 A	50 mA
$\partial U/\partial T$		9.36 μV K^{-1}

*Assumed same uncertainty as thermocouple 1.

3.3. Irreversible Heating

3.3.1. Experimental Facility and Procedure

The irreversible heat generation rate was calculated from the cell overpotential (Equations 2.2 and 3.1). The OCP was determined first for the two sample batteries using the method described above. However, the battery heat generation during operation, coupled with the poor heat removal mechanisms in the environmental chamber, necessitated the development of an experimental setup that could maintain a constant battery temperature. Thus, a specially designed wind tunnel with built-in temperature control (Figures 3.7 and 3.8) was fabricated to ensure a constant battery surface temperature throughout all operation potential tests. The components of this test

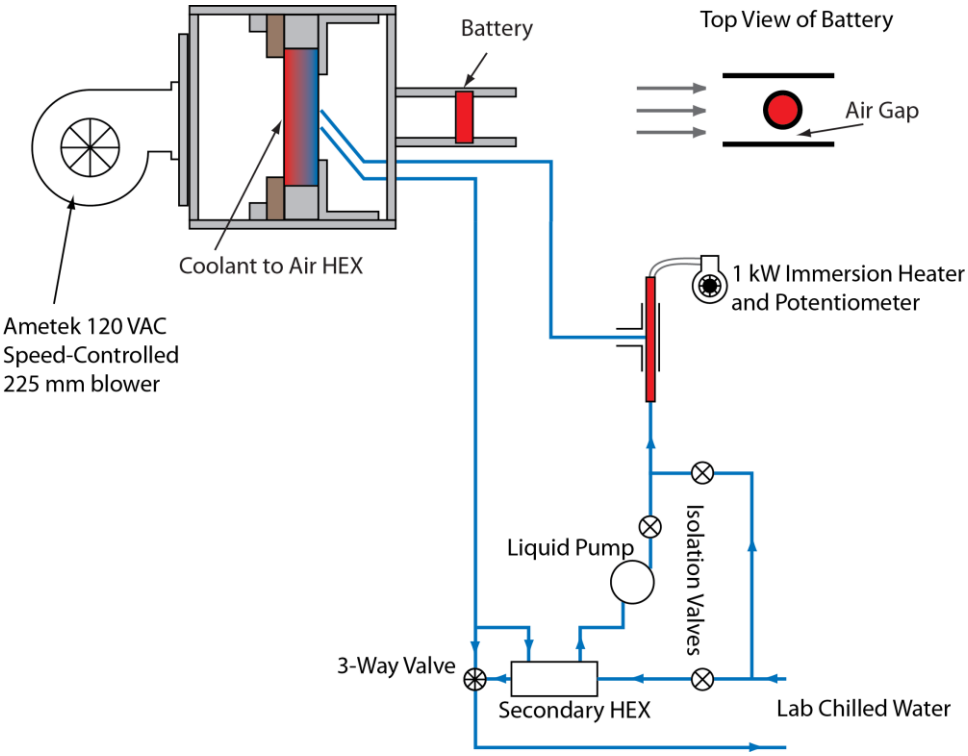

Figure 3.7: Schematic of Temperature-Controlled Wind Tunnel used for Battery Operation Tests

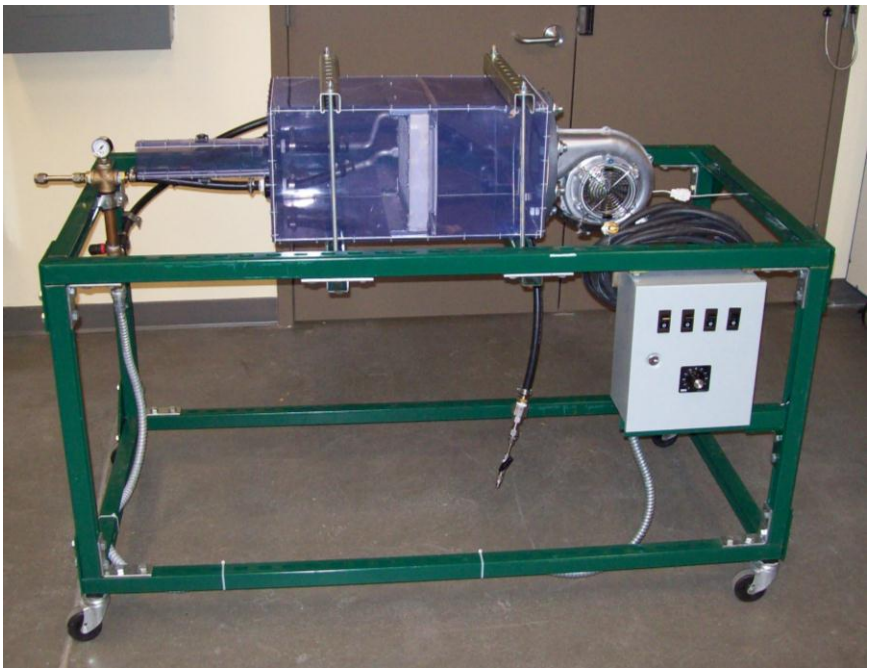

Figure 3.8: Picture of Temperature-Controlled Wind Tunnel used for Battery Operation Tests

facility are tabulated in Table 3-5. In this test facility, a centrifugal blower (AMETEK Nautilair 226 mm model 150330-00) forced air through a heat exchanger coupled to a primary coolant loop. The air temperature flowing over the battery was controlled by adjusting the primary coolant flow rate and temperature. The battery was installed in a rectangular duct (41 mm × 79 mm × 305 mm) downstream of the air-coupled heat

Table 3-5: Components in the Irreversible Heat Generation Test Facility

Item	Description	Supplier	Part Number
Centrifugal Blower	Nautilair 225 mm model, potentiometer speed control, 120 VAC	AMETEK	150330-00
Air-Coupled Heat Exchanger	Two-pass liquid loop cross-counter flow air-coupled aluminum brazed heat exchanger; 7 mm tall × 0.127 mm thick fin with 0.925 mm fin pitch, 40 tubes, 21 fins	N/A	Unknown: stamped Ford with 3350-4 identification
Mixing Fan	119 × 119 × 38 mm axial flow fan, 115 VAC, 18 W power input	ebm-papst	4600 Z
Thermocouples	Type K surface mount thermocouple probes with 1.83 m connecting wire	Omega	SA1-K-72-SC
Immersion Heater	Compact Cartridge-Style Immersion Heater Incoloy Element, 120 VAC, 1 kW, 124 mm Length	McMaster-Carr	4654T13
Liquid Pump	Gear pump with 90 VDC motor and speed controller	Micropump, Leeson	Series 5000 H21 (pump head), C42D28FK1C (motor), 174307.00 (controller)
Secondary Heat Exchanger	254 mm long tube in tube HEX: 12.7 × 8.89 mm interior copper tube, 19.05 × 15.75 mm exterior 316L stainless steel tube	N/A	N/A

exchanger. A mixing fan (EBM Papst model 4600 Z) was placed between the air-coupled heat exchanger and the battery duct to ensure uniform air temperature over the battery. The temperature of the primary coolant was controlled using a secondary heat exchanger that was coupled to a colder secondary coolant (building chilled water) and a 1 kW immersion heater (McMaster Carr part number 4654T13) for fine control. The secondary coolant could also be directly supplied to the primary coolant loop if colder temperatures than were achievable with the secondary heat exchanger were desired. Throughout each test, adjustments were made to the heater power and coolant flow rates to maintain the desired battery surface temperature. (It should be noted that it was the battery surface temperature, not the internal temperature, which is maintained constant in this manner – an isothermal interior was not possible to achieve without internal cooling of batteries.) The battery surface temperature was assumed to be the arithmetic average of 4 thermocouples placed on the surface of the battery (Figure 3.9). (It should be noted that these thermocouples were calibrated after the tests were completed because the adhesive containing the probes is damaged when calibrated in an oil bath.. In addition, one thermocouple was damaged after testing was completed, but before it could be calibrated; thus, stock calibration values were used for this thermocouple.) The maximum difference in an individual temperature measurement was at most ±0.88°C, while the largest difference between the average temperature of the four thermocouples was ±0.89°C (both at 5 A and a 45°C test temperature). In addition, there were a few tests where apparently erroneous temperature measurements on one thermocouple were observed (which was not the same thermocouple damaged before calibration). These included the discharge tests at 0.5 A and 25°C (at normalized *DOD*s of 0.220, 0.618,

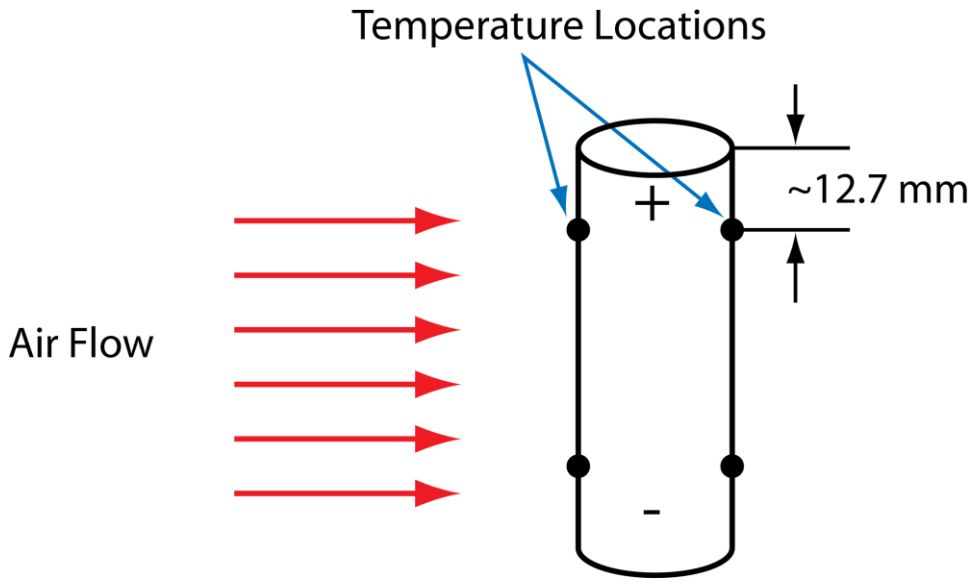

Figure 3.9: Thermocouple Locations on Battery during Operation Tests

0.878, and 0.879) and 1.0 A and 55°C (at a normalized *DOD* of 0.176) and the charge test at 0.5 A and 25°C (at a normalized *DOD* of 0.788). The temperature versus time graphs for this thermocouple over these three tests is shown in Figure 3.10. The temperature spikes occurred in very short pulses, and were not consistent with the preceding and subsequent trends. In addition, these spikes were not observed on the other three thermocouples, which all had measurements consistent with this thermocouple. Hence, these erroneous points for this thermocouple were removed from the analysis.

During operation, the battery was held at a constant current using the same battery cycler used in the OCP tests. Sample 1 was tested for both charge and discharge over a *DOD* range from 0.15 Ah to 0.95 Ah at rates of 0.25 A, 0.5 A, 1 A, 2 A, 3 A, and 5 A. The test procedure for both samples (Table 3-6) is described here. As in the method used for OCP, the battery was first charged at 0.5 A to 3.65 V, followed by a taper charge to

50 mA while maintaining a 25°C surface temperature. Upon charging, the battery was immediately discharged at 1 A to a *DOD* of 0.15 Ah, followed by a rest period. At this stage, adjustments were made to the heater power and coolant flow rates to achieve the

Table 3-6: Operation Voltage Test Procedure

Step	Description	Duration [hr]	Set Temperature(s) [°C]
1	Constant current at 0.5 A to 3.65 V	varies	25
2	Constant voltage at 3.65 V to 50 mA		
3	Discharge at 1 A to 0.15 Ah	0.15	
4	Rest	0.17 to 0.5	25 to Test T
5	Discharge at Test Rate to 2.5 V or 0.95 Ah	varies	Test T
6	If reach 2.5 V first, discharge at 0.5 A to 0.95 Ah		
7	Rest	0.17	
8	Charge at Test Rate to 4.2 V or 0.15 Ah	varies	

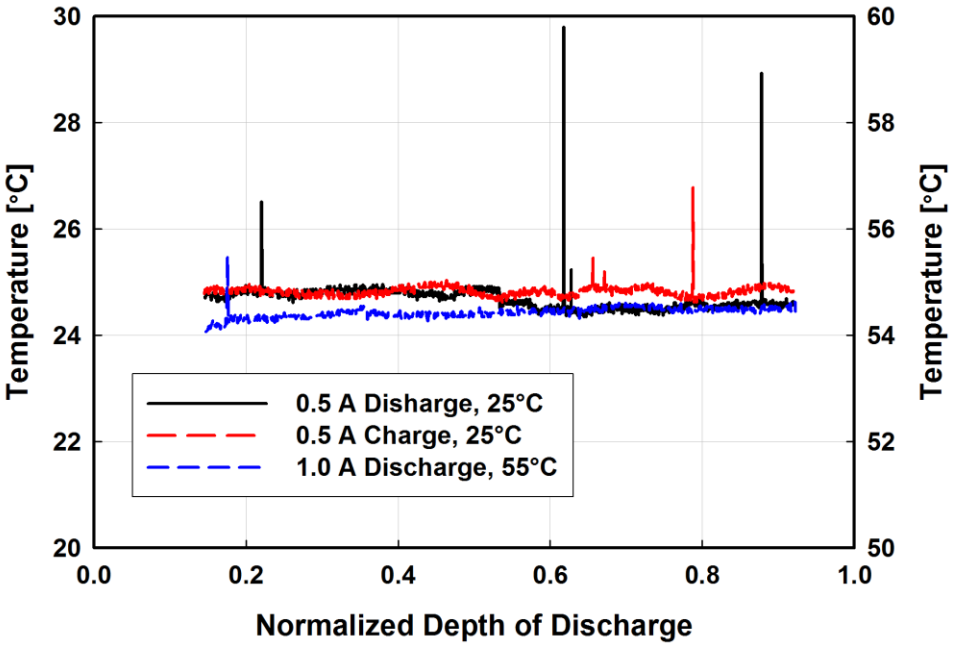

Figure 3.10: Temperature versus Time for Thermocouple 4 during the Following Tests: (a) 0.5 A discharge at 25°C, (b) 0.5 A charge at 25°C, and (a) 1.0 A discharge at 55°C

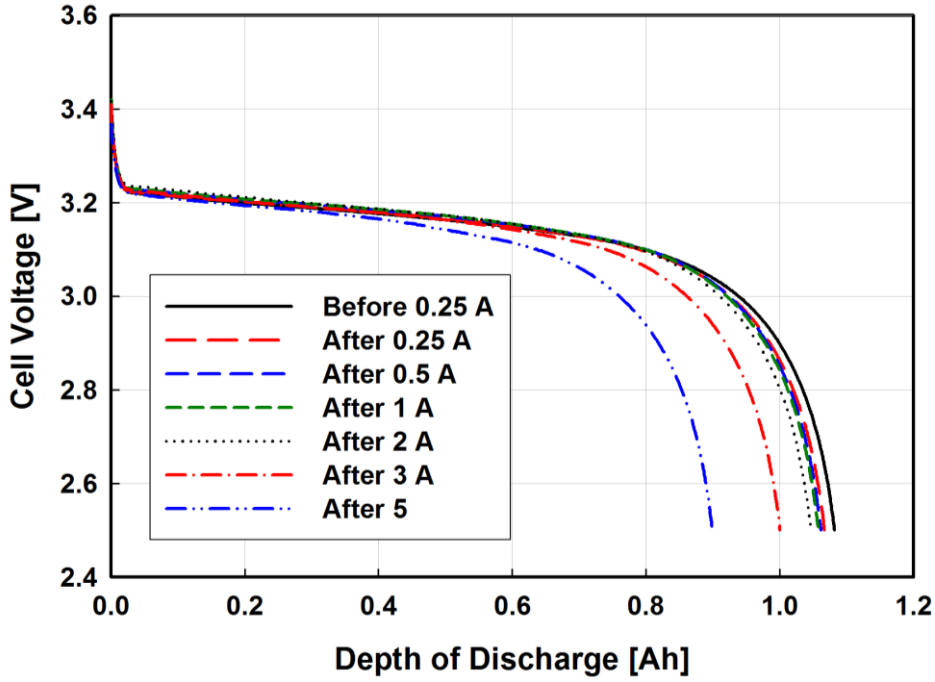

Figure 3.11: Reference Performance Tests for Sample 1

desired battery surface temperature. The maximum time elapsed during this adjustment was 30 minutes. The battery was then discharged at the testing rate to a *DOD* of 0.95 Ah, followed by a 10 minute rest period. At high discharge rates, it was not possible to discharge to 0.95 Ah prior to reaching the cutoff voltage (2.5 V). If this occurred, the battery was discharged to a *DOD* of 0.95 Ah at a rate of 0.5 A so that all charge tests began at the same *DOD*. After resting, charging at the same rate commenced until either a *DOD* of 0.15 Ah or an operation voltage of 4.2 V was reached.

To document and account for capacity fade and sample variability, the tests on battery Samples 1 and 2 were conducted in single current batches (Tables 3-7 and 3-8). A test batch for Sample 1 consisted of five separate tests at the same current, but at different temperatures, ranging from 15°C to 55°C in 10°C increments. After each test batch (including the OCP tests), a reference performance test was also conducted to

Table 3-7: Sample 1 Operation Voltage Test Batches

Batch	Test Description
1	OCP
2	Reference performance at 1 A
3	0.25 A performance
4	Reference performance at 1 A
5	0.5 A performance
6	Reference performance at 1 A
7	1.0 A performance
8	Reference performance at 1 A
9	2.0 A performance
10	Reference performance at 1 A
11	3.0 A performance
12	Reference performance at 1 A
13	5.0 A performance
14	Reference performance at 1 A

Table 3-8: Sample 2 Operation Voltage Test Batches

Batch	Test Description
1	OCP
2	Reference performance at 1 A
3	1.0 A at 15°C
4	1.0 A at 55°C
5	0.5 A at 25°C
6	3.0 A at 25°C
7	Reference performance at 1 A
8	Power cycle at 15°C
9	Power cycle at 35°C
10	Power cycle at 55°C
11	Reference performance at 1 A

Table 3-9: Reference Performance Test Procedure

Step	Description	Duration [hr]	Set Temperature(s) [°C]
1	Constant current at 0.5 A to 3.65 V	varies	25
2	Constant voltage at 3.65 V to 50 mA		
3	Rest	~0.17	
4	Discharge at 1 A to 2.5 V	~1	

document capacity degradation (Figure 3.11). The batteries in these reference tests were charged according to the same regimen as describe above, followed by a 10 minute rest and subsequent discharge to 2.5 V at 1 A (Table 3-9).

Sample 2 was tested primarily to document sample variation, and it was also used in a dynamic profile test (Section 3.4.3) at three temperatures: 15°C, 35°C, and 55°C. Sample 2 was subjected to charge and discharge rates of: 0.5 A and 3.0 A at 25°C, and 1.0 A at 15°C and 55°C. Three reference performance tests were conducted: after the OCP, repeatability, and dynamic tests.

3.3.2. Data Normalization

As stated previously, the sample batteries lose capacity with repeated testing, especially at increased charge/discharge rates. Figure 3.11 shows the operation voltage versus discharged capacity for the six reference capacity tests conducted on Sample 1. As can be seen in this figure, the capacity dropped precipitously as testing progressed, especially after the battery was tested at 3 A and 5 A. If the overpotential was calculated using the same *DOD* for the operation and OCP tests, significant errors may result, especially near a *DOD* of 0.95 Ah. Thus, all data collected were normalized using the estimated battery capacity at the 1*C* discharge rate (Cap_{Norm}). The normalizing capacity was calculated by averaging the reference test rate (1 A) and the discharge capacities before and after the tests conducted at each rate batch (Cap_{Before} and Cap_{After}, respectively) as follows:

$$Cap_{\text{Norm}} = \frac{2 + Cap_{\text{Before}} + Cap_{\text{After}}}{4} \tag{3.5}$$

Instead of iterating on the discharge rate, it was assumed that the 1*C* rate was the

Table 3-10: Estimated Battery Capacities for each Test Batch on Sample 1

Preceding Tests	Capacity [Ah]
OCP	1.041
0.25 A	1.037
0.5 A	1.032
1.0 A	1.030
2.0 A	1.026
3.0 A	1.012
5.0 A	0.975

arithmetic average of the measured capacity and the test rate applied for 1 hour (*i.e.*, 1 Ah). This is the source of the "2" in the numerator in the above equation. For example, the capacities before and after the 0.5 A tests were 1.067 Ah and 1.062 Ah, respectively. Thus, Cap_{Norm} was 1.032 Ah for this rate. Table 3-10 shows Cap_{Norm} for each test rate and the OCP tests for Sample 1. The discharge capacity in Ah was divided by the estimated Cap_{Norm} to obtain the normalized *DOD*. (It should be noted that the first reference test was conducted after the OCP tests. Therefore, it was assumed that the capacity fade was minimal, and, thus, the discharge capacity at the 1*C* rate determined from the first reference test sufficiently normalized the data.) For example, at a test rate of 0.5 A at 25°C, the normalized *DOD* at a discharge capacity of 0.523 Ah was 0.507. Figure 3.12 shows that the voltage curves for the reference tests nearly collapse onto the same curve when plotted versus normalized *DOD*. However, the voltage curve for the 5A test appears to be slightly lower than those for all other tests. For example, at a normalized *DOD* of 0.8, the operation potential is 21.4 mV lower for the 5 A test than for the 0.25 A test. In either case, these results appear consistent with the study by Liu *et al.* (2010), which shows that the capacity is controlled by the amount of cyclable lithium. Lithium is consumed when the negative electrode solid-electrolyte interphase is damaged

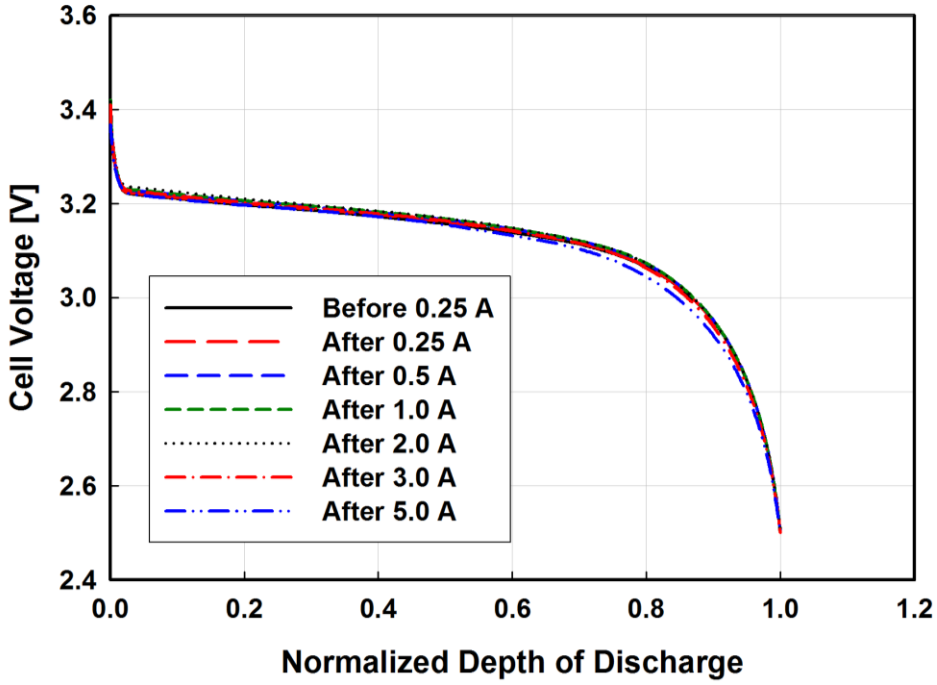

Figure 3.12: Normalized Reference Performance Tests for Sample 1

and subsequently repaired, which may explain the increase in resistance seen after the 5 A tests.

3.3.3. Sample Variation

Two samples were tested to observe variations due to processing and manufacturing. Figure 3.13 shows a comparison of the results for the two samples under the following conditions: OCP at 30°C, 0.5A, 1.0A, and 3.0A at 25°C, 1.0A at 15°C, and 1.0A at 55°C. When normalized (using capacities of 1.028 Ah and 1.025 Ah for the OCP and discharge tests, respectively, for Sample 2), the results show remarkably little variation between samples for these test conditions. The largest operation potential deviation appears at the end of discharge at the highest compared rate (3.0 A), with Sample 1 operating at 0.15 V below Sample 2. This resulted in a volumetric heat rate difference of 34.4 W L^{-1}, which is significant. However, this difference was most

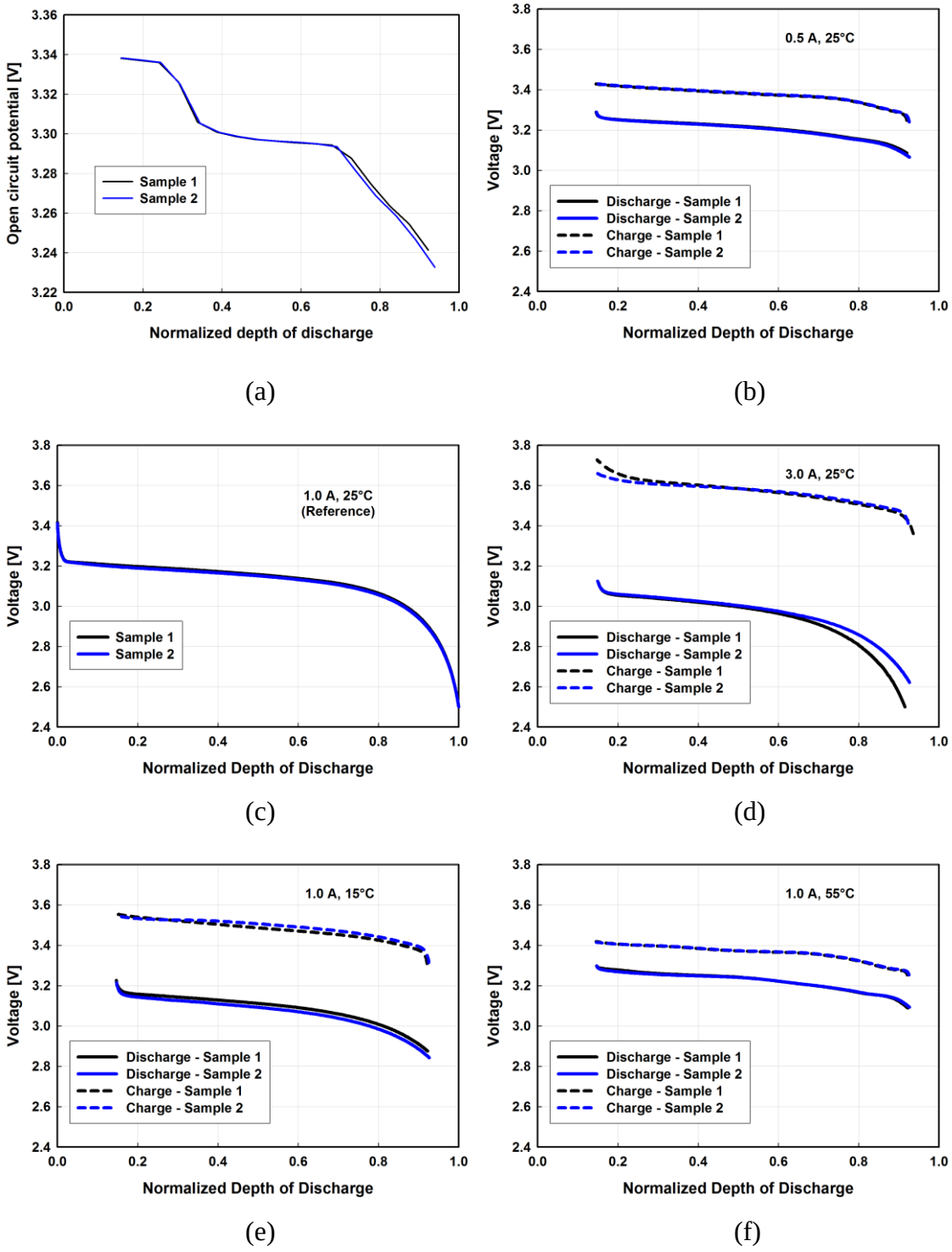

Figure 3.13: Comparison between Samples 1 and 2: (a) OCP at 30°C, (b) 0.5 A at 25°C, (c) 1.0 A at 25°C, (d) 3.0 A at 25°C, (e) 1.0 A at 15°C, and (f) 1.0 A at 55°C

likely due to a larger capacity fade for Sample 1, which was cycled much more than Sample 2.

3.3.4. Data Analysis and Uncertainty

After the open circuit potential and operation potential test results were normalized, the irreversible overpotential was calculated using Equation 3.1. However, because the OCP data were not collected at the same temperatures as for the operation potential tests, and OCP was collected at only 18 discrete normalized *DOD*s between 0.15 and 0.95, the OCP was calculated using two-dimensional linear interpolation, using a built in function (interpolate2DM) in *Engineering Equation Solver* (Klein, 2010) at unknown *DOD*s and temperatures. In addition, the temperature used for calculating the OCP was the arithmetic average of the four thermocouple temperature measurements collected throughout the test, which had a maximum difference between any two instantaneous measurements within a single test of less than 1.8°C (at 5 A charge at 45°C). Similarly, although the environmental chamber had the same temperature set point at each 0.15 Ah increment, there was a slight variation in temperature among the different *DOD*s for the OCP tests. However, the average temperature was within a maximum of only ±0.35°C at a nominal soak temperature of 30°C. Therefore, the arithmetic average of the temperatures measured at each *DOD* was utilized for calculating the necessary OCP for the overpotential.

An example calculation is summarized here. At a normalized *DOD* of 0.55, a discharge rate of 1 A, and an average test temperature of 34.91°C, the operation potential (V) was 3.1984 V. The measured OCPs at normalized *DOD*s of 0.532 and 0.581 were 3.2963 V and 3.2956 V, respectively, at 29.21°C and 3.2983 V and 3.2979 V, respectively, at 38.74°C. Using linear interpolation, the estimated OCP at a normalized

DOD of 0.550 for these same two temperatures were 3.2961 V and 3.2982 V, respectively, resulting in an OCP of 3.2973 V at 34.91°C. Therefore, the irreversible overpotential at this normalized *DOD* was 98.9 mV.

The remaining overpotentials for Sample 1 for discharging and charging for normalized *DOD*s between 0.2 and 0.9 taken at 0.044 normalized *DOD* intervals are shown in Figures 3.14 and 3.15, respectively. A discussion of the results (including comparison with the reversible heat) is provided in Section 3.4.1. Estimation of uncertainties in the measurements and results is shown in detail in Appendix A. A summary of the bias and precision uncertainties for the measured voltage, temperature, and current assuming a 95% confidence interval is provided in Table 3-4. Using the maximum total uncertainties in temperature, current, overpotential, and entropic heat coefficient, the maximum uncertainty for the total volumetric heat generation rate for Sample 1 varied from ±0.06 W L^{-1} at 0.25 A to ±2.84 W L^{-1} at 3 A.

3.4. Results and Discussion

In this section, the observed electrochemical volumetric heat rate results for constant current and dynamic loading of the battery are discussed in detail. To understand the relative importance of the two electrochemical heat generation rates, the relative magnitudes of the irreversible and reversible electrochemical overpotentials are presented and discussed first for both charge and discharge. The total estimated volumetric heat generation rate is then presented, followed by a discussion of performance characteristics and predicted heat generation using a vehicle power profile determined from the US06 High Speed Drive Cycle (USEPA, 1996). The latter is important to justify using the constant current heat generation rate data to develop the

parameterized electrochemical-thermal model.

3.4.1. Comparison of Reversible and Irreversible Heating

The irreversible and reversible overpotentials measured on Sample 1 are shown in Figures 3.14 and 3.15 for discharge and charge, respectively. The irreversible overpotential was calculated using Equation 3.1, and the reversible overpotential was calculated as follows:

$$\eta_{\text{rev}} = -T \frac{\partial U}{\partial T} \tag{3.6}$$

For example, at normalized *DOD*s of 0.532 and 0.581, the entropic heat coefficients were 0.2057 mV K^{-1} and 0.2068 mV K^{-1}, respectively. Using linear interpolation, the entropic heat coefficient was 0.2061 mV K^{-1} at a normalized *DOD* of 0.55, which resulted in a reversible overpotential of -62.5 mV at 30°C. The irreversible overpotential will always be positive for discharge, but negative for charge. Conversely, the reversible overpotential is independent of charge and discharge and only slightly dependent on temperature.

As shown in these figures, the value of the reversible overpotential was primarily negative for the *DOD* range in this investigation because the entropic heat coefficient was mostly positive (Figure 3.6). As expected, the irreversible overpotential was a strong function of rate. For example, at a normalized *DOD* of 0.506 and a test temperature of 35°C, the irreversible overpotential increased from 0.034 V to 0.369 V when the discharge rate increased from 0.25 A to 5 A. Similarly, the overpotential decreased from –0.048 V to –0.322 V over the same rates when charging. However, the change in irreversible overpotential versus rate depended strongly on the temperature. For

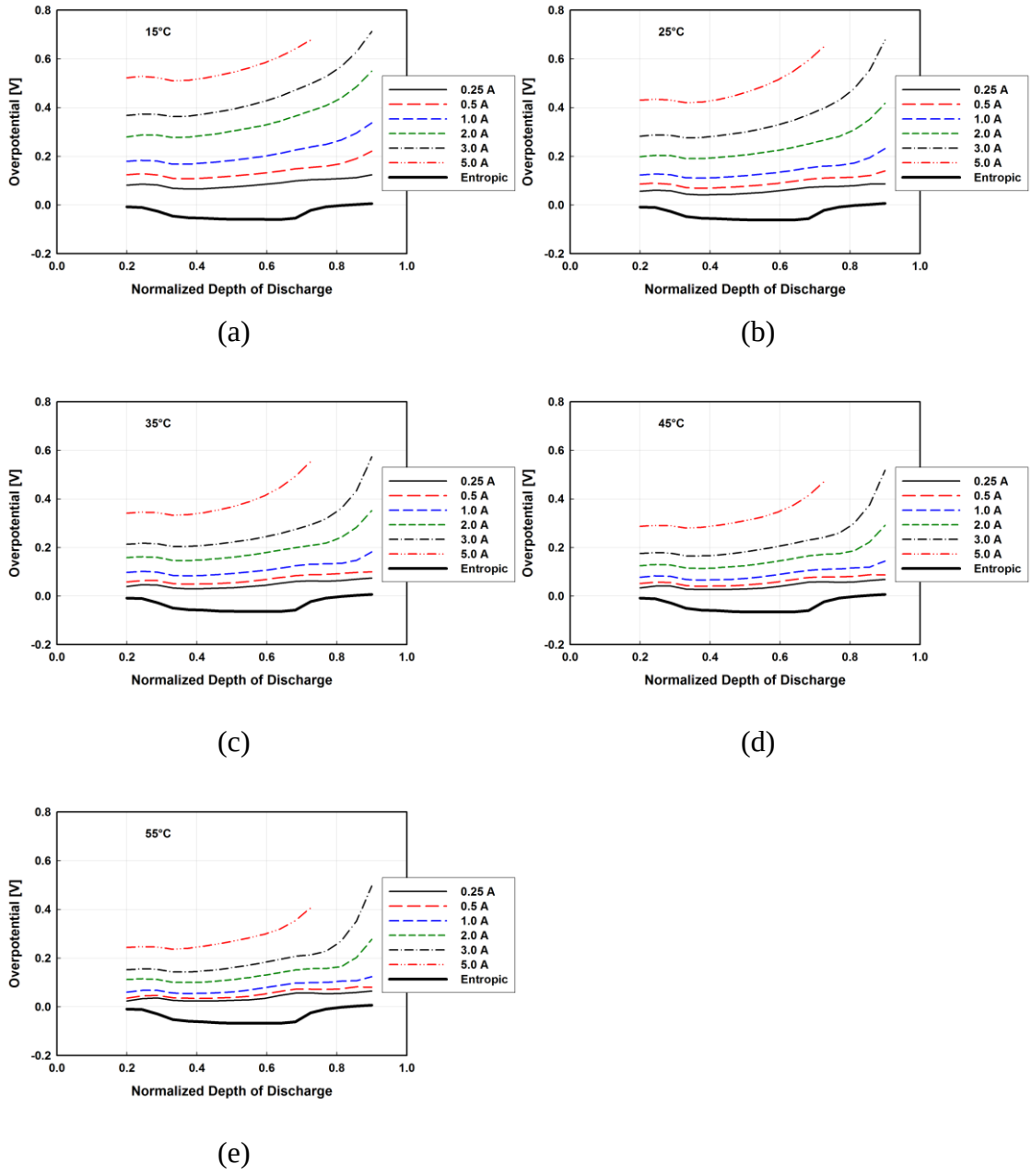

Figure 3.14: Reversible and Irreversible Discharge Overpotential for Sample 1: (a) 15°C, (b) 25°C, (c) 35°C, (d) 45°C, and (e) 55°C

example, at the same normalized *DOD* and rates, the discharge irreversible overpotential increased from 0.074 V to 0.546 V at 15°C, but only from 0.026 V to 0.270 V at 55°C. Similarly, the overpotential decreased from -0.085 V to -0.456 V at 15°C and from -0.036 V to -0.231 V for 55°C at the same conditions. This suggests that the

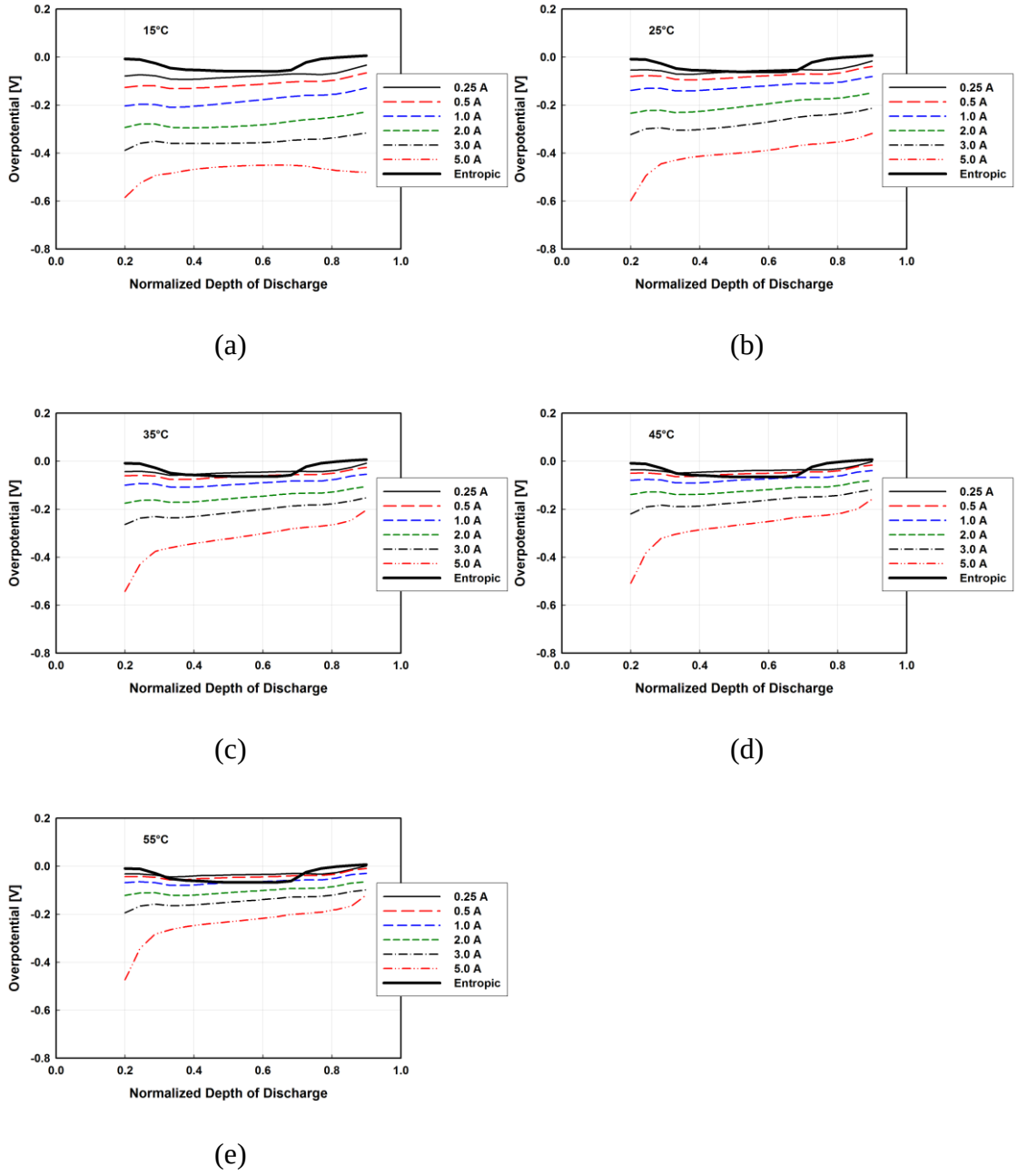

Figure 3.15: Reversible and Irreversible Charge Overpotential for Sample 1: (a) 15°C, (b) 25°C, (c) 35°C, (d) 45°C, and (e) 55°C

electrochemical heat generation rate was a strong function of temperature between 15°C and 55°C, especially for high rates. This is not surprising, because it has been shown that transport properties and kinetics are both strong functions of temperature in lithium-ion

batteries (Kumaresan *et al.*, 2008; Valoen and Reimers, 2005). The irreversible overpotential was also a function of normalized *DOD*. There also appeared to be a large overpotential increase near the end of discharge and decrease near the end of charge. This is because the electrochemical reactions can no longer be sustained due to the depletion of lithium in the negative and positive electrodes, respectively. This effect was more pronounced primarily as the rate increased and secondarily as the temperature decreased. This is because at low rates, the electrochemical reaction rates are sufficiently slow to overcome the mass transfer and kinetic limitations at lower temperatures. For example, at 3 A and 45°C, the overpotential ranged from 0.165 V to 0.259 V when discharged from a normalized *DOD* of 0.200 to 0.769, but it increased to 0.518 V at a normalized *DOD* = 0.900. Conversely, at 25°C, the irreversible overpotential at the same rate increased from 0.275 V to 0.429 V when discharged from a normalized *DOD* of 0.200 to 0.769 and ended at 0.677 V at 0.900. Moreover, the overpotential ranged from only 0.107 V to 0.220 V when discharged at 0.5 A and 15°C over the entire discharge range. This effect was even more pronounced for charging, where exothermic reversible heat augmented the irreversible heat between *DOD*s of 0.35 to 0.7. As a result, the rapid increase in charge overpotential near the end of charging appeared to be primarily a function of rate. For example, when charged at 5 A, the irreversible overpotential at normalized *DOD* of 0.2 (*i.e.*, near the end of charge) ranged from only -0.585 V to -0.474 V between test temperatures of 15°C and 55°C, respectively. However, between the normalized *DOD*s of 0.288 and 0.900, the overpotential at this same rate ranged from -0.450 to -0.493 and from -0.120 to -0.283 for these same temperatures, respectively.

Although the reversible overpotential was not a strong function of temperature,

the reversible overpotential appeared to be significant, even at the highest rates. This can be seen easily in the charge overpotential curves (Figures 3.14 and 3.15) because the reversible and irreversible contributions were both negative. However, as the temperature decreased, the irreversible overpotential increased significantly due to mass transport and kinetic limitations, while there was little change in the reversible overpotential. Thus, the relative contribution of the reversible heat to the total electrochemical heat decreased with decreasing temperature. For example, at 55°C, the ratio of reversible to irreversible overpotential was 0.292 at a 5 A charge rate and a normalized *DOD* of 0.506. In contrast, this ratio decreased to 0.197 and 0.130 at 35°C and 15°C, respectively. For discharge at the same rate, this ratio changed from -0.109 to -0.250 as the temperature increased from 15°C to 55°C. The impact of reversible heat on the total heat evolved is not clear for a battery that is being rapidly cycled in an HEV application due to the changing relative impacts as both the *DOD* and rate change. Nevertheless, it is clear that reversible heating will be significant. This is discussed in detail in Section 3.4.3.

3.4.2. Total Volumetric Heat Generation Rate

Using the overpotential results from Figures 3.14 and 3.15 with the applied current and estimated unit cell volume (13.08 mL), the total volumetric heat generation rate was calculated as follows:

$$\dot{Q}''' = \frac{I}{v_{\text{nom}}}\left(U - V - T\frac{\partial U}{\partial T}\right) \tag{3.7}$$

The current was positive and negative for discharging and charging, respectively. For example, the reversible and irreversible overpotentials at a normalized *DOD* of 0.55 and

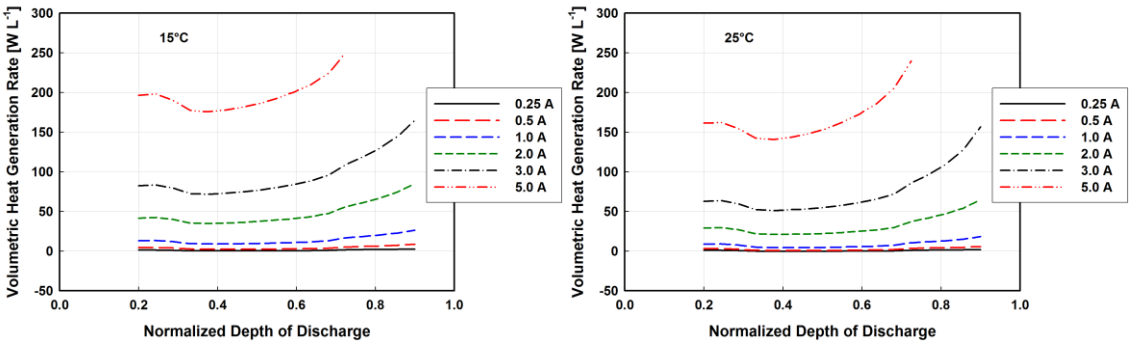

(a)

(b)

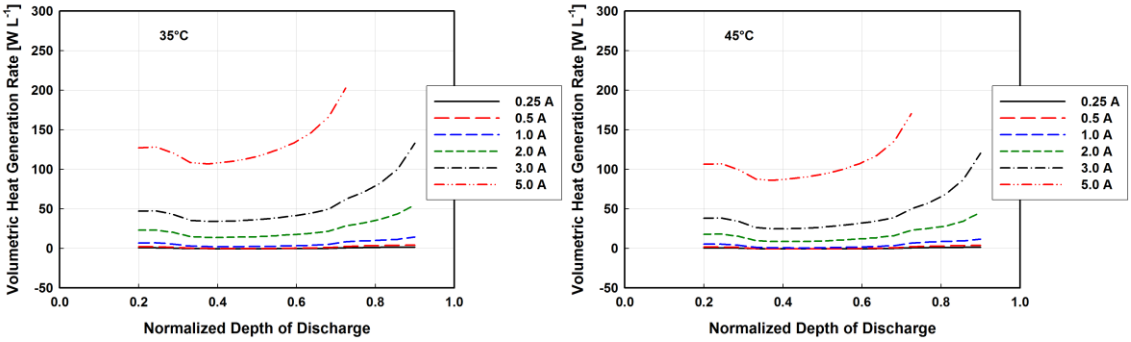

(c)

(d)

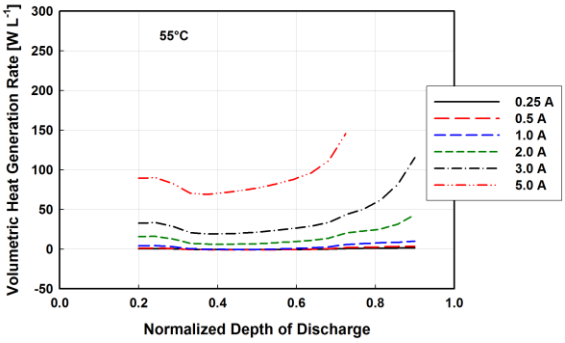

(e)

Figure 3.16: Total Discharge Volumetric Heating Rate for Sample 1: (a) 15°C, (b) 25°C, (c) 35°C, (d) 45°C, and (e) 55°C

a temperature of 34.91°C were -63.5 mV and 98.9 mV, respectively, at a discharge rate of 1 A. Therefore, the total volumetric heat rate for this data point was 2.71 W L^{-1}.

The results for Sample 1 are shown in Figures 3.16 and 3.17 for discharging and

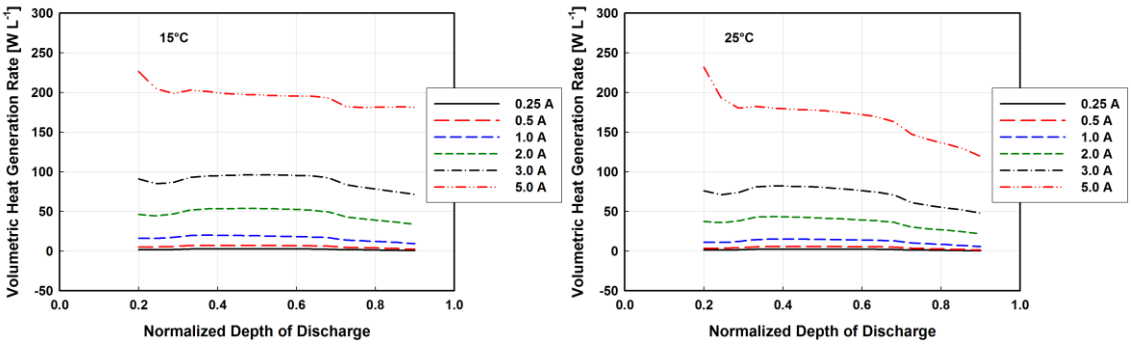

(a)

(b)

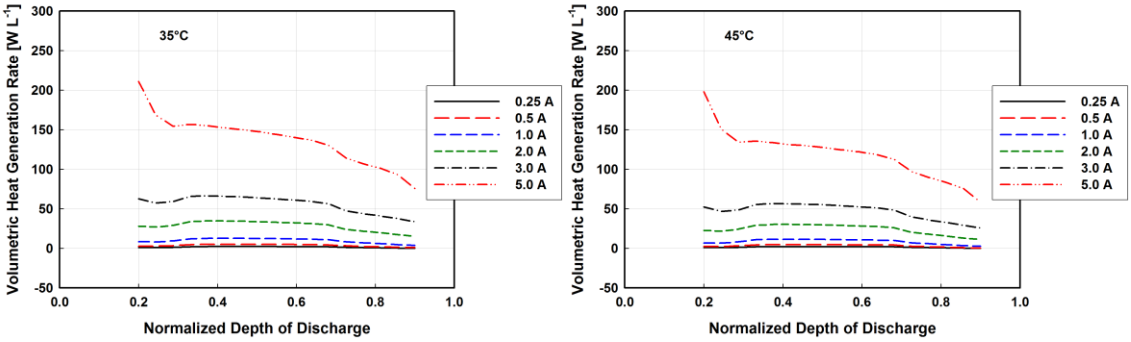

(c)

(d)

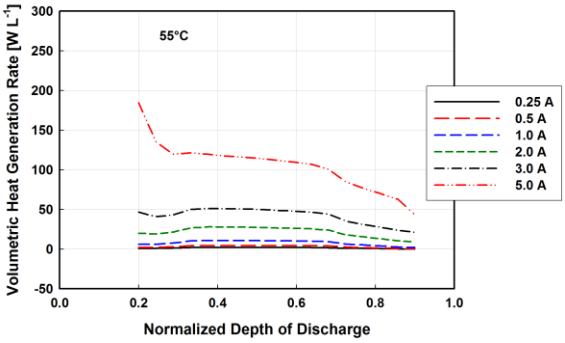

(e)

Figure 3.17: Total Charge Volumetric Heating Rate for Sample 1: (a) 15°C, (b) 25°C, (c) 35°C, (d) 45°C, and (e) 55° C

charging, respectively. The magnitudes of total volumetric heat generation rate appear to be consistent with previously measured values on different chemistries. For example, at 35°C and a discharge rate of 1 A (which is nominally the 1*C* rate), the total volumetric

heat rate ranged from 1.98 W L^{-1} to 14.4 W L^{-1} between a normalized *DOD* of 0.2 and 0.9. By comparison, the volumetric heat generation rate ranged from 0 to 27.7 W L^{-1} at the same temperature for a variety of lithium-ion batteries tested by Al Hallaj *et al.* (2000a) with different carbon-based negative electrodes and a $LiCoO_2$ positive electrode (Bandhauer *et al.*, 2011).

When compared to the irreversible overpotentials, the total volumetric heat rate appeared to be strongly influenced by the reversible heat rate. For example, there was a significant reduction in the total discharge heating rate over the normalized *DOD* range of 0.35 to 0.7, where the entropic heat coefficient was at its maximum values (Figure 3.6). Although there was an irreversible overpotential increase from 0.204 V to 0.214 V, the total volumetric heat generation rate decreased from 35.4 to 35.0 W L^{-1} as the normalized *DOD* increased from 0.33 to 0.46 for a discharge rate of 3.0 A at 35°C. Similarly, charge heating was increased over the same range. For example, as the normalized *DOD* decreased from 0.73 to 0.64, the magnitude of the irreversible overpotential increased slightly from -0.183 V to -0.195 V while the total heat rate increased from 47.3 W L^{-1} to 59.3 W L^{-1}. In addition, as the end of operation was approached, there was a larger rise in total heat rate for discharge and a smaller rise for charge than would be expected if only the irreversible overpotential were considered. This can be clearly seen in the total heat generation rate for charging at 5 A and 15°C, which varied only between 180.8 W L^{-1} and 226.8 W L^{-1}. To further illustrate the influence of entropic heating on heat generation, Figure 3.18 shows the reversible, irreversible, and total heat generation rates for charging and discharging at 3 A and 35°C. Although positive during charge, the reversible heat rate was mostly negative due to the

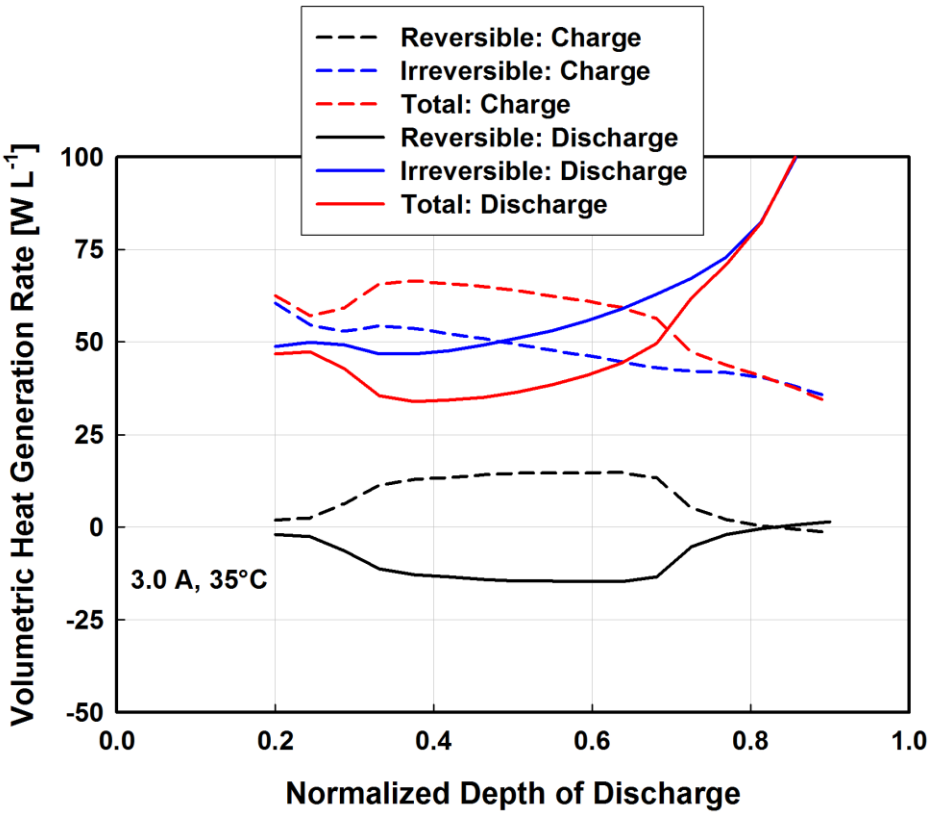

Figure 3.18: Reversible, Irreversible, and Total Volumetric Heat Generation Rates for Charging and Discharging at 3.0 A and 35°C

primarily positive entropic heat coefficient (Figure 3.6). As a result, although the irreversible heat rates were similar, the total charge heat rate was significantly higher than the total discharge heat rate. For example, at a normalized *DOD* of 0.55, the irreversible heat rates were 47.7 W L^{-1} and 53.4 W L^{-1} for charge and discharge, respectively, while the total heat rates were 62.3 W L^{-1} and 38.5 W L^{-1}, respectively. Therefore, the reversible heat caused the spike in total heat rate at the end of charge to be less than the corresponding spike for the discharge at the end of discharge.

To further understand the impact of reversible heating on the total volumetric heat, Figure 3.19 shows the absolute value of the ratio of total reversible to total irreversible heat energy generated for discharge and charge, respectively. The ratio

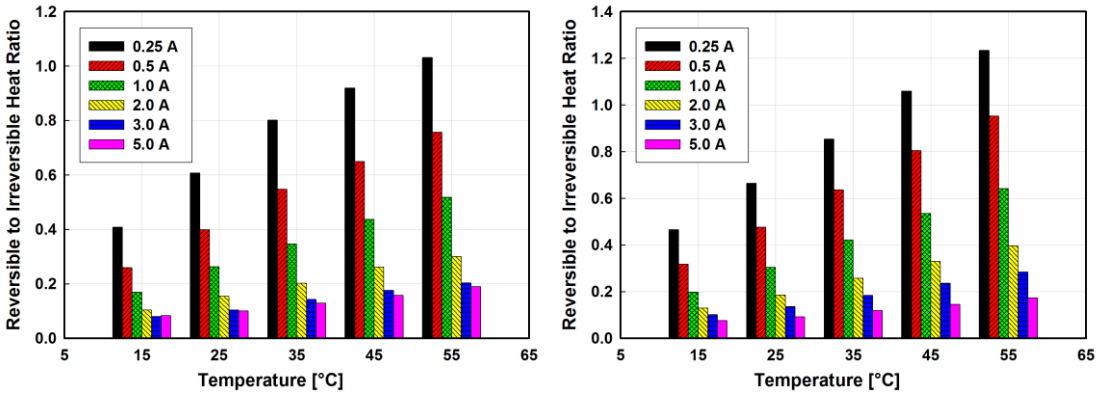

Figure 3.19: Ratio of Cumulative Reversible Heat to Irreversible Heat (Absolute Values) for (a) Discharge and (b) Charge

increases as the temperature increases for all rates. As the temperature increased, the cell overpotential decreased, while the reversible heat remained approximately the same over the tested test range. In addition, the overpotential increased with rate, which caused the ratio to decrease. It is clear that the irreversible heat dominated in all but a few cases, especially at the higher rates and lower temperatures. However, reversible heat was not a negligible quantity, accounting for a minimum of 7.5% of the total heat when charged at 15°C and 5 A. This significant influence of reversible heating may be attributable to the cell design, which was intended for high rate applications. The total electrode material thickness (162 μm) was only 57% of the total unit cell thickness (284 μm, Table 3-1). In other cell designs intended for higher energy density, the total electrode thickness may be a higher percentage, which significantly increases the mass transport resistance and may dominate any temperature related effects. However, because this is the first study to adequately control battery temperature during measurement, additional research on alternative battery designs is needed to better understand these phenomena.

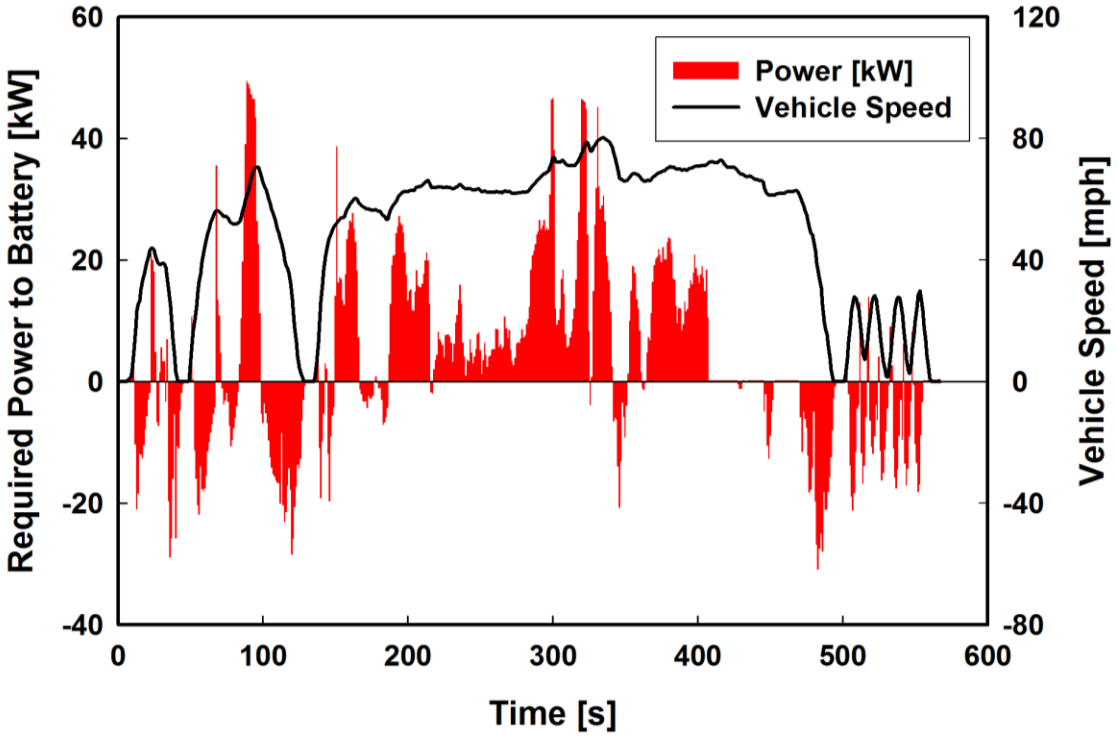

Figure 3.20: Representative Speed Profile and Requisite Pack Power Simulation (Melsert, 2009)

3.4.3. Heat Generation under Dynamic Load

Coupled electrochemical-thermal modeling consumes significant computational resources. As described in Chapter Five, the data collected in the present study are used to reduce computational effort so that different thermal management strategies can be assessed for batteries subjected to realistic dynamic loads. However, all test data were collected for constant current charge and discharge, which may not be applicable for HEV applications. Therefore, after the above tests were completed, Sample 2 (the less cycled battery) was subjected to the US06 drive cycle, which represents aggressive highway driving, to validate using the constant current data for dynamic battery simulation. Figure 3.20 shows representative battery power requirements for an HEV

application with a 9.6 kWh battery pack (Melsert, 2009). For the present investigation, it was assumed that 3000 individual batteries (39.23 L) were required to replace the existing battery pack, and thus the required power was scaled accordingly. (It should be noted that the battery power was determined using the stock calibrated voltage measured by the battery cycler during the tests due to calibration occurring after the tests were completed. However, the difference in power calculated using the calibrated voltage is at most 0.017% different than using the stock calibrated voltage. Therefore, all calculations in this section use the calibrated value.) The battery was placed in the same wind tunnel as for the operation voltage tests, where the surface temperature was maintained at 15°C, 35°C, and 55°C. The battery was cycled beginning at a normalized *DOD* of 0.49. The constant power required from and delivered to the battery was controlled with the Arbin BT-2000 battery controller used previously.

This experiment was conducted to answer the following questions:

- Can constant current data reasonably predict the performance of a dynamic power profile?
- Is it better to use constant current or dynamic profile data to predict the heat generation rate in an HEV application?
- What are the effects of reversible heating during an HEV simulation?

In the following discussion, *Predicted* values refer to predictions based on the previously collected constant current data on Sample 1, whereas *Measured* refers to the data collected during the dynamic simulation on Sample 2. The predicted data were linearly interpolated without compensation for the differences between the actual temperature and the measured temperature during the power simulation test. Using the arithmetic average

values of the four thermocouples throughout the duration of each test, the largest difference between the two temperatures was only 2.14°C (52.82°C and 54.96°C during the power simulation and discharge at 2.0 A, respectively). However, this temperature difference was accounted for in the electrochemical-thermal model described in Chapter Five.

Figure 3.21 shows the relative error between predicted and measured values, defined as follows:

$$Relative\ Error = \frac{Predicted\text{-}Measured}{Measured} \tag{3.8}$$

For example, at a normalized *DOD* of 0.520 and a required discharge power of 8.073 W

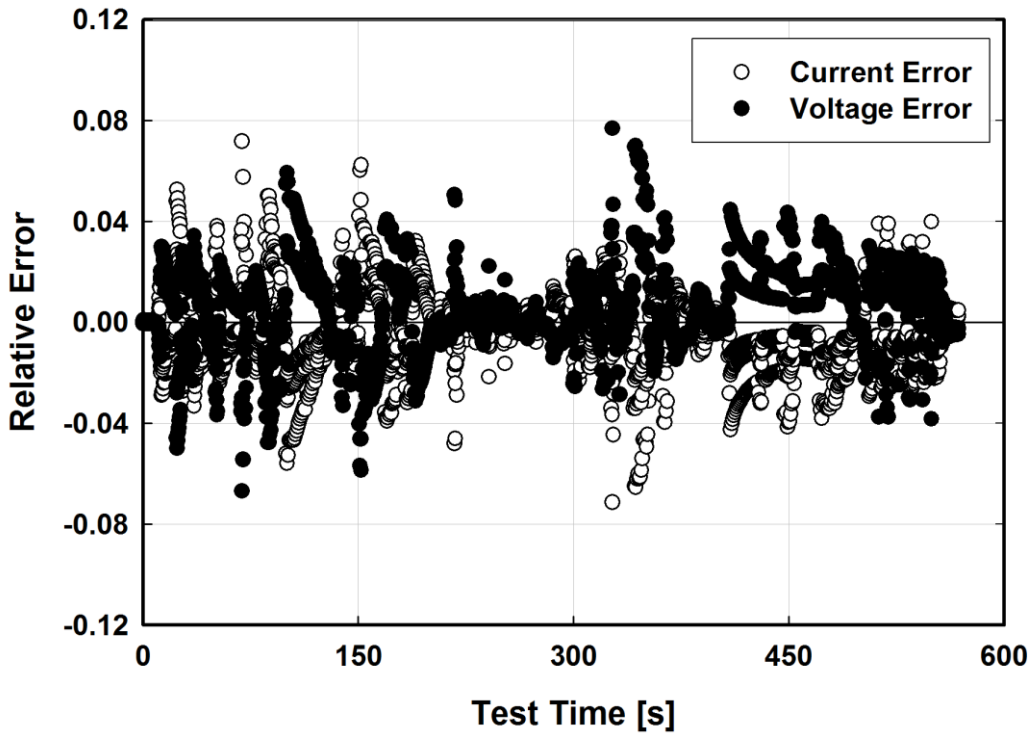

Figure 3.21: Relative Error of Current and Voltage for the Dynamic Simulation Predicted from Constant Current Data

Table 3-11: Predicted and Measured *DOD* at the End of the Dynamic Simulation

Test Temperature	*DOD* at *EOD*	
	Predicted	Measured
[°C]	[Ah]	
15	0.564	0.562
35	0.554	0.552
55	0.554	0.552

at a nominal test temperature of 35°C 290.2 s into the HEV cycle, the measured current and voltage were 2.584 A and 3.124 V. At this same normalized *DOD* and temperature, the cell voltages at discharge currents of 2.000 A and 3.000 A were 3.135 V and 3.073 V, respectively, resulting in delivered powers of 6.270 W and 9.219 W, respectively. Linearly interpolating between two values yielded a required current and voltage of 2.606 A and 3.097 V, respectively, to deliver 8.073 W of power. Therefore, the relative current and voltage error were 0.85% and -0.86%, respectively. As can be seen in Figure 3.21, the current and voltage were both predicted within ±7.7% of the measured value, with 90% of the data predicted within ±2.5%. The predicted charge depletion is calculated as follows:

$$DOD_{\text{fin}} = DOD_{\text{init}} + \sum \frac{I}{Cap_{\text{norm}}} \Delta t_{\text{hr}} \tag{3.9}$$

For example, the normalized *DOD* at 289.5 s and 35°C is 0.51991, and the nominal battery capacity is 1.021 Ah. After discharging for 0.7 s at the predicted rate of 2.606 A, the normalized *DOD* increased to 0.52041. As shown in Table 3-11, the charge depletion rate in the cycled battery was nearly the same for each method due to the similarity between the predicted and measured values.

In the dynamic simulation, sometimes the switching between charge and

discharge was so rapid that the measured overpotential had either a sign opposite of what was expected or was lower than predicted using the constant current data. For example, at 35°C between 326.1 s and 326.9 s, the battery switched from being discharged at 2.77 W to being charged at 1.14 W. Figure 3.22 shows that although the battery was being charged at 326.9 s, it had a positive overpotential (0.07 V), which suggests an unrealistic negative irreversible heat. In this and similar cases, the predicted data always yield positive values for irreversible heating. In addition, the cycle also switches from discharging at 0.74 W to charging at 3.5 W at cycle times of 12.1 s and 12.5 s, respectively. During charging at the latter time, the measured and predicted irreversible overpotentials were -0.043 V and -0.101 V, respectively, resulting in a lower predicted heat generation rate for the former.

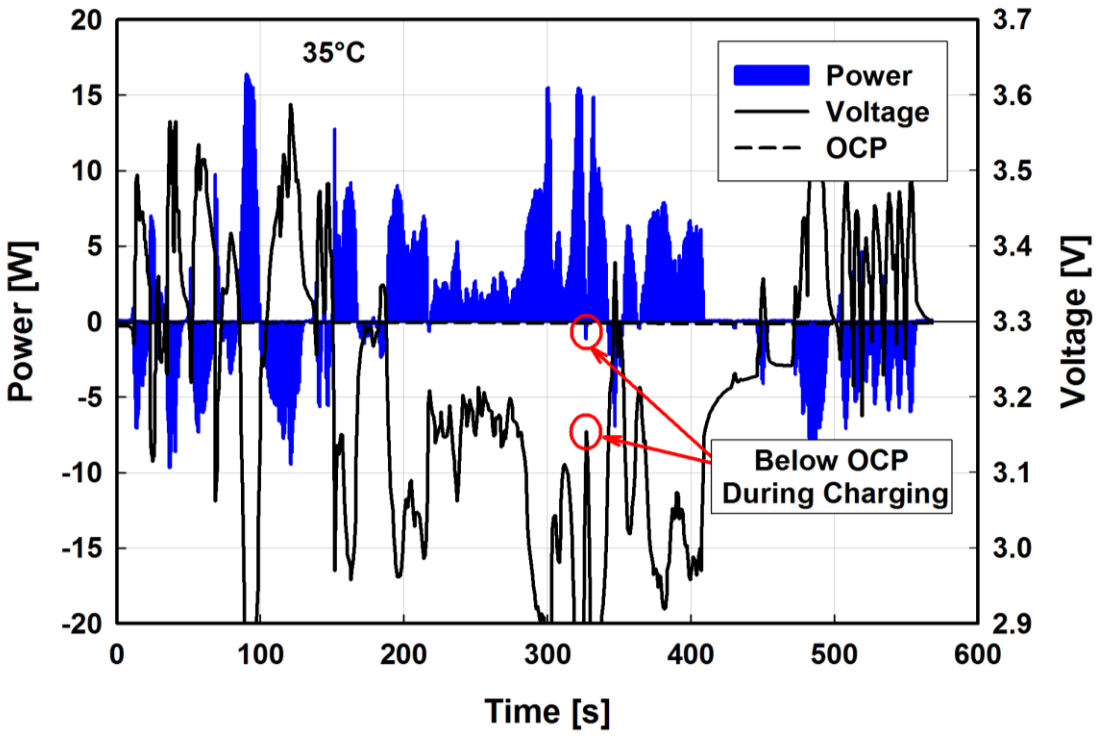

Figure 3.22: Performance during Dynamic Discharge Cycle at 35° C

The cumulative irreversible and reversible heat generation is calculated as follows:

$$Q_{\text{IR,fin}} = Q_{\text{IR,init}} + \sum I\left(U - V\right)\cdot \Delta t \tag{3.10}$$

$$Q_{\text{rev,fin}} = Q_{\text{rev,init}} + \sum I\left(-T\frac{dU}{dT}\right)\cdot \Delta t \tag{3.11}$$

The cumulative irreversible heat is always positive, but the cumulative reversible heat may be negative or positive depending on the sign and magnitude of the current generation (positive for discharge, negative for charge) and entropic heat coefficient. Because the entropic heat coefficient is mostly positive, and the HEV cycle is generally charge depleting, the cumulative reversible heat is primarily negative. For example, after 289.5 s at 35°C, the predicted cumulative irreversible heat generation and reversible heat absorption were 54.63 J and -6.96 J, respectively, and the OCP and entropic heat coefficients were 3.298 V and 0.206 mV/K. After being discharged at predicted values of 2.606 A and 3.097 V for 0.7 s, the cumulative irreversible generated and reversible absorbed heats increased to 54.99 J and -7.07 J, respectively. Similarly, the measured cumulative irreversible heat generation and reversible heat absorption increased from 39.25 J to 39.56 J and decreased from -6.67 J to -6.78 J, respectively, after being discharged at the measured currents and voltage of 2.584 A and 3.124 V, respectively, over this same period. As shown in Table 3-12, the cumulative heat predicted was larger than the value estimated directly from the measurements, which was probably due to the voltage lag experienced in actual operation relative to prediction from the constant current data. It is clear from the results that one cannot directly use the dynamic data to predict instantaneous heat generation. Thus, in the subsequent analyses shown in

Table 3-12: Cumulative Heat Generation Predicted using Constant Current and Measured Values for the Dynamic Simulation

Test Temperature	Total Heat Dissipation	
	Predicted	Measured
[°C]	[J]	
15	192.9	166.1
35	98.2	73.0
55	63.4	45.8

Chapters Four and Five, the heat generation rate was predicted from constant current data for a dynamic cycle.

The effect of entropic heating is observed in Figure 3.23 for the 15°C test, which had the lowest reversible heat contribution due to increased overpotential at this low temperature. It has been suggested by Smith and Wang (2006) that during HEV applications, reversible heating can be neglected. The cumulative impact from reversible

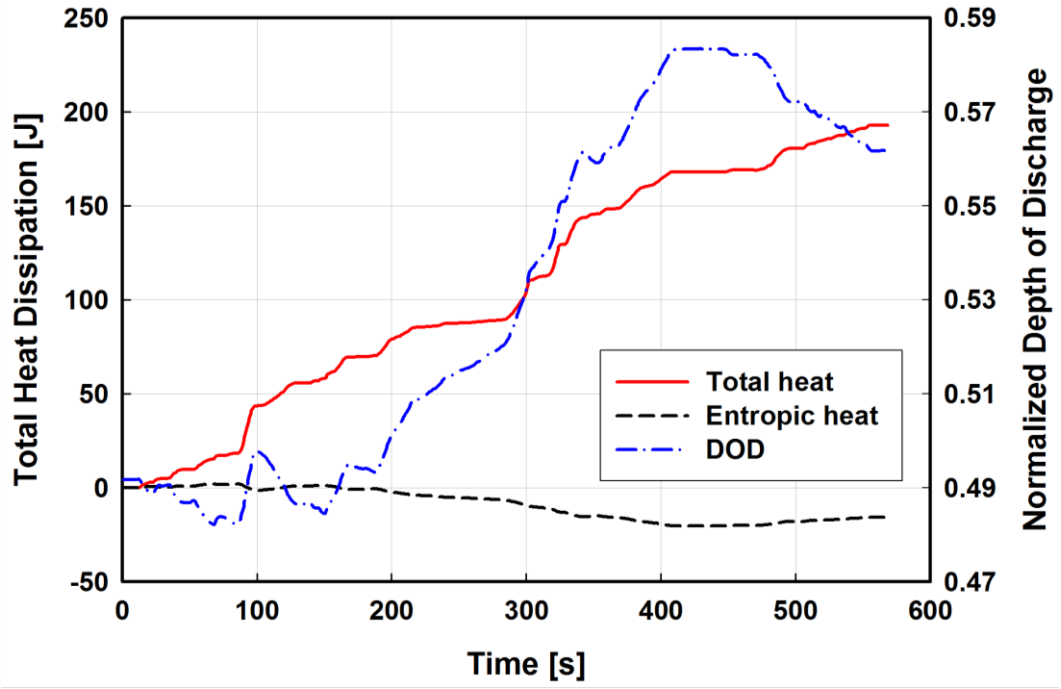

Figure 3.23: Predicted Cumulative Reversible and Total Heat and *DOD* for Dynamic Simulation at 15° C

heat should generally be negligible if the battery is cycled about a fixed SOC, and if the charge and discharge rates are nominally the same. As shown in Figure 3.23, when the battery was cycled back to its original SOC at 118 s and 160 s, the cumulative reversible heat was indeed negligible. However, as the battery is depleted, it becomes significant. For example, at 15°C, the total heat load was reduced by 7.5% (from 208.6 J to 192.9 J) when reversible heat is included.

3.5. Summary

Entropic heat coefficient and reversible heat rate for a commercially available C/$LiFePO_4$ lithium-ion battery were determined using OCP versus temperature data ranging from 10°C to 60°C. Irreversible heat generation rates were estimated on a commercially available cell for both discharge and charge at rates up to 5 A at temperatures from 15°C to 55°C. During the irreversible tests, the battery surface was maintained at a constant temperature by using a specially designed wind tunnel that allowed for rapid adjustment to the time-varying heat generation rate. The setup was capable of maintaining surface temperature within ±0.88°C for all tests. Data normalization was required to account for capacity fade, which was significant and appeared to occur more rapidly at higher rates. After normalization, data from the reference tests conducted at periodic intervals collapsed onto the same discharge curve, and little variation was observed between two different samples. In contrast to prior investigations (*e.g.*, Hong *et al.* (1998)), the total electrochemical heat generation rate was found to be a strong function of rate and temperature between 15°C and 55°C. The total heat generation rate was significantly affected by reversible heat, even at rates as high as 5 A. This may be partly due to the relatively thin electrode material layers, which

causes improved mass transport and, thus, reduces cell overpotential and reversible heating. The reversible heat contribution was largest at higher temperatures and lower rates, which have the lowest irreversible overpotentials.

A dynamic cycle profile based on the US06 drive cycle showed that reasonably good prediction of actual data can be achieved using constant current data. This has significant implications on reducing battery model complexity. In realistic dynamic applications, neither heat nor current generation are known *a priori*, and must be solved iteratively from the mass transport and kinetics at the particle level to the heat removal at the macroscopic cell level. Instead of simulating the electrochemical-thermal transport at the microscopic level, the constant current data can be utilized to simulate dynamic performance, which substantially reduces computational effort. Therefore, as described in Chapter Five, this allows thermal management strategies to be assessed for scaled-up batteries subjected to dynamic loads for the first time. For this battery design and particular HEV simulation, the cumulative reversible heating appears negligible when the battery returns to the original SOC, but significant when charge is depleting. Thus, it is important to include accurate reversible heating estimations during battery thermal simulations.

In Chapter Four, the total electrochemical heat generation rates measured here are used to guide the design of a passive internal cooling system that utilizes microchannel liquid-vapor phase change. After developing the thermal-hydraulic model for this system, the current and heat generation characteristics determined in Chapter Three are used to for the development of a parameterized electrochemical-thermal model for scaled-up battery designs.

CHAPTER 4. PASSIVE INTERNAL COOLING SYSTEM

Conventional thermal management systems for lithium-ion batteries remove heat from the exterior surface of the battery. When surface convective heat transport is poor, the battery experiences an undesirable temperature increase. Convective heat transport can be increased, but this could cause substantial thermal gradients to form inside the cell. This is the result of the low effective thermal conductivity of the battery perpendicular to the stack (Figure 3.1) or its long thermal pathway parallel to the stack. As a result, a charge imbalance inside the cell can develop, potentially leading to non-uniform rates of degradation or thermal runaway. In contrast, internal cooling systems can substantially reduce the thermal resistance between the hotter interior portions of the cell and the cooling fluid, mitigating both temperature rise and thermal gradients simultaneously.

In this chapter, the development of a novel internal cooling thermal management system that utilizes liquid-vapor phase change is described. First, an overview of the cooling concept is presented, which includes a description of possible internal heat removal structures. Because of the necessarily small dimensions for the internal evaporator, a brief overview of prior work on two-phase liquid-vapor phase change frictional pressure drop is presented, concluding that new experiments are needed to support the development of these devices that rely on passive evaporation in microscale channels. The experimental facility and measured performance characteristics for a

system with representative evaporator geometry are subsequently described. The results obtained from these experiments are used to develop a new two-phase frictional pressure drop correlation, which serves as the basis for a combined evaporation heat transfer and buoyancy driven fluid flow model developed in Chapter Five. In Chapter Five, this model is coupled to an electrochemical-thermal model to show the possible improvement in the performance of lithium-ion batteries through improved thermal management.

4.1. Concept Description

The cooling system developed in the present study *addresses the singular limiting feature of all battery cooling systems proposed thus far* – conventional cooling systems are external to the batteries, which implies that substantial temperature gradients could exist between the heat generation location (the cells) and the surface of the battery, with a variety of intervening thermal resistances. Therefore, a cooling system integrated with the internal heat generation sites (Figure 4.1) and utilizing efficient, yet passive, thermal transport between the heat generation sites and the external heat sinks is developed in the present study. The heat removal in the cooling system occurs as follows. Thermal energy dissipated during charge and discharge of the battery is transferred across chemically inert walls of microchannels embedded into the cells to a phase-change fluid at the appropriate saturation pressure and temperature. The heat generated by the battery is used to vaporize a refrigerant that flows passively due to buoyancy to an external condenser. Here, the fluid is condensed and transported back to the inlet of the evaporator via gravitational forces, similar to a loop thermosyphon.

The system developed here represents significant advances over the state of the art. The cooling structures are incorporated internally in the battery to remove heat

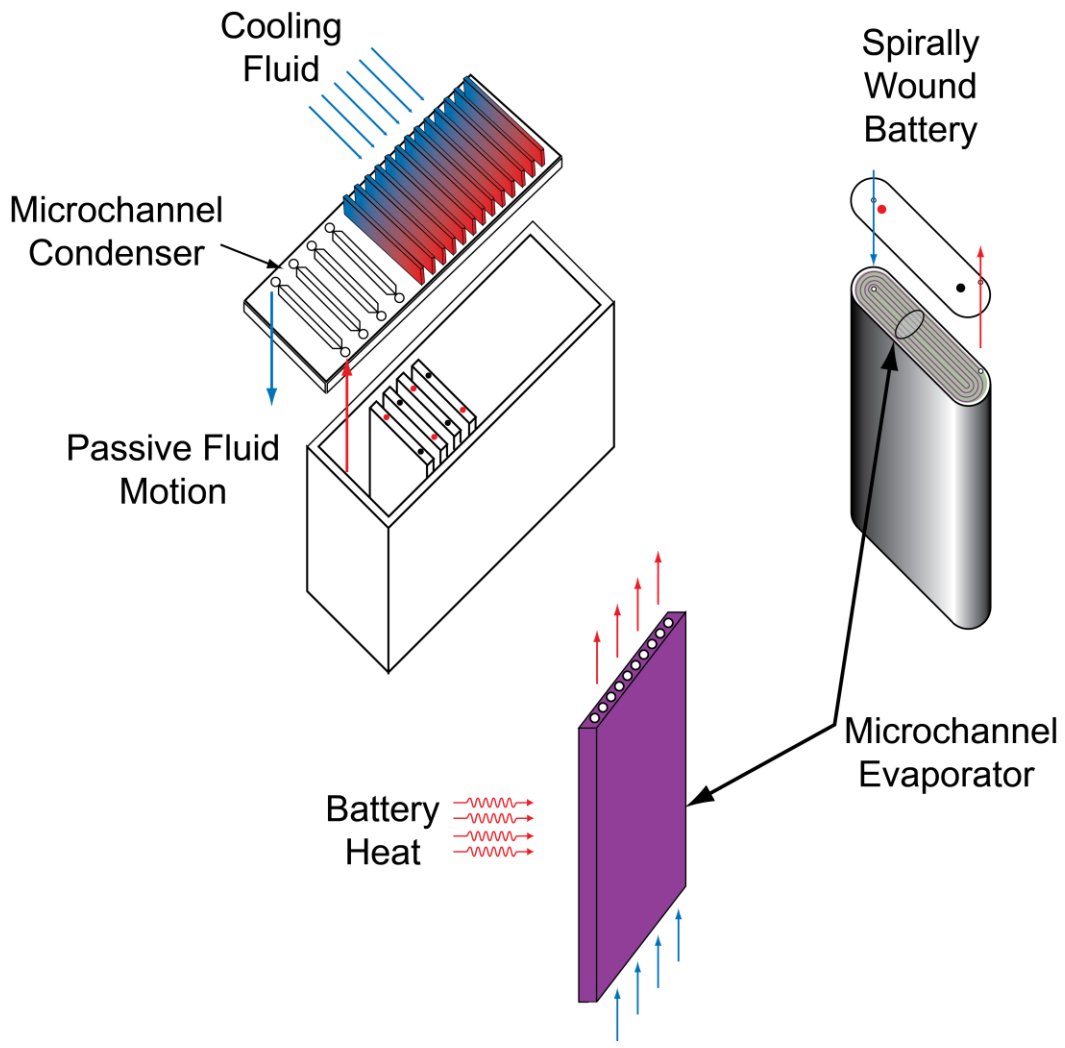

Figure 4.1: Microscale Phase Change Internal Cooling Concept Schematic

directly from the site of generation. The phase change process, which can be tuned to the desired operating temperature by selecting an appropriate charge of the working fluid in the microchannels, results in a *near-isothermal* heat removal from the batteries. In addition, this phase-change process is achieved entirely passively, without any liquid pumps or other auxiliary fluid-moving equipment or parasitic losses. The high heat transfer coefficients seen in microchannel phase-change at ~100 μm result in negligible thermal resistances from the heat generation site to the air-coupled heat sink. The phase-

change process also implies that multiple cells within a high energy density pack can be cooled to the same temperature, minimizing corrosion rates and other adverse battery life and safety related effects.

For the system to function, the density driven gravity head between condenser outlet and the evaporator inlet must balance the frictional, expansion/contraction, and other minor losses throughout the entire flow loop, with flow through the channels of the thin evaporator sheet causing the major portion of the pressure drop in the system. Embodiments of the internal cooling evaporator are shown schematically in Figure 4.2. In these examples, the microscale channels can either be integrated into a current collector or in a separate sheet that is inserted into a split current collector, both of which have minimal impact on the ion and electron flow within the battery. Because incorporation of these channels within the unit cell will add additional volume to the battery, it is critical that the channels be made as small as possible. In addition, the heat flux applied to the channels when the battery is operating is very low. For example, as shown in Figures 3.16 and 3.17, the maximum volumetric heat generation rate is near 200

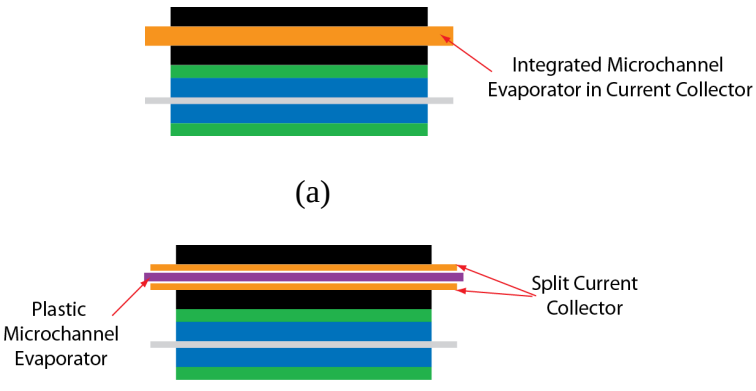

Figure 4.2: Embodiments of Evaporator Sheet Into the Unit Cell: (a) Thicker Current Collector and (b) Split Current Collector

W L^{-1} at 5.0 A at 15°C for the tested commercial battery. For a unit cell volume of 13.08 mL, this results in a total heat load of only 2.62 W. For a unit cell thickness of 284 μm, the heat transfer area of one side of the unit cell is 0.0460 m^2, yielding a heat flux of only 56.9 W m^{-2}. Furthermore, for a jelly roll height of 58.74 mm, the total length of the unit cell is 782.6 mm, which requires many cooling channels. Therefore, because the flow is buoyancy driven, the low heat flux will result in a small working fluid mass flow distributed among many parallel passages. However, as discussed in the next section, the frictional pressure drop characteristics at dimensions approaching the unit cell thickness (284 μm) for these low flow conditions are not well known.

4.2. Prior Work on Two-Phase Frictional Pressure Drop

In this section, the prior work on liquid-vapor phase change frictional pressure drop is briefly discussed. As D_h decreases, the relative magnitudes of surface tension, gravity, inertial, and viscous shear forces change, causing the observed flow regime to change (Coleman and Garimella, 2000). This in turn affects both the heat transfer and pressure drop characteristics, and several recent review papers have summarized these in micochannels for both boiling (Ribatski *et al.*, 2006; Ribatski *et al.*, 2007) and condensing (Cavallini *et al.*, 2006) liquid-vapor flows. Table 4-1 summarizes selected prior work that has yielded correlations to predict frictional pressure drop in channels with D_h < 1 mm. The literature was subdivided into two main categories based on the type of test fluid: non-condensable gas-liquid mixtures and pure refrigerants.

In the internal cooling system, the driving force for fluid flow is the gravitational potential between the condenser and the evaporator. Therefore, the mass flow through the system is expected to be much lower than experienced in applications where the fluid

Table 4-1: Summary of Prior Work on Two-Phase Frictional Pressure Drop Correlations

Investigator	Test Fluid	Heat transfer	Geometry	Channel size [mm]	G [kg m^{-2} s^{-1}]
Non-Condensable Gas and Liquid Correlations					
Moriyama *et al.* (1992b)	Nitrogen-R113	Adiabatic	Rectangular	30 × 0.098	not given - as low as 45 possible
				30 × 0.052	not given - as low as 7.5 possible
				30 × 0.025	not given - as low as 15 possible
				30 × 0.007	not given - as low as 3 possible
Stanley *et al.* (1997)	Water-Gas (Ar, He, N_2)	Adiabatic	Rectangular	0.056 to 0.256	Re = 30 to 10,000
Chung *et al.* (2004)	Nitrogen-Water	Adiabatic	Square	0.096	14 to 4290
			Circular	0.1	25 to 4507
Chung and Kawaji (2004)	Nitrogen-Water	Adiabatic	Circular	0.05	34 to 4360
				0.1	38 to 2330
				0.25	32 to 5580
				0.53	29 to 4050
Cubaud and Ho (2004)	Air-Water	Adiabatic	Rectangular	0.2	13 to 200
				0.525	2.4 to 36
Saisorn and Wongwises (2008)	Air-Water	Adiabatic	Circular	0.53	6.85 to 3269
Saisorn and Wongwises (2009)	Air-Water	Adiabatic	Circular	0.15	20 to 501
Refrigerant Correlations					
Lin *et al.* (1991)	R12	Adiabatic	Circular	0.66, 1.17	1440 to 5090
Moriyama *et al.* (1992a)	R113	Evaporating	Rectangular	0.035 to 0.110 × 30	200 to 1000

Table 4-1: Cont…

Investigator	Test Fluid	Heat transfer	Geometry	Channel size [mm]	G [kg m^{-2} s^{-1}]
Refrigerant Correlations					
Lee and Lee (2001)	Air-water	Adiabatic	Rectangular	0.4 × 20	not given - as low as 260 possible
				1 × 20	not given - as low as 70 possible
				2 × 20	not given - as low as 50 possible
				4 × 20	not given - as low as 50 possible
Webb and Ermis (2001)	R134a	Condensing	Rectangular	0.611, 1.564, 0.44, 1.3	300 to 1000
Baird *et al.* (2003)	R123, R11	Condensing	Circular	0.92, 1.95	70 to 600
Garimella *et al.* (2003)	R134a	Condensing	Square	0.762	150 to 750
			Barrel	0.799	150 to 750
			N-shaped	0.536	300 to 750
			Rectangular	0.424	450 to 750
			Triangular	0.839	150 to 750
			W-insert	0.732	150 to 750
Koyama *et al.* (2003)	R134a	Condensing	Rectangular	0.807, 0.889, 0.937, 1.062	100 to 700
Qu and Mudawar (2003)	Water	Evaporating	Rectangular	0.231 × 0.713	135 to 400
Garimella *et al.* (2005)	R134a	Condensing	Circular	0.506	450 to 750
				0.761	300 to 750
				1.524	150 to 750
				3.048	300 to 750
				4.91	150 to 750

Table 4-1: Cont…

Investigator	Test Fluid	Heat transfer	Geometry	Channel size [mm]	G [kg m^{-2} s^{-1}]
Refrigerant Correlations					
Lee and Mudawar (2005)	R134a	Evaporating	Rectangular	0.231 × 0.713	127 to 654
Agarwal (2006)	R134a	Condensing	Rectangular	0.1 × 0.1	600 to 800
				0.1 × 0.2	300 to 800
				0.1 × 0.3	
				0.1 × 0.4	
Hwang and Kim (2006)	R134a	Adiabatic	Circular	0.244	480 to 950
				0.430	270 to 900
				0.792	104 to 470
Revellin and Thome (2007)	R134a, R245fa	Adiabatic	Circular	0.509, 0.790	210 to 2094
Lee and Garimella (2008)	Deionized Water	Evaporating	Rectangular	0.102 × 0.367	328 to 902
				0.242 × 0.365	270 to 655
				0.4 × 0.498	210 to 526
				0.997 × 0.369	223 to 551

is pumped using mechanical work. In addition, the channel dimensions must approach the thickness of the unit cell (284 μm). Very few of the available correlations shown in Table 4-1 investigate frictional pressure drop during phase change at this scale for pure refrigerants at low mass fluxes. All of the non-condensable gas-liquid studies reviewed here address sufficiently low mass fluxes (down to 2.4 kg m^{-2} s^{-1} for Cubaud and Ho (2004)) and channel sizes. However, it is expected that the frictional pressure drop characteristics for pure refrigerant phase change will differ from those for non-condensable gas-liquid mixtures due to the substantially different gas and liquid phase fluid properties and the effects of the phase change process. For example, at a pressure and temperature of 200 kPa and 25°C, the ratios of liquid to gas densities and viscosities for an air-water mixture are 427 and 48, respectively. The corresponding ratios are 37 and 16, respectively for R134a at a saturation temperature of 25°C. As the density ratio increases, the differences in velocity between the two phases increase, causing increased drag at the interface. However, as the viscosity ratio increases, the momentum transport at the interface decreases. Furthermore, the surface tensions of water and R134a at 25°C are 0.072 and 0.008 N m^{-1}, respectively. Surface tension is important as the D_h decreases, which can cause bridging of the liquid film and a transition from the annular flow regime to an intermittent flow regime. These regimes have substantially different momentum transfer between the two phases. Therefore, it is uncertain how well frictional pressure drop models based on non-condensable gas and liquid data can predict the performance phase change in pure refrigerants.

The prior work conducted on pure refrigerants is also limited to higher mass fluxes. In addition, as D_h decreases, the minimum mass flux measured typically

increases. For example, in the study conducted by Garimella *et al.* (2005), as D_h is reduced from 4.91 mm to 506 μm, the minimum G increases from 150 to 450 kg m^{-2} s^{-1}. Similarly, in the adiabatic tests conducted by Hwang and Kim (2006), the minimum G increases from 104 to 480 kg m^{-2} s^{-1} as D_h decreases from 792 to 244 μm. These limitations in mass flux in the available data at small D_h are primarily due to difficulties in accurately measuring the low mass flow rates and heat transfer rates in channels with such small dimensions, especially at the low mass fluxes. In addition, many of these investigations yield correlations that are specific to condensing flows (*e.g.*, Baird *et al.* (2003)), and may not be applicable to the evaporation observed in the internal cooling system under consideration here. Moreover, the heat fluxes in lithium-ion batteries are very low compared to those experienced in microprocessor electronics cooling, which is the target application for most studies on evaporation heat transfer. For example, at a volumetric heat generation rate of 200 W L^{-1} (Figure 3.16) and a unit cell thickness of 284 μm, the applied heat flux in one direction would merely be 0.006 W cm^{-2}. In contrast, the minimum applied heat fluxes for the studies of Qu and Mudawar (2003)[3], Lee and Mudawar (2005), Lee and Garimella (2008), and Moriyama *et al.* (1992a) are 40, 31.6, 10, and 0.4 W cm^{-2}, respectively. This substantial difference may lead to less bubble growth and different flow mechanisms in the battery cooling application, which may affect the frictional pressure drop characteristics. Finally, in most applications, the frictional pressure drop is simply overcome by increasing the pumping power of the fluid movement device. The only means to do this in the internal cooling system is either to increase the liquid density of the refrigerant, which is only possible by reducing its

[3] The lower heat flux limit in this study was deduced from the figures available in their paper.

saturation pressure, or increasing the liquid column height. Therefore, it is imperative to validate the applicability of the previously developed correlations at the low heat fluxes and buoyancy driven pumping capabilities of the internal cooling system under consideration so that system performance can be successfully predicted.

4.2.1. Objectives of Cooling System Performance Assessment

In the remainder of this chapter, an experimental investigation of a representative cooling system is discussed. The objectives of this phase of the study are to measure the frictional and heat transfer characteristics of a representative cooling system over a range of heat inputs (120 to 6,500 W L^{-1}) and saturation temperatures (24°C to 33°C). In addition, the experimentally obtained two-phase frictional pressure drops in the microchannel evaporator (3.175 mm × 160 μm channels) are compared to the pertinent correlations from the literature and used to develop a new frictional pressure drop model with improved accuracy. This new model is used in the development of a simplified thermal-hydraulic model for coupling with the battery model described in Chapter Five.

4.3. Experimental Facility and Procedure

4.3.1. Test Facility Description

The performance of the internal cooling system was measured using a representative evaporator geometry and surrogate heat sources. A detailed schematic and picture of the test facility are shown in Figures 4.3 and 4.4, respectively, and the major components and instrumentation are tabulated in Tables 4-2 and 4-3, respectively. The test facility was designed to measure the generated mass flow rate as a function of heater power input, and to obtain the corresponding evaporator outlet quality and two-phase frictional pressure drop for several different test pressures. Secondary objectives were to

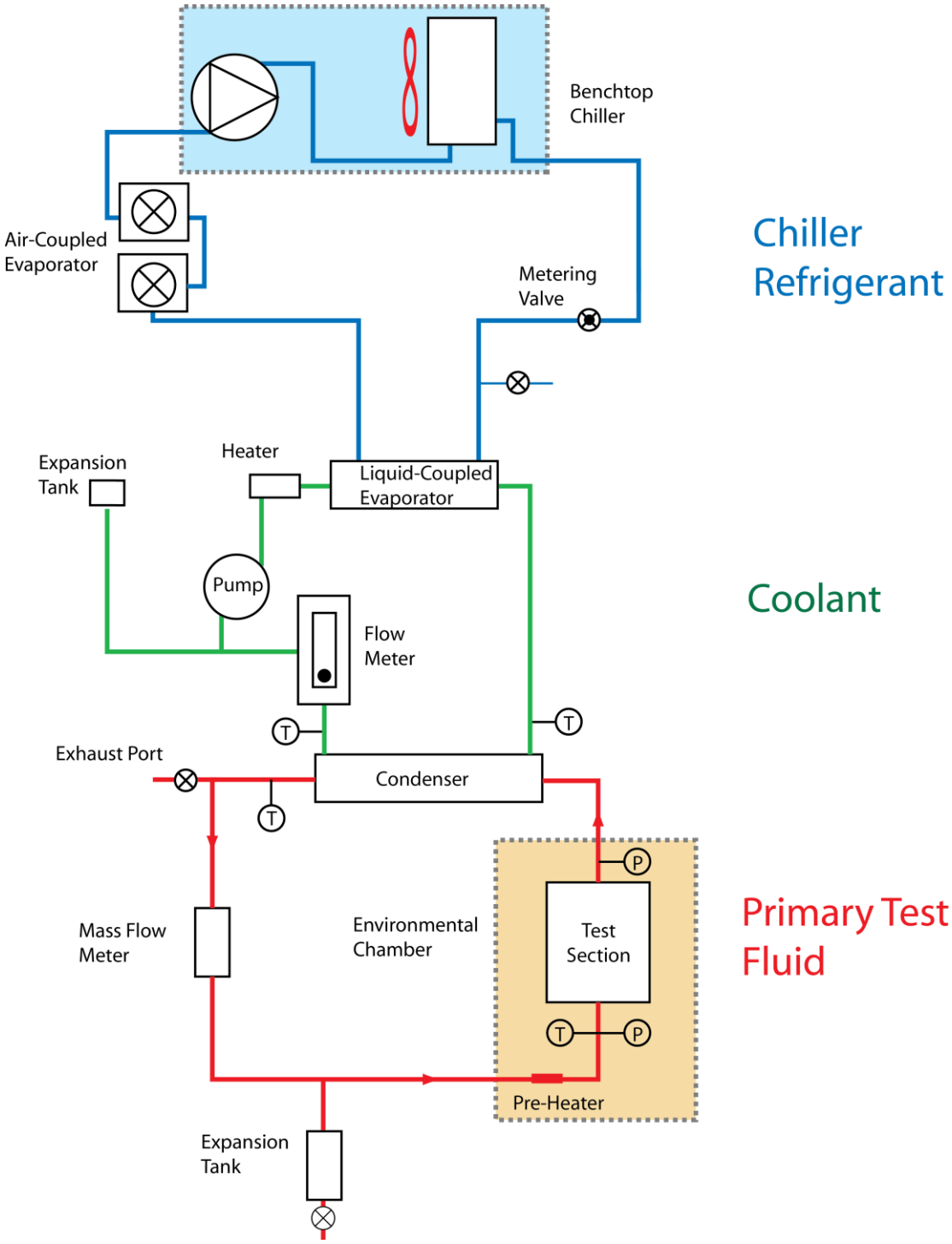

Figure 4.3: Microscale Phase Change Internal Cooling Test Facility Schematic

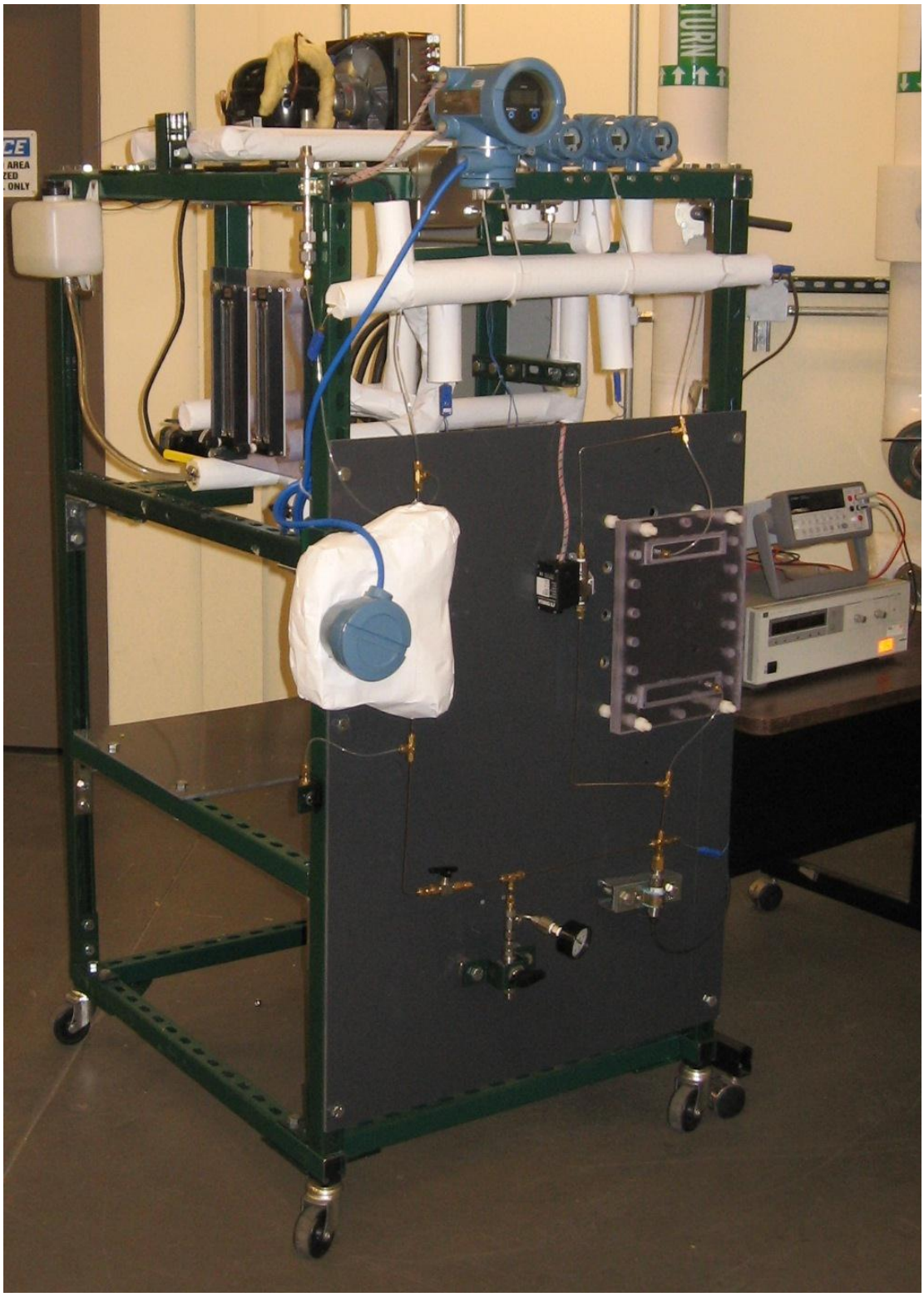

Figure 4.4: Microscale Phase Change Internal Cooling Test Facility (environmental enclosure and expansion tank not shown for clarity)

Table 4-2: Component Specifications for Microscale Phase Change Internal Cooling Test Facility

Item	Description	Supplier/ Manufacturer	Part Number
Primary Test Fluid Loop			
Condenser	273 mm long tube-in-tube HX: 6.35 × 3.2 mm interior copper tube, 12.7 mm OD exterior 316L stainless steel tube	In house	N/A
Heater – Test Section	Kapton film flexible heater, 127 mm × 203 mm, 200 W at 115 V, pressure sensitive backing	Omega	KH-508/5-P
Pre-Heater	Kapton film flexible heater, 25.4 mm × 102 mm, 40 W at 115 V	Omega	KHLV-104/10
Potentiometer – Heater	Single phase, 120 VAC input, 0-118 VAC output, 50/60Hz, 10 A fuse, 1.2 kW	Payne Engineering	18 TBP-1-10
Potentiometer – Pump	Single phase, 120 VAC input, 0-118 VAC output, 50/60Hz, 5 A fuse, 0.6 kW	Payne Engineering	18 TBP-1-5
Power Supply: Pre-Heater	0 to 30 VDC, 0 to 3 Am Single Output, Digital Display	McMaster-Carr	7686K24
Power Supply: Test Section	DC power supply, 0 to 60 VDC, 0 to 50 A, 1 kW	HP	6012B
Reflective Tape	VentureTape®1525CW Cold Weather FSK	McMaster-Carr	76145A42
Space Heater #1	1.5 kW space heater	Seabreeze Electrical Corp.	SF12ST
Space Heater #2	1.5 kW space heater	Black and Decker	HF2004
Coolant Loop			
Expansion Tank	165 mm × 102 mm × 127 mm plastic tank	Balkamp	7304514
Heater	Compact Cartridge-Style Immersion Heater 316L SS Element, 120 VAC, 0.41 kW, 113 mm Length	McMaster-Carr	4668T56

Table 4-2: Cont…

Item	Description	Supplier/ Manufacturer	Part Number
Coolant Loop			
Liquid Coupled Evaporator	276 mm long tube in tube HEX: 6.35 × 3 interior copper tube, 12.7 × unknown mm exterior 316L stainless steel tube	In house	N/A
Pump	Centrifugal pump head: 0 to 27 lpm, 0 to 13.6 bar; Adjustable VAC speed controlled motor: 500 to 9000 RPM	Micropump	Series 101 (pump head) 405 A(motor)
Chiller Loop			
Air-Coupled Heat Exchangers	Fin and tube HEX: 0.376 m^2 × 2 heat transfer area	Lytron	4105G1SB
Chiller	124 W, 115V, R-134a, Air-Cooled, Condensing Unit	Copeland	M2FH-0017-SAA-106
Fan #1	113 mm axial flow fan, 0 to 187 m^3 hr^{-1}, 0 to 80 Pa	Shung Kwei	SK109AP-11-1
Fan #2	120 mm axial flow fan, 0 to 178 m^3 hr^{-1}, 0 to 56 Pa	Comair Rotron	MX243-028316

Table 4-3: Instrumentation for Microscale Phase Change Internal Cooling Test Facility

Item	Description	Supplier/ Manufacturer	Part Number
Primary DAQ	USB-based, 22-Bit data acquisition module with 20 SE/10 DE inputs, 16 digital I/O, and 4 frequency/pulse inputs	Measurement Computing	Personal DAQ/56
DAQ Expansion Module	Snap-on expansion DAQ expansion module with 60 SE/10 DE inputs, 32 digital I/O, and 4 frequency/pulse inputs	Measurement Computing	PDQ2
Multimeters: *V* and *I*	6.5 Digit multimeter, 0 to 120 VC, -3 A to 3 A	Agilent	34401A
Mass Flow Meter and Transmitter	0 to 108 kg h^{-1} Coriolis mass flow meter with transmitter	Micromotion	CMF010H521NQBAE444
Pressure Transducers	0 to 250 psia pressure transducer, 0 to 5 VDC signal output	Omega	PX409-250A5V
Thermocouples - Surface	Type T surface mount thermocouple probes with 1.83 m connecting wire	Omega	SA1-T-72-SC
Thermocouples – Test Fluid	1.59 mm Type T thermocouples with mini quick disconnects, 152 mm length	Omega	TMQSS-062U-6
Volume Flow Meter	0 to 37.9 LPM clear acrylic rotameter	Omega	FL4401-V

observe the flow inside the loop and to document the test section surface temperature for verification of adequate flow and temperature distribution.

The test facility consisted of three flow loops: primary test fluid, coolant, and chiller refrigerant. Flow was initiated in the primary loop by supplying heat to the test section through a thin film Kapton heater (Omega part number KH-508/10-P) mechanically bonded to the back surface of the test section (Figure 4.12 and Section 4.3.2). The heat input was controlled using a 0 to 60 VDC power supply (HP Model number 6012B). The power was calculated from the voltage and current measured by two high accuracy 6.5 digit multimeters (Agilent model 34401a). According to the manufacturer, the resistance of the heater was 66.1 Ω. In comparison, the resistance of the connecting wire between the voltage sensing location and the heater was merely 0.16 Ω. Thus, 99.8% of the heat measured by product of measured current and voltage was dissipated in the heater, and it was assumed that power dissipated by the heater was equal to the product of the measured voltage and current.

Two-phase refrigerant exited the evaporator and entered a liquid-coupled, tube-in-tube condenser, where it was completely condensed to a slightly subcooled liquid state. The condensed refrigerant then flowed through a Coriolis mass flow meter (Micromotion CMF010) en route to the evaporator inlet. To ensure minimal subcooling at the evaporator inlet, an additional Kapton heater (Omega part number KHLV-104/10) was installed between the flow meter and the evaporator, and its power was controlled by an adjustable power supply (McMaster-Carr part number 7686K24). Flow was sustained in the primary test fluid loop by the net gravitational potential head from the condenser outlet to the evaporator inlet (ΔH = 0.711 m) balancing the frictional,

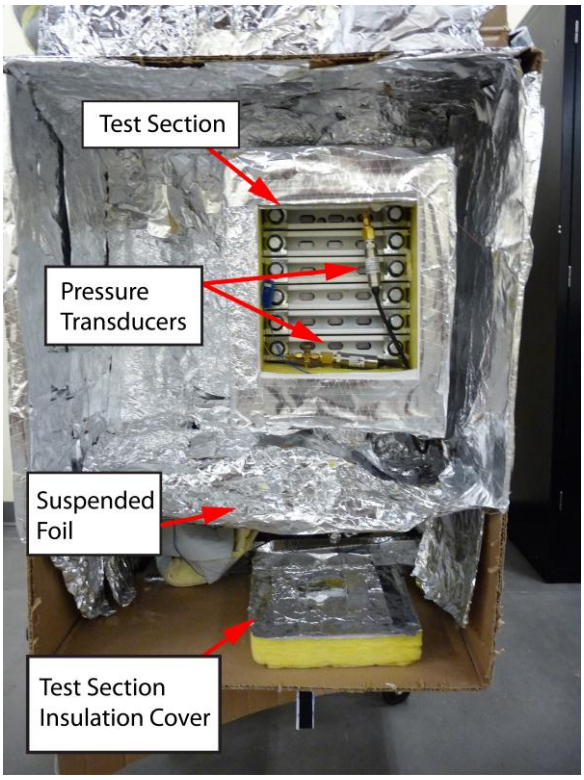

Figure 4.5: Microscale Phase Change Test Section and Environmental Chamber

expansion/contraction, and other minor losses in the flow loop. Because flow was in the vertical direction, the *differential* pressure between the inlet and outlet of the evaporator cannot be measured directly without accurate knowledge of the void fraction. However, the pressure at the test section inlet and outlet was measured using *absolute* pressure transducers (Omega part number PX409-250A5V) (Figure 4.5). These measurements were used to calculate inlet refrigerant subcooling and enthalpy and, in conjunction with the measured mass flow rate and energy balance (Section 4.4.2), the outlet quality. The condenser outlet and evaporator inlet temperatures were also measured using type T 1.59 mm OD thermocouples (Omega Part number TMQSS-062U-6). Temperature and pressure data were collected using Measurement Computing Personal DAQ/56^{TM} with attached expansion module PDQ2 data acquisition system.

Heat from the primary loop was rejected to the high velocity coolant (water) circulated by a speed-controlled centrifugal pump (Micropump Series 101 pump head with Micropump model 405A motor). The coolant flow rate was monitored using a volumetric flow meter (Omega part number FL4401-V). Changes in the coolant volume due to operating conditions were accommodated by connecting the water loop to an expansion tank (Balkamp model number BK 7304514). The coolant loop temperature was maintained by either rejecting heat to a tube-in-tube evaporator of a benchtop chiller (Copeland mode number M2FH-0017-SAA-106) or through heat addition from a 0.41 kW immersion heater (McMaster Carr part number 4668T56) inserted in the flow loop. The coolant pump speed and heater input power were controlled separately by solid state controllers (Payne Engineering models 18TBP-1-5 and 18TBP-1-10, respectively). The chiller (Copeland model M2FH-0017-SAA-106) evaporator temperature was controlled by adjusting the position of the expansion valve (Swagelok part number SS-4L-MH-NE), while compressor inlet superheat was maintained by removing heat from the chiller refrigerant using two air-coupled evaporators (Lytron model number 4105G1SB) with attached axial flow fans (Sheng Kwei 109AP-11-1 and Muffin XL model MX243) downstream of the liquid-coupled evaporator.

To minimize ambient heat loss, the test section was covered with 50.8 mm of rigid fiberlass insulation (k_{ins} = 0.043 W m^{-1} K^{-1}). The outside surface of the insulation was covered with aluminum facing tape (VentureTape®1525CW Cold Weather FSK), which has a low assumed spectral emissivity (aluminum, 0.07 (Incropera and DeWitt, 1996)). In addition, a temperature-controlled environmental chamber was built around the test section to minimize the temperature difference between the test section surface

temperature and its surrounding environment. The temperature of the surrounding environment was taken as the arithmetic average of two thermocouples suspended above and below the test section exterior. The inside surface of the chamber was covered with aluminum foil to reduce the radiative heat exchange, while the temperature of the chamber was controlled using two 1.5 kW space heaters (Seabreeze Electric Corp. model SF12ST and Black and Decker model HF2004) placed below the chamber. To reduce temperature non-uniformity in the chamber and to reduce the bottom surface temperature, the aluminum foil was spaced 0.254 m above the bottom surface of the chamber. The details of the ambient heat loss calculation and results are provided in Section 4.4.2.

It should be noted that in the results discussed in Section 4.4.2 some portions of the inside surface and the back of the test section were not covered in low emissivity material. However, this was taken into account in the detailed calculations in Section 4.4.2, and repeatability results with all surfaces covered showed no appreciable difference (Appendix B). Furthermore, the stock calibration and conservatively large uncertainties were assumed for these thermocouples (Section 4.4.2).

4.3.2. Test Section Description

Schematics and pictures of the evaporator test section are shown in Figures 4.6 through 4.14. Figures 4.6 and 4.7 show an exploded view assembly and the top view of the final assembled test section, respectively. The test section consisted of a 6.35 mm plate with thirteen 3.18 mm wide × 121 μm deep × 210 mm long channels machined into the top surface (Figures 4.8 and 4.9). Inlet and outlet headers 127 mm wide × 1.52 mm deep × 12.7 mm long were machined into same face on the plate. A hermetic seal was formed by compressing a 12.7 mm thick sheet of polycarbonate with a machined groove

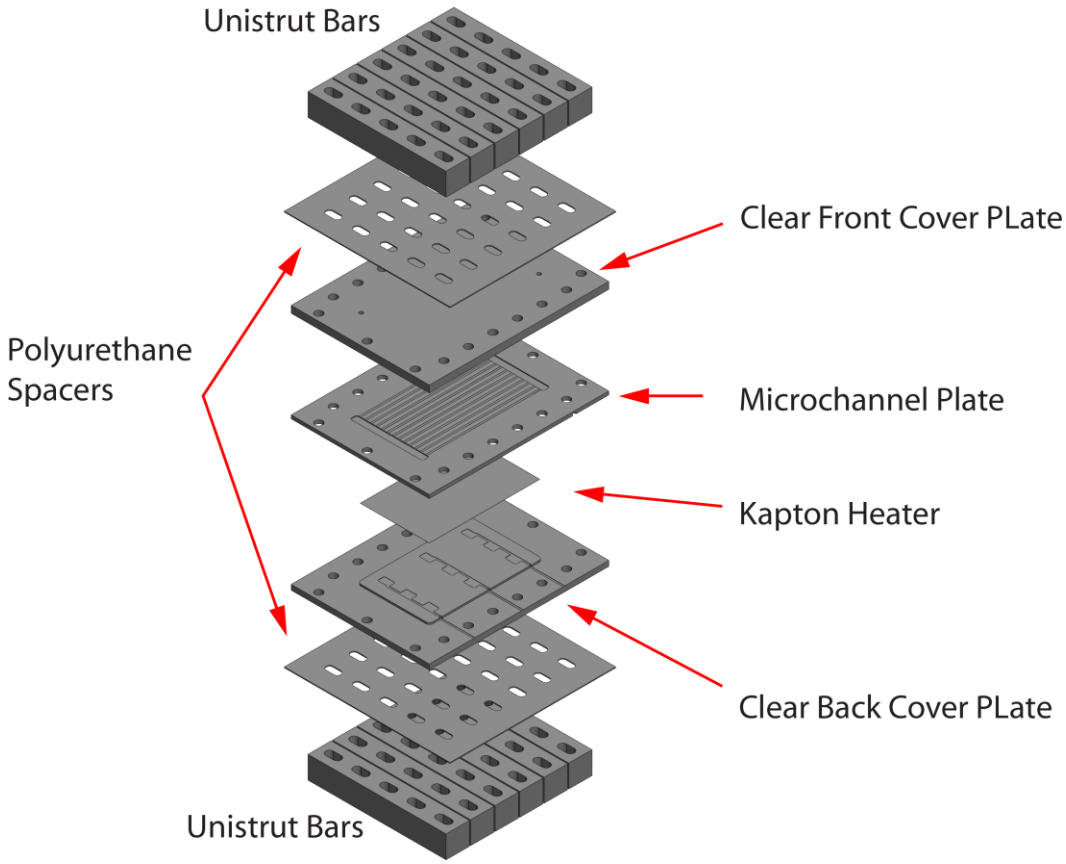

Figure 4.6: Exploded View of Test Section Assembly

Figure 4.7: Final Test Section Assembly

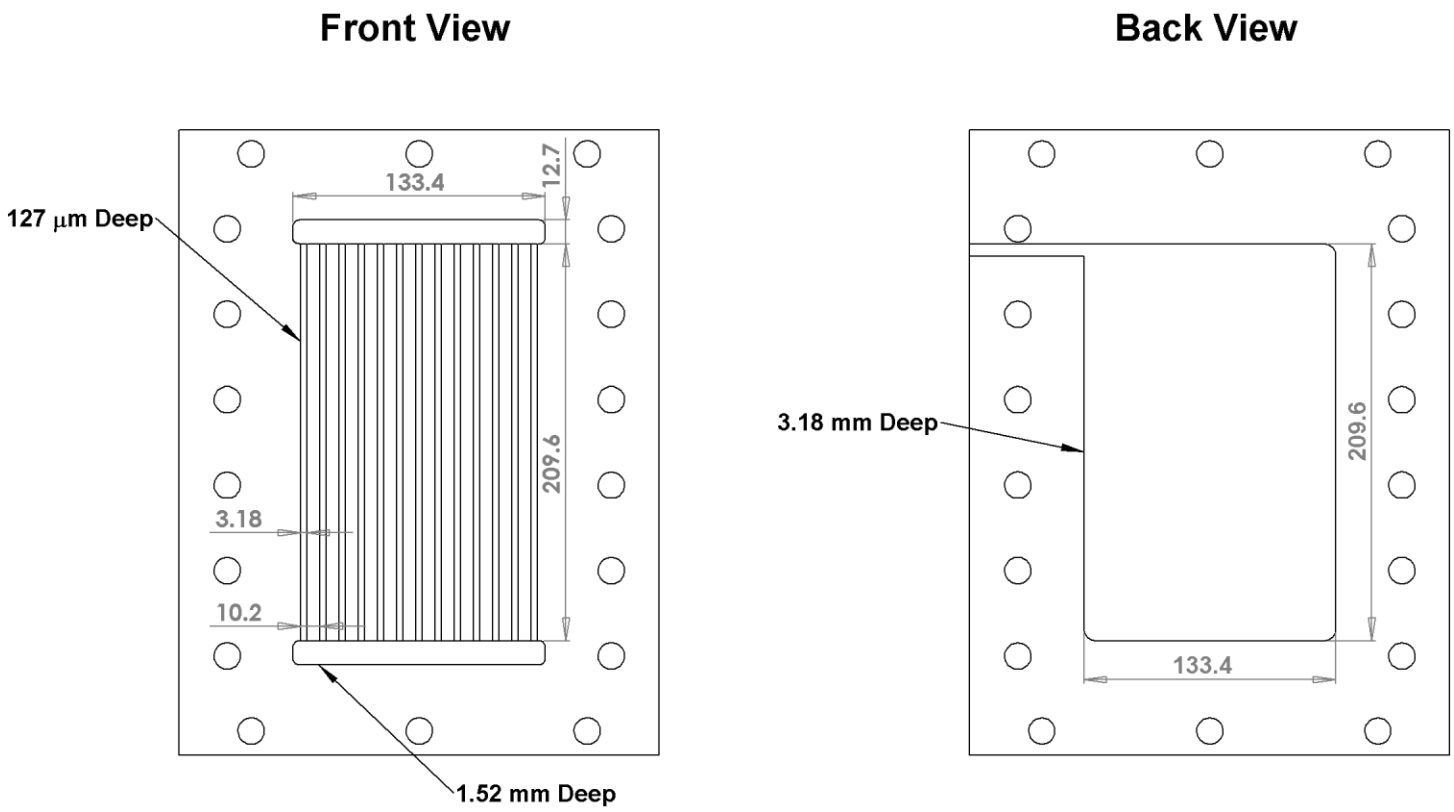

Figure 4.8: Test Section Aluminum Plate Dimensions

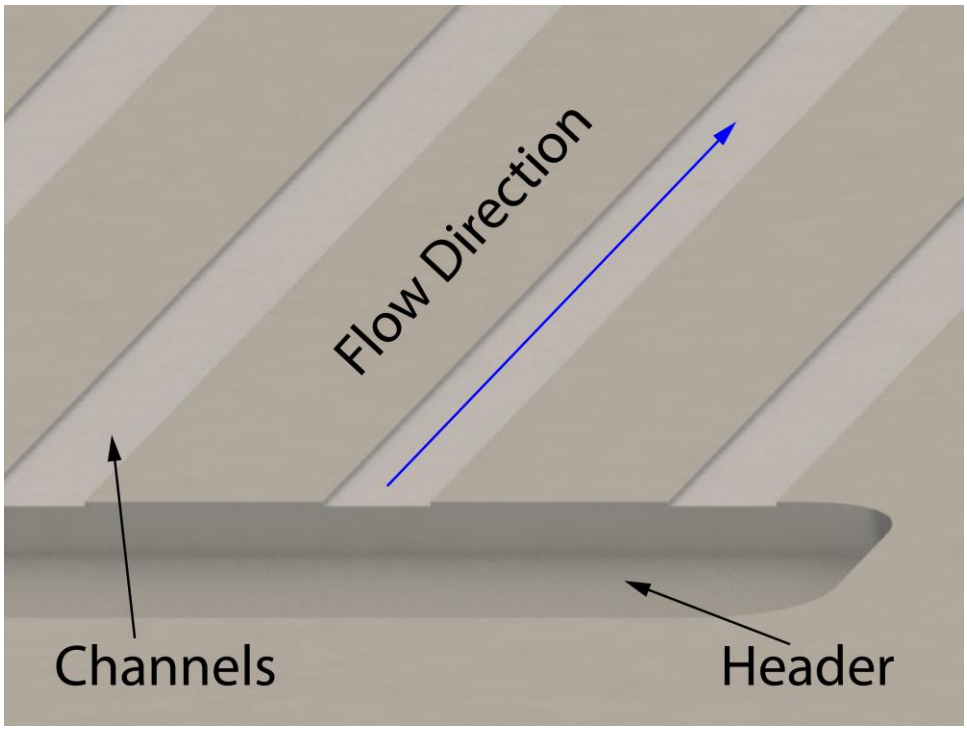

Figure 4.9: Test Section Aluminum Plate Picture

for an O-ring (McMaster-Carr part number 9452K373), which also contained inlet and outlet refrigerant ports (Figures 4.10 and 4.11), onto the front face of the aluminum plate. The back face of the aluminum plate had a 133 mm wide × 210 mm long × 3.18 mm deep pocket for accurate placement of the 500 μm thick heater (Figures 4.8 and 4.12). A second 12.7 mm thick polycarbonate sheet with a mating protrusion (3.18 mm high) was compressed onto the back to ensure adequate thermal contact between the heater and aluminum plate. (The heater was supplied with a pressure sensitive adhesive already adhered to one surface.) In addition, nine 508 μm deep pockets for placement of type T surface mount temperature probes (Omega part number SA1-T-72) were machined into the raised surface of the second polycarbonate sheet (Figure 4.13) to accommodate the

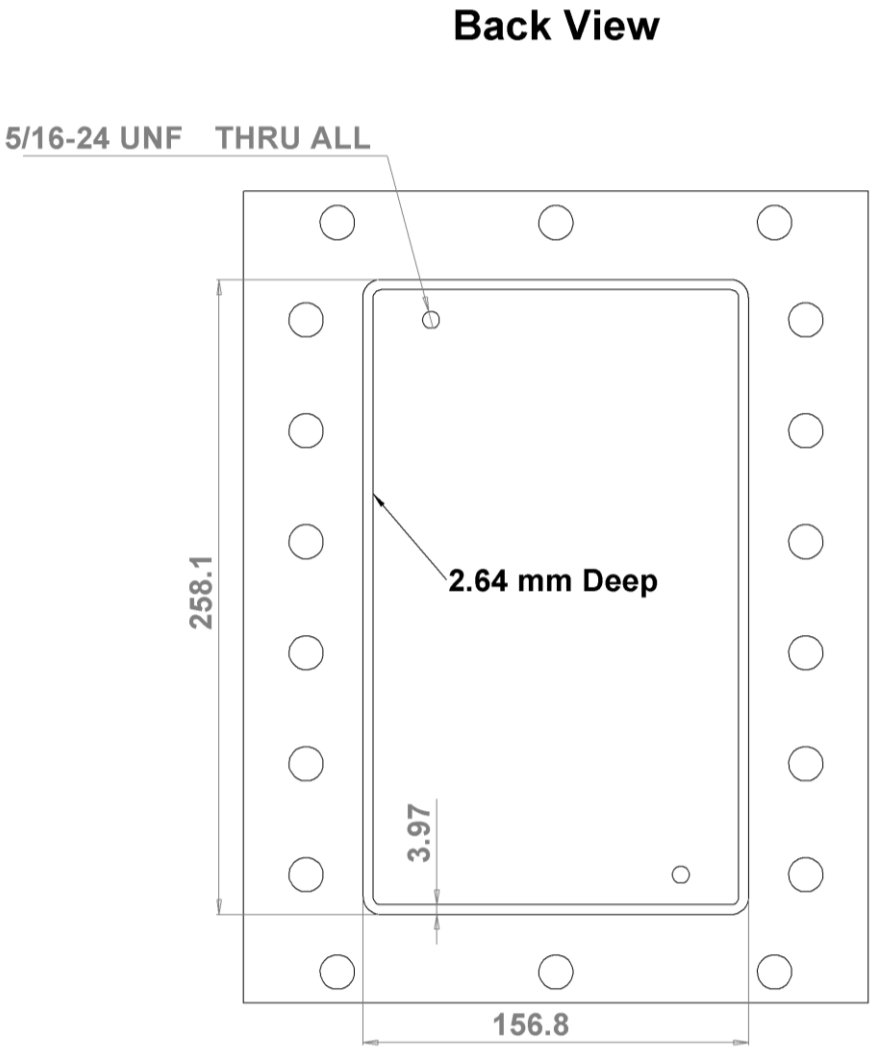

Figure 4.10: Test Section Front Cover Plate Dimensions

finite thickness of the surface temperature sensors and to enable temperature sensing of the back heater surface.

The compression necessary for sealing the assembly and maintaining adequate pressure on the heater was maintained using twelve steel Unistrut bars (McMaster-Carr part number 3310T257) bolted to the front and back of the test section. As shown in Figure 4.14, the flat portion of the Unistrut was compressed onto the test section by

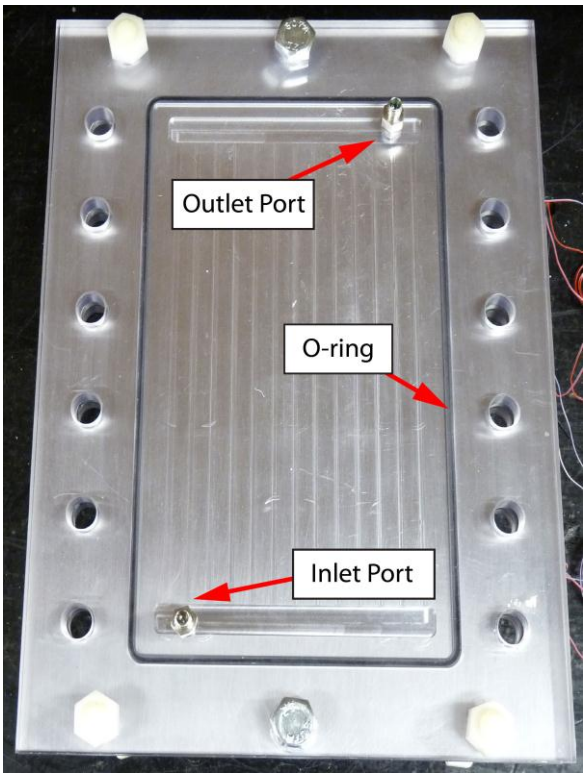

Figure 4.11: Test Section Assembly: Front View

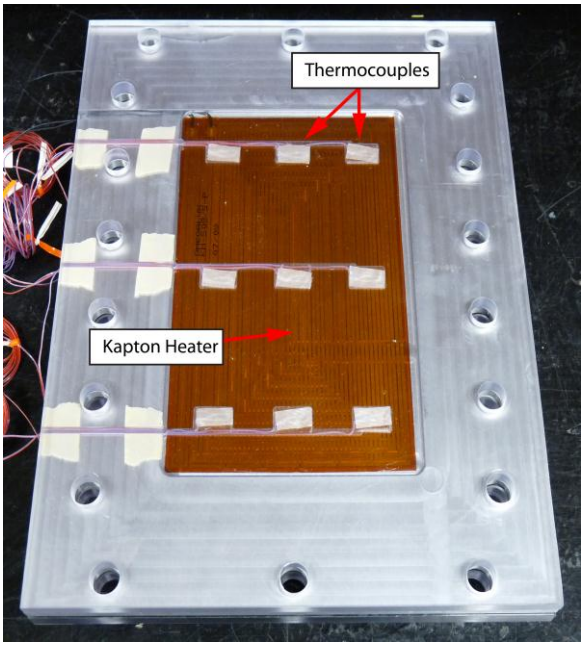

Figure 4.12: Test Section Assembly: Back View

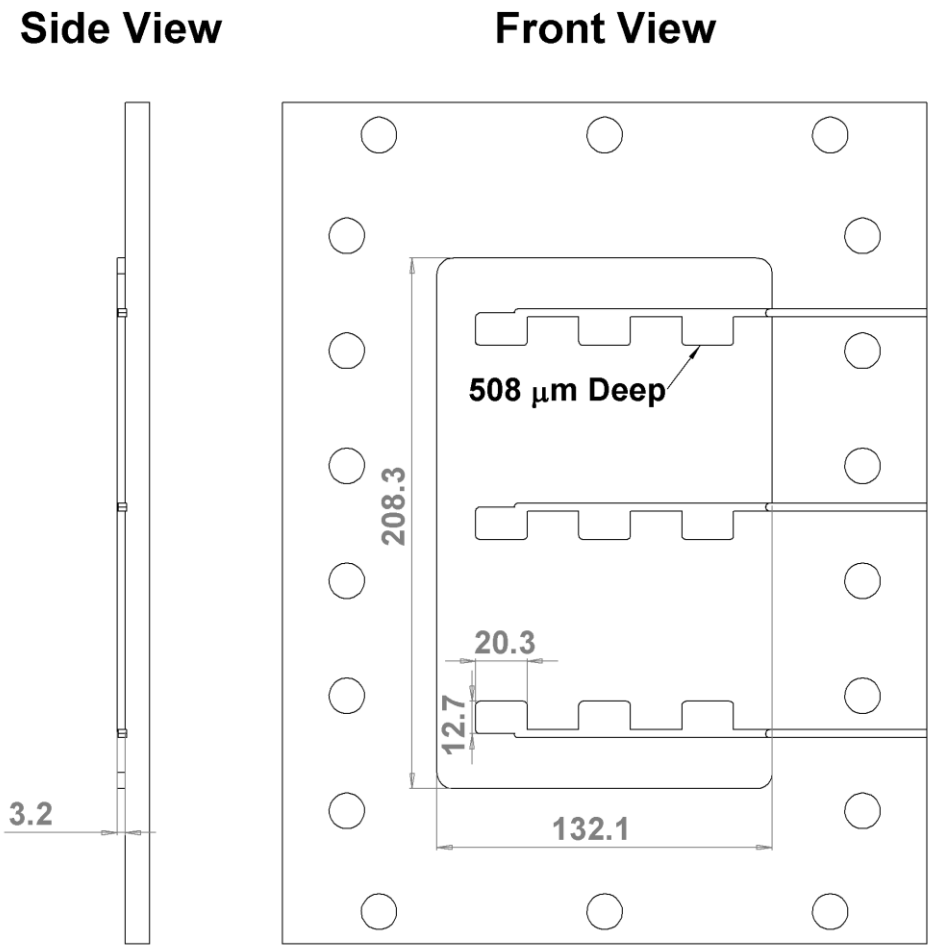

Figure 4.13: Test Section Back Support Plate Dimensions

applying force to its 90° legs using no-spin strut channel washers (McMaster-Carr part number 3585T13) and 12.7 mm bolts that passed through the slots machined in each plate. Contact pressure was improved by inserting a 1.59 mm thick sheet of polyurethane (McMaster-Carr part number 2178T33) between the unistrut and the front and back cover plates of the test section. However, as detailed in Section 4.4.1, there was still some deflection of the front polycarbonate due to pressure exerted by the test fluid (nominally 650 to 850 kPa). As a result, the effective channel height (160 μm) was slightly larger than the measured machined height (121 μm).

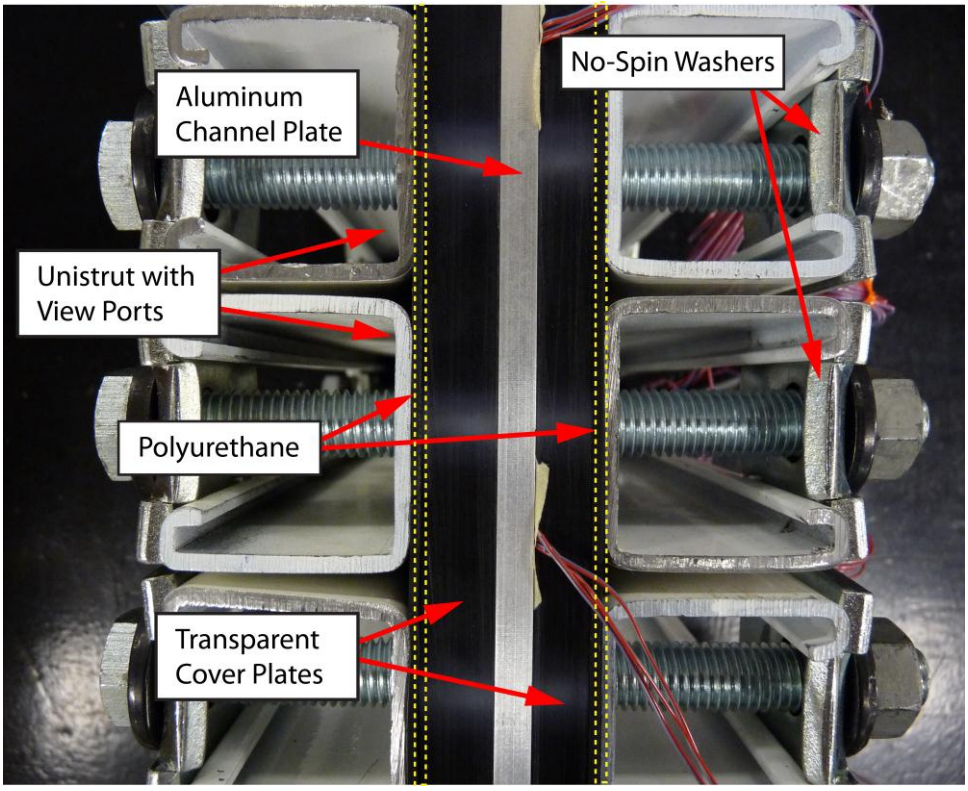

Figure 4.14: Test Section Assembly: Side View

4.3.3. Filling and Testing Procedure

Liquid refrigerant was first added to the primary loop through the expansion tank on the bottom of the test loop after evacuating to a sufficiently low pressure (nominally less than 500 microns or 0.07 kPa), which ensured minimal presence of non-condensable gases. To ensure that there was sufficient liquid in the test system, additional refrigerant was added through the expansion tank while venting the condenser until only liquid was present in the test section and connection lines. Test section pressure was controlled using two methods. As mentioned above, the coolant temperature was controlled by either adjusting the chiller evaporation temperature or the immersion heater power input, which in turn affected the primary fluid saturation pressure. However, the required system charge changed with saturation pressure. The amount of refrigerant in the loop

was controlled by adjusting the external pressure on the expansion tank bladder using a dry nitrogen cylinder.

To mimic heat rejection from the battery, heat inputs into the test section were necessarily low. For example, using the heater width and length dimensions (127 × 203 mm, respectively) and the unit cell thickness of the tested battery (284 μm), the equivalent battery volume was 7.34 mL. Hence, the heat input required to simulate 120 W L^{-1} of heat generation was merely 0.88 W. When conducting an energy balance around the test section, this low heat rate was difficult to measure, even when using the environmental chamber described in Section 4.3.1. In the tests conducted here, the heat rate was varied from 0.88 W to 48 W, which corresponds to effective volumetric battery heat generation rates of 120 and 6,500 W L^{-1}, respectively.

Refrigerant R134a was used as the test fluid, and tests were conducted at three fluid pressures (650 kPa, 750 kPa, and 850 kPa) that correspond to saturation temperatures of 24°C, 29°C, and 33°C, respectively. At each test temperature, tests were first conducted at the highest heat input (48 W), which was then decreased until the lowest heat input was reached (0.88 W). At each heat input, data were collected after steady state was reached. Subcooling at the condenser outlet was established visually through the clear connection tubing (2.438 mm ID high strength Nylon tubing, McMaster-Carr part number 8359K11) during data collection. After the data point collection, flow visualization video was taken across the entire test section to verify that the flow was distributed through the channels, which occurred in the majority of cases. In the next section, results from these tests are discussed and analyzed in detail.

4.4. Data Analysis and Uncertainty

In this section, the calculation methodologies for the desired quantities are discussed in detail. Estimation of the effective channel height is presented first. Then, a detailed sample calculation on the test section energy balance is presented, which includes estimation of the ambient heat loss and its associated uncertainty. The methodology and assumptions used to calculate the evaporator pressure drop from the results from these two sections is presented next. The two-phase frictional pressure drop in the test section is a critical parameter for understanding and quantifying the performance of the system, and these results are used in Section 4.5.3 to develop a new correlation for pure refrigerant flow in small passages.

4.4.1. Verification of Effective Channel Height

As mentioned in Section 4.3.2, pressure exerted on the front cover plate by the working fluid caused it to deflect, which increased its spacing from the bottom of the channel in the aluminum plates. To verify the effective channel height, the pressure drop in the test section was measured using dry nitrogen flowing through the test facility described in Section 4.3.1. However, the deflection of the plate increases slightly with pressure. Therefore, a nominal deflection height (39 μm) was verified by comparing single-phase pressure drop measurements to predictions from standard relationships for flow through a rectangular duct over a range of pressures. The deflection height is a weak function of system pressure (*i.e.*, increased pressure results in more deflection), and the purpose of these tests was to select a single value that was representative of the deflection height for the subsequent two-phase tests (Section 4.4.3). In this section, the assumptions and calculation methodology used to calculate the measured single-phase

pressure drop of dry nitrogen in the channels are presented. The measured values for five flow rates (0.07 g s^{-1} to 0.169 g s^{-1}) at two nominal test pressures (670 kPa and 870 kPa) are compared to the results calculated for the effective channel height (160 μm) to verify the nominal deflection of the aluminum plate (ΔH_{exp} = 39 μm) assuming the same channel width (3.175 mm).

Figure 4.15 shows the modified flow path for the dry nitrogen, which flowed from the pressure regulated cylinder through a partially open ball valve toward the test section. The pressure drop across the test section was measured using a differential pressure transducer (Omega model PX2300-1DI, 0 to 6.9 kPa range). The offset of the pressure transducer was set to zero to eliminate the effect of gravity on the measurement. This effect is minimal due to the low density of air. For example, at 900 kPa and 25°C, the density of nitrogen is 10.5 kg m^{-3}. At an overly conservative height of 0.5 m, the gravitational head is merely 0.05 kPa, which is at most 2.5% of the lowest measured pressure drop. The nitrogen then flowed through the mass flow meter before being exhausted to the ambient. The system pressure and flow rate were controlled by a combination of the nitrogen tank regulator and the exhaust ball valve setting.

The pressure drop in the test section channels (ΔP_{ch}) was calculated from the measured pressure drop (ΔP_{ch}) as follows:

$$\Delta P_{ch} = \Delta P_{meas} - \left(\Delta P_{f,i/o} + \Delta P_{minor,i/o} + \Delta P_{f,ih/oh} + \Delta P_{minor,ih/oh} + \Delta P_{minor,tee} \right) \quad (4.1)$$

Assuming no test section leakage, no momentum changes occurred between the two measurement locations. The component pressure drops in the parentheses in this equation, in order from left to right, are the frictional and minor losses in the connection

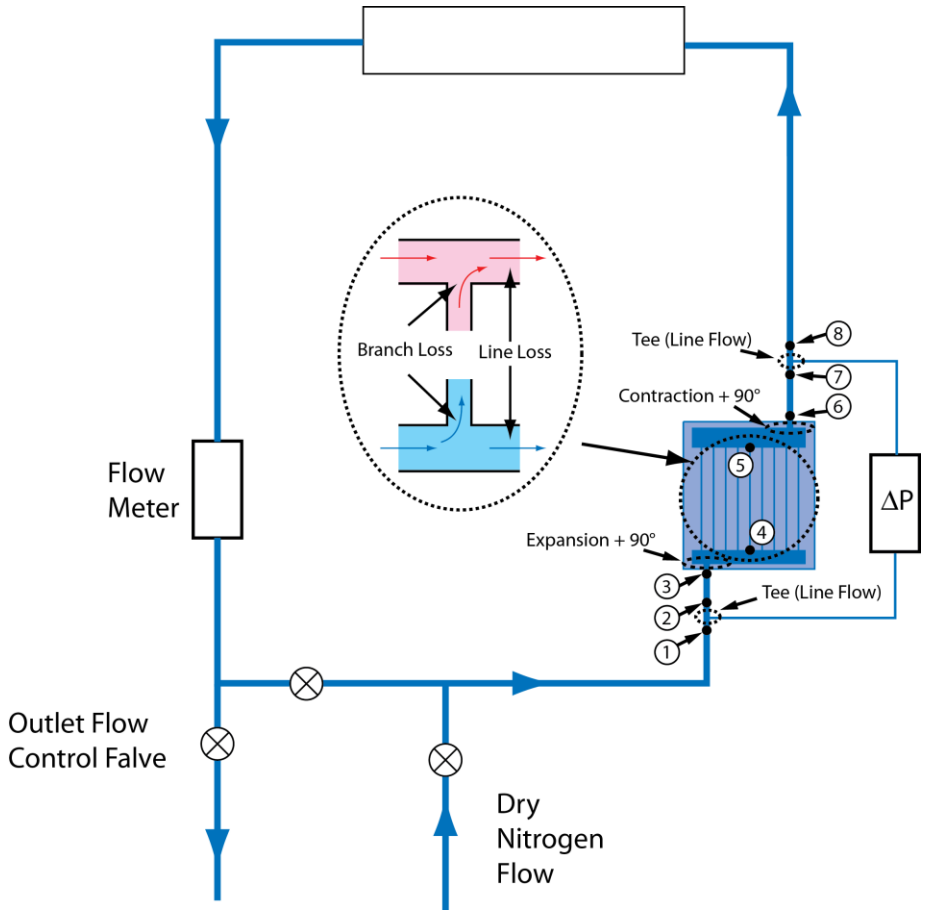

Figure 4.15: Dry Nitrogen Flow Path for Test Section Single-Phase Pressure Drop Measurement and Effective Channel Height Establishment

tubing and inlet and outlet headers and the minor loss across the connection tee. The calculation procedure for each of these is described in this section, which includes an analysis of a sample data point (Table 4-4).

The frictional pressure drops in the connection tubing between the test section inlet and outlet ($\Delta P_{f,i/o}$) were calculated as follows:

$$\Delta P_{f,i/o} = \frac{1}{2}\rho V_{i/o}^2 f_{Churchill} \frac{L_{i/o}}{D_{i/o}} \tag{4.2}$$

where the friction factor was calculated using the Darcy form of the Churchill (1977)

Table 4-4: Sample Data Point for Calculation of the Effective Channel Height

Item	Units	Value
P_i	kPa	861.5
T_i	°C	23.48
$\dot{m}$	g s^{-1}	0.169
ΔP	kPa	6.184
ρ	kg m^{-3}	9.801
μ	kg m^{-1} s^{-1}	1.784×10^{-5}

equation:

$$f_{\text{Churchill}} = 8\left[\left(\frac{8}{Re}\right)^{12} + \left(\left[2.457 \cdot \ln\left(\left[\frac{7}{Re}\right]^{0.9} + 0.27\frac{\varepsilon}{D}\right)\right]^{16} + \left[\frac{37530}{Re}\right]^{16}\right)^{-1.5}\right]^{\frac{1}{12}} \quad (4.3)$$

The velocity and cross sectional area were calculated as follows:

$$V_{i/o} = \frac{\dot{m}}{\rho A_{c,i/o}} \quad (4.4)$$

$$A_{c,i/o} = \frac{\pi D_{i/o}^2}{4} \quad (4.5)$$

The Reynolds number for the connection tubing was calculated as follows:

$$Re_{i/o} = \frac{4\dot{m}}{\mu \pi D_{i/o}} \quad (4.6)$$

The length and inside diameter of the plastic connection tubing were 0.508 m and 2.438 mm, respectively. Using the values listed in Table 4-4 and roughness value (ε) of 0, the Reynolds number for the sample data point was 4947, which results in a friction factor of 0.038. Hence, the total pressure drop for a velocity of 3.69 m s^{-1} in the inlet and outlet connection tubing was 0.529 kPa. In addition, the minor pressure loss for flow through the two connection tees was calculated as follows:

$$\Delta P_{\text{minor,tee}} = \frac{1}{2}\rho V_{\text{i/o}}^2 K_{\text{tee,line}} \tag{4.7}$$

Assuming a minor loss coefficient (K) of 0.2 for flow through the line of a tee (Munson *et al.*, 1998) and the same diameter as the connection tubing (2.438 mm), the total minor pressure drop through both tees was 0.027 kPa.

As shown in Figure 4.15, the flow turns by 90^o and also expands as it enters the test section inlet header from the connection tubing after point 3. It also similarly turns and contracts as it exits the outlet header before point 6. The pressure drop associated with these two effects was calculated as follows:

$$\Delta P_{\text{minor,tee}} = \frac{1}{2}\frac{\dot{m}^2}{\rho A_{\text{c,min}}^2}\left(2 \cdot K_{90^\circ} + K_{\text{exp}} + K_{\text{con}}\right) \tag{4.8}$$

The cross sectional areas of the circular connection tube and the (partially expanded) inlet and outlet headers were calculated using Equation 4.5 and as follows, respectively:

$$A_{\text{c,header}} = W_{\text{header}} \cdot \left(H_{\text{header}} + \Delta H_{\text{exp}}\right) \tag{4.9}$$

As shown in Figure 4.8, the width and height of the header were 12.7 mm and 1.52 mm, respectively. The deflection height (ΔH_{exp}) is the estimated amount of deflection between the aluminum microchannel plate and the clear cover plate. This deflection height (39 μm) is verified using pressure drop measurements during flow of dry nitrogen through the test section. The cross section areas of the connection tubing and test section headers were 4.67 mm^2 and 19.9 mm^2, respectively, which was consistent with assuming expansion and contraction at the inlet and outlet of the test section, respectively. The minor loss coefficients were calculated using the values given by Munson *et al.* (1998) for a sudden expansion and contraction (Figure 4.16). For an area ratio of 0.24, the minor

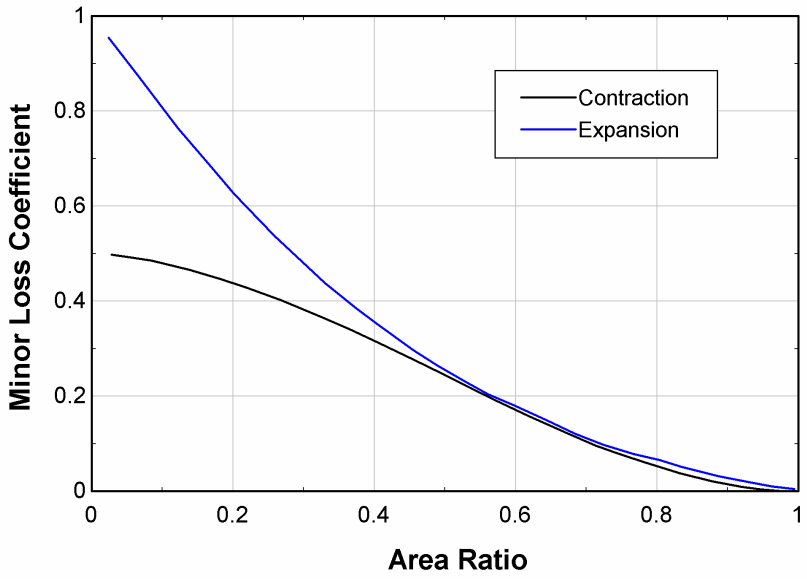

Figure 4.16: Minor Loss Coefficients for a Sudden Expansion or Contraction (Munson *et al.*, 1998)

losses from expansion and contraction were 0.57 and 0.42, respectively. Assuming minor loss coefficients of 0.3 for the 90° bends, the total minor loss from expansion and contraction and the turns at the test section inlet and outlet was 0.107 kPa.

The frictional loss inside the header was calculated assuming even flow distribution in the channels (Figure 4.17). In the inlet header, it was assumed that the flow enters the header from the left and that the frictional pressure drop length was equal to the channel pitch (10.2 mm for the test section) for every segment except the first, which was assumed to be half of the pitch (5.1 mm). The pressure drop in the outlet header was similarly estimated, and the total frictional pressure drop in one header was calculated as follows:

$$\Delta P_{\text{f,header}} = \frac{1}{2} \frac{\sum_{i}^{N_{\text{ch}}} \left(\dot{m}_i\right)^2 f_{\text{SB,i}} L_{\text{i}}}{\rho A_{\text{c,header}}^2} \frac{1}{D_{\text{header}}} \tag{4.10}$$

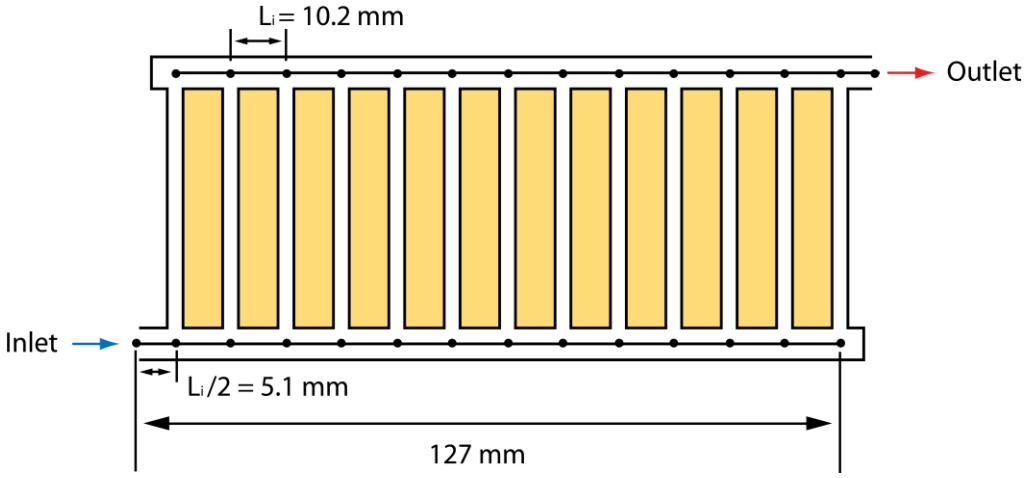

Figure 4.17: Frictional Pressure Drop Length Assumptions for Test Section Inlet and Outlet Header

Because the flow is laminar (verified below), it can be shown that the frictional pressure drop in the header can be calculated using the average mass flow rate as follows:

$$\Delta P_{\text{f,header}} = \frac{1}{2}\frac{\left(\frac{\dot{m}}{2}\right)^2}{\rho A_{\text{c,header}}^2} f_{\text{SB}} \frac{L_{\text{header}}}{D_{\text{header}}} \tag{4.11}$$

The laminar friction factor was calculated as follows (Shah and Bhatti, 1987):

$$f_{\text{SB}} = \frac{96}{Re}\left(1 - 1.3553\cdot\alpha + 1.9467\cdot\alpha^2 - 1.7012\cdot\alpha^3 + 0.9564\cdot\alpha^4 - 0.2537\cdot\alpha^5\right) \tag{4.12}$$

where the hydraulic diameter, aspect ratio, and Reynolds number were calculated as follows:

$$D_{\text{header}} = \frac{2\cdot\left(H_{\text{header}} + \Delta H_{\text{exp}}\right)W_{\text{header}}}{W_{\text{header}} + H_{\text{header}} + \Delta H_{\text{exp}}} \tag{4.13}$$

$$\alpha = \frac{H_{\text{header}} + \Delta H_{\text{exp}}}{W_{\text{header}}} \tag{4.14}$$

$$Re = \frac{\dot{m}}{\mu \cdot \left(H_{\text{header}} + \Delta H_{\text{exp}} + W_{\text{header}} \right)} \tag{4.15}$$

In the example data point, the aspect ratio and Reynolds number were 0.123 and 664.2, respectively, resulting in a friction factor of 0.124. The hydraulic diameter and length of the header were 2.783 mm and 0.127 m, respectively, resulting in a total frictional pressure drops in the headers of 0.010 kPa.

The branch and line losses in the inlet and outlet header were calculated using the methodology given by Idel'chik and Shteĭnberg (1994). The nomenclature for the calculation of these minor losses is shown in Figure 4.18. As shown in Figure 4.19, the flow was assumed to enter on one side of the inlet header and branch off to each subsequent channel by the same amount for each channel. The flow exited the outlet header on the opposite side from the test section, and it was similarly assumed that flow was collected in the header at each subsequent channel leading up to the exit. The velocities at the inlet and outlet of each branch in the inlet and outlet headers,

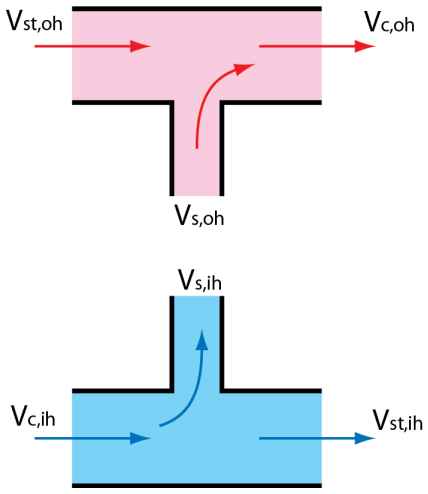

Figure 4.18: Inlet and Outlet Header Flow Loss Velocities

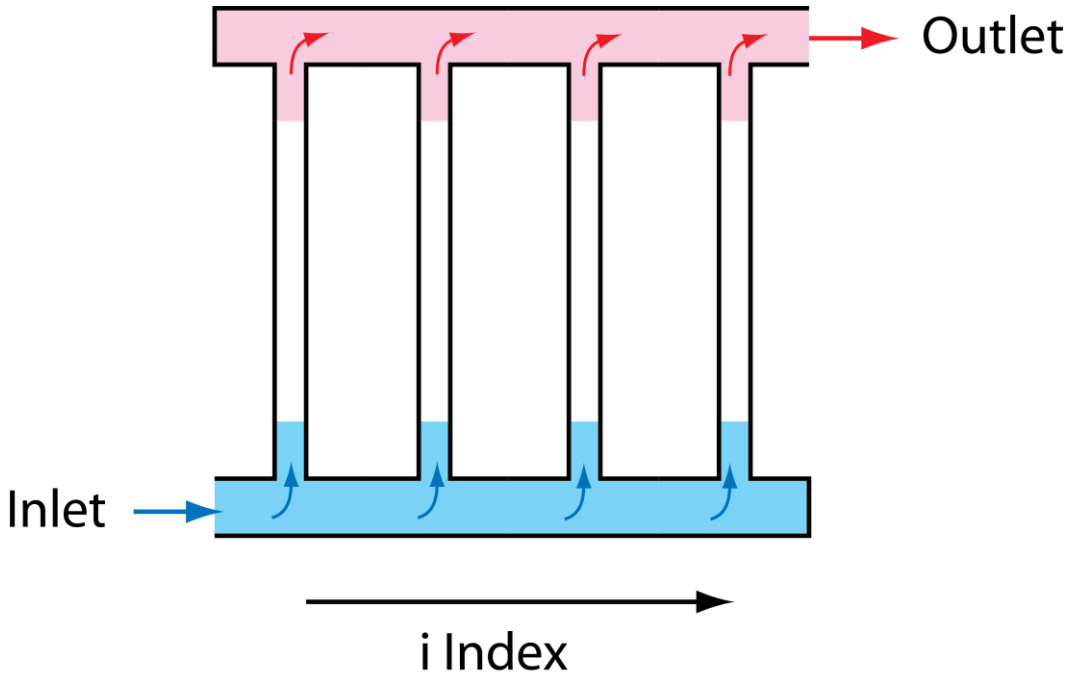

Figure 4.19: Assumed Flow Distribution in the Test Section

respectively, were calculated as follows:

$$V_{c,ih,i} = \frac{\dot{m}}{\rho A_{c,header}} \frac{N_{ch} + 1 - i}{N_{ch}} \tag{4.16}$$

$$V_{c,oh,i} = \frac{\dot{m}}{\rho A_{c,header}} \frac{i}{N_{ch}} \tag{4.17}$$

where index i is the channel number indexed from the inlet of inlet header (Figure 4.19), and the number of channels (N_{ch}) is 13. For example, i = 4 for the 4th channel from the inlet. Using these equations, the branch inlet and outlet velocities were 0.668 m s^{-1} and 0.267 m s^{-1} for the inlet and outlet headers, respectively, at this channel. The velocity in the channels was calculated as follows:

$$V_{ch} = \frac{\dot{m}}{N_{ch} \rho \cdot \left(W_{ch} \cdot H_{ch,eff} \right)} \tag{4.18}$$

In this representative case, the width and effective height of the channels are 3.175 mm and 160 μm, respectively, and the velocity in the channels is 2.611 m s^{-1}. The individual branch losses in the inlet and outlet headers were calculated using the following equations (Idel′chik and Shteĭnberg, 1994):

$$\Delta P_{\text{br,ih}} = \frac{1}{2}\rho V_{\text{c,ih}}^2 \left[1+\left(\frac{V_{ch}}{V_{\text{c,ih}}}\right)^2\right] \tag{4.19}$$

$$\Delta P_{\text{br,oh}} = \frac{1}{2}\rho V_{\text{c,oh}}^2 \left[1+\left(\frac{V_{\text{ch}}}{V_{\text{c,oh}}}\right)^2 - 2\left(1-\frac{\left(W_{\text{ch}}\cdot H_{\text{ch,eff}}\right)V_{\text{ch}}}{A_{\text{c,header}}V_{\text{c,oh}}}\right)^2\right] \tag{4.20}$$

Using the values above for the 4$^{\text{th}}$ channel from the inlet, the branch losses in the inlet and outlet header were 0.036 kPa and 0.033 kPa, respectively. The individual line losses in the inlet and outlet headers were calculated as follows (Idel′chik and Shteĭnberg, 1994):

$$\Delta P_{\text{line,ih}} = \frac{1}{2}\rho V_{\text{c,ih}}^2 K_{\text{c,ih}} \tag{4.21}$$

$$\Delta P_{\text{line,oh}} = \frac{1}{2}\rho V_{\text{c,oh}}^2 \left[1.55\left(\frac{\left(W_{\text{ch}}\cdot H_{\text{ch,eff}}\right)V_{\text{ch}}}{A_{\text{c,header}}V_{\text{c,oh}}}\right)-\left(\frac{\left(W_{\text{ch}}\cdot H_{\text{ch,eff}}\right)V_{\text{ch}}}{A_{\text{c,header}}V_{\text{c,oh}}}\right)^2\right] \tag{4.22}$$

The minor loss coefficient ($K_{\text{c,ih}}$) for the line loss in the inlet header as a function of the ratio of the volumetric flow is shown in Figure 4.20. The requisite volumetric flow rate was calculated as follows:

$$\frac{\dot{V}_{\text{ch}}}{\dot{V}_{\text{c,ih}}} = \frac{\left(W_{\text{ch}}\cdot H_{\text{ch,eff}}\right)V_{\text{ch}}}{A_{\text{c,header}}V_{\text{c,ih}}} \tag{4.23}$$

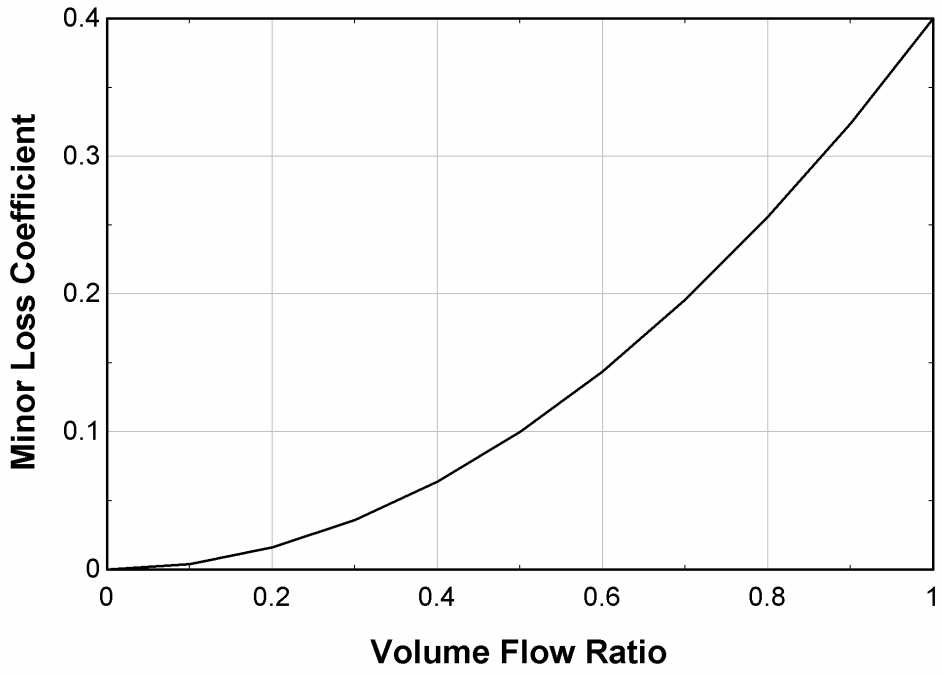

Figure 4.20: Minor Loss Coefficient for Flow through a Straight Portion of a Tee (Idel′chik and Shteĭnberg, 1994)

Thus, for the 4th channel, the volumetric flow rate ratio was 0.1, resulting in a minor loss coefficient of 0.004. Using the values above for the 4th channel from the inlet again, the line losses in the inlet and outlet header were merely 0.009 Pa and 0.114 Pa, respectively. The cumulative individual branch and line losses of both headers were the sum of the individual losses experienced at each channel, and were 0.876 kPa and 0.003 kPa, respectively, for this sample data point.

Using Equation 4.1, subtracting the above values for the connection tubing friction (0.529 kPa) and minor losses (0.107 kPa), tee line losses (0.027 kPa), header friction (0.010 kPa), and header line and branch losses (0.003 kPa and 0.876 kPa, respectively) from the measured pressure drop (6.184 kPa) yielded a measured channel

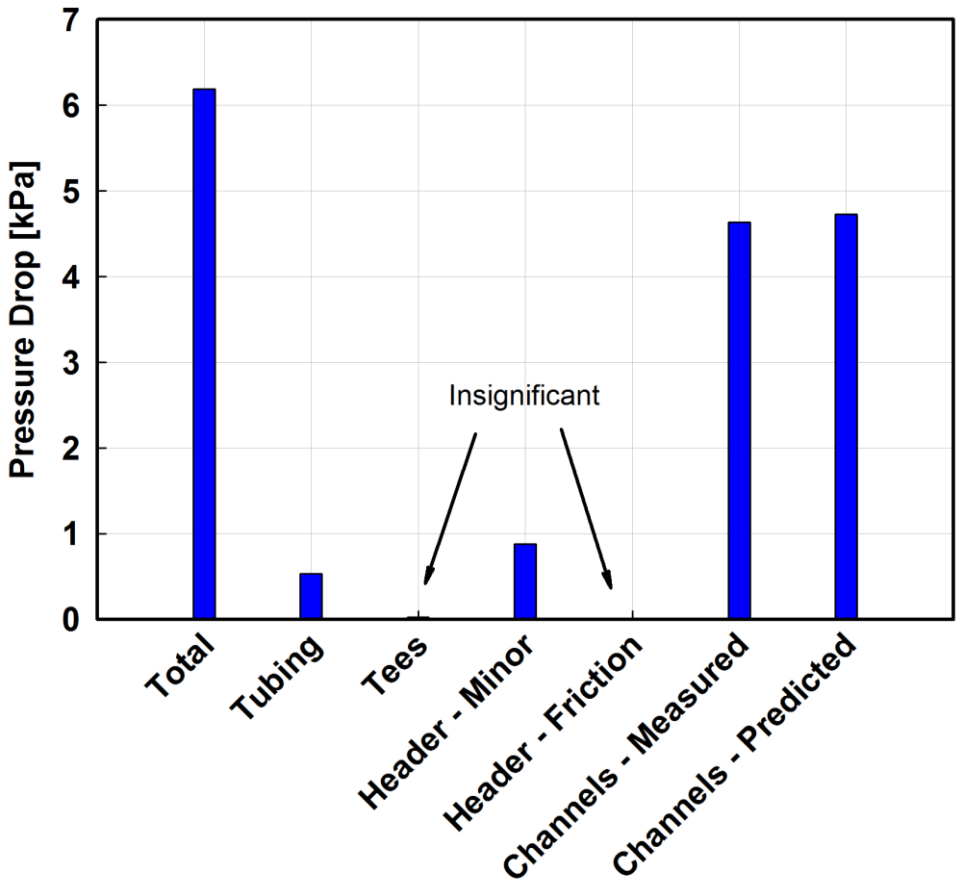

Figure 4.21: Representative Component Pressure Drop for the Single-Phase Pressure Drop Tests: 862 kPa and 0.169 g s^{-1}

pressure drop of 4.633 kPa for an effective channel height of 160 μm. As shown in Figure 4.21, the major portion of the measured pressure drop was within the channels, yielding accurate results as detailed in the uncertainty analysis below. Figure 4.22, shows the local pressure (neglecting influence of gravity due to the low density of gaseous nitrogen) inside the system between the measurement locations (positions 1 through 8 in Figure 4.15) as a function of distance along the flow path. This figure also shows that the major portion of the pressure loss in the system is within the channels.

To validate the deflection height estimation, the pressure drop for the channel was

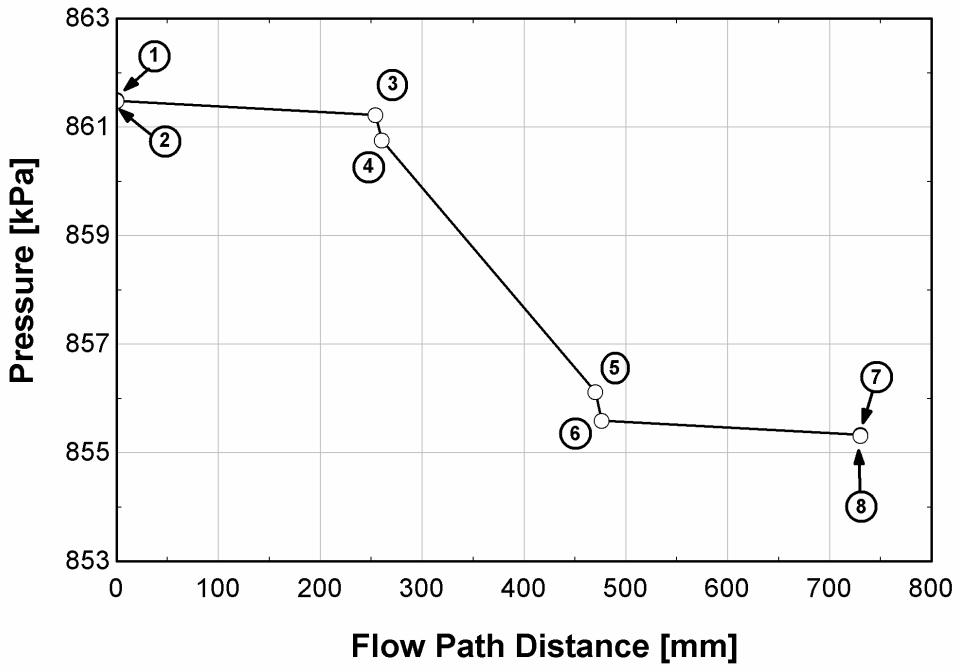

Figure 4.22: Local Pressure vs. Flow Position for the Single-Phase Pressure Drop Tests at a Representative Data Point: 862 kPa and 0.169 g s^{-1}

calculated using the following equation:

$$\Delta P_{\mathrm{f,ch}} = \frac{1}{2}\left(\frac{\dot{m}}{N_{\mathrm{ch}} \cdot \left(W_{\mathrm{ch}} \cdot H_{\mathrm{ch,eff}}\right)}\right)^2 \frac{f_{\mathrm{SB}}}{\rho}\frac{L}{D_{\mathrm{ch}}} \tag{4.24}$$

The friction factor was calculated using Equation 4.12, and hydraulic diameter, aspect ratio, and Reynolds number were calculated as follows:

$$D_{\mathrm{ch}} = \frac{2H_{\mathrm{ch,eff}}W_{\mathrm{ch}}}{H_{\mathrm{ch.eff}} + W_{\mathrm{ch}}} \tag{4.25}$$

$$\alpha_{\mathrm{ch}} = \frac{H_{\mathrm{ch,eff}}}{W_{\mathrm{ch}}} \tag{4.26}$$

$$Re_{\mathrm{ch}} = \frac{2\dot{m}}{\mu \cdot N_{\mathrm{ch}} \cdot \left(W_{\mathrm{ch}} + H_{\mathrm{ch,eff}}\right)} \tag{4.27}$$

The hydraulic diameter and aspect ratio of the 13 160 μm × 3.175 mm channels were 305 μm and 0.05, respectively. Assuming evenly distributed flow, the Reynolds number and corresponding friction factor were 437 and 0.206, respectively, yielding a calculated pressure drop of 4.73 kPa for a flow length of 0.210 m. As shown in Figure 4.21, this value slightly overpredicts the measured channel pressure drop by 0.1 kPa (2%), which is well within its uncertainty, as calculated below.

Combining the effects of bias and precision, the uncertainty of the measured channel pressure drop was calculated using a propagation of uncertainty approach without cross-correlation as follows:

$$UN_{\Delta P_{ch}} = \sqrt{\begin{aligned}&\left(UN_{\Delta P_{meas}}\right)^2 + \left(UN_{\Delta P_{f,i/o}}\right)^2 + \left(UN_{\Delta P_{minor,tee}}\right)^2 \\ &+ \left(UN_{\Delta P_{minor,i/o}}\right)^2 + \left(UN_{\Delta P_{f,ih/oh}}\right)^2 + \left(UN_{\Delta P_{minor,ih/oh}}\right)^2\end{aligned}} \tag{4.28}$$

Assuming a conservative ±50% uncertainty in each quantity calculated, using assumptions regarding the minor loss mechanisms and the respective loss coefficients, and using the published uncertainty of ±17.2 Pa for the pressure drop measurement, the measured channel pressure drop was known to within ±0.51 kPa. Figure 4.23 shows that the measured and predicted channel pressure drop for each data point collected assuming an effective channel height of 160 μm were well within the band of uncertainty of the measurement. To further substantiate this effective channel height, the channel height that exactly matches the measured pressure drop was calculated. Table 4-5 shows that slightly lower values were predicted at the lower test pressure, which was consistent with increased deflection with pressure. However, all values were within ±2.1 μm of its arithmetic average: 160 μm. Therefore, 160 μm was selected as effective channel height

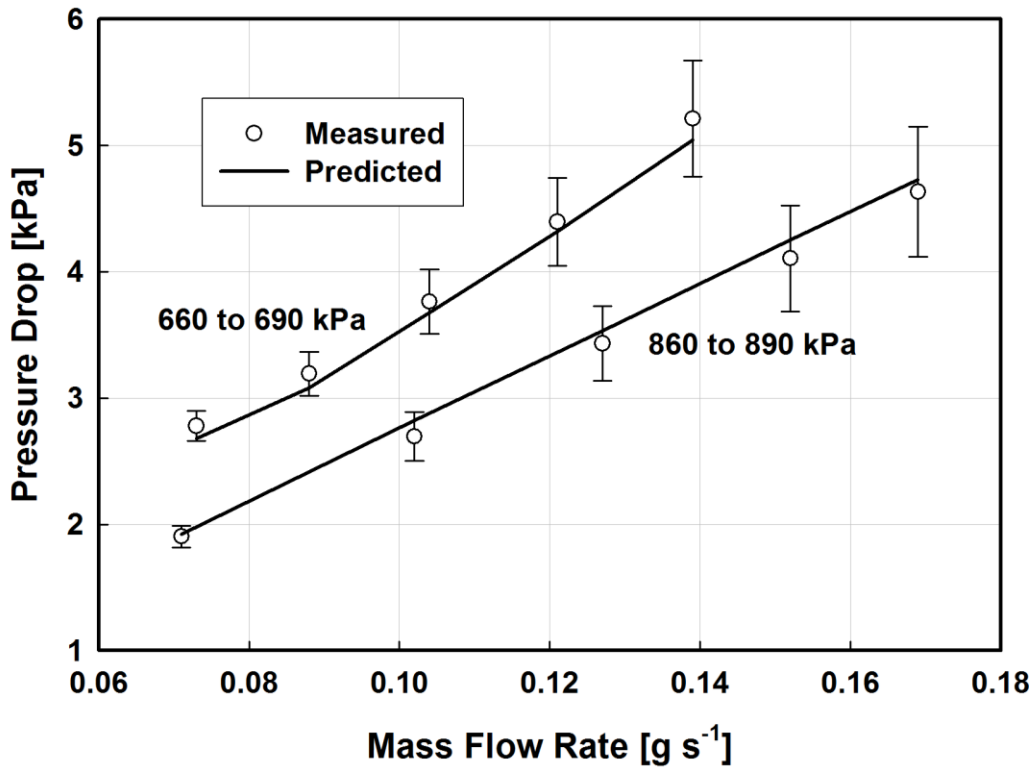

Figure 4.23: Predicted versus Measured Dry Nitrogen Test Section Pressure Drop Data

for all tests.

After these single phase tests were completed and the effective channel height established, the liquid-vapor phase-change performance of the system was assessed using R134a as the working fluid. However, during these two-phase flow tests, some bypass between adjacent channels was observed. Therefore, the potential for bypass in these single phase tests was quantified, and, as shown here, was small. Assuming that the pressure drop through the 12 bypass and 13 machined channels (Figure 4.24) were the same and laminar, the ratio of the mass flow rate through each channel and bypass was determined using the following equation:

$$\frac{\dot{m}_{ch}}{\dot{m}_{byp}} = \frac{func\left(\alpha = \frac{H_{ch,eff}}{W_{ch}}\right)}{func\left(\alpha = \frac{\Delta H_{eff}}{N_{pitch} - W_{ch}}\right)} \left(\frac{D_{ch}}{D_{byp}}\right)^2 \frac{N_{ch} H_{ch,eff} W_{ch}}{(N_{ch} - 1)\Delta H_{exp} W_{flat}} \tag{4.29}$$

It was assumed that bypass flow occurs only between channels, which results in the (N_{ch} – 1) term in the denominator. The aspect ratio function is within the parentheses in Equation 4.12, and the hydraulic diameter and cross-sectional area of the bypass were calculated as follows:

$$D_{byp} = \frac{2 \cdot \Delta H_{eff} \cdot W_{flat}}{\Delta H_{eff} + W_{flat}} \tag{4.30}$$

The width of the bypass (W_{flat}) was 6.985 mm, resulting in a hydraulic diameter of 77.6 μm for a 39 μm deflection gap (Figure 4.24). The aspect ratio functions for these two geometries (α = 0.050 and 0.006) were 0.936 and 0.992 for the channel and bypass gap, respectively. Therefore, for a channel hydraulic diameter of 305 μm, the mass flow rate ratio required for equal pressure drop through these channels and bypass paths was 33,

Table 4-5: Calculated Effective Channel Heights from the Single-Phase Tests

P_i	T	$\dot{m}$	ΔP_{ch}	$H_{ch,eff}$
kPa	**°C**	**g s^{-1}**	**kPa**	**μm**
662.3	23.21	0.139	6.605	158.4
674.4	23.55	0.121	5.449	159.2
680.9	23.49	0.104	4.542	158.9
686.9	23.30	0.088	3.718	158.2
656.3	23.50	0.073	3.136	158.1
890.7	23.56	0.071	2.154	160.5
871	23.59	0.102	3.282	162.3
865.4	23.31	0.127	4.332	161.4
861.7	23.7	0.152	5.373	161.7
861.5	23.48	0.169	6.184	161.0

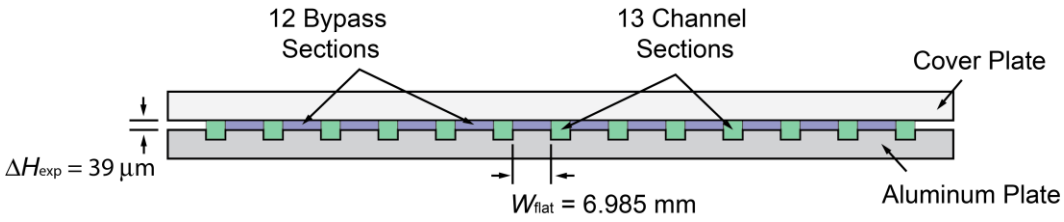

Figure 4.24: Cross Section of Assumed Bypass between Aluminum and Transparent Cover Plates

resulting in an estimated 97% of the flow passing through the channels.

4.4.2. Test Section Energy Balance and Uncertainty

During the two-phase experiments, heat was supplied to the test section using a thin-film heater adhered to the back surface of the aluminum plate (Figure 4.12). Although most of this heat was rejected to the test fluid (R134a), some of this heat was lost to its surrounding. In this section, the assumptions and methodology used for calculating the test section heat duty and outlet vapor quality (with their associated uncertainties) are described for a sample data point.

Performing an energy balance around the test section, the amount of heat supplied to the test fluid was calculated as follows:

$$\dot{Q}_{test} = \dot{Q}_{htr} - \dot{Q}_{amb} \tag{4.31}$$

As mentioned in Section 4.3.3, the power supplied to the heater was calculated from the measured voltage and current as follows:

$$\dot{Q}_{htr} = I_{htr} \cdot V_{htr} \tag{4.32}$$

Table 4-6 shows the measured quantities for a sample two-phase test data point taken at a nominal heat rate of 796 W L^{-1} for an R134a saturation temperature of 24.5°C. In this example, the measured current and voltage were 0.309 A and 19.95 V, respectively,

Table 4-6: Sample Data Point for Passive Microchannel Phase Change Testing: 796 W L^{-1}, 24.5°C R134a Saturation Temperature

Item	Units	Value	Item	Units	Value
Refrigerant			**Test Section**		
$\dot{m}_r$	g s^{-1}	0.563	$T_{s,top,L}$	°C	24.56
$T_{r,e,i}$	°C	23.63	$T_{s,top,M}$	°C	24.48
$T_{r,e,i,sat}$	°C	24.54	$T_{s,top,R}$	°C	24.51
$P_{r,e,i}$	kPa	656.7	$T_{s,mid,L}$	°C	24.23
$P_{r,e,o}$	kPa	653.8	$T_{s,mid,M}$	°C	24.23
$x_{r,e,o}$		0.052	$T_{s,mid,R}$	°C	24.42
Environmental Chamber			$T_{s,bot,L}$	°C	24.27
$T_{a,top}$	°C	23.74	$T_{s,bot,M}$	°C	24.34
$T_{a,bot}$	°C	23.37	$T_{s,bot,R}$	°C	24.15
T_{amb}	°C	23.55	$T_{s,i}$	°C	24.35
$T_{s,left}$	°C	23.90	$T_{s,o}$	°C	23.86
$T_{s,right}$	°C	23.89	**Film Properties**		
$T_{s,top}$	°C	23.64	T_{film}	K	296.9
$T_{s,bot}$	°C	23.41	ρ_{air}	kg m^{-3}	1.189
$T_{s,front}$	°C	24.04	Pr_{air}		0.728
$T_{s,back,1}$	°C	23.84	k_{air}	W m^{-1} K^{-1}	0.0254
$T_{s,back,2}$	°C	23.61	μ_{air}	cP	1.843×10^{-5}
$T_{s,back}$	°C	23.72			

yielding a heater power dissipation ($\dot{Q}_{htr}$) of 6.16 W.

Heat was lost from the test section to the surroundings through natural convection and radiation. For natural convection, the ambient temperature was the arithmetic average of two thermocouples suspended above and below the test section (Figure 4.25). For radiative heat losses, the temperature of each face of the inside surface of the chamber was measured. The majority of the surfaces were covered in low emissivity (ε = 0.07) aluminum foil or tape. However, the back surface of the chamber was only partially covered with these, and the back surface of the test section insulation was

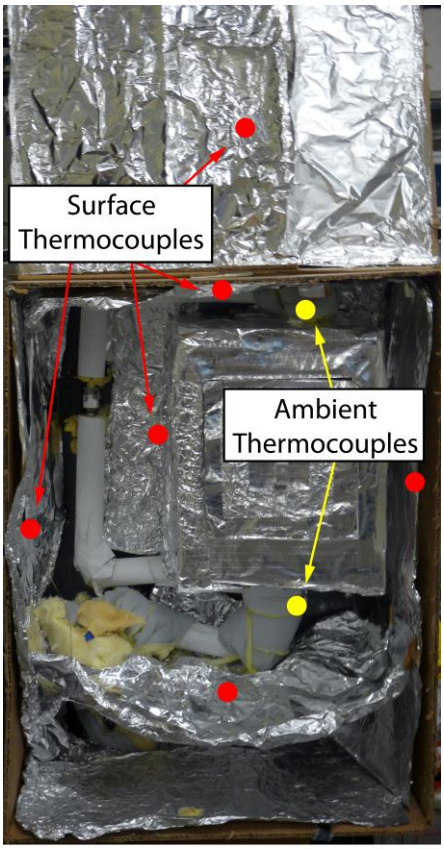

Figure 4.25: Thermocouple Locations in Partially Covered Environmental Chamber

covered with white paper (Figure 4.26). Figure 4.27 shows the assumed idealization of the back surface of the environmental chamber, which was used in the ambient heat loss calculation described in this section. It should be noted that several data points were repeated with every surface completely covered with aluminum foil or tape. As shown in Appendix B, there was no appreciable difference between the data obtained in both cases.

Figure 4.28 shows a schematic of the thermal resistance network for the test section ambient heat loss. The inside and outside surface of the insulation were assumed to be of uniform temperatures, with the former equal to the arithmetic average of the nine surface temperatures measured on the back side of the heater surface (Figure 4.12). It

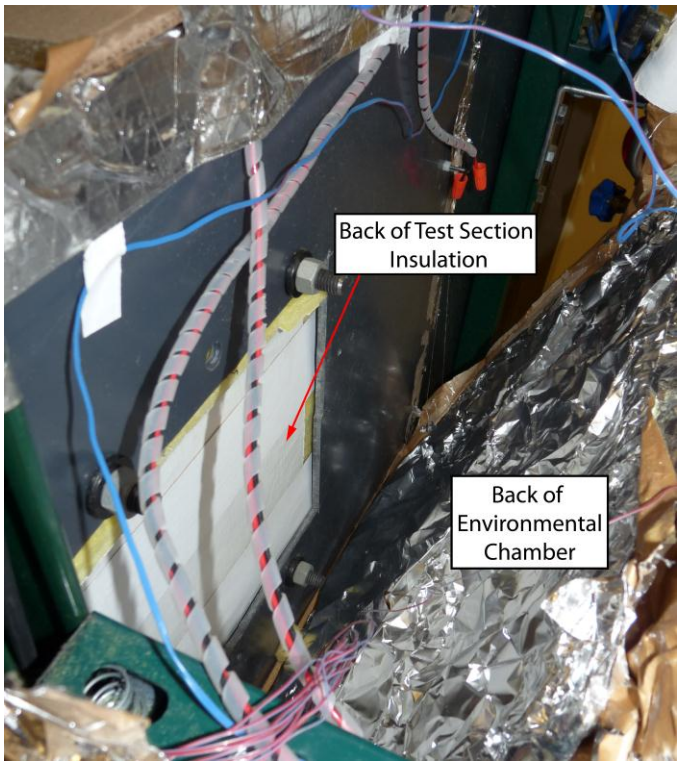

Figure 4.26: Back Surface of Insulated Test Section

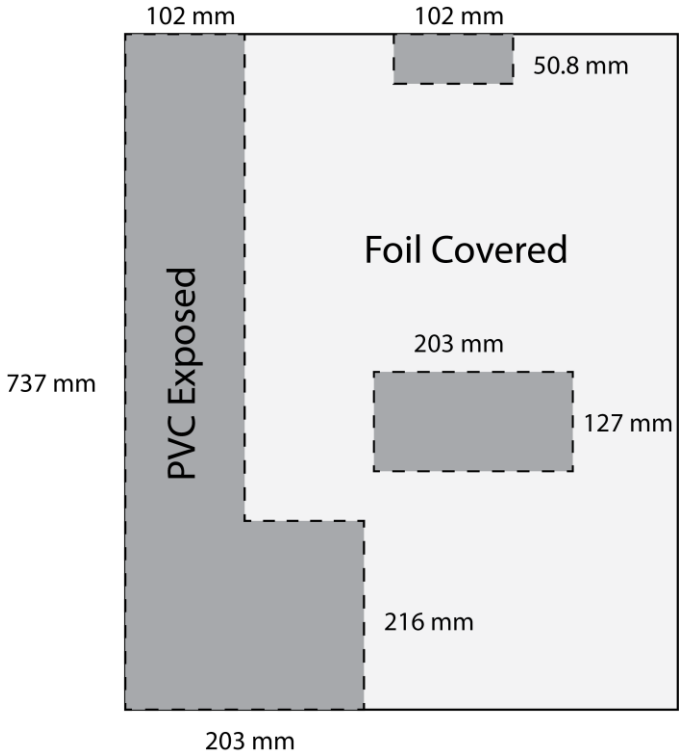

Figure 4.27: Back Surface Idealization for Ambient Heat Loss Calculation

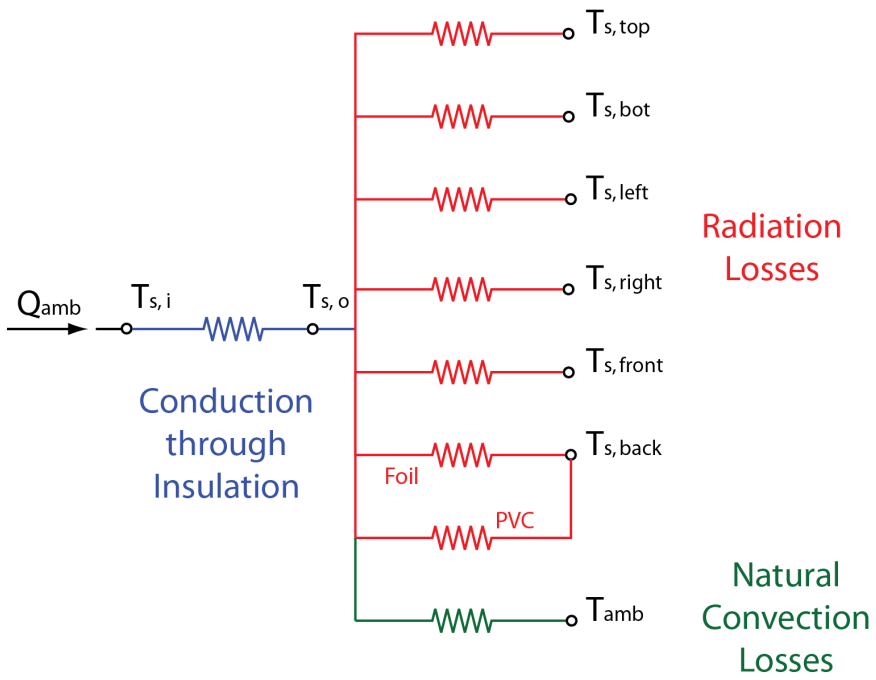

Figure 4.28: Thermal Resistance Network for Ambient Heat Loss Calculation

was also assumed that radiation leaving the outside surface of the covered insulation was intercepted only by the opposing surface of the environmental chamber (*i.e.*, a view factor of 1 for radiation leaving the insulation surface). The resulting energy balance at the outside surface of the insulation was as follows:

$$\dot{Q}_{\text{amb}} = \frac{k_{\text{ins}} A_{\text{s}}}{t_{\text{ins}}}\left(T_{\text{s,i}} - T_{\text{s,o}}\right) = \left(T_{\text{s,o}} - T_{\text{amb}}\right)\sum_{i=1}^{6} h_{\text{NC,i}} A_{\text{s},i} + \sum_{j=1}^{7} \frac{\sigma\left(T_{\text{s,o}}^4 - T_{\text{s,c,j}}^4\right)}{\dfrac{1-\varepsilon_{\text{s,j}}}{\varepsilon_{\text{s,j}} A_{\text{s,j}}} + \dfrac{1}{A_{\text{s,j}}} + \dfrac{1-\varepsilon_{\text{s,c,j}}}{\varepsilon_{\text{s,c,j}} A_{\text{s,c,j}}}} \quad (4.33)$$

The first term after the first equal sign is the heat conducted across the insulation. The terms after the second equal sign are the natural convective heat lost and the radiative heat exchanged between the test section insulation surface and the environmental chamber, respectively. The summation for the natural convective losses accounts for the calculation of the losses on each of the six sides of the test section insulation individually.

Similarly, the radiation exchange is estimated in seven parts to account for the six sides and an extra calculation used for subdividing the back surface into aluminum-covered and uncovered portions. In this equation, the outside surface temperature of the insulation ($T_{s,o}$) was solved iteratively, yielding the calculated ambient heat lost from the test section. As given in Table 4-6, this surface temperature was equal to 23.86°C for the example calculation.

The conduction surface area was calculated as follows:

$$A_s = 2\left(A_{s,side} + A_{s,top} + A_{front}\right) \tag{4.34}$$

where:

$$A_{s,side} = L_{s,side} \cdot H_{s,top} \tag{4.35}$$

$$A_{s,top} = A_{s,bot} = W_{s,top} \cdot H_{s,top} \tag{4.36}$$

$$A_{s,front} = A_{s,back} = L_{s,side} \cdot W_{s,top} \tag{4.37}$$

The test section insulation has a side length ($L_{s,side}$), top width ($W_{s,top}$), and top depth ($H_{s,top}$) of 457 mm, 356 mm, and 267 mm, respectively, resulting in side ($A_{s,side}$), top ($A_{s,top}$), front ($A_{s,front}$), and total conduction (A_s) surface areas of 0.122 m^2, 0.095 m^2, 0.163 m^2, and 0.759 m^2, respectively. The insulation thermal conductivity and thickness were 0.043 W m^{-1} K^{-1} and 50.8 mm, respectively. The inside surface temperature was the arithmetic average of the nine measured thermocouples (Table 4-6), which was 24.36°C for the sample data point. Thus, the resulting ambient heat loss was 0.322 W, which was confirmed by calculating the natural convective and radiative heat losses below.

Assuming laminar flow, the natural convection heat transfer coefficient from the

vertical surfaces of the test section were calculated as follows (Incropera and DeWitt, 1996):

$$h_{\mathrm{NC,vert}}\frac{L_{\mathrm{s,side}}}{k_{\mathrm{air}}}=0.68+\frac{0.67Ra_{\mathrm{L,vert}}^{1/4}}{\left[1+\left(\frac{0.492}{Pr_{\mathrm{air}}}\right)^{9/16}\right]^{4/9}} \tag{4.38}$$

For the top and bottom surfaces, the heat transfer coefficient is dependent on the calculated surface and surrounding ambient temperatures. The buoyancy driving force for natural convection is the same for hotter top and colder bottom surfaces, as well as for colder top and hotter bottom surfaces, which are calculated as follows, respectively (Incropera and DeWitt, 1996):

$$h_{\mathrm{NC,top,h}}\frac{L_{\mathrm{s,top}}}{k_{\mathrm{air}}}=h_{\mathrm{NC,bot,c}}\frac{L_{\mathrm{s,bot}}}{k_{\mathrm{air}}}=\begin{cases}0.54Ra_{\mathrm{L,bot}}^{1/4} & Ra_{\mathrm{L,bot}}\le 10^{7}\\ 0.15Ra_{\mathrm{L,bot}}^{1/3} & Ra_{\mathrm{L,bot}}>10^{7}\end{cases} \tag{4.39}$$

$$h_{\mathrm{NC,top,c}}\frac{L_{\mathrm{s,top}}}{k_{\mathrm{air}}}=h_{\mathrm{NC,bot,h}}\frac{L_{\mathrm{s,bot}}}{k_{\mathrm{air}}}=0.27Ra_{\mathrm{L,top}}^{1/3} \tag{4.40}$$

where the characteristic lengths for the top and bottom surfaces were calculated as follows:

$$L_{\mathrm{s,top}}=L_{\mathrm{s,bot}}=\frac{H_{\mathrm{s,top}}W_{\mathrm{s,top}}}{2\left(H_{\mathrm{s,top}}+W_{\mathrm{s,top}}\right)} \tag{4.41}$$

The Rayleigh number was calculated as follows:

$$Ra_{\mathrm{L}}=\frac{g\rho_{\mathrm{air}}^{2}Pr_{\mathrm{air}}\left(\frac{1}{T_{\mathrm{film}}}\right)\left(T_{\mathrm{s,o}}-T_{\mathrm{amb}}\right)L^{3}}{\mu_{\mathrm{air}}^{2}} \tag{4.42}$$

For the sample data point, the two measured ambient temperatures were 23.73°C and 23.37°C, respectively, yielding an average environmental temperature of 23.55°C. (These two temperature measurements were within ±0.4°C of each other for all tests.) Because this is colder than the surface temperature (23.86°C), the top and bottom heat transfer coefficients were calculated using Equations 4.39 and 4.40, respectively. The film temperature (T_{film}) was the arithmetic average of surface and ambient temperatures, and was equal to (296.9 K) for the sample data point. The necessary properties for the air inside the environmental chamber were evaluated at this temperature and are listed in Table 4-6. For this representative case, the characteristic length for the top and bottom surface was 76.2 mm, and the Rayleigh numbers for the side and top/bottom surfaces were 2.903×10^6 and 1.344×10^4, respectively. This resulted in natural convective heat transfer coefficients of 1.221 W m^{-2} K^{-1}, 1.939 W m^{-2} K^{-1}, and 0.970 W m^{-2} K^{-1} for the side/front, top, and bottom surfaces, respectively. Therefore, using Equation 4.33, the total heat lost from the test section to ambient via natural convection was 0.294 W.

The areas of the aluminum covered surfaces in the environmental chamber were calculated as follows:

$$A_{s,c,side} = L_{c,side} \cdot H_{c,top} \tag{4.43}$$

$$A_{s,c,top} = A_{s,c,bot} = W_{c,top} \cdot H_{c,top} \tag{4.44}$$

$$A_{s,c,front} = L_{c,side} \cdot W_{c,top} \tag{4.45}$$

The length ($L_{c,side}$), top width ($W_{c,top}$), and top depth ($H_{c,top}$) of the chamber were 737 mm, 699 mm, and 445 mm, respectively, resulting in side, top/bottom, and front surface areas of 0.328 m^2, 0.311 m^2, and 0.515 m^2, respectively. Using the dimensions in Figure 4.27,

the surface areas of the aluminum and PVC covered portions of the back chamber surface were 0.387 m^2 and 0.128 m^2, respectively. Conservatively assuming ε = 0.97 for the PVC and paper, and using the temperatures listed in Table 4-6, the radiative heat loss from the top, bottom, front, left and right sides, and back sides of the test section were 0.007 W, 0.014 W, -0.010 W, -0.002 W, -0.001 W, and 0.020 W, respectively, for the sample data point, where the negative numbers constitute ambient heat gain. Thus, the total radiative heat lost from the test section was 0.028 W, which, when combined with the natural convective loss (0.294 W), yields the same total heat loss as calculated from conduction through the insulation: 0.322 W.

Using Equation 4.31 and Q_{htr} = 6.16 W, this calculated heat rejection of 0.322 W yields a heat input to the test fluid of 5.84 W for the sample data point. The enthalpy of the primary refrigerant at the test section outlet is then calculated as follows:

$$h_{r,e,o} = \frac{\dot{Q}_{test}}{\dot{m}_r} + h_{r,e,i} \tag{4.46}$$

The inlet enthalpy (84.47 kJ kg^{-1}) was calculated from the measured inlet conditions ($T_{r,e,i}$ = 23.63°C, and $P_{r,e,i}$ = 656.8 kPa), yielding an outlet enthalpy of 94.85 kJ kg^{-1} for a mass flow rate of 0.563 g s^{-1}. Using the outlet pressure ($P_{r,e,o}$ = 653.8 kPa), the vapor quality was calculated to be 0.052 for the sample data point.

The uncertainties in the measured quantities for the passive two-phase test facility are given in Table 4-7. All uncertainties were assumed from manufacturer specifications, except the uncertainty in the environmental chamber temperatures. During the higher ambient temperature tests, the maximum temperature difference between any two points on the surface of the environmental chamber was 6.9°C ($\dot{Q}_{htr}$ = 1.52 W at 33°C $T_{r,sat}$ =

Table 4-7: Uncertainty in Measured Quantities for the Passive Microchannel Phase Change Test Facility

Item	Value
$\dot{m}_r$	0.19% (maximum)
$P_{re,i}$, $P_{re,o}$	1.38 kPa
T_s	3.5°C
T_{amb}	0.5°C
$L_{c,side}$, $H_{c,top}$, $W_{c,top}$	25.4 mm
$A_{back,PVC}$	20% (0.026 m^2)
t_{ins}	3.175 mm
I	0.0011 A
V	0.0033 V

33°C). Therefore, as a conservative assessment, the uncertainty of the surface temperatures was set to ±3.5°C. Furthermore, because the outside insulation surface temperature was determined iteratively using Equation 4.33, the uncertainty in $T_{s,o}$ and $\dot{Q}_{amb}$ require simultaneous determination. Therefore, the uncertainty in the ambient heat loss was calculated using the uncertainty propagation function in EES (Klein, 2010). For the sample data point, the propagated uncertainty for the ambient heat loss was ±0.822 W.

The uncertainty in the heat supplied to the fluid was calculated as follows:

$$UN_{\dot{Q}_{test}} = \sqrt{\left(\frac{\partial \dot{Q}_{test}}{\partial I_{htr}} UN_{I_{heater}}\right)^2 + \left(\frac{\partial \dot{Q}_{test}}{\partial V_{htr}} UN_{V_{htr}}\right)^2 + \left(UN_{\dot{Q}_{amb}}\right)^2} \tag{4.47}$$

where the partial derivatives with respect to the measured current and voltage were calculated as follows:

$$\frac{\partial \dot{Q}_{\text{test}}}{\partial I_{\text{htr}}} = V_{\text{htr}} \tag{4.48}$$

$$\frac{\partial \dot{Q}_{\text{test}}}{\partial V_{\text{htr}}} = I_{\text{htr}} \tag{4.49}$$

For the sample case under consideration, these partial derivatives were 19.95 W A^{-1} and 0.309 W V^{-1}, respectively. Therefore, using the uncertainties in listed in Table 4-7 and the uncertainty in heat loss to the ambient, the uncertainty in $\dot{Q}_{\text{test}}$ was ±0.822 W. The uncertainty in the test section outlet enthalpy was calculated as follows:

$$UN_{h_{\text{r,e,o}}} = \sqrt{\left(\frac{\partial h_{\text{r,e,o}}}{\partial \dot{Q}_{\text{test}}} UN_{\dot{Q}_{\text{test}}}\right)^2 + \left(\frac{\partial h_{\text{r,e,o}}}{\partial \dot{m}_{\text{r}}} UN_{\dot{m}_{\text{r}}}\right)^2 + \left(UN_{h_{\text{r,e,i}}}\right)^2} \tag{4.50}$$

where the partial derivatives with respect to the measured mass flow rate and test section heat duty are calculated as follows:

$$\frac{\partial h_{\text{r,e,o}}}{\partial \dot{Q}_{\text{test}}} = \frac{1}{\dot{m}_{\text{r}}} \tag{4.51}$$

$$\frac{\partial h_{\text{r,e,o}}}{\partial \dot{m}_{\text{r}}} = -\frac{\dot{Q}_{\text{test}}}{\dot{m}_{\text{r}}^2} \tag{4.52}$$

These were 1.776 s g^{-1} and 18.43 W g^{-2}, respectively, for the sample data point. The uncertainty in inlet enthalpy was calculated as follows:

$$UN_{h_{\text{r,e,i}}} = \sqrt{\left(\frac{\partial h_{\text{r,e,i}}}{\partial P_{\text{r,e,i}}} UN_{P_{\text{r,e,i}}}\right)^2 + \left(\frac{\partial h_{\text{r,e,i}}}{\partial T_{\text{r,e,i}}} UN_{T_{\text{r,e,i}}}\right)^2} \tag{4.53}$$

where the partial derivatives with respect to the measured temperature and pressure were calculated as follows:

$$\frac{\partial h_{\mathrm{r,e,i}}}{\partial P_{\mathrm{r,e,i}}} = \frac{h_{\mathrm{r,e,i}}\left(T_{\mathrm{r,e,i}}, P_{\mathrm{r,e,i}} + 10\,\mathrm{kPa}\right) - h_{\mathrm{r,e,i}}\left(T_{\mathrm{r,e,i}}, P_{\mathrm{r,e,i}} - 10\,\mathrm{kPa}\right)}{20\,\mathrm{kPa}} \tag{4.54}$$

$$\frac{\partial h_{\mathrm{r,e,i}}}{\partial T_{\mathrm{r,e,i}}} = \frac{h_{\mathrm{r,e,i}}\left(T_{\mathrm{r,e,i}} + 0.001°\mathrm{C}, P_{\mathrm{r,e,i}}\right) - h_{\mathrm{r,e,i}}\left(T_{\mathrm{r,e,i}} - 0.001°\mathrm{C}, P_{\mathrm{r,e,i}}\right)}{0.002°\mathrm{C}} \tag{4.55}$$

For this representative data point, these values were -4.85×10^{-4} kJ kg^{-1} kPa^{-1} and 1.417 kJ kg^{-1} K^{-1}, respectively, which yielded uncertainties in the inlet and outlet enthalpies of 0.709 kJ kg^{-1} and 1.623 kJ kg^{-1}, respectively. The uncertainty in outlet quality was calculated as follows:

$$UN_{x\,\mathrm{r,e,o}} = \sqrt{\left(\frac{\partial x_{\mathrm{r,e,o}}}{\partial P_{\mathrm{r,e,o}}} UN_{P_{\mathrm{r,e,o}}}\right)^2 + \left(\frac{\partial x_{\mathrm{r,e,o}}}{\partial h_{\mathrm{r,e,o}}} UN_{h\,\mathrm{r,e,o}}\right)^2} \tag{4.56}$$

The partial derivative with respect to the measured outlet pressure and enthalpy was calculated as follows:

$$\frac{\partial x_{\mathrm{r,e,o}}}{\partial P_{\mathrm{r,e,o}}} = \frac{x_{\mathrm{r,e,o}}\left(P_{\mathrm{r,e,o}} + 0.001\,\mathrm{kPa}, h_{\mathrm{r,e,o}}\right) - x_{\mathrm{r,e,o}}\left(P_{\mathrm{r,e,o}} - 0.001\,\mathrm{kPa}, h_{\mathrm{r,e,o}}\right)}{0.002\,\mathrm{kPa}} \tag{4.57}$$

$$\frac{\partial x_{\mathrm{r,e,o}}}{\partial h_{\mathrm{r,e,o}}} = \frac{x_{\mathrm{r,e,o}}\left(P_{\mathrm{r,e,o}}, h_{\mathrm{r,e,o}} + 0.001\,\mathrm{J}/g\right) - x_{\mathrm{r,e,o}}\left(P_{\mathrm{r,e,o}}, h_{\mathrm{r,e,o}} - 0.001\,\mathrm{J}/g\right)}{0.002\,\mathrm{J}/g} \tag{4.58}$$

For the sample data point, these values were -3.944×10^{-4} kPa^{-1} and 0.006 g J^{-1}, respectively, which yielded an uncertainty in the outlet quality of ±0.009.

Figures 4.29 and 4.30 show the mass flow rate and outlet test section quality versus measured test section heat duty, respectively, for all the data points collected. The uncertainty in each data point is included on this graph. These results are discussed in Section 4.5.1.

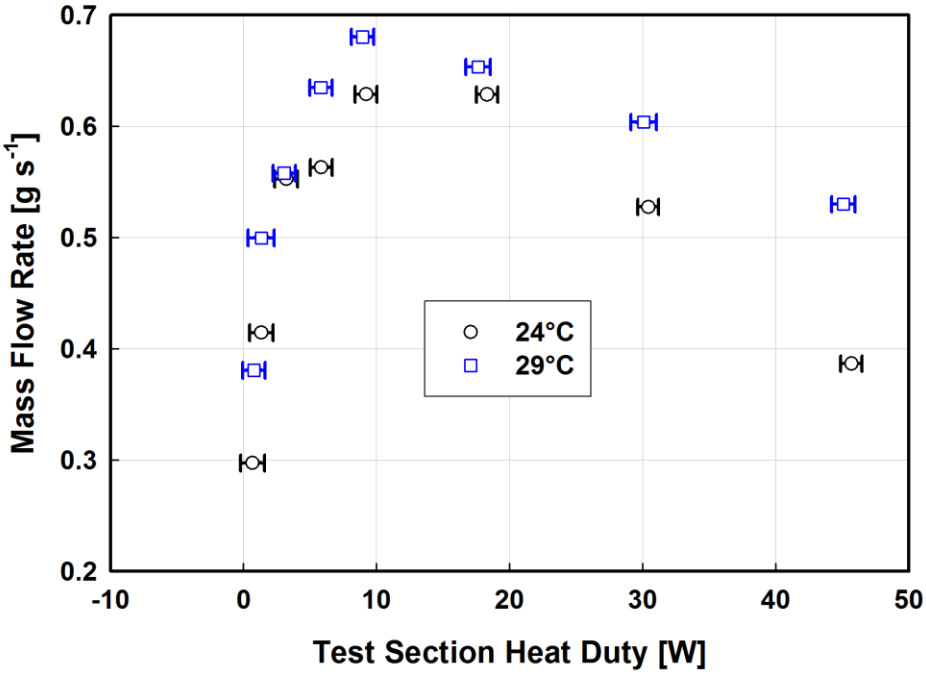

(a)

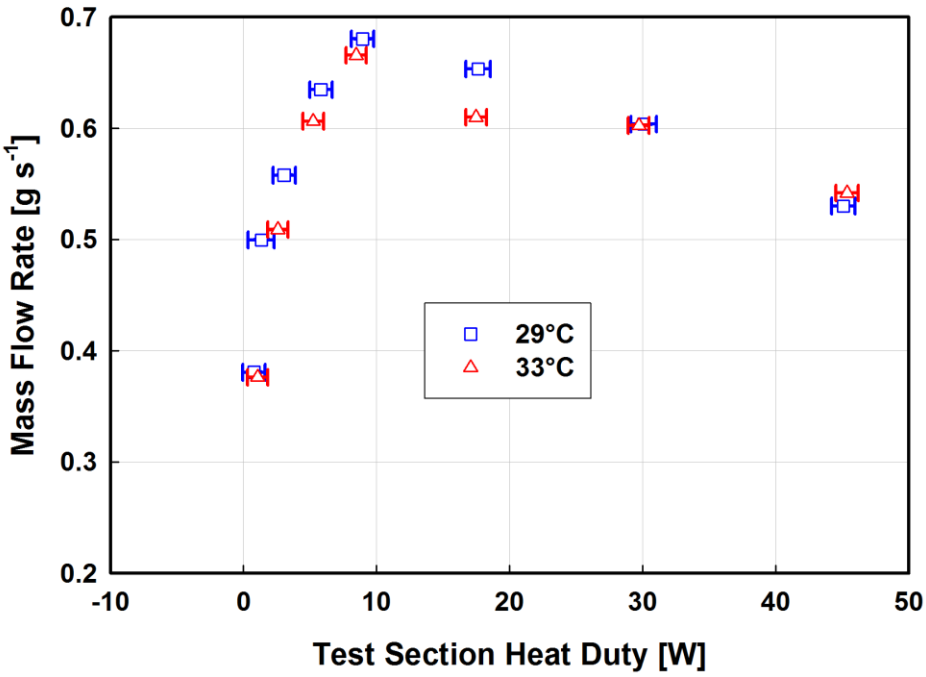

(b)

Figure 4.29: Mass Flow Rate Comparison for Passive System Performance Tests: (a) 24°C versus 29°C and (b) 29°C versus 33°C Saturation Temperatures

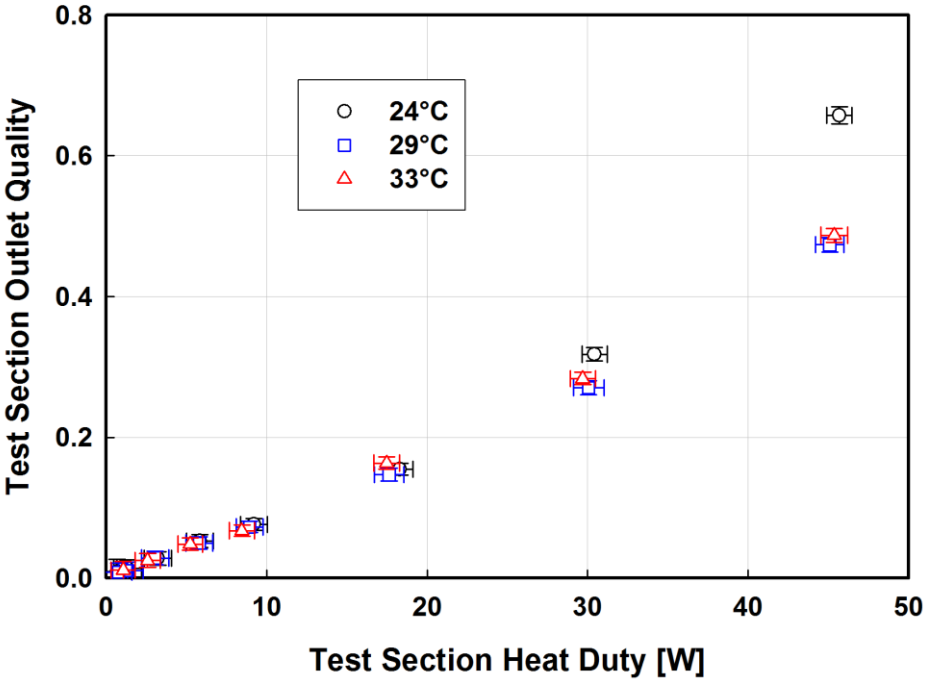

Figure 4.30: Calculated Test Section Outlet Quality for Passive Microchannel Phase Change Tests

4.4.3. Calculated Phase-Change Frictional Pressure Drop in the Test Section

In Section 4.4.1, the effective channel dimensions were established and validated based on pressure drop experiments using a single-phase fluid (dry nitrogen). These channel dimensions are used in conjunction with the measured mass flow rate and test section outlet quality to determine the phase-change frictional pressure drop inside the these channels for the two-phase tests described here. In contrast to the single phase tests, it was possible to see the bypass in these two-phase tests due to the existence of both liquid and vapor. However, because both phases were laminar in the two-phase tests, and the calculated bypass was minimal for the single phase tests (Section 4.4.1), the bypass was expected to have minimal impact on the two-phase results described here.

In this section, the assumptions and methodology used to calculate two-phase

frictional pressure drop (and its associated uncertainty) are presented. The frictional pressure drop results calculated here are compared with values obtained from correlations from prior relevant studies on microchannel two-phase flow in Section 4.5.3, and serve as the basis for the development of a new frictional pressure drop model. In Chapter Five, this new model is integrated into a simplified system model that is linked to the coupled electrochemical-thermal model for verification of the battery performance improvement possible through internal cooling.

A schematic of the passive microchannel test facility is shown in Figure 4.31. Fluid motion was sustained in the primary loop by the gravitational potential between the condenser and the evaporator (ΔP_{head}) overcoming frictional, expansion/contraction ($\Delta P_{\text{exp/con}}$), and other minor losses (ΔP_{minor}) in the loop. The two-phase frictional pressure drop in the evaporator ($\Delta P_{\text{f,tp,e}}$) was calculated as follows:

$$\Delta P_{\text{f,tp,e}} = \Delta P_{\text{head}} - \left(\Delta P_{\text{f,other}} + \Delta P_{\text{exp/con}} + \Delta P_{\text{minor}} \right) \tag{4.59}$$

The additional frictional pressure loss ($\Delta P_{\text{f,other}}$) included single phase and two-phase losses in the loop as well as the single phase loss in the test section channels. There is no net momentum change in the closed loop; thus, these losses are not incorporated into this analysis.

The gravity head is calculated from a hydrostatic force balance on the loop as follows:

$$\begin{aligned} \Delta P_{\text{head}} = {} & \rho_{\text{l,i}} g \left(\Delta H - L_{\text{sp}} \right) - \left[\left(1 - VF_{\text{SF}} \right) \rho_{\text{l}} + VF_{\text{SF}} \rho_{\text{v}} \right] \left(\Delta H - L_{\text{ch}} - W_{\text{header}} \right) \\ & - \left[\left(1 - VF_{\text{HG,o}} \right) \rho_{\text{l}} + VF_{\text{HG,o}} \rho_{\text{v}} \right] g \cdot W_{\text{header}} \\ & - \sum_{i=1}^{20} \left[\left(1 - VF_{\text{HG,i}} \right) \rho_{\text{l}} + VF_{\text{HG,i}} \rho_{\text{v}} \right] g \frac{\left(L_{\text{ch}} - L_{\text{sp}} \right)}{20} \end{aligned} \tag{4.60}$$

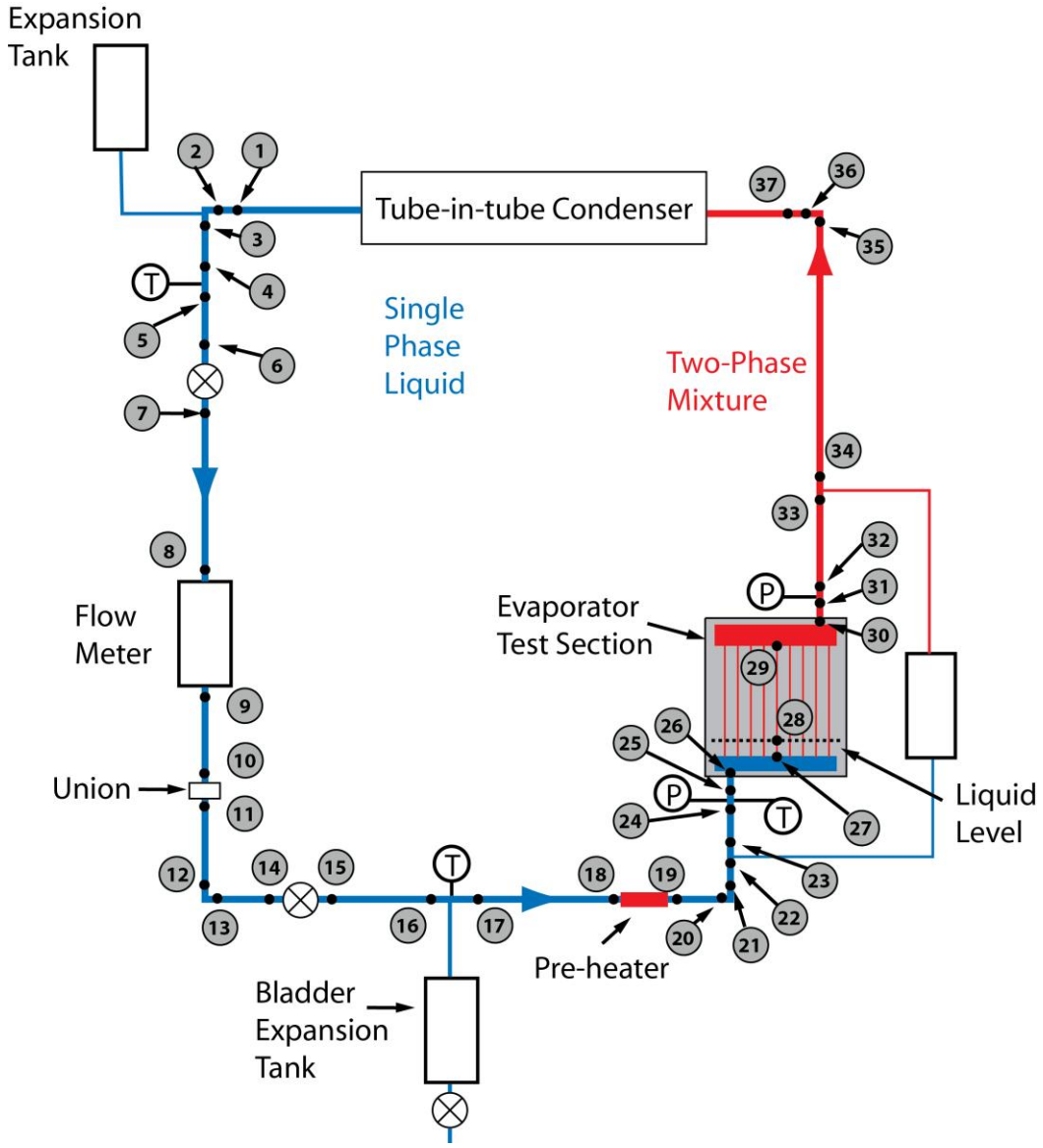

Figure 4.31: Passive Microchannel Test Fluid Flow Schematic

The first term is due to the liquid column height (ΔH) from the exit of the condenser (point 1) to the inlet of the test section channels (point 27) corrected for the single-phase length in the test section (L_{sp}, between points 27 and 28). Assuming that the test section heat flux is uniform, and because the mass flow rate and test section heat duty are known, the single-phase length was calculated as follows:

$$L_{sp} = \frac{h_{r,sat,l} - h_{r,e,i}}{h_{r,e,o} - h_{r,e,i}} L_{ch} \tag{4.61}$$

Based on the average test section pressure (655.3 kPa) for the sample data point, the liquid saturation enthalpy is 85.64 kJ kg^{-1}. Using the inlet and outlet enthalpies of 84.47 kJ kg^{-1}and 94.85 kJ kg^{-1}, respectively, the single phase length in the test section is 23.6 mm from the inlet (point 27) of the 209.6 mm long test section. For ΔH = 0.711 m and an inlet density of 1212 kg/m^3 (Table 4-8), the liquid column height exerted a pressure of 8.178 kPa.

The second term in Equation 4.60 is the gravity head of the two-phase fluid between the evaporator outlet (point 30) and the condenser inlet (point 37). The third and fourth terms in this equation are the gravity head of the outlet header (between points 29 and 30) and microchannels (between points 28 and 29) in the test section. The gravity head in the microchannels is computed in twenty equal segments. For the computation of each of these three final terms, the void fraction (*VF*) is required.

There have been many studies that measure void fraction of two-phase mixtures, but, similar to the frictional pressure drop studies discussed in Section 4.2, they have mostly been confined to either large diameter tubes or to small hydraulic diameter

Table 4-8: Fluid Properties for the Passive Microchannel Test Facility Sample Data Point

Item	Units	Value	Item	Units	Value
$P_{r,e,i}$	kPa	656.8	$P_{r,e,a}$	kPa	655.3
$T_{r,e,i}$	°C	23.63	σ	N m^{-1}	8.153 × 10^{-3}
Liquid Properties			**Vapor Properties**		
$\rho_{l,i}$	kg m^{-3}	1212	ρ_v	kg m^{-3}	31.82
ρ_l	kg m^{-3}	1209	μ_v	kg m^{-1} s^{-1}	1.194 × 10^{-5}
$\mu_{l,i}$	kg m^{-1} s^{-1}	1.980 × 10^{-4}			
μ_l	kg m^{-1} s^{-1}	1.957 × 10^{-4}			

channels at high G for pure refrigerants or low G with non-condensable gas and water mixtures. Recently, Revellin *et al.* (2006) showed that the homogeneous flow assumption predicted *VF* well for R134a flowing in a 500 μm circular tube. Triplett *et al.* (1999) showed that the homogenous flow overpredicted their data collected on a triangular tubes with D_h = 1.1 and 1.45 mm for high gas velocities, but predicted the remaining data well. Several additional studies (Ali *et al.*, 1993; Choi *et al.*, 2011; Chung and Kawaji, 2004) have found that air-water void fraction data are predicted well by an Armand-type correlation, which is defined as follows:

$$VF = K_{\text{Armand}} \cdot VF_{\text{HG}} \tag{4.62}$$

Chung and Kawaji (2004) noted that this type of correlation predicted their air-water data on circular channels with D_h > 250 μm, but not well for tubes with D_h = 100 μm and 50 μm. However, in a subsequent study by this group, they noted that the compressibility of the non-condensable gas caused the large deviation from the homogenous model in these smaller diameter tubes (Ide *et al.*, 2008). Similarly, Choi *et al.* (2011) recently found that as both aspect ratio and hydraulic diameter decreased from 0.91 to 0.17 and from 490 μm to 143 μm, respectively, their air-water data were predicted well by assuming homogenous flow. Based on these findings in the literature, the homogeneous void fraction defined below was used here for the test section microchannels and header:

$$VF_{\text{HG}} = \left[1 + \left(\frac{1 - x_{\text{r,e}}}{x_{\text{r,e}}} \right) \frac{\rho_{\text{v}}}{\rho_{\text{l}}} \right]^{-1} \tag{4.63}$$

For the microchannels, the void fraction was calculated at the local average quality within each segment, and the void fraction in the outlet header was calculated at the test section

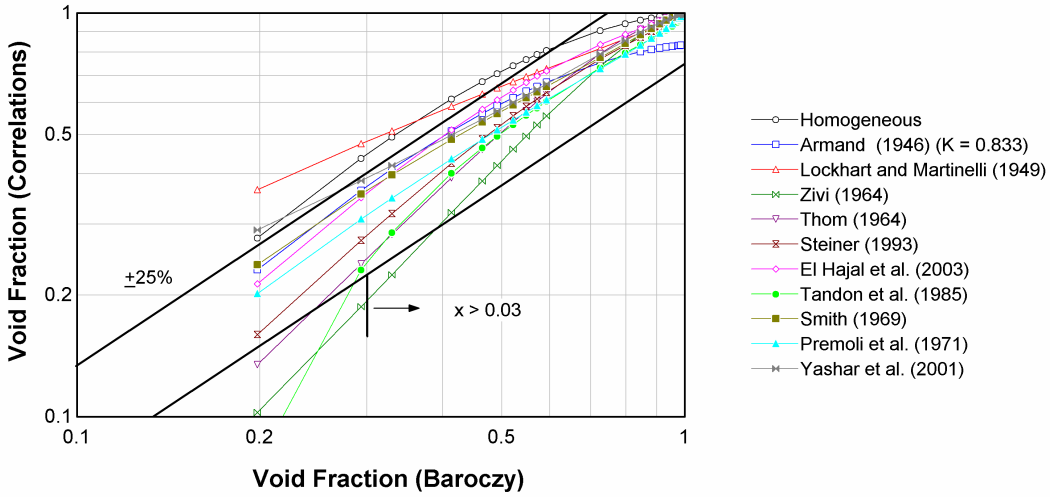

Figure 4.32: Comparison of Various Void Fraction Correlations

outlet quality. The required saturation fluid properties were all evaluated at the average test section pressure, and are summarized in Table 4-8 for the sample data point. Thus, the void fraction inside the header was 0.677 for an outlet vapor quality of 0.052. The void fraction for the 20 segments in the test section microchannels is summarized in Table 4-9 for the sample data point. The resulting gravity heads in the test section header and microchannels were 0.051 kPa and 1.228 kPa, respectively.

There are many void fraction correlations for estimating the gravity head in the 2.438 mm connecting tube between the evaporator outlet and condenser inlet. Garimella (2006) has given a comprehensive review of the available void fraction correlations. Figure 4.32 shows the predictions of some of these correlations (Armand, 1946; El Hajal *et al.*, 2003; Lockhart and Martinelli, 1949; Premoli *et al.*, 1971; Smith, 1969; Steiner, 1993; Tandon *et al.*, 1985; Thom, 1964; Yashar *et al.*, 2001; Zivi, 1964) compared to the prediction from the Baroczy (1965) correlation for R134a at a saturation pressure of 655 kPa flowing at G = 150 kg m^{-2} s^{-1} inside a circular tube of D_h = 2.438 mm from 0.01 < x < 0.95. (A sample calculation for these correlations is given in Table C-5.) As shown in

Table 4-9: Segmental Void Fraction and Gravity Head in the Test Section Microchannels for the Sample Data Point

Segment	$x_{r,e,a}$	VF_{HG}	ΔP_{head}
1	0.001	0.047	0.105
2	0.004	0.130	0.096
3	0.007	0.200	0.089
4	0.009	0.260	0.082
5	0.012	0.311	0.077
6	0.014	0.357	0.072
7	0.017	0.396	0.068
8	0.020	0.432	0.064
9	0.022	0.463	0.061
10	0.025	0.492	0.058
11	0.027	0.517	0.055
12	0.030	0.541	0.052
13	0.033	0.562	0.050
14	0.035	0.582	0.048
15	0.038	0.600	0.046
16	0.041	0.616	0.044
17	0.043	0.631	0.043
18	0.046	0.646	0.041
19	0.048	0.659	0.040
20	0.051	0.671	0.038
		Total	1.228

the figure, all of these correlations except the homogenous, Lockhart and Martinelli, and Zivi correlations were within ±25% of the Baroczy correlation for qualities greater than 0.025, which encompasses 18 of the 23 data points collected in this study. Therefore, the correlation by Baroczy was used to calculate the void fraction in the connecting tube as follows:

$$VF_{SF} = \left[1 + \left(\frac{1 - x_{r,e,o}}{x_{r,e,o}} \right)^{0.74} \left(\frac{\rho_v}{\rho_l} \right)^{0.65} \left(\frac{\mu_l}{\mu_v} \right)^{0.13} \right]^{-1} \tag{4.64}$$

For an outlet vapor quality of 0.052, and using the properties listed in Table 4-8, the void

fraction in the connecting tube is 0.464, which results in a connection tubing gravity head of 3.179 kPa. Therefore, the ΔP_{head} was equal to 3.719 kPa for the sample data point.

The expansion and contraction losses in the primary flow loop are shown schematically in Figure 4.33. These included losses at the inlet and exit of the Swagelok elbows (E1, E3, E4), tees (T1 through T6), and union (U1) and the flow meter (FM1), open ball valves (B1, B2), pre-heater (PH1), thermocouples (TC1, TC2, TC3), condenser (C1, C2), and test section (TS1, TS2). As explained below, expansion and contraction losses at the inlet and outlet of the microchannels in the test section were accounted separately using the methodology described in Section 4.4.1. In all cases, these pressure losses were calculated as follows:

$$\Delta P_{\text{exp/con}} = \frac{1}{2}\frac{\left(\frac{\dot{m}_{\text{r}}}{A_{\text{min}}}\right)^2}{\rho} K_{\text{exp/con}} \tag{4.65}$$

The minimum cross-section areas were straightforward for the circular (*i.e.*, elbows, tees, union, flow meter, ball valve, pre-heater, and connection tubing) and rectangular (*i.e.*, header) cross-sections. The minimum area for the 1.59 mm thermocouple (T1, T2, and T3) inserted in a 3.175 mm channel was calculated as follows:

$$A_{\text{min,t/c}} = \frac{\pi D_{\text{tube}}^2}{4} - \frac{D_{\text{tube}}}{2}\left[D_{\text{tc}}\cos(\theta) + D_{\text{tube}}\cdot\theta\right] \tag{4.66}$$

where θ was calculated as follows:

$$\theta = \sin^{-1}\left(\frac{D_{\text{t/c}}}{D_{\text{tube}}}\right) \tag{4.67}$$

This angle was 0.524 radians, resulting in a minimum area of 3.096 mm^2. The flow

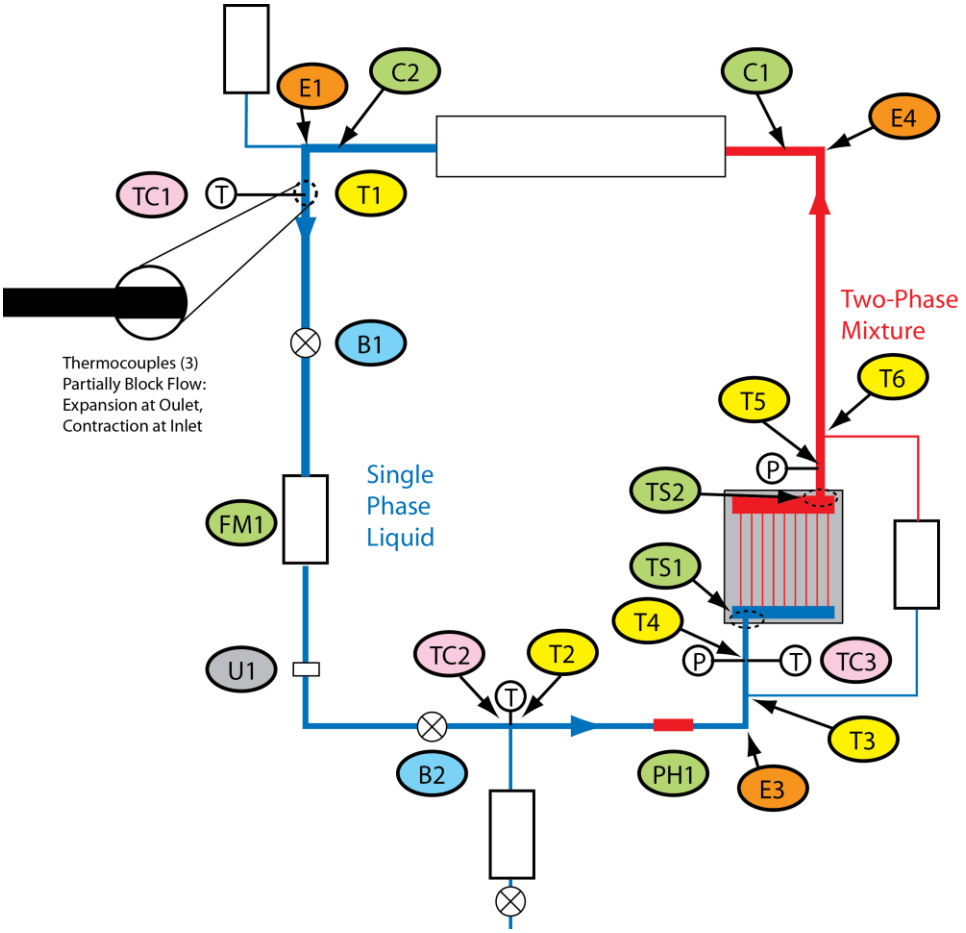

Figure 4.33: Expansion and Contraction Losses in the Passive Microchannel Test Facility

exiting the test section (TS2) and entering the condenser (C1) was a two-phase vapor mixture. The homogenous density was used in the above equation for these cases, and was defined as follows:

$$\rho_{\text{tp,HG}} = \left[\left(\frac{1 - x_{\text{r,e,o}}}{\rho_{\text{l}}} \right) + \left(\frac{x_{\text{r,e,o}}}{\rho_{\text{v}}} \right) \right]^{-1} \tag{4.68}$$

In the continuing example, the homogenous density at the test section outlet was 413 kg m^{-3}. The minor loss coefficients were determined using the values for sudden expansions and contractions shown in Figure 4.16. An additional loss of K = 0.3 was added for the

Table 4-10: Expansion and Contraction Pressure Losses for the Sample Data Point

Item	Location	$\dot{m}_r$	ρ	D_i	D_o	A_i	A_o	A_r	V_i	V_o	K	ΔP
		[g s^{-1}]	[kg m^{-3}]	[mm]	[mm]	[mm^2]	[mm^2]		[m s^{-1}]	[m s^{-1}]		[Pa]
Contraction (Outlets)	C2	0.563	1212	4.826	2.096	18.29	3.45	0.189	0.025	0.135	0.443	4.87
	E1, E3, T2, T3, U1			3.175	2.667	7.92	5.59	0.706	0.059	0.083	0.504	2.11
	T1			3.175	2.159	7.92	3.66	0.462	0.059	0.127	0.272	2.65
	TC1, TC2, TC3			3.175		7.92	3.10	0.391	0.059	0.150	0.968	13.2
	B1			6.350	2.438	31.67	4.67	0.147	0.015	0.099	0.462	2.77
	B2			6.350	2.667	31.67	5.59	0.176	0.015	0.083	0.449	1.88
	FM1			2.896	2.667	6.59	5.59	0.848	0.070	0.083	0.031	0.13
	PH1			6.350	2.667	31.67	5.59	0.176	0.015	0.083	0.449	1.49
	T4			3.175	2.438	7.92	4.67	0.590	0.059	0.099	0.178	1.06
	TS2		412	4.572	2.667	16.42	5.59	0.340	0.028	0.083	0.357	8.54
	T5, T6			3.175	2.438	7.92	4.67	0.590	0.172	0.292	0.355	6.26
	E4			3.175	2.096	7.92	3.45	0.436	0.172	0.396	0.291	9.39
Expansion (Inlets)	E1		1212	2.096	3.175	3.45	7.92	0.436	0.135	0.059	0.317	3.49
	E3, T1, T2, T3, U1			2.667	3.175	5.59	7.92	0.706	0.083	0.059	0.538	2.25
	TC1, TC2, TC3			N/A	2.667	19.85	5.59	0.281	0.069	0.244	0.694	15.0
	B1			2.438	2.896	4.67	6.59	0.709	0.099	0.070	0.106	7.57
	B2			2.159	6.350	3.66	31.67	0.116	0.127	0.015	0.776	2.80
	FM1			2.667	6.350	5.59	31.67	0.176	0.083	0.015	0.669	0.63
	PH1			2.159	6.350	3.66	31.67	0.116	0.127	0.015	0.776	1.78
	T4			2.438	3.175	4.67	7.92	0.590	0.099	0.059	0.185	1.11
	TS1			2.667	6.350	5.59	31.67	0.176	0.083	0.015	0.669	5.23
	T5		412	2.667	3.175	5.59	7.92	0.706	0.244	0.172	0.108	1.32
	E4, T6			2.438	3.175	4.67	7.92	0.590	0.292	0.172	0.371	6.53
	C1			2.667	4.572	5.59	16.42	0.340	0.083	0.028	0.425	20.9
Total												123.0

inlet and outlet test section 90° turns (TS1, TS2). These coefficients and corresponding pressure losses for the sample data point are summarized in Table 4-10, which resulted in a $\Delta P_{exp/con}$ of 0.123 kPa.

The additional minor losses in the test facility included flow through tees (T1 through T6), elbows (E1 through E4), and open ball valves (B1, B2) and the branch (BR) and line losses (LN) in the headers (Figure 4.34). The pressure drop for flow through the

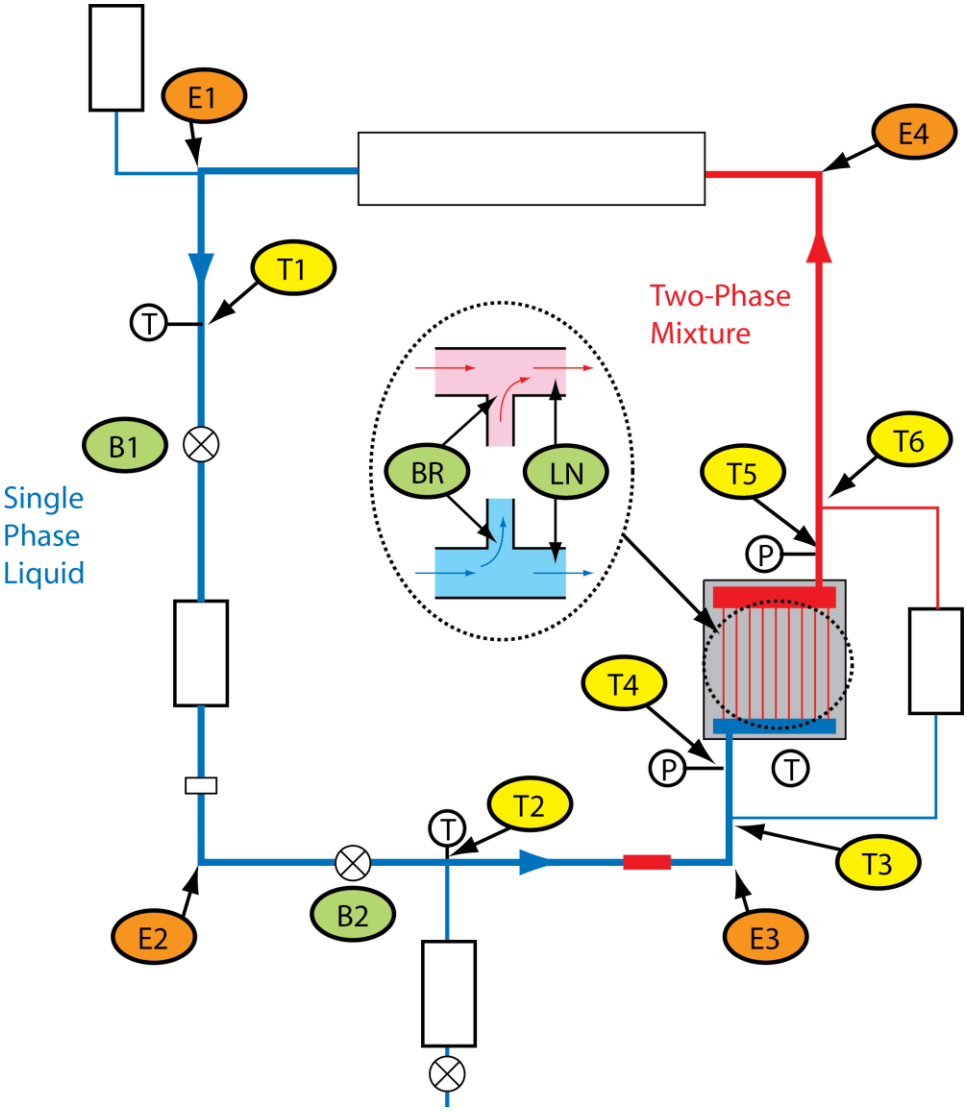

Figure 4.34: Additional Minor Losses in the Passive Microchannel Test Facility

Table 4-11: Additional Minor Pressure Losses in the Sample Data Point

Locations	$\dot{m}_r$	ρ	D_i	A_i	V_i	K	ΔP
	[g s^{-1}]	[kg m^{-3}]	[mm]	[mm^2]	[m s^{-1}]		[Pa]
E1, E3	0.563	1212	3.175	7.92	0.059	0.6	1.25
E2			2.667	5.59	0.083	0.3	1.26
T1 to T4			3.175	7.92	0.059	0.8	1.67
B1, B2			6.350	31.67	0.015	0.1	0.03
T5, T6		412	3.175	7.92	0.172	0.4	2.45
E4			3.175	7.92	0.172	0.3	1.84

former was calculated as follows:

$$\Delta P_{minor} = \frac{1}{2} \frac{\left(\frac{\dot{m}_r}{A_{minor}} \right)^2}{\rho} K_{minor} \tag{4.69}$$

The density of the two-phase flow mixture was calculated using the homogeneous mixture density Equation 4.68. The minor loss coefficients were assumed to be 0.3, 0.2, and 0.5 for flow through 90° turns (E1 through E4), tee straight legs (T1 through T6), and open ball valves (B1, B2, B3), respectively (Munson *et al.*, 1998). The cross-sectional areas, minor loss coefficients, and resulting pressure loss are given in Table 4-11 . The total minor pressure loss for these components was only 0.008 kPa.

The pressure loss due to branching and line flow in the inlet and outlet header was calculated using the methodology described in Section 4.4.1 for the single phase tests. The mixture density in the outlet header was calculated using Equation 4.68, which was consistent with the homogenous flow assumption made previously for calculating the void fraction. Tables 4-12 and 4-13 show the branch and line pressure losses in the inlet and outlet headers, respectively, for the sample data point. The total branch and line losses were 0.152 kPa and 0.64 Pa, respectively, for the headers. Therefore, the total minor loss (ΔP_{minor}) for this data point was 0.162 kPa.

Table 4-12: Branch and Line Pressure Losses in Inlet Header of the Test Section for the Sample Data Point

Channel Index	$\dot{m}_c$	V_c	$\dot{V}_c \times 10^7$	V_r	$\dot{V}_r$	$\Delta P_{line} \times 10^4$	ΔP_{br}
	[g s^{-1}]	[m s^{-1}]	[m^3 s^{-1}]			[Pa]	[Pa]
1	0.563	0.023	4.657	3.006	0.077	7.876	3.339
2	0.520	0.022	4.299	3.256	0.083	7.876	3.290
3	0.476	0.020	3.941	3.552	0.091	7.876	3.244
4	0.433	0.018	3.583	3.908	0.100	7.875	3.203
5	0.390	0.016	3.224	4.342	0.111	7.875	3.166
6	0.346	0.014	2.866	4.884	0.125	7.875	3.132
7	0.303	0.013	2.508	5.582	0.143	7.875	3.103
8	0.260	0.011	2.150	6.513	0.167	7.874	3.077
9	0.217	0.009	1.791	7.815	0.200	7.875	3.055
10	0.173	0.007	1.433	9.769	0.250	7.875	3.038
11	0.130	0.005	1.075	13.025	0.333	7.874	3.024
12	0.087	0.004	0.717	19.538	0.500	7.875	3.014
13	0.043	0.002	0.358	39.075	1.000		3.008
					Total	94.50	40.69

Table 4-13: Branch and Line Pressure Losses in Outlet Header of the Test Section for the Sample Data Point

Channel Index	$\dot{m}_c$	V_c	$\dot{V}_c \times 10^7$	V_r	$\dot{V}_r$	ΔP_{line}	ΔP_{br}
	[g s^{-1}]	[m s^{-1}]	[m^3 s^{-1}]			[Pa]	[Pa]
1	0.563	0.069	13.660	3.006	0.077		8.130
2	0.520	0.064	12.609	3.256	0.083	0.102	8.251
3	0.476	0.058	11.558	3.552	0.091	0.093	8.361
4	0.433	0.054	10.507	3.908	0.100	0.084	8.459
5	0.390	0.048	9.457	4.342	0.111	0.075	8.545
6	0.346	0.042	8.406	4.884	0.125	0.066	8.620
7	0.303	0.037	7.355	5.582	0.143	0.057	8.684
8	0.260	0.032	6.304	6.513	0.167	0.048	8.736
9	0.217	0.026	5.254	7.815	0.200	0.039	8.776
10	0.173	0.021	4.203	9.769	0.250	0.030	8.805
11	0.130	0.016	3.152	13.025	0.333	0.021	8.822
12	0.087	0.011	2.101	19.538	0.500	0.012	8.828
13	0.043	0.005	1.051	39.075	1.000	0.003	8.822
					Total	0.628	111.8

The frictional pressure drops inside the system are summarized Table 4-14, with locations denoted in Figure 4.31. No frictional pressure drop was calculated for the inlet and outlet headers due to the small fraction (less than 0.2% of the total) observed in the

Table 4-14: Single and Two-Phase Frictional Pressure Drop in the Passive Microchannel Test Facility for the Sample Data Point

Phase	Location Number		*D*	*L*	ΔP
	Start	End	mm	mm	Pa
Single Phase	1	2	2.096	13.3	2.6
	3	4	2.667	44.5	3.3
	4	5			5.8
	5	6	2.159	31.8	5.5
	7	8	2.438	152.4	16.1
	8	9			104.9
	9	10	2.667	50.8	3.8
	11	12	2.667	222.3	16.5
	13	14	2.667	31.8	2.4
	15	16	2.667	82.6	6.1
	16	17			5.8
	17	18	2.667	85.7	6.3
	18	19	4.572	63.5	0.5
	19	20	2.667	66.7	4.9
	21	22	2.667	82.6	6.1
	23	24	2.438	254.0	26.9
	24	25			5.8
	25	26	2.438	38.1	4.0
	27	28	0.305	23.6	157.9
Two Phase	28	29	0.305	185.9	2.727
	30	31	2.667	46.0	18.0
	32	33	2.438	254.0	138.9
	34	35	2.438	254.0	138.9
	36	37	2.096	13.3	12.8
	37	1	4.826	495.3	14.4

single-phase tests for gas flow. The geometric dimensions used to calculate each component pressure drop are also shown in the table. The pressure drop across the mass flow meter was calculated using the manufacturer's specification (Micromotion Elite Model CMF010M), which is shown graphically in Figure 4.35 using the average inlet conditions for the entire data set at each test temperature. As shown in the figure, there

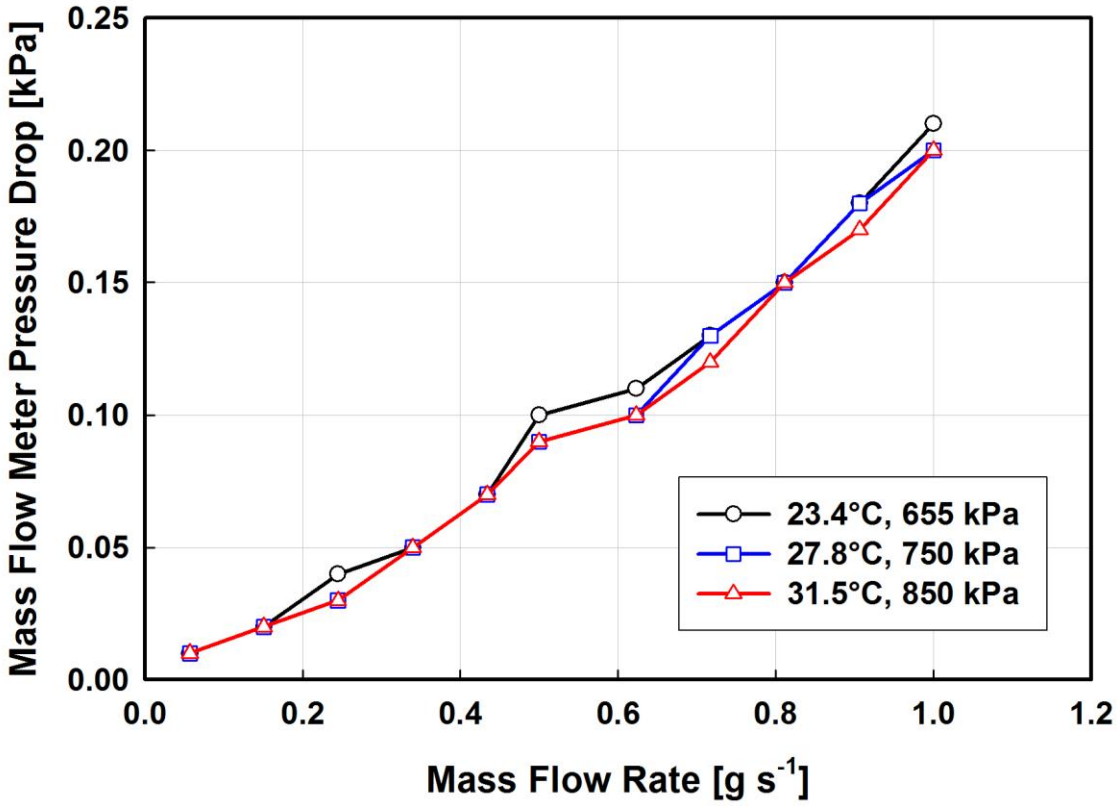

Figure 4.35: Mass Flow Meter Pressure Drop at Different Fluid Conditions

was very little difference in the predicted pressure drop as the R134a conditions changed, but a correction based on the liquid viscosity was still employed. At the average test temperatures of 23.4°C, 27.8°C, and 31.5°C, the liquid viscosities of R134a were 0.1982 cP, 0.1879 cP, and 0.1796 cP, respectively. The pressure drop was then determined using the interpolate2DM function in EES (Klein, 2010). For example, at a mass flow rate of 0.563 g s^{-1} and a liquid inlet viscosity of 0.1987 cP, the pressure drop across the mass flow meter for the sample data point was 0.105 kPa.

The single phase frictional pressure drops in the connecting lines and the test section were calculated using Equations 4.1 and 4.3 and Equations 4.12 and 4.24, respectively. As shown in Table 4-14 and using the property values in Table 4-8, the frictional pressure drop in the pre-heater (between points 18 and 19 in Figure 4.31) was

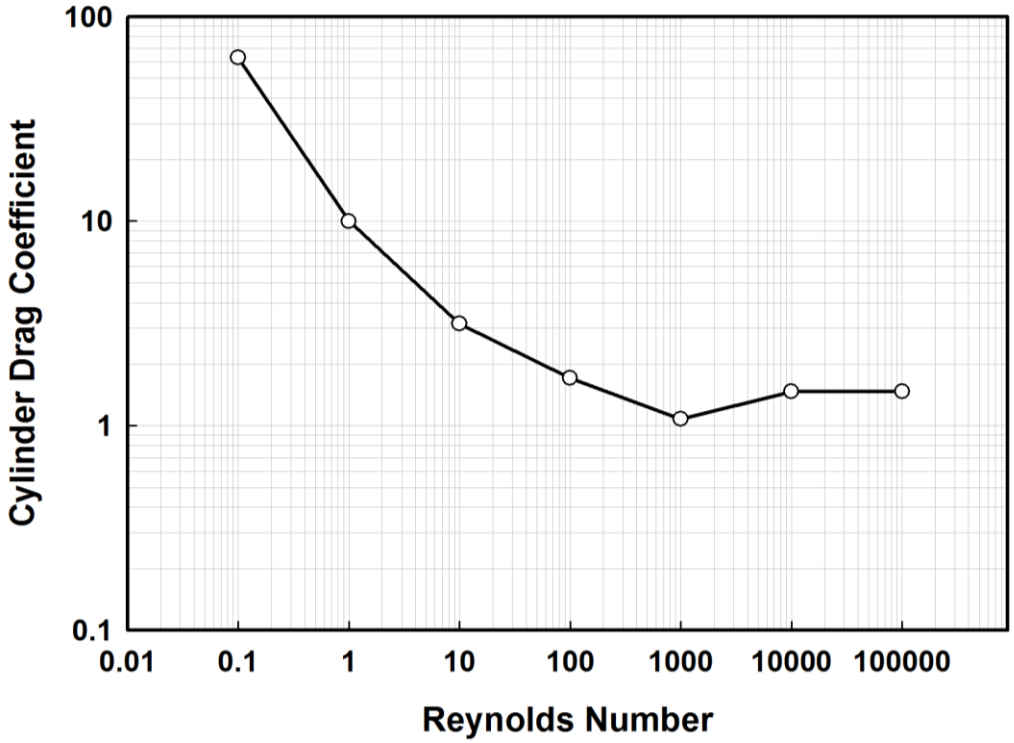

Figure 4.36: Drag Coefficient for Flow over a Cylinder

0.5 Pa, while it was 0.105 kPa in the remaining single phase connections lines (*i.e.*, entrance location numbers of 1, 3, 5, 7, 9, 11, 13, 15, 17, 19, 21, 23, and 25). The pressure drop for the 23.6 mm long single phase portion of the test section was 0.158 kPa.

Frictional pressure drop is also experienced as the single-phase fluid flows across the three thermocouple probes (from 4 to 5, 16 to 17, and 24 to 25) inserted into the single-phase liquid portion of the loop. The frictional pressure was calculated using available drag coefficients (Munson *et al.*, 1998) for a cylinder in cross flow and based on the upstream cross-sectional area as follows:

$$\Delta P_{t/c,f} = \frac{1}{2} C_d \frac{\dot{m}_r^2}{\rho_l \left(\frac{\pi D_{tube}^2}{4} \right)^2} \frac{A_{s,t/c}}{A_{c,t/c}} = \frac{1}{2} C_d \frac{\dot{m}_r^2}{\rho_l \left(\frac{\pi D_{tube}^2}{4} \right)^2} \frac{4 D_{t/c}}{D_{tube}} \tag{4.70}$$

The requisite drag coefficient is shown in Figure 4.36 for a Reynolds number range of $0.1 < Re < 10^5$. For a Reynolds number of 570 based on the thermocouple diameter (3.175 mm) and upstream velocity (0.0587 m/s), the drag coefficient in the sample data point is 1.381. Therefore, using the inlet properties summarized in Table 4-8, the total frictional pressure drop for the three thermocouples for the sample data point was 0.017 kPa.

Two-phase pressure drops in the connecting lines (from 30 to 31, 32 to 33, 34 to 35, and 36 to 37) and the condenser (from 37 to 1) were calculated using the Friedel (1979) correlation, which is as follows:

$$\Delta P_{tp} = \Delta P_{lo} \cdot \phi_{lo}^2 \tag{4.71}$$

The liquid-only pressure drop is calculated using Equations 4.24 and 4.12, with a liquid-only Reynolds number defined as follows:

$$Re_{lo} = \frac{GD}{\mu} \tag{4.72}$$

The two-phase multiplier is calculated as follows:

$$\phi_{lo}^2 = E_{FR} + \frac{3.21 \cdot F_{FR} \cdot H_{FR}}{Fr_{tp}^{0.0454} We_{tp}^{0.035}} \tag{4.73}$$

The other necessary variables are calculated as follows:

$$E_{FR} = (1-x)^2 + x^2 \left(\frac{\rho_l f_{vo}}{\rho_v f_{lo}} \right) \tag{4.74}$$

$$F_{FR} = x^{0.78} (1-x)^{0.224} \tag{4.75}$$

$$H_{FR} = \left(\frac{\rho_l}{\rho_v} \right)^{0.91} \left(\frac{\mu_v}{\mu_l} \right)^{0.19} \left(1 - \frac{\mu_v}{\mu_l} \right)^{0.7} \tag{4.76}$$

$$Fr_{tp} = \frac{G^2}{gD\rho_{tp}^2} \tag{4.77}$$

$$We_{tp} = \frac{G^2 D}{\rho_{tp}\sigma} \tag{4.78}$$

The condenser pressure drop was calculated at the arithmetic average quality (0.026 for the sample data point). Table 4-15 summarizes sample calculations for the connecting line between points 32 and 35 and the condenser (from 37 to 1), which show pressure drops of 0.278 kPa and 0.014 kPa, respectively. Using the values given in Table 4-14 and excluding the two-phase frictional pressure drop in the test section (*i.e.*, between points 28 and 29), the total frictional pressure drop in the system ($\Delta P_{f,other}$) was 0.708 kPa.

Figure 4.37 shows the component pressure drops in the test facility for the representative case. As shown in the figure, the pressure drops due to expansion and contraction (0.123 kPa) and minor (0.162 kPa) are small fractions of the gravity head (3.719 kPa). Using Equation 4.59, the two-phase pressure drop in the test section for the sample data point was 2.727 kPa, which is 73% of the gravity head. The local pressure as a function of the distance along the flow path is shown in Figure 4.38, and the component pressure drops for all test data collected are summarized in Figure 4.39. As noted in Figure 4.38, the pressure difference between the inlet and out of the test section (from 25 to 31) was 4.726 kPa. The significant difference between this value and the two-phase pressure drop (2.727 kPa) emphasizes the difficulty of extracting the two-phase frictional pressure drop for flow in the vertical direction due to the gravity head difference between

Table 4-15: Two-Phase Pressure Drops in the Connecting Line and Condenser for the Sample Data Point

Item	Units	Connecting Line (32 to 35)	Condenser (37 to 1)
$\dot{m}_r$	[g s^{-1}]	0.563	
D	[mm]	2.438	4.826
L	[m]	0.508	0.546
G	[kg m^{-2} s^{-1}]	120.6	30.778
x		0.052	0.026
ρ_l	[kg m^{-3}]	1209	
ρ_v	[kg m^{-3}]	31.82	
ρ_{tp}	[kg m^{-3}]	412.1	614.731
μ_l	[kg m^{-1} s^{-1}]	1.957×10^{-4}	
μ_v	[kg m^{-1} s^{-1}]	1.194×10^{-5}	
σ	[N m^{-1}]	8.153×10^{-3}	
Re_{lo}		1502	759
Re_{vo}		24619	12437
f_{lo}		0.043	0.084
f_{vo}		0.025	0.029
Fr_{tp}		3.580	0.053
We_{tp}		10.55	0.912
E_{FR}		0.958	0.957
F_{FR}		0.099	0.058
H_{FR}		15.40	
ϕ^2		5.205	4.240
ΔP_{lo}	Pa	53.407	3.739
ΔP_{tp}	kPa	0.278	0.016

the inlet and outlet locations (points 25 and 31, respectively). If the differential pressure was directly measured, fluid contained in the lines connecting the taps to the transducer can significantly influence the recorded measurement. In contrast, the method described in this section allows for reasonably accurate measurement of the two-phase frictional pressure drop in the channels without an appreciable influence of transducer plumbing and orientation.

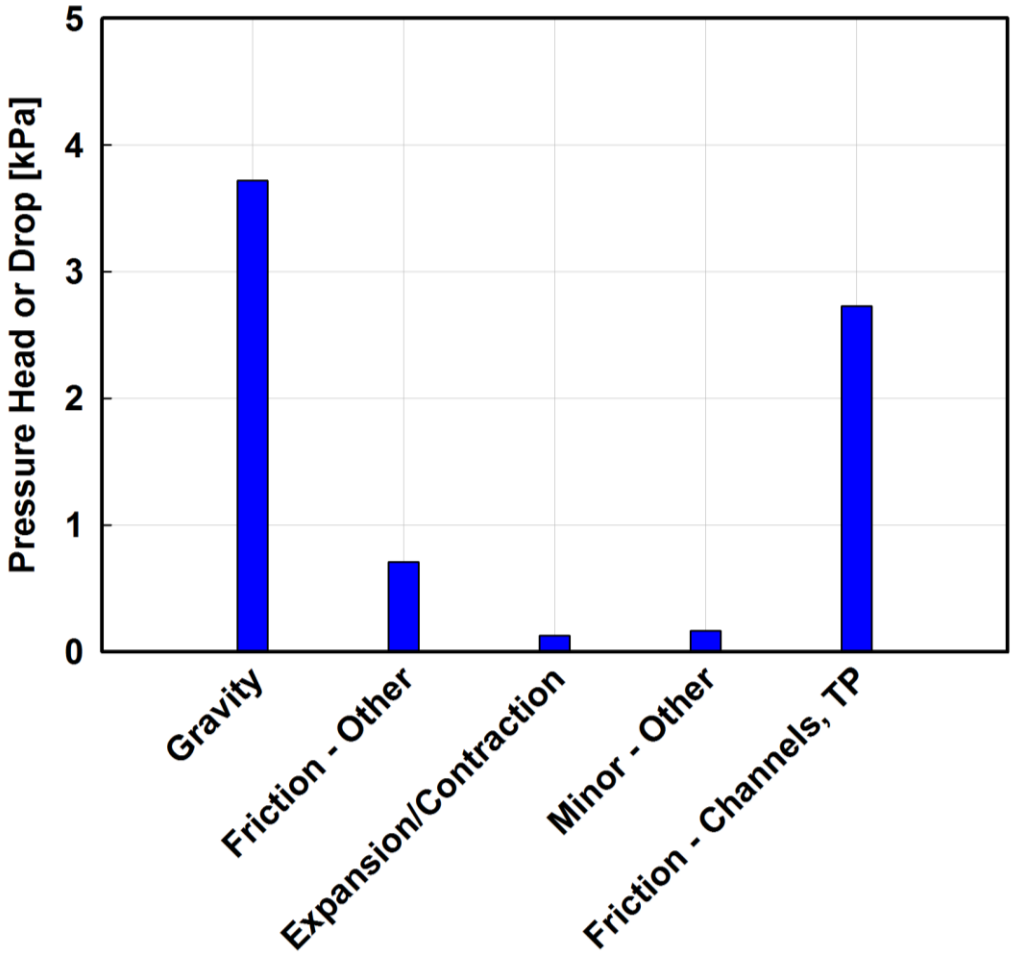

Figure 4.37: Component Pressure Drop for the Passive Microchannel Test Facility Sample Data Point

The uncertainty in two-phase frictional pressure drop in the microchannels was calculated as follows:

$$UN_{\Delta P_{\mathrm{f,tp,e}}} = \sqrt{\left(UN_{\Delta P_{\mathrm{head}}}\right)^2 + \left(UN_{\Delta P_{\mathrm{f,other}}}\right)^2 + \left(UN_{\Delta P_{\mathrm{exp/con}}}\right)^2 + \left(UN_{\Delta P_{\mathrm{minor}}}\right)^2} \qquad (4.79)$$

The uncertainty in the miscellaneous losses was assumed to be ±50% of the calculated value, which were ±0.062 kPa, ±0.081 kPa, and ±0.354 kPa for the

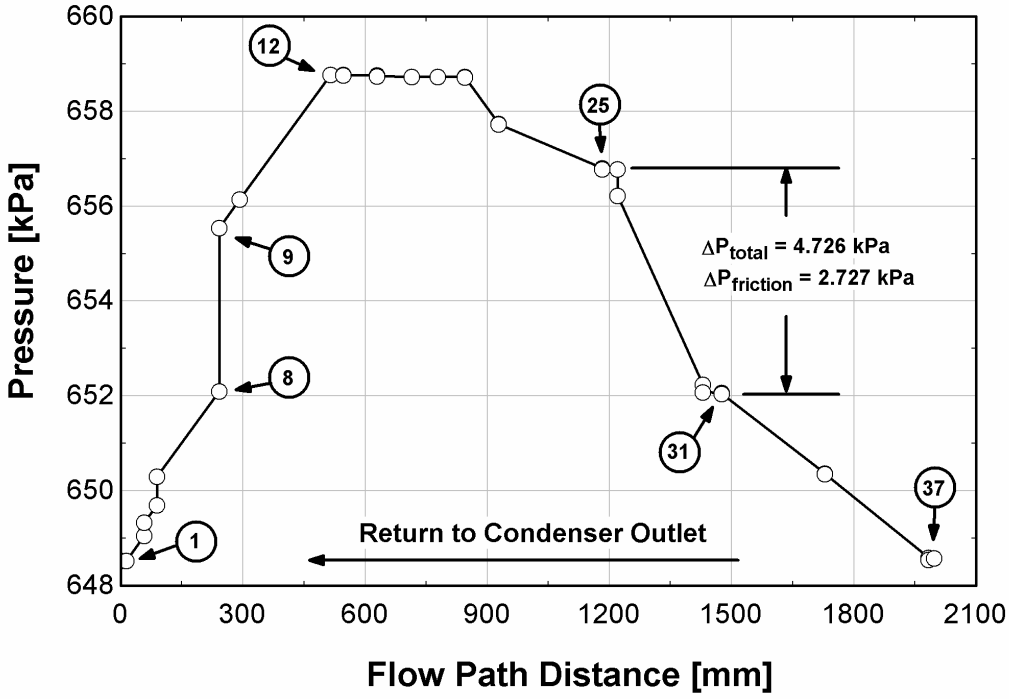

Figure 4.38: Local Pressure vs. Flow Position for the Passive Microchannel Test Facility Sample Data Point

expansion/contraction, minor, and frictional losses, respectively, for the sample data point. The uncertainty in the pressure head was determined from the assumed uncertainties of the void fraction (±25% of calculated value) and condenser to evaporator height (±25.4 mm) as follows:

$$UN_{\Delta P_{head}} = \sqrt{\left(\frac{\partial \Delta P_{head}}{\partial \Delta H}\Delta H\right)^2 + \left(\frac{\partial \Delta P_{head}}{\partial VF_{SF}}UN_{VF}\right)^2 + \left(\frac{\partial \Delta P_{head}}{\partial VF_{HG,o}}UN_{VF}\right)^2 + \sum_{i=1}^{20}\left(\frac{\partial \Delta P_{head}}{\partial VF_{HG,i}}UN_{VF}\right)^2} \quad (4.80)$$

The partial derivatives of the calculated pressure drop with respect to the condenser to test section inlet height and connecting tube, outlet header, test section, and test section

segment void fraction were calculated as follows:

$$\frac{\partial \Delta P_{\text{head}}}{\partial \Delta H} = \rho_{\text{l,i}} g - \left[\left(1 - VF_{\text{SF}}\right) \rho_{\text{l}} + VF_{\text{SF}} \rho_{\text{v}} \right] g \tag{4.81}$$

$$\frac{\partial \Delta P_{\text{head}}}{\partial VF_{\text{SF}}} = \left(\rho_{\text{l}} - \rho_{v}\right) g \left(\Delta H - L_{\text{ch}} - W_{\text{header}}\right) \tag{4.82}$$

$$\frac{\partial \Delta P_{\text{head}}}{\partial VF_{\text{HG,o}}} = \left(\rho_{\text{l}} - \rho_{v}\right) g \cdot W_{\text{header}} \tag{4.83}$$

$$\frac{\partial \Delta P_{\text{head}}}{\partial VF_{\text{HG,i}}} = \left(\rho_{\text{l}} - \rho_{\text{v}}\right) g \frac{\left(L_{\text{ch}} - L_{\text{sp}}\right)}{20} \tag{4.84}$$

For the sample data point, these partial derivatives were 5.391 kPa m^{-1}, 5.646 kPa, 0.147 kPa, and 0.107 kPa, respectively. Using these and the segmental void fraction values listed in Table 4-9, the total uncertainty in the pressure head was 0.672 kPa. Therefore, the uncertainty in the calculated two-phase frictional pressure drop was 0.766 kPa, or 28.1% of the measured value. All of the two-phase frictional pressure drop data collected on the passive microchannel phase test facility are shown in Figure 4.40. Most of the data (18 of 23 points) have uncertainties less than ±35%. The largest uncertainties occurred at the low flow rate conditions (up to 131% of the measured vale at 850 kPa and 1.067 W) where the various component pressure losses were near or greater than calculated for $\Delta P_{\text{f,tp,e}}$ (Figure 4.39). These results are discussed further in Section 4.5.

4.5. Results and Discussion

In this section, the results from the passive two-phase microchannel test facility are discussed in detail. The impact of increased heat load and system pressure on the performance of the system is discussed first, followed by a discussion of the observed

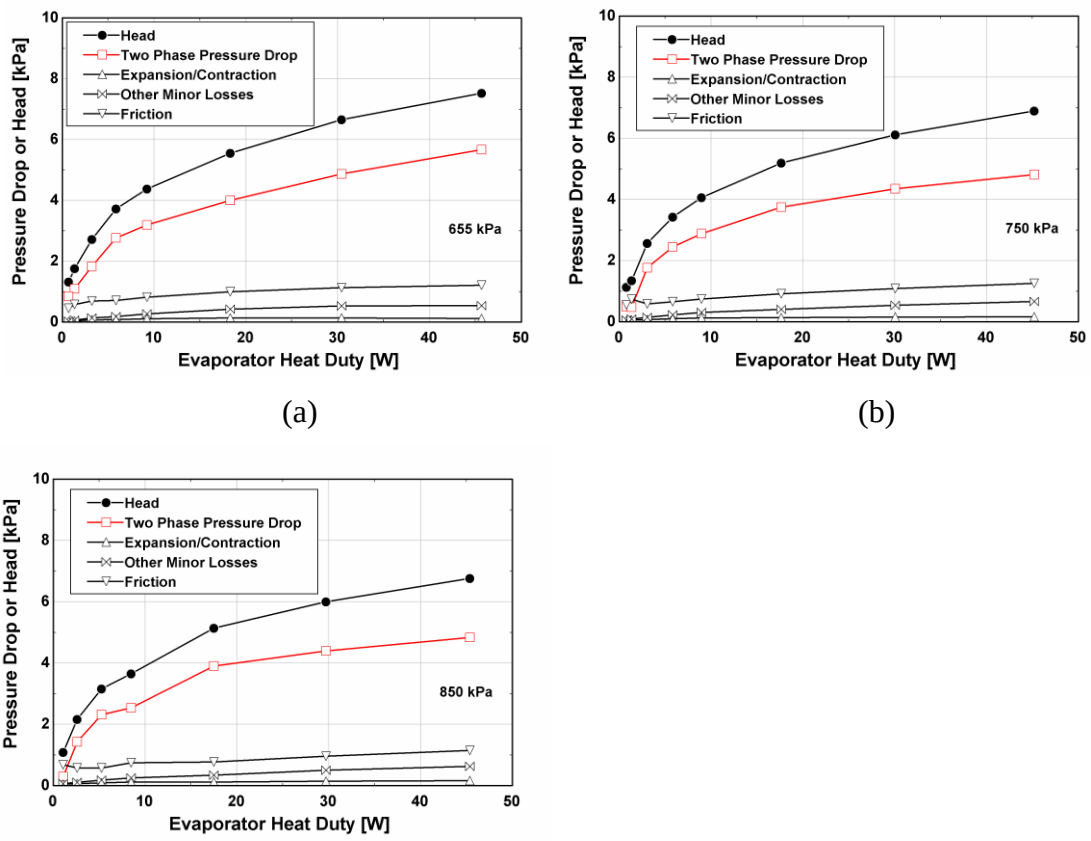

Figure 4.39: Measured Component Pressure Drops at Different Saturation Pressures: (a) 655 kPa (24°C), (b) 750 kPa (29°C), and (c) 850 kPa (33° C)

maldistribution in flow and temperature in some instances. Finally, the calculated frictional pressure drop is compared with results from the literature, which leads into the development of a new two-phase frictional pressure drop correlation for pure refrigerant flow inside microchannels. This model is used in the development of a simplified system model for coupling with the electrochemical-thermal battery model in Chapter Five.

4.5.1. Effect of Increased Heat Load and System Pressure on Performance

As shown in Figure 4.29, the observed mass flow rate increased to a maximum as the test section heat duty increased to near 10 W. Thereafter, the mass flow rate decreased precipitously. For example, at a nominal saturation temperature of 29°C, the

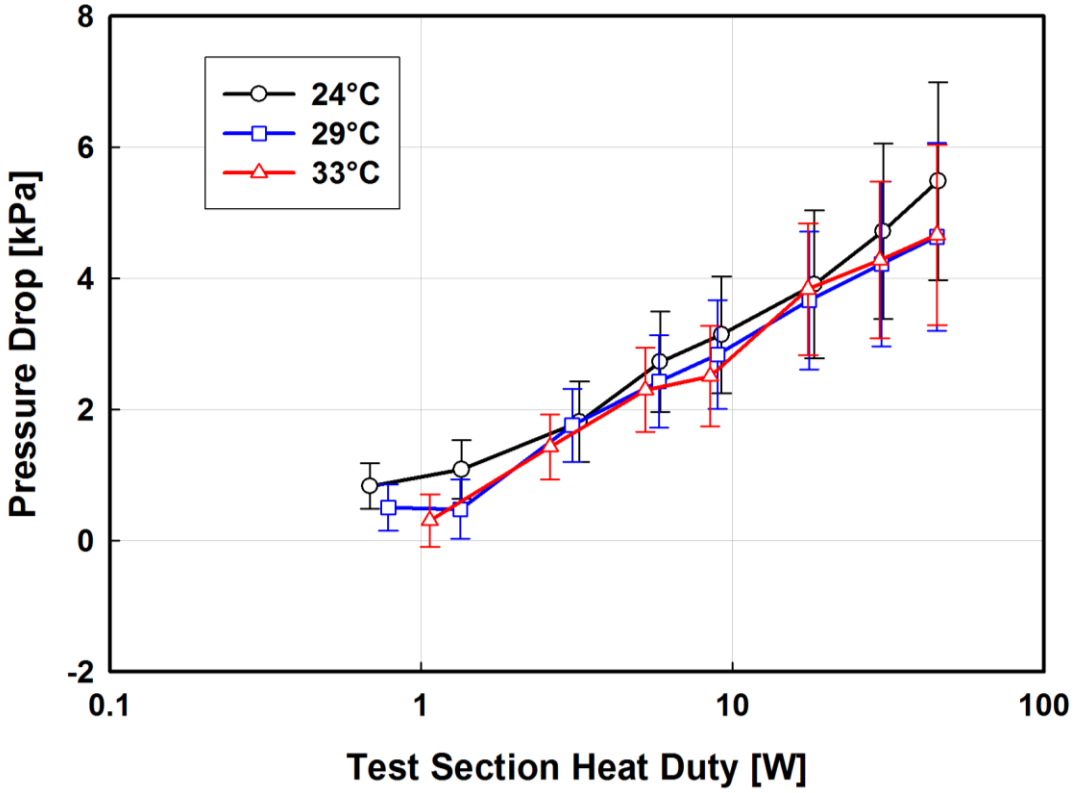

Figure 4.40: Measured Two-Phase Test Section Pressure Drop

mass flow rate increased from 0.381 g s^{-1} to 0.680 g s^{-1} as the heat duty increased from 0.784 W to 8.955 W. When the heat input was increased further to 17.63 W, the mass flow rate decreased to 0.653 g s^{-1}, and subsequently to 0.530 g s^{-1} for a test section heat duty of 45.19 W. Furthermore, Figure 4.30 shows that as the heat duty increased, the outlet vapor quality increased. This occurs because the fluid momentum balance cannot allow an increase in mass flow rate for a fixed outlet quality to accommodate the increased heat load. With an increased outlet quality, the void fraction in the test section and the connecting tubing increased, which increases ΔP_{head}. $\Delta P_{f,tp,e}$ also increased with outlet vapor quality. For example, as shown in Figure 4.29 and Table 4-16, the measured mass flow rate was approximately the same for test section heat duties of 5.250 W and

Table 4-16: Comparison of Representative Data Point at $T_{r,sat}$ = 33.5°C: Effect of Test Section Heat Duty Increase

$\dot{Q}$	$\dot{m}_r$	$x_{r,e,o}$	ΔP_{head}	$\Delta P_{f,tp,e}$
[W]	[g s^{-1}]		[kPa]	[kPa]
29.71	0.603	0.283	5.996	4.278
5.25	0.606	0.048	3.160	2.299

29.71 W (0.606 g s^{-1} and 0.603 g s^{-1}, respectively), while the outlet quality was significantly different (0.048 and 0.283, respectively). The pressure head increased from 3.160 kPa to 5.996 kPa for these respective data points. In spite of no nominal increase in the mass flow rate, the frictional pressure drop also increased from 2.229 kPa to 4.278 kPa between these two data points due to an increase in vapor quality.

Figure 4.41 shows the predicted total system pressure drop for two fixed mass flow rates (0.6 g s^{-1} and 0.63 g s^{-1}) at an 850 kPa system pressure with a fixed inlet subcooling (0.95°C). The two-phase evaporator pressure drop was calculated using a newly developed correlation, which accurately predicted the measured data and is detailed in Section 4.5.3. The frictional pressure drop is also shown in the figure where it

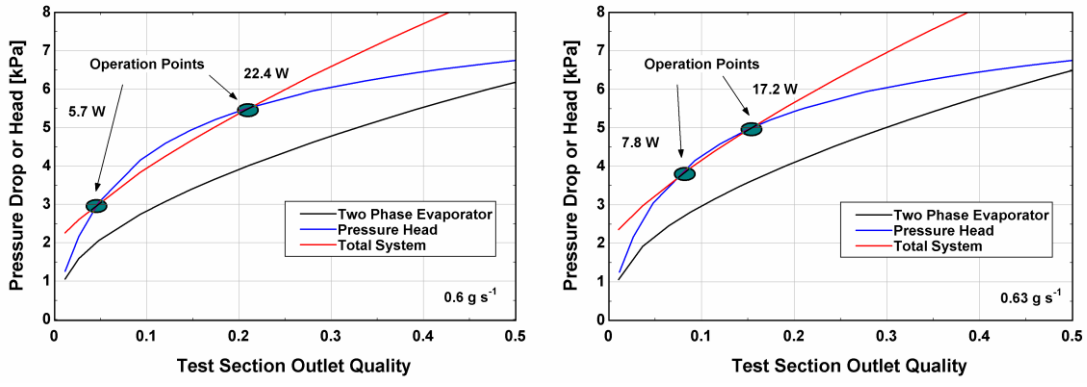

(a) (b)

Figure 4.41: Predicted Pressure Drop and Pressure Head at $P_{r,sat}$ = 850 kPa and $T_{r,e,i}$ = 32.5°C at Different Mass Flow Rates: (a) 0.6 g s^{-1} and (b) 0.65 g s^{-1}

can be seen that this is the dominant flow loss mechanism. The intersection between the total system loss and the pressure head determined the operating point for a specific heat load. For example, it can be see that at 0.6 g s^{-1}, the operation points were at outlet vapor qualities of 0.048 and 0.212, which correspond to test section heat duties of 5.7 W and 22.4 W, respectively. As the mass flow rate increased to 0.63 g s^{-1}, these two intersection points corresponded to outlet vapor qualities of 0.065 and 0.153, which yield test section heat duties of 7.8 W and 17.2 W, respectively. These curves have two intersection points because the initial slope of the gravity head was higher than for the pressure drop versus quality at low qualities, but was lower at higher qualities. Therefore, it is clear that as the test heat duty increased, the flow losses in the loop increased faster than the pressure head can sustain, which caused the mass flow rate to decrease at higher heat loads.

Figure 4.29 also shows that as the system saturation temperature increased from 24°C to 29°C, the observed mass flow rate increased slightly, especially at higher heat loads. For example, at test section heat duties of nominally 9 W, the mass flow rate increased from 0.629 g s^{-1} to 0.680 g s^{-1} as the test temperature increased from 24°C to 29°C. In general, as the saturation temperature increased, the enthalpy of vaporization decreased, which caused an increase in either (or both) outlet quality or mass flow rate. For example, as the saturation temperature increased between the same two values, h_{lv} decreased from 178.7 J g^{-1} to 174.1 J g^{-1}. However, the frictional pressure gradient should also decrease due to a reduction in the slip ratio and the liquid viscosity. For example, the ratio of liquid to vapor density decreased from 38.6 to 32.7, and the liquid viscosity decreased from 0.197 cP to 0.185 cP over this same temperature range. Thus, the mass flow rate increased at a specific test section heat duty because the frictional

pressure drop decreased. This was the case at a test section heat duty of nominally 9 W, which had a decrease in frictional pressure drop from 3.137 kPa to 2.428 kPa as the temperature increased from 24°C to 29°C.

In contrast, there was a minimal decrease in the mass flow as the saturation temperature increased further from 29°C to 33°C. The pressure drop generally decreased over this same range, but the pressure head also decreased due to a reduction in liquid density. For example, as the saturation temperature increased over this same range, the saturated liquid density decreased from 1195 kg m^{-3} to 1183 kg m^{-3}, which decreased the gravity head (Equation 4.60) and, therefore, pumping power available for fluid motion. This can be seen in Figure 4.42, which shows the predicted pressure head and test section outlet quality as a function of mass flow rate for a fixed test section heat duty (19 W) and

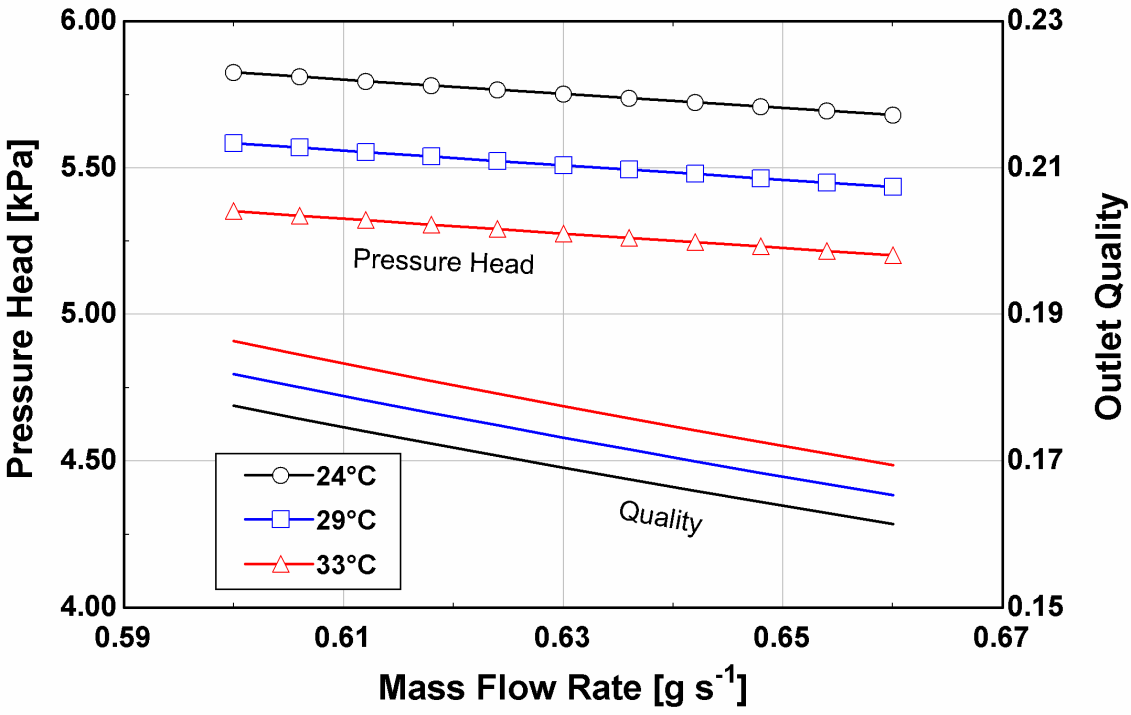

Figure 4.42: Calculated Pressure Head and Outlet Vapor Quality for a $\dot{Q}_{test}$ = 19 W and ΔT_{sub} = 0.02°C

Table 4-17: Maximum Surface Temperature Differences for the Passive Microchannel Phase Change Tests

Heater Input	Test Temperature		
[W]	24°C	29°C	33°C
47.0	1.642	1.169	1.095
31.4	0.851	0.572	0.806
19.1	0.443	0.502	0.552
9.7	0.377	0.301	0.293
6.2	0.409	0.190	0.302
3.5	0.366	0.179	0.284
1.5	0.233	0.296	0.257
0.9	0.176	0.353	0.393

minimal subcooling at the inlet (0.02°C). As shown in the figure, the gravity head decreased as the saturation pressure increased in spite of the increase in outlet vapor quality. For example, at a mass flow rate of 0.63 g s^{-1}, the gravity head decreased from 5.752 kPa to 5.276 kPa when the temperature increased from 24°C to 33°C, while the outlet quality increased from 0.169 to 0.178 over this same range. This decrease in the pressure head coupled with only a slight decrease in the frictional pressure drop (Figure 4.40) caused the mass flow rate to decrease slightly when the test temperature increased from 29°C to 33°C. However, it should be noted that the frictional pressure drop was known to within a minimum of ±26%. Thus, more investigation of the frictional pressure drop characteristics of pure refrigerants flowing in microchannels at a low mass flux is needed to substantiate this explanation.

4.5.2. Observed Maldistribution of Flow and Temperature

During the tests, the surface temperature of the heater was measured (Figure 4.12). Table 4-17 shows the maximum observed temperature difference among the nine thermocouples for the collected data. This temperature spread was minimal for all test

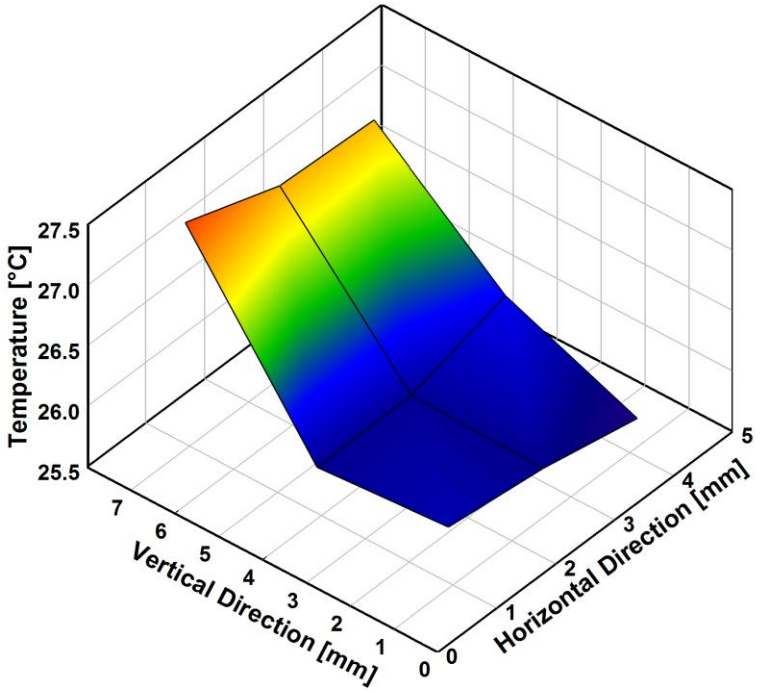

Figure 4.43: Contour Plot of Measured Test Section Surface Temperatures at $T_{r,sat}$ = 33°C and $\dot{Q}_{htr}$ = 47 W

temperatures until the heat duty was increased beyond 31 W (*i.e.,* 4360 W L^{-1}). The highest temperatures were observed near the outlet header. For example, as shown in Table 4-18 and Figure 4.43, the top left thermocouple measured an average surface temperature of 27.3°C, which is ~1.4°C above the arithmetic average temperature of the six thermocouples closer to the inlet header. Referring to Figure 4.30, this temperature spread above 31 W corresponded to outlet vapor qualities greater than 0.2. This is consistent with the recent boiling heat transfer review conducted by Bertsch *et al.* (2008b). For example, in a prior study (Bertsch *et al.*, 2008a) at a D_h = 1.09 mm and mass fluxes ranging from 20.3 kg m^{-2} s^{-1} to 81.0 kg m^{-2} s^{-1}, they observed a peak in heat transfer coefficient near this quality for R134a. Nucleate boiling was suppressed at higher qualities, which reduced surface heat removal. This explains the observed

Table 4-18: Measured Surface Temperatures at $T_{r,sat}$ = 33°C and $\dot{Q}_{htr}$ = 47 W

Vertical Location	Horizontal Location		
	Left	Middle	Right
Top	27.33	27.05	27.01
Middle	25.88	25.89	26.13
Bottom	25.96	25.86	25.69

increase in temperature in the test section near the outlet header. However, this spread was confined to volumetric heat rates beyond those expected in a battery (*i.e.*, a maximum of 1200 W L^{-1}), as detailed in Section 5.3.3 below.

In addition to the observed surface temperature variation, the flow in the test section experienced some maldistribution. For example, at a test temperature of 29°C, flow was visually observed in only twelve channels at test section heat inputs ranging from 3.053 to 8.955 W. Furthermore, as described in Section 4.3.3, the tests at each temperature first began at the highest heat input, followed by a systematic decrease in the heat duty after each data point was taken. During the 29°C tests, when the heat duty was decreased from 2.023 W to 1.335 W, the number of channels with flow decreased from twelve to seven. To mitigate these problems, changes were made to the test loop to allow flow in each channel. In particular, the exhaust port (Figure 4.3) was quickly cycled, allowing for some refrigerant to escape. Charge was then added to the loop via the pressurized expansion tank. Repeating this several times appeared to sufficiently prime flow in the test section.

A possible explanation for this effect is given here, which depends on two distinct causes. The first is due to Ledinegg instability (Carey, 1992). As the mass flow rate in a channel is decreased at a specific heat duty, the outlet vapor quality increases. This can cause the frictional pressure drop to increase, which can cause a further decrease in mass

flow. For a fixed test section mass flow rate, this causes increased mass flow through adjacent channels. Furthermore, as shown in Figure 4.44, there was a standing liquid level in the outlet header. Once it left the channel, the exiting vapor moved at a higher velocity than the liquid. This vapor jet transferred some momentum to the liquid in the outlet header, slightly increasing its liquid level relative to nearby channels. When combined with Ledinegg instability, this can lead to less flow in the nearby channels due to the increased force exerted on the channel outlet, eventually blocking flow in these channels. In light of these noted effects, more investigation of the observed flow maldistribution is warranted in geometries that more closely represent the intended battery internal cooling system design.

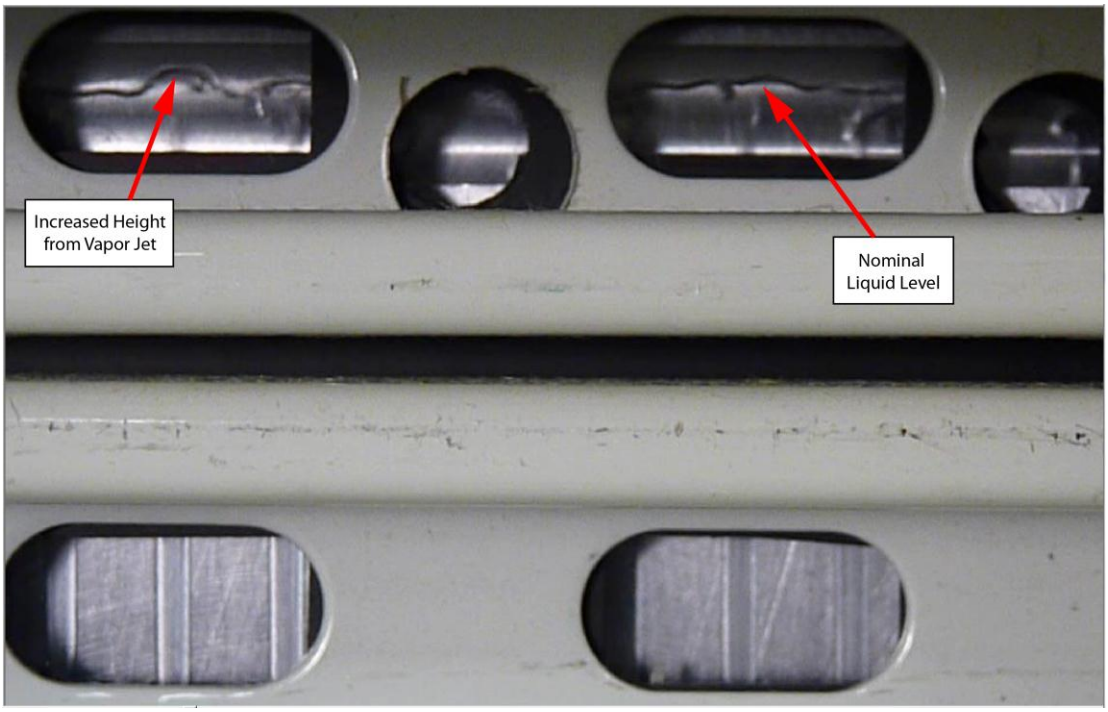

Figure 4.44: Observed Increase of Local Liquid Level due to Vapor Jetting in the Outlet Header

4.5.3. Frictional Pressure Drop Results and Modeling

In this section, the frictional pressure drop results summarized in Figure 4.40 were

compared to the correlation database summarized in Table 4-1. The air-water correlations of Moriyama *et al.* (1992b) and Stanley *et al.* (1997) and the refrigerant-based correlations of Webb and Ermis (2001), Baird *et al.* (2003), Garimella *et al.* (2005), Agarwal (2006) were not compared due to duplication with other studies included in the comparison, missing information, finned tube geometry specificity, condensation specificity, and unstable solutions due to inapplicability of operating conditions, respectively. Detailed sample calculations of the remaining correlations are given in Tables C-1 through C-4 of Appendix C. As shown in Figure 4.45, none of these correlations adequately predict the measured data from this study. For example, although Lee and Mudawar (2005) investigated R134a evaporating in 231 × 710 μm channels for mass fluxes as low as 127 kg m^{-2} s^{-1}, their correlation mostly underpredicted the data in this investigation, with only 8 data points predicted within ±25%. This was perhaps due to the measured mass flow rates being lower in the present study (*i.e.*, $45 < G < 112$ kg m^{-2} s^{-1}). The RMS errors for the correlation database are shown in Table 4-19, which was defined as follows:

$$RMS_{\text{error}} = \sqrt{\sum_{i=1}^{N} \frac{\left(\Delta P_{\text{f,tp,e}} - \Delta P_{\text{f,tp,prediction}}\right)^2}{N}} \tag{4.85}$$

As shown in the table, the investigations by Saisorn and Wongwises (2009), who studied air-water flow inside a 150 μm circular microchannel, had a relatively low RMS errors (43.6%) and high correlation coefficient (0.936) as compared to the measured data. This correlation mostly underpredicted the data, but it had a relatively high R^2 value. This suggested that the correlation might be of the appropriate form, but that the fitting parameters were inappropriate. Therefore, it served as the basis for developing a new

correlation in this investigation.

The correlation of Saisorn and Wongwises (2009) utilized a two-phase multiplier based on the pressure drop of the liquid as follows:

$$\Delta P_{tp} = \Delta P_l \cdot \phi_l^2 \tag{4.86}$$

The liquid pressure drop was calculated using Equations 4.12 and 4.24, with a liquid Reynolds number defined as follows:

$$Re_l = \frac{\frac{\dot{m}}{A}(1-x)D}{\mu} \tag{4.87}$$

The liquid two-phase multiplier was calculated as follows:

$$\phi_l^2 = 1 + \frac{c_1}{X_{\text{Martinelli}}^{c_2}} \tag{4.88}$$

The constants c_1 and c_2 were 2.844 and 1.666 in their correlation. The Martinelli parameter was calculated as follows:

$$X_{\text{Martinelli}} = \left(\frac{dP/dz|_l}{dP/dz|_v} \right)^{0.5} = \left[\frac{\rho_v}{\rho_l} \left(\frac{1-x}{x} \right)^2 \frac{f_l}{f_v} \right]^{0.5} \tag{4.89}$$

For consistency when comparing with the correlation database, the friction factor was calculated using Equation 4.12 for laminar flow. For turbulent flow, the friction factor was calculated using the Churchill friction factor for a smooth tube (Equation 4.3) with an aspect ratio modification as follows (Bhatti and Shah, 1987):

$$f_{\text{turb}} = (1.0875 - 0.1125 \cdot \alpha) f_{\text{Churchill}} \tag{4.90}$$

The transition from laminar to turbulent flow for rectangular ducts occurred at the critical

Reynolds number defined as follows (Shah and Bhatti, 1987):

$$Re_{\text{crit}} = 4650 \frac{m \cdot n}{(m+1)(n+1)} \tag{4.91}$$

where:

$$m = 1.7 + 0.5 \cdot \alpha^{-0.25} \tag{4.92}$$

$$n = \begin{cases} 2 & \alpha < \frac{1}{3} \\ 2 + 0.3\left(\alpha - \frac{1}{3}\right) & \alpha \geq \frac{1}{3} \end{cases} \tag{4.93}$$

The liquid and vapor Reynolds number were calculated using Equation 4.87 and as follows, respectively:

$$Re_{\text{v}} = \frac{\frac{\dot{m}}{A} x \cdot D}{\mu} \tag{4.94}$$

This procedure described here was also used for the new correlation, but with new constants for the two-phase multiplier.

To determine the new constants, the Martinelli parameter and required liquid two-phase multiplier were calculated from the data using Equations 4.88 and 4.89 at the average test section quality. For example, in the sample data point summarized in Table 4-6, the liquid and vapor Reynolds numbers were 129.2 and 56.8, respectively, at an average vapor quality of 0.026. The corresponding friction factors were 0.696 and 1.584, respectively, yielding a Martinelli parameter of 4.012. For a two-phase length of

Table 4-19: RMS Errors and Correlation Coefficients for the Correlation Database and Correlation Developed in the Current Study

Investigation	RMS_{error}	R^2
Chung *et al.* (2004)	53.4%	0.702
Chung and Kawaji (2004)	65.1%	0.619
Cubaud and Ho (2004)	56.6%	0.779
Garimella *et al.* (2003)	49.3%	0.934
Hwang and Kim (2006)	48.0%	0.833
Koyama *et al.* (2003)	54.3%	0.671
Lee and Garimella (2008)	42.1%	0.838
Lin *et al.* (1991)	67.9%	0.096
Lee and Lee (2001)	54.1%	0.673
Lee and Mudawar (2005)	45.5%	0.743
Moriyama *et al.* (1992a)	41.5%	0.943
Qu and Mudawar (2003)	54.3%	0.671
Revellin and Thome (2007)	78.6%	0.926
Saisorn and Wongwises (2008)	99.0%	0.830
Saisorn and Wongwises (2009)	43.6%	0.936
Present Study	35.9%	0.961

0.186 m, the liquid pressure drop was 1.211 kPa, resulting in a two-phase multiplier (ϕ_l^2) of 2.253. The calculated constants for the new correlation were c_1 = 6.27 and c_2 = 1.49:

$$\phi_l^2 = 1 + \frac{6.27}{X_{\text{Martinelli}}^{1.49}} \tag{4.95}$$

This analysis did not include the most uncertain values for two-phase evaporator pressure drop (*i.e.*, 0.784 W and 1.335 W at 29°C and 1.067 W at 33°C). In these cases, the required two phase multipliers were less than 1, which does not allow the pressure drop to asymptotically approach the liquid pressure drop at low qualities. The test results were compared to calculations from this new correlation in Figure 4.45 and Table 4-19. All data were predicted within an RMS error of 35.9% with 19 of the 23 data points predicted within ±20%, which represents substantial improvements over the available correlation database.

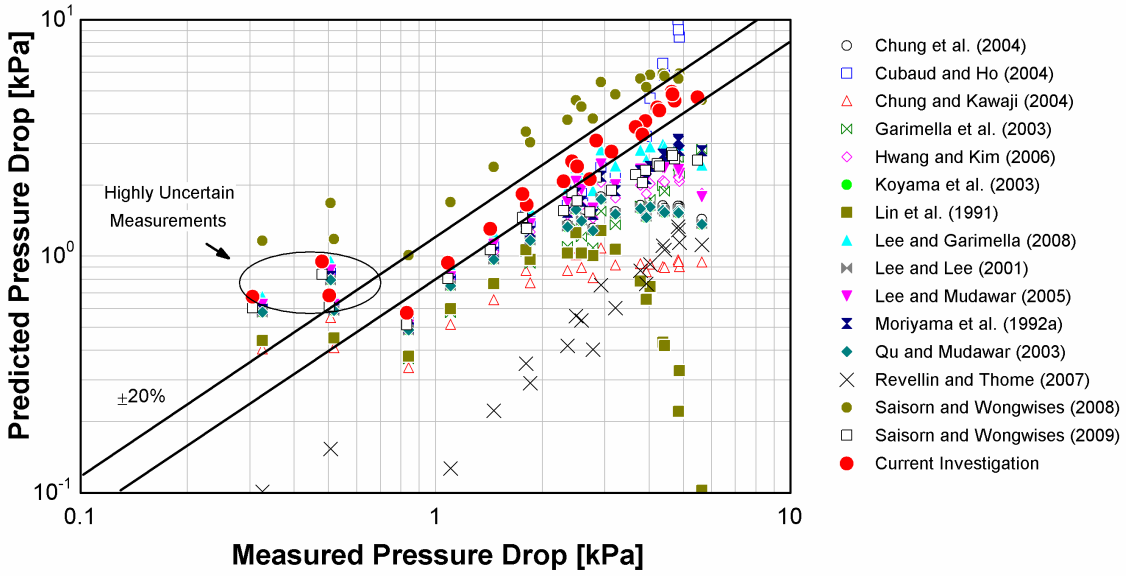

Figure 4.45: Comparison of Measured Two-Phase Pressure Drop with Various Correlations based on D_h < 1 mm Data

4.6. Summary

The performance of a representative passive microchannel phase change system for internal cooling of batteries was investigated in this chapter. The test section consisted of a thirteen 160 μm (effective) × 3.175 mm channels machined into a 6.35 mm aluminum plate and covered with a 6.35 mm thick clear polycarbonate cover compressed and sealed on an O-ring. A thin film heater was adhered to the back surface of the aluminum plate, and served as a surrogate heat source that simulated battery heat generation. This test section was placed in a test facility that contained a temperature controlled liquid-coupled condenser. In the primary loop, no fluid movement devices were used, and fluid motion was induced by buoyancy when the power was supplied to the heater. The system was tested over the heat input range of 0.88 W to 48 W for R134a saturation temperatures of nominally 24°C, 29°C, and 33°C. The generated mass flow

rate and outlet vapor quality were measured for these conditions, and the resulting two-phase frictional pressure drop in the test section was calculated to with ±35% for 18 of the 23 data points. The mass flow rate increased to a maximum near a heat input of 10 W, and there was a slight influence of system pressure on the performance of the system. The frictional pressure drop results were compared with predictions from the available literature on two-phase flow inside channels of $D_h < 1$ mm. These correlations did not predict the data well. Therefore, a new correlation based on the formulation of Saisorn and Wongwises (2009) was developed. This new correlation predicted 19 of the 23 data points to within ±20%, which was a substantial improvement over existing correlations. In the following chapter, this correlation is used to predict the performance of a simplified internal cooling battery system. This is coupled to the electrochemical-thermal model also developed in Chapter Five.

CHAPTER 5. COUPLED BATTERY MODELING

To determine the performance improvement in large lithium-ion battery packs intended for HEV applications through internally cooling, a detailed understanding of three basic items is required: local heat generation, internal cooling system performance, and coupled electrochemical-thermal performance. The first two aspects were addressed in Chapters Three and Four, while the third item is addressed in this chapter. The coupled nature of the electrochemical and thermal phenomena leads to considerable complexity in modeling. In addition, in contrast to the majority of prior investigations, a realistic evaluation of various cooling strategies in HEV applications requires the battery pack to be subjected to a dynamic, time-varying load. This adds a significant demand onto system resources, making current approaches to battery modeling either unrealistic or cumbersome. Therefore, in the present study, a first of its kind model to bridge the gap between the particle level electrochemistry and pack level thermal transport in a self-consistent and efficient manner is developed so that various thermal management strategies for batteries can be assessed when subjected to dynamic loads.

As discussed in Section 5.2.1, the coupled electrochemical-thermal performance of the battery design investigated here was modeled based on the temperature-dependent data presented in Chapter Three. This yields substantially reduced computational intensity, allowing for realistic assessment of different external cooling strategies under operating schedules with rapid changes in battery power demand. Furthermore, a

Table 5-1: Summary of Simulations Performed in the Present Study

Cell Design	Current Collection	Cooling Condition	Size Reduction Factors
8 Ah	ideal	air, liquid, internal	1 to 5
	non-ideal	edge (top or bottom), internal	
20 Ah	ideal	air, liquid	1 to 5
		internal	1 to 5, 10

thermal-hydraulic model of the passive microchannel phase-change system described in Chapter Four was efficiently integrated into the battery model to understand the possible system performance improvement, specifically the ability to reduce pack size, with internal cooling. The possible pack size reduction, while keeping the power requirements the same and, thus, increasing thermal load, up to maximum temperature limit of 35°C was determined for each cooling strategy and cell design (Table 5-1).

This chapter is organized as follows. First, the performance of the thermal management options investigated for the 9.6 kWh battery pack designs is discussed in detail. This section also includes a discussion of the two different scaled-up cell sizes for these pack designs: 8 Ah and 20 Ah. Next, the electrochemistry, heat transfer, and current collection models are described. The model inputs for a specific HEV application are also discussed in this section. In Section 5.3, the simplified two- and quasi-three-dimensional domains used to investigate the different thermal management strategies are described. This section also includes the assumptions and methodology for coupling the thermal-hydraulic performance of the passive microchannel phase change internal cooling system to the battery model. Finally, the simulation results are described, which show the larger pack size reduction for batteries in HEV application with the use of

internal cooling instead of external cooling.

5.1. Battery Pack Designs and Thermal Management Options

In this investigation, scaled-up battery pack designs based on a commercially available cell studied in Chapter Three are investigated. The details of this cell are provided in Section 3.1, and a summary of the cell and battery pack designs is given in Table 5-2. A 9.6 kWh battery pack was targeted for the simulations, which is the same as the pack level requirements used previously in the HEV simulation tests (Section 3.4.3 and Figure 3.20). This was achieved with a 240 V pack capable of nominally delivering 40 Ah. It is assumed that each cell operated at 3.2 V, thus requiring 75 batteries to be connected in series. Two different cell designs are investigated in this study: 8 Ah and 20 Ah. To deliver the required energy, the 8 and 20 Ah battery designs require five and two parallel modules, respectively, which results in 375 and 150 cells, respectively, for each pack.

Table 5-2: Cell and Pack Design Summarizes in the Present Investigation

Pack	Energy	kWh	9.6
	Voltage	V	240
	Capacity	Ah	40
	Nominal Cell Voltage	V	3.2
	Required # of Series Cells		75
Cell Design 1	Nominal Capacity	Ah	8
	Width	mm	84.8
	Height	mm	153
	Thickness	mm	9.77
	Unit Cell Length	m	2.31
Cell Design 2	Nominal Capacity	Ah	20
	Width	mm	95.0
	Height	mm	153
	Thickness	mm	20.0
	Unit Cell Length	m	5.78

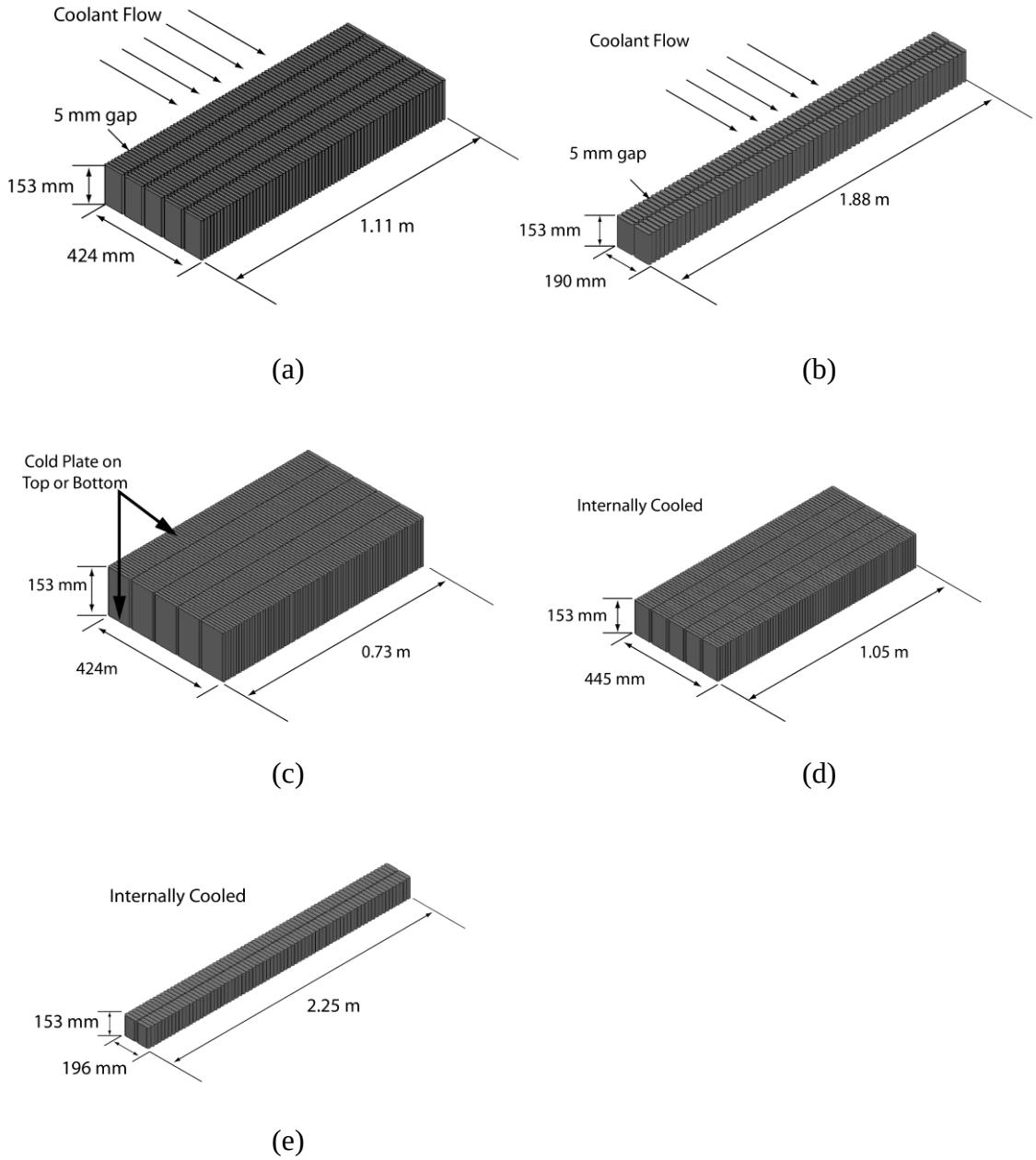

Figure 5.1: Investigated Battery Pack Layouts: (a) 8 Ah, Air/Liquid Cooled, (b) 20 Ah, Air/Liquid Cooled, (c) 8 Ah, Edge Cooled, (d) 8 Ah, Internally Cooled, and (e) 20 Ah, Internally Cooled

Three different external cooling options were investigated: air cooling, liquid cooling, and edge cooling. For air and liquid cooling, each in-series cell within a module was spaced 5 mm apart to allow the flow of cooling fluid, and the modules were stacked

adjacent to each other. The cooling fluid cools each module in series and each cell in parallel (Figure 5.1). For edge cooling and internal cooling, all the cooling gaps were eliminated, and heat was removed from either the top or bottom surface to a cooling fluid through an (assumed) negligible thermal resistance. In this investigation, the 8 Ah edge cooled battery was studied first and exhibited poor performance; therefore, the 20 Ah design was not investigated for edge cooled cases (Section 5.4.1). However, both 8 Ah and 20 Ah designs were investigated for the passive internal cooling system case.

The 20 Ah cell was investigated to assess the impact of thicker batteries on electrochemical performance for a reduced pack volume. If the same cross section as the 8 Ah cell is utilized and the pack energy remains the same (9.6 kWh), the height of the 20 Ah cell must increase by a factor of 2.5. However, the total pack volume remains the same because the volume occupied by the coolant gaps is unchanged. This is because cooling gaps are taller, which compensates for their reduced number. Thus, the cross

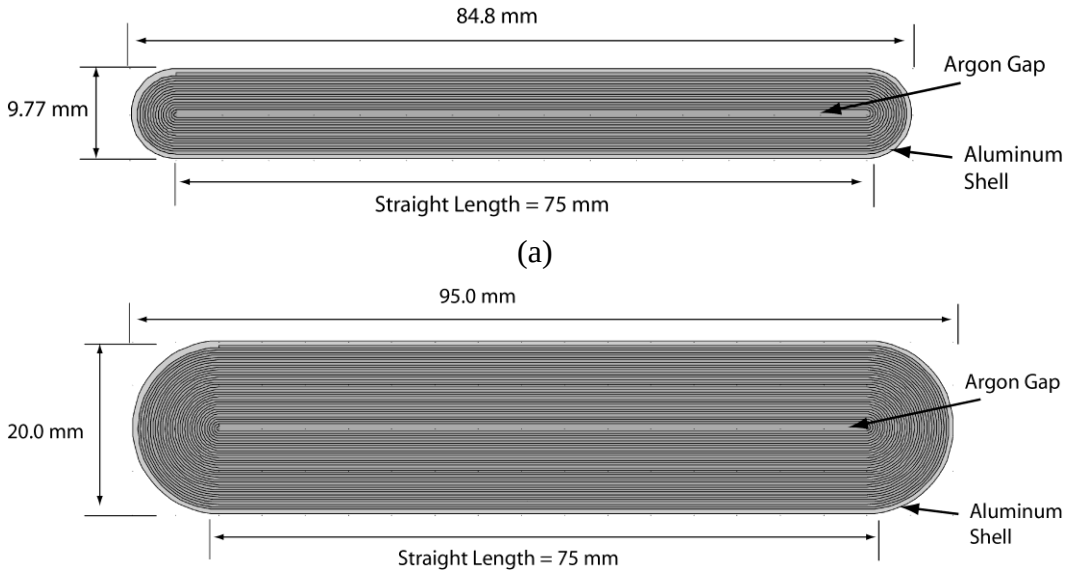

Figure 5.2: Cell Design Dimensions: (a) 8 Ah Battery and (b) 20 Ah Battery

section of the 20 Ah cell must be thicker to reduce pack volume. To accomplish this, it was assumed that the aluminum shell thickness, internal argon gap thickness, battery height, and straight length (Figure 5.2) were the same for each battery (0.504 mm, 0.5 mm, 153 mm and 75 mm, respectively). As a result, the 20 Ah battery has a longer unit cell length, which was calculated as follows:

$$L_{\text{wind}} = 2 \cdot N_{\text{wind}} \cdot L_{\text{straight}} + \sum_{i=1}^{N_{\text{wind}}} \left[gap + \frac{t_{\text{unit cell}}}{2}(4i - 1) \right] \tag{5.1}$$

The first term on the right-hand side is the total length of the straight portions, while the summation accounts for the curved portions of the battery. There were 14 and 32 winds for the 8 Ah and 20 Ah batteries, respectively, which result in total lengths of 2.30 m and 5.78 m, respectively. Thus, multiplying these by the unit cell thickness and height, the total unit cell volumes were 100.3 cm^3 and 251.6 cm^3. Using the cell volumetric capacity (79.6 Ah L^{-1}), the actual battery capacities were 7.98 Ah and 20.02 Ah, respectively. The total individual cell volume was calculated as follows:

$$v_{\text{cell}} = \left(L_{\text{straight}} \cdot W_{\text{cell}} + \frac{\pi W_{\text{cell}}^2}{4} \right) H_{\text{cell}} \tag{5.2}$$

The width of the cell was calculated as follows:

$$W_{\text{cell}} = gap + 2 \cdot t_{\text{shell}} + (2 \cdot N_{\text{wind}} + 1) t_{\text{unit cell}} \tag{5.3}$$

Using the dimension mentioned above for the argon gap and shell thickness, the width for the 8 Ah and 20 Ah cell designs were 9.77 mm and 20.01 mm. Thus, for a cell height of 153 mm, the total cell volumes were 123.5 cm^3 and 277.7 cm^3 for the 8 Ah and 20 Ah designs, respectively. The total pack volume, including the cooling fluid gaps between

the cells, was calculated as follows:

$$v_{\text{pack}} = N_{\text{cell}}\left[v_{\text{cell}} + gap_{\text{cool}} \cdot H_{\text{cell}}\left(W_{\text{cell}} + L_{\text{straight}}\right)\right] \tag{5.4}$$

For 375 and 150 cells, the volumes for the 8 Ah and 20 Ah air and liquid cooled packs were 70.6 L and 52.6 L, respectively. The latter was substantially smaller due to the reduced volume of cooling fluid gaps (10.9 L versus 24.3 L). However, the cell thickness of the 20 Ah cell was thicker by a factor of 2.05, which increases the thermal resistance between the cooling fluid and heat generation location. The volume for the 8 Ah edge cooled pack was substantially smaller (46.3 L) than the air and liquid cooled packs based on either cell size due to the elimination of the cooling fluid gaps.

For the internally cooled system, the unit cell thickness is larger by the effective channel height (160 μm) measured in Section 4.4.1 to 444 μm. Using Equation 5.1 and assuming 14 battery winds, the total length of the unit cell was 2.405 m, which was 102 mm longer than for the externally cooled batteries. However, if 1 straight length (75 mm) and 1 curved portion were removed (20.3 mm), the total length decreases to 2.31 m, which is very close to the original unit cell length. Therefore, using the same straight length, the battery and pack volumes were similarly calculated using Equations 5.2 and 5.4, respectively, but the final width for the batteries was calculated as follows:

$$W_{\text{cell,ic}} = gap + 2 \cdot t_{\text{shell}} + 2 \cdot N_{\text{wind}}\left(t_{\text{unit cell}} + h_{\text{ch,eff}}\right) \tag{5.5}$$

The number of winds for the 8 Ah and 20 Ah cells were 14 and 32, respectively, which result in cell widths of 13.96 mm and 29.96 mm, respectively. Thus, the total pack volumes were 68.9 L and 67.7 L, respectively. As compared to the air and liquid cooled packs, there was less reduction in the pack volume as the cell design changed from 8 Ah

to 20 Ah due to the presence of the channels. However, as described in Section 5.4.3, the internally cooled batteries can be cycled more aggressively, leading to a decrease in the pack size not possible with external cooling.

5.2. Model Description

In this section, the governing equations for the battery model are described. As mentioned above, the electrochemical model was based on the data presented in Chapter Three. In addition, the coupling between the heat transfer and current collection models is also described. As highlighted in Section 5.3, the modeling domains are different for the air and liquid cooling and the edge and internal cooling thermal management options. The differences in the modeling approach are described in this section, while the boundary and initial conditions are described in Section 5.3

5.2.1. Electrochemistry

As shown in Section 3.4.2, battery heat generation is a strong function of temperature, depth of discharge (*DOD*), and current. Thus, predicting local current and heat generation inside the battery is the most complicated feature of this model. As detailed in the literature review (Section 2.2), prior investigators have computed the local reaction rate using detailed electrochemical models that solve species transport and interfacial kinetics down to the particle level. Correctly accounting for temperature dependence for these reactions consumes significant computational resources and has perhaps contributed to there being relatively few studies that investigate the impact of thermal management on battery performance under dynamic loads. HEV simulations are a further complication because the battery potential and current are not known

Table 5-3: Summary of Sample Calculations for the Electrochemical-Thermal Model

Item		Units	Value	Units	Value
		Input		Calculated	
DOD			0.45		
T		°C	36.85		
λ				mV K^{-1}	0.203
U				V	3.300
Charge, High	η	V	-0.202		
	i'''			A L^{-1}	-221.03
	$\dot{Q}'''_{ECM}$			W L^{-1}	55.56
Charge, Transition	η	V	-0.102		
	i'''			A L^{-1}	-84.23
	$\dot{Q}'''_{ECM}$			W L^{-1}	13.89
Charge, Low	η	V	-0.025		
	i'''			A L^{-1}	-15.33
	$\dot{Q}'''_{ECM}$			W L^{-1}	1.35
Discharge, Low	η	V	0.003		
	i'''			A L^{-1}	1.725
	$\dot{Q}'''_{ECM}$			W L^{-1}	-0.10
Discharge, Transition	η	V	0.108		
	i'''			A L^{-1}	88.61
	$\dot{Q}'''_{ECM}$			W L^{-1}	3.994
Discharge, High	η	V	0.182		
	i'''			A L^{-1}	179.24
	$\dot{Q}'''_{ECM}$			W L^{-1}	21.71

beforehand and must be solved iteratively.

To address these difficulties, a parameterized electrochemical model using the temperature-dependent data on the relatively small cell (~1 Ah) described in Chapter Three as the basis is presented here. As shown in Section 3.4.3, the measured current and voltage responses of this battery subjected to a dynamic HEV load were both predicted within ±7.7% using interpolation of the constant current data, with 90% of the data predicted within ±2.5%. Thus, it appears reasonable to assume that the battery performs

similarly in both constant current and dynamic discharge, which was the method used by Chen and Evans (1994b) in their simulations.

The parameterized electrochemical model was applied locally within the scaled-up battery, where the local depth of discharge and temperature affect the local overpotential and entropic heat coefficient. The local overpotential affects the local current generation rate, which in turn affects the local temperature (through heat generation) and depth of discharge. For simplicity, the local current generation rate (i''') was assumed to be a function of the local depth of discharge, temperature, and overpotential (η). The data used to develop the curve fit included data from normalized *DOD*s ranging from 0.2 to 0.8 and 0.1 increments at the five test temperatures (15°C to 55°C). First, the entropic heat coefficient was estimated from the local normalized depth of discharge (*DOD*) using the following curve fit of the data:

$$\frac{dU}{dT} = 5.34\times10^{-6} + 9.22\times10^{-5}\cdot\tanh\left(17.1394\cdot DOD - 5.1828\right) - 1.069\times10^{-4}\cdot\tanh\left(25.2754\cdot DOD - 18.2118\right) \tag{5.6}$$

To facilitate discussion, sample calculations at several different simulation time instances at fixed normalized *DOD* (0.45) and temperature (36.85°C) are summarized in Table 5-3. For example, at a *DOD* of 0.45, the predicted entropic heat coefficient was 0.203 mV K-1. A comparison between the predicted and measured entropic heat coefficients is shown in Figure 5.3. This figure shows that the largest difference in magnitude at a normalized *DOD* of 0.922 was 0.022 mV K-1. When multiplied by its temperature (310 K), this translated into an overpotential difference of 6.87 mV, which has a minimal impact on the local heat generation rate. For example, the measured overpotential at 3 A was 573 mV and -153 mV for discharge and charge, respectively, at a normalized *DOD* of 0.9

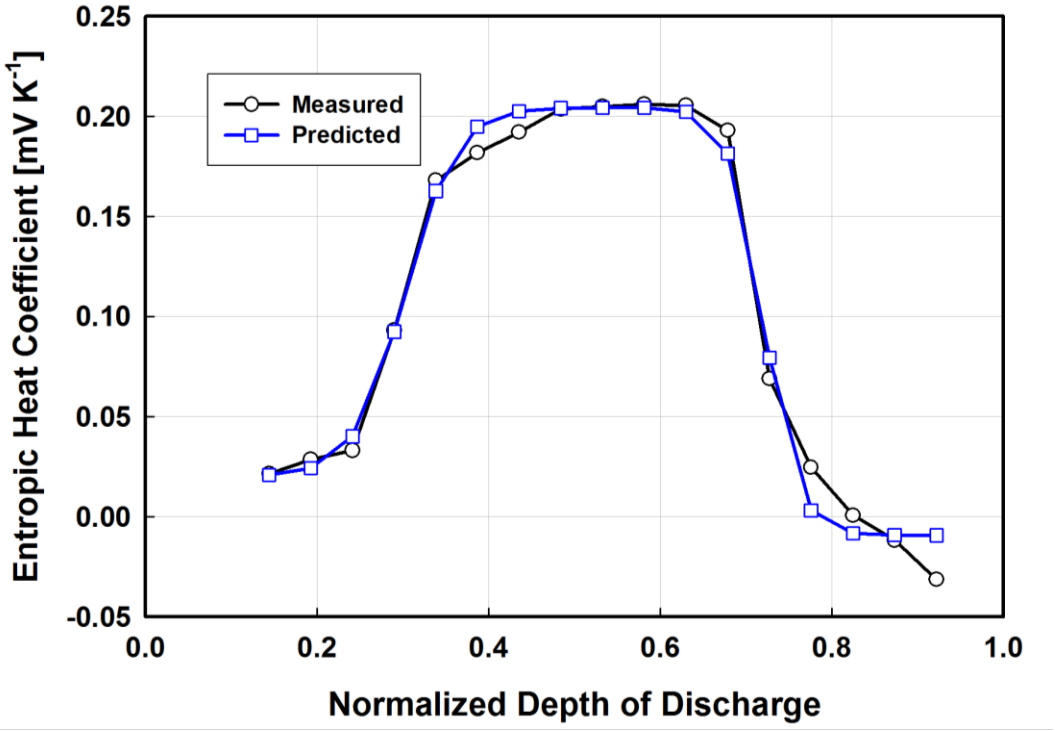

Figure 5.3: Predicted versus Actual Entropic Heat Coefficient for Sample 1

(Figures 3.14 and 3.15).

Next, the open-circuit potential was predicted using a curve fit of the data collected at ~30°C and then linearly extrapolating to the actual temperature using the entropic heat coefficient as follows:

$$\begin{aligned} U = {} & 3.302 + 0.0185 \cdot \tanh\left(-24.857 \cdot DOD + 7.655\right) \\ & - 0.0045 \cdot \left(\frac{1}{\left(1.0063 - DOD\right)^{0.8928}} - 2.2459 \right) \\ & + 0.0123 \cdot \tanh\left(-20.0265 \cdot DOD + 15.3859\right) + \left(T_C - 29.2075\right) \frac{dU}{dT} \end{aligned} \tag{5.7}$$

In this equation, the temperature is in degrees Celsius (T_C). For example, at the representative point summarized in Table 5-3, the predicted open circuit potential was 3.300 V. Figure 5.4 shows the comparison of the predicted versus measured open circuit

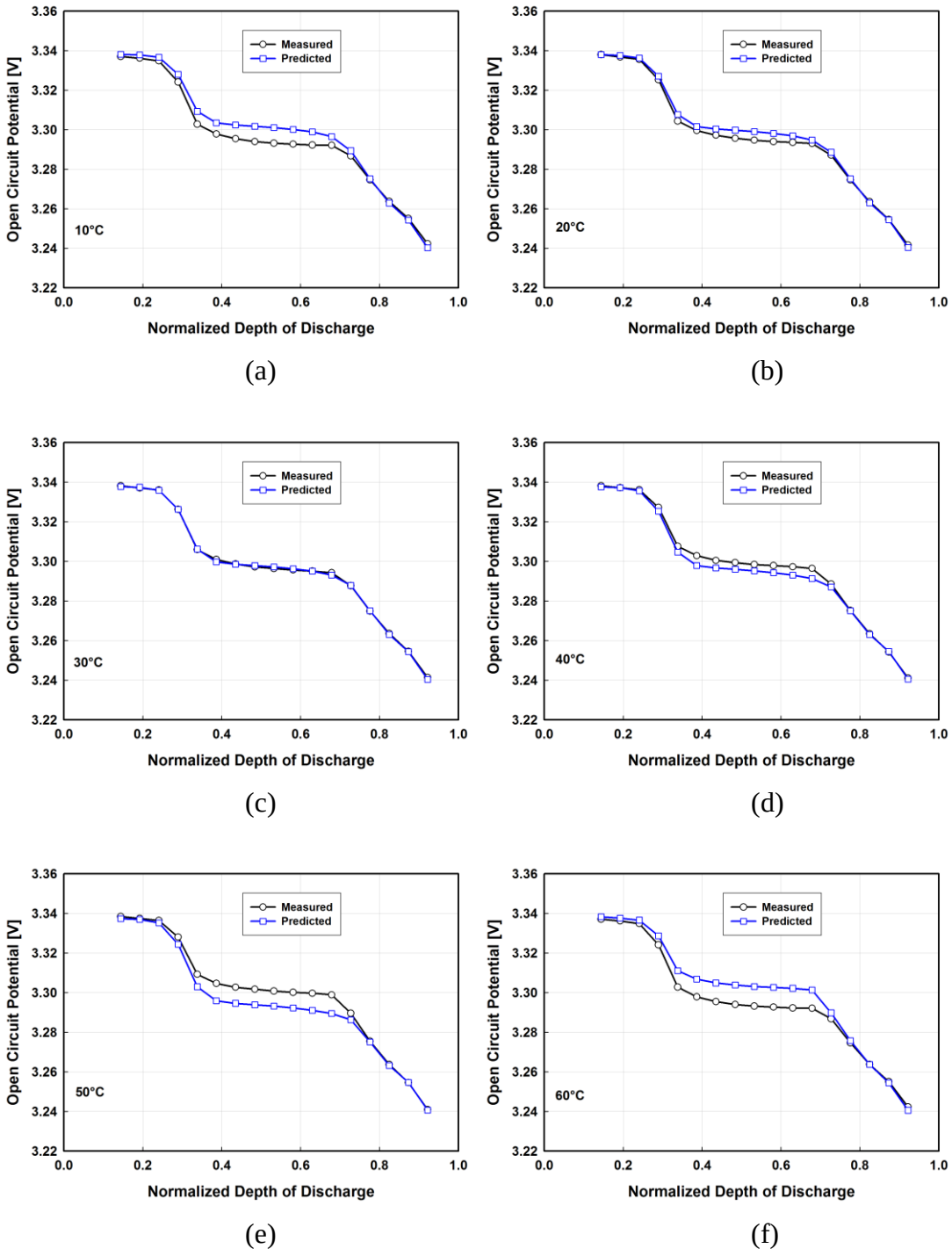

Figure 5.4: Predicted versus Actual Open Circuit Potential for Sample 1 at Different Test Temperatures: (a) 10°C, (b) 20°C, (c) 30°C, (d) 40°C, (e) 50°C, and (f) 60°C

potential for the six collected temperatures. As shown in the figure, the maximum difference between the predicted and measured data was at most 13.7 mV at 60°C, which has minimal impact on the simulation results. For example, at a discharge rate of 5 A, the measured discharge overpotential ranges from 236 mV to 406 mV at a test temperature of 55°C (Figure 3.14).

The local current production was calculated from the local overpotential (Equation 3.1), normalized *DOD*, and temperature. A piecewise linear fit of the data was used for the relationship between local current generation and overpotential at a fixed *DOD* and temperature. There were three different regions: high-rate charge, high-rate discharge, and low-rate charge/discharge. Furthermore, there was a transition region from low to high rates, which is discussed below. The relationship for high rate (*i.e.*, $|I|$ > 1 A) charge and discharge are as follows:

$$i'''_{\text{cha}} \cdot v_{\text{nom}} = \left\{ \begin{array}{l} \left[4.4250 \cdot DOD - 2.7874\right] \\ +\left[5.6691 - 6.0559 \cdot DOD\right] \exp\left[-0.0231 \cdot T_{\text{C}}\right] \end{array} \right\} + \left\{ \begin{array}{l} \left[14.7424 - 2.5963 \cdot \exp\left(1.5261 \cdot DOD\right)\right] \\ +10^4 \times \left[6.0579 \cdot DOD - 1.3634\right]\left[1 - \exp\left(-1.3952 \times 10^{-5} \cdot T_{\text{C}}\right)\right] \end{array} \right\} \eta \tag{5.8}$$

$$i'''_{\text{dis}} \cdot v_{\text{nom}} = \left\{ \begin{array}{l} \left[0.4926 \cdot DOD - 1.8837\right] \\ +\left[0.8416 \cdot DOD + 1.5588\right]\left[1 - \exp\left(-0.0314 \cdot T_{\text{C}}\right)\right] \end{array} \right\} + \left\{ \begin{array}{l} \left[8.1255 - 2.2525 \cdot DOD\right] + 10^4 \times \left[3.5779 - 3.3286 \cdot DOD\right] \\ \times \left[1 - \exp\left(-9.8946 \times 10^{-6} \cdot T_{\text{C}}\right)\right] \end{array} \right\} \eta \tag{5.9}$$

The nominal volume for the sample battery tested in this investigation was 13.08 mL. For the sample high-rate charge and discharge data point summarized in Table 5-3, the volumetric current production rates were -221.03 A L-1 and 179.24 A L-1, respectively.

For low-rate data (*i.e.*, $|I|$ < 0.5 A), the following equation was used:

$$i'''_{\text{low}} \cdot v_{\text{nom}} = \left\{ \begin{array}{l} \left[1.2520 - 2.9662 \cdot \exp\left(-3.5629 \cdot DOD\right)\right] \\ + \left[19.6631 - 11.4291 \cdot DOD\right]\left[1 - \exp\left(-0.0166 \cdot T_{\text{C}}\right)\right] \end{array} \right\} \eta \qquad (5.10)$$

At an overpotential of 0 (*i.e.*, at the open circuit), this equation returned a current generation rate of 0. In addition, the sign convention for current generation rate was positive for discharge and negative for charge. Similarly, charge data have a negative overpotential, while discharge has a positive overpotential, making the irreversible heat always positive. These requirements are reflected in this equation. For example, as summarized in Table 5-3, at low charge and discharge overpotentials of -0.027 V and 0.003 V, the volumetric current generation rates were -15.33 A L-1 and 1.73 A L-1, respectively.

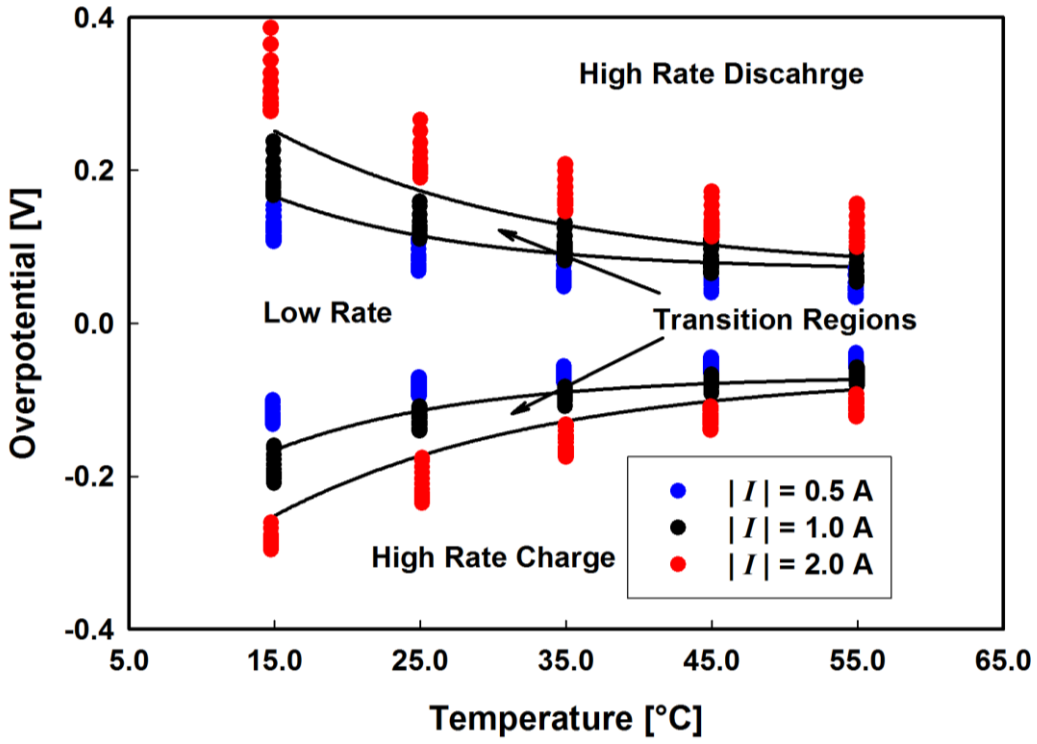

Figure 5.5: Piecewise Curve Fit Regions

It was assumed that the high and low rate equations given above were valid for currents magnitudes greater or less than 1 A, respectively. The following relationship was used to smooth the transition from low to high rates:

$$i'''_{\text{trans}} = \frac{\eta - \eta_{\text{low}}}{\eta_{\text{high}} - \eta_{\text{low}}}\left(i'''_{\text{high}} - i'''_{\text{low}}\right) + i'''_{\text{low}} \tag{5.11}$$

The high transition current generation rates were evaluated using Equations 5.8 and 5.9, respectively, for discharge and charge using the same overpotential. Similarly, the low rate current generation was calculated using Equation 5.10 at the same overpotential. As shown in Figure 5.5, the majority of the 1 A data fall within the following relationships for the absolute value of the low and high transition overpotentials for data collected between 0.20 < *DOD* < 0.73:

$$\left|\eta_{\text{low}}\right| = 0.0692 + 0.3043 \cdot \mathrm{e}^{(-0.0764 \cdot T_{\text{C}})} \tag{5.12}$$

$$\left|\eta_{\text{high}}\right| = 0.0664 + 0.4226 \cdot \mathrm{e}^{(-0.0550 \cdot T_{\text{C}})} \tag{5.13}$$

The transition overpotentials for charge and discharge have negative and positive signs, respectively. For example, at 36.85°C, the upper and lower transition overpotential limits were ±0.088 V and ±0.122 V, respectively. At the sample overpotentials of -0.102 V and 0.108 V, the high rate transition currents were -94.31 A L^{-1} and 95.49 A L^{-1}, respectively, while the low rate transition currents were -57.00 A L^{-1} and 60.11 A L^{-1}, respectively. Therefore, using Equation 5.11, the current generation rates were -84.23 A L^{-1} and 88.61 A L^{-1}, respectively.

Figure 5.6 shows the results of the piecewise linear curve fit for selected data (twenty points between normalized *DOD*s of 0.2 and 0.8) collected at the five nominal

surface temperatures. In general, the fit did a reasonably good job of capturing the magnitudes and trends in the data. The poorest fit is at the highest discharge rate at the highest *DOD* (0.8) at temperatures greater than 15°C. Thus, that the best range of applicability for this fit is in the range $0.2 < DOD < 0.7$ for rates up to ~5*C*. In this range, 90% of the charge data greater than -0.5 A, 93.5% of the discharge greater than 0.5 A, and 99.7% of the remainder were predicted to within ±35 mV. It should be noted here that during the power cycle used in this investigation, for the discharge and charge pulse rates beyond this range (which occurred for approximately 2.5% of the cycle at a compactness factor of 1, Section 5.3.1) Equations 5.8 and 5.9 were extrapolated to predict the local current generation.

The final equation required for the electrochemical model was the relationship between current and *DOD*, which was as follows:

$$i''' = i'''_{\text{nom}} \frac{\partial DOD}{\partial t} \tag{5.14}$$

The nominal volumetric current generation rate (i'''_{nom}) is the same as the tested battery volumetric capacity (79.6 Ah L^{-1}). Equations 5.6 through 5.14 comprise the parameterized electrochemical model. All of these equations were solved simultaneously with the heat transfer and current collection models (described in Sections 5.2.2 and 5.2.3) using a commercially available finite element analysis platform (COMSOL, 2010).

5.2.2. Heat Transfer

Heat transfer was modeled using the transient heat conduction equation (Equation 2.6.) This equation was applied to the battery in each domain: battery wind, aluminum shell, and argon gap. As shown in Figure 3.1, the battery wind consists of multiple layers

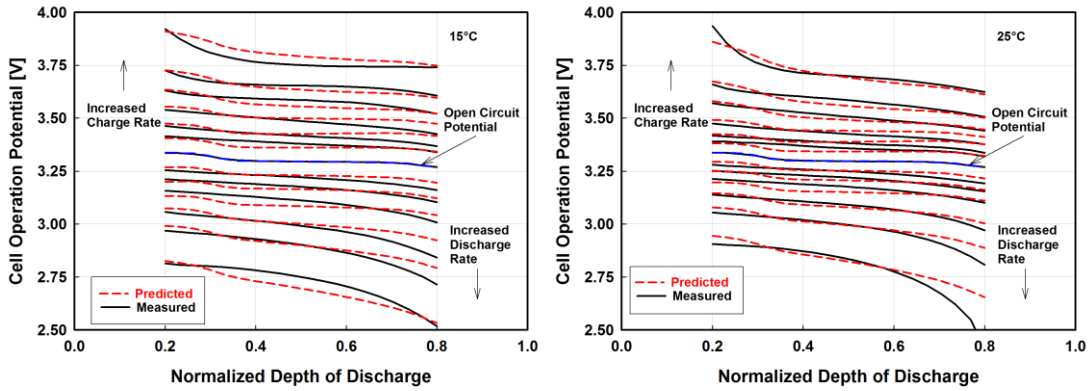

(a)

(b)

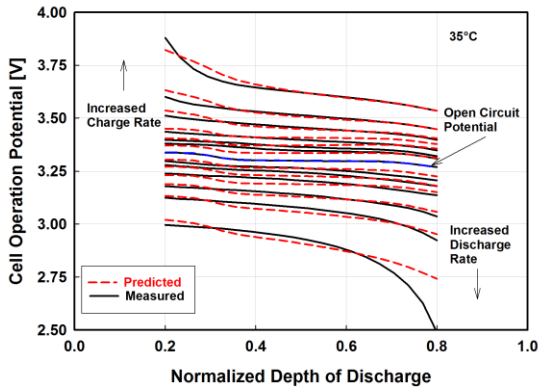

(c)

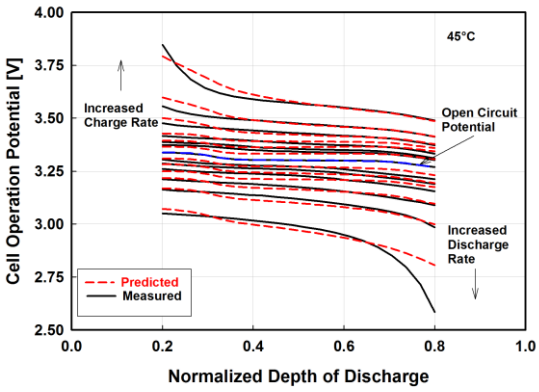

(d)

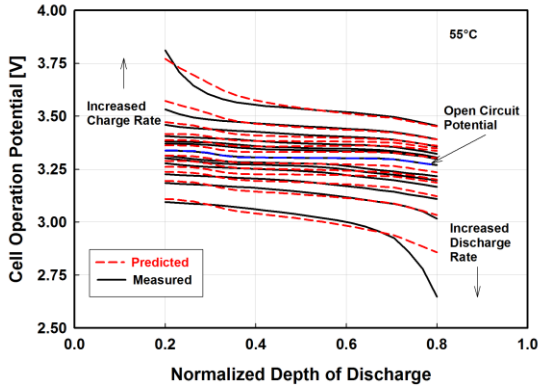

(e)

Figure 5.6: Predicted versus Experiment for the Electrochemical Model at Different Test Temperatures: (a) 15°C, (b) 25°C, (c) 35°C, (d) 45°C, (e) 55°C

wound together in a spiral. Thus, heat flowing from the center of the battery to the surface must pass through each layer in series, while heat conducting along the spiral flows through each layer in parallel. Chen and Evans (1993) showed that since these layers were thin relative to the battery thickness, the unit cell can be modeled as a bulk material. However, due to the different thickness and thermal conductivity of each component in the unit cell, the bulk thermal conductivity perpendicular to and along the spiral is different. Many researchers (*e.g.*, Chen *et al.*, 2005, and Chen and Evans, 1993) have used this method for thermal modeling, with the perpendicular and parallel thermal conductivities expressed as follows:

$$k_{\perp} = \frac{\sum t_{\mathrm{i}}}{\sum t_{\mathrm{i}} / k_{\mathrm{i}}} \tag{5.15}$$

$$k_{\parallel} = \frac{\sum k_{\mathrm{i}} t_{\mathrm{i}}}{\sum t_{\mathrm{i}}} \tag{5.16}$$

These relations were derived by equating an equivalent thermal resistance to a network of perpendicular and parallel resistances. Using the unit cell thickness and properties listed in Table 5-4, the perpendicular and parallel thermal conductivities for the present investigation are 1.013 W m^{-1} K^{-1} and 80.3 W m^{-1} K^{-1}, respectively. A discussion of the

Table 5-4: Battery Unit Cell Component Thermal Properties

Component	Total Thickness	k	C_p	Property Source
	[μm]	[W m^{-1} K^{-1}]	[MJ m^{-3}]	
Al Current Collector	35.56	238	2.440	Chen *et al.* (2005)
Positive Electrode Material	66.04	1.48	1.890	Guo *et al.* (2010)
Cu Current Collector	35.56	398	3.462	Chen *et al.* (2005)
Negative Electrode Material	96.52	1.04	1.937	Chen *et al.* (2005)
Electrolyte Soaked Separator	50.8	0.3344	1.996	Chen *et al.* (2005)

application of this idealization for the different domains used for air/liquid and edge/internal cooling domains is given in Section 5.3.1. Similar to the approach used by Chen *et al.* (2006) and others, the cell heat capacity ($\rho\ C_p$) was calculated from the volumetric average as follows:

$$\rho C_p = \frac{\sum \left(\rho C_p\right)_i t_i}{\sum t_i} \tag{5.17}$$

Using the data in Table 3-1, the bulk cell heat capacity is 2.185 MJ m^{-3} K^{-1}.

The thermal conductivities and bulk cell heat capacities of the aluminum (3003-H18) shell and argon gap are 155 W m^{-1} K^{-1} and 2.438 MJ m^{-3} K^{-1}, and 0.0178 W m^{-1} K^{-1} and 0.844 kJ m^{-3} K^{-1}, respectively. These values were utilized in the two-dimensional model, but not incorporated into the quasi-three-dimensional model. However, in the latter, the weighted heat capacities and thermal conductivities of the aluminum and copper positive and negative tabs were calculated as follows:

$$k_{cc,eff} = k_{cc} \frac{t_{cc}}{t_{unit\ cell}} \tag{5.18}$$

$$\left(\rho C_p\right)_{cc,eff} = \left(\rho C_p\right)_{cc} \frac{t_{cc}}{t_{unit\ cell}} \tag{5.19}$$

This approach was used because the thickness of the tabs is less than the thickness of the unit cell. Using properties listed in Table 3-1, these effective properties are 49.75 W m^{-1} K^{-1} and 0.433 MJ m^{-3} K^{-1}, and 29.75 W m^{-1} K^{-1} and 0.305 MJ m^{-3} K^{-1} for the positive and negative current collector tabs, respectively.

The volumetric heat generation rate for the battery wind was calculated using Equation 2.4, shown here in a modified form:

$$\dot{Q}''' = \dot{Q}'''_{\text{ECM}} + \dot{Q}'''_{\text{cc}} = i'''\left(U - V - T\frac{\partial U}{\partial T}\right) + \dot{Q}'''_{\text{cc}} \tag{5.20}$$

Representative values for the electrochemical heat generation rate using the first term on the right-hand side of this equation are shown in Table 5-3. For example, at high rates of charge and discharge of -221.03 A L-1 and 179.24 A L-1, the total electrochemical heat generation rates were 55.56 W L-1 and 21.71 W L-1, respectively. However, the current collection heat, as described in Section 5.3, was applied differently in each domain used for the air/liquid and edge/internal cooling strategies. For air and liquid cooling, the current distribution was assumed uniform in the vertical direction, which results in the following relationship between the current flux and volumetric current generation at the top of the cell:

$$i'' = i'''H_{\text{cell}} \tag{5.21}$$

Ohm's law and the relationship for resistive heating are given as follows:

$$i'' = \sigma \nabla V \tag{5.22}$$

$$\dot{Q}''' = i'' \nabla V \tag{5.23}$$

Therefore, substituting Equations 5.21 and 5.22 into Equation 5.23 and correcting for the thicknesses in both current collectors, the maximum resistive heating for the air and liquid cooled cells was calculated as follows:

$$\dot{Q}'''_{\text{cc}} = \frac{\left(i'''H_{\text{cell}}\right)^2}{t_{\text{unit cell}}}\left(\frac{t_{\text{cc,Al}}}{\sigma_{\text{Al}}} + \frac{t_{\text{cc,Cu}}}{\sigma_{\text{Cu}}}\right) \tag{5.24}$$

This was the maximum heat generation determined by assuming perfect current collection in the vertical direction the battery, and was applied locally across the domain

used for air/liquid cooling. Using conductivities of the aluminum positive and copper negative current collectors of 3.774×10^7 S m^{-1} and 5.998×10^7 S m^{-1}, respectively, the maximum current collection heat rates were only 0.006 W L^{-1} and 0.004 W L^{-1}, respectively, at the high charge and discharge rates shown in Table 5-3 for a 153 mm cell height. For the edge and internal cooling domains, the local current collection heat was calculated using the current collection model described in the next section as follows:

$$\dot{Q}_{cc}''' = \left(\sigma \left|\nabla \phi\right|^2\right)_{cc,pos} \frac{t_{cc,pos}}{t_{unit\ cell}} + \left(\sigma \left|\nabla \phi\right|^2\right)_{cc,neg} \frac{t_{cc,neg}}{t_{unit\ cell}} \tag{5.25}$$

Because there was a single thermal domain for these cooling strategies, the actual heat rates applied in the collectors were corrected by the thickness of the current collectors.

In either case, the heat generation coupled the primary models together. The volumetric current generation, potential, open-circuit potential, and entropic heat coefficient were determined from the electrochemical model described in Section 5.2.1 and, in the case of edge and internal cooling, the current collection model described in the next section.

5.2.3. Current Collection

As current was generated locally inside the battery, it migrated towards the tabs. Charge movement in the collectors caused resistive heating, which in turn affects the local temperature and current generation rates. For the edge and internal cooling modeling domains, the flow of current was computed using the conservation of current (modified by Ohm's law) in each collector as follows:

$$-\nabla \cdot \left(\sigma \nabla V\right) + i''' = 0 \tag{5.26}$$

As discussed in the next section, the boundary condition for the cell was the

instantaneous power generated by the cell calculated at the tab voltage. Because electron movement was substantially faster than heat transport, the equation was solved at each instant in time without accounting for the charge storage. The driving force for current migration was the local potential gradient. As a result, the local potential within the battery was different than the potential difference between the tabs. This affects the local overpotential and, thus, current generation. Therefore, the local overpotentials for the edge and internal cooling domains were calculated as follows:

$$\eta = U - \left(V_{\text{pos}} - V_{\text{neg}} \right) \tag{5.27}$$

During discharge, the current migrates from the positive current to the negative collector. This resulted in higher and lower potentials in the positive and negative electrodes, respectively, as the distance from the current generation location to the tabs increased. Hence, the local potential for discharge increased, thus lowering the overpotential and, therefore, the local current generation. The local overpotential magnitude for charging was also similarly lower at locations far away from the tabs. In the next section, the assumptions for the applied power condition are discussed in detail.

5.3. Modeling Domains and Simulation Parameters

In this section, the modeling domains for each cooling method are described. In this investigation, only one cell within the packs was simulated. For air and liquid external cooling, a two-dimensional cross-section of the cell was investigated. In contrast, a quasi-three-dimensional split current collector model was used for edge and internal cooling. The required boundary and initial conditions for these domains are also presented, including a separate section that discusses the simplifications used for

Table 5-5: Summary of Boundary and Initial Conditions for Both Model Domains

Thermal and Electrochemical Initial Conditions			
Temperature		°C	26.85
DOD	*CF* = 1		0.45
	CF = 2		0.40
	CF = 3		0.35
	CF = 4		0.25
	CF = 5		0.20
Electrochemical Boundary Conditions			
Input Power		W	Equation 5.35 or 5.38
Maximum Charge Power	*CF* = 1	W	-82.6
	CF = 2	W	-165.1
	CF = 3	W	-247.7
	CF = 4	W	-270
	CF = 5	W	-240
Maximum Discharge Power	*CF* = 1	W	131.7
	CF = 2	W	215
	CF = 3	W	208
	CF = 4	W	206
	CF = 5	W	205
2-D Model Thermal Boundary Conditions			
Cooling Fluid Temperature		°C	26.85
Surface Convection		$W\ m^{-2}\ K^{-1}$	21.0 and 375.5
Perpendicular Wind Contact Resistance		$m^2\ K\ W^{-1}$	2.773×10^{-4}
Parallel Wind to Shell Contact Resistance		$m^2\ K\ W^{-1}$	∞
Parallel Wind to Gap Contact Resistance		$m^2\ K\ W^{-1}$	0
Quasi 3-D Model Thermal Boundary Conditions			
Edge Cooling Surface Temperature		°C	26.85
Internal Cooling Surface Convection		$W\ m^{-2}\ K^{-1}$	Equation 5.49

coupling the simplified passive microchannel phase change internal cooling system to the battery model.

5.3.1. Two-Dimensional Model for Air and Liquid Cooling

A two-dimensional slice of a single cell was modeled for external air and liquid cooling. The boundary conditions needed for the heat transfer model are shown schematically in Figure 5.7. Table 5-5 summarizes the heat transfer and electrochemical

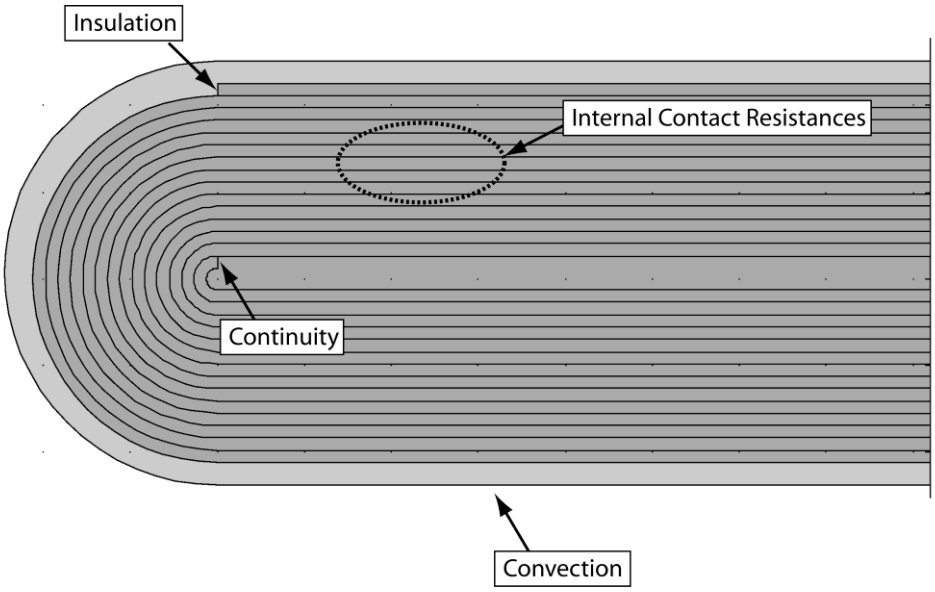

Figure 5.7: Summary of Internal and External Boundary Conditions for the Two-Dimensional Model

boundary and initial conditions used in this investigation. The only initial condition for heat transfer was temperature, which was assumed to be 26.85°C everywhere. However, there were two primary types of boundary conditions for this domain: internal and external. The internal boundary conditions included contact resistance within the battery (perpendicular to the spiral) and at the beginning and end of the battery wind (parallel to the spiral). Heat was conducted along and perpendicular to the spiral across different effective thermal resistances. However, the flat spirally-wound battery has both straight and curved portions, which make implementing the anisotropic thermal conductivity difficult. Thus, for simplicity, a thermal contact resistance was placed between each successive layer to simulate the perpendicular thermal conductivity (1.013 W m^{-1} K^{-1}), while the bulk material was assigned the parallel thermal conductivity (80.3 W m^{-1} K^{-1}). This allowed heat to be transported along the spiral through the correct thermal resistance. In addition, since the parallel thermal conductivity was much larger than the

perpendicular, the largest changes in temperature occurred across the contact resistance, with little change in temperature in the wind itself in the perpendicular direction. Thus, at each spiral location, the battery temperature was approximately constant across the thickness, followed by a step change in temperature to the adjacent wind, which was consistent with assuming bulk properties for the cell. The specific contact resistance was calculated using an equivalent thermal resistance network as follows:

$$R''_{\text{cont}} = t_{\text{unit cell}} \left(\frac{1}{k_{\perp}} - \frac{1}{k_{\parallel}} \right) \tag{5.28}$$

Using the properties listed in Table 5-4, the effective contact resistance is 2.773×10^{-4} m^2 K W^{-1}. All perpendicular boundaries on the battery wind, including those in contact with the aluminum shell and argon gap, were assumed to have this contact resistance value.

The other internal boundary conditions were located at the beginning of the wind next to the argon gap and at the end of the wind adjacent to the aluminum shell. Near the argon gap, heat was transferred unimpeded in the direction parallel to the battery wind. Thus, a thermal contact resistance of 0 m^2 K W^{-1} was used between the end of the battery wind and the argon gap in this direction. Although shown in the drawing and approximated in the model, the curved left side of the battery was not actually in contact with the wind, but was separated by a small sliver of argon. This small sliver was difficult to represent in a finite element model, and, thus, it was neglected. Therefore, the contact resistance between the end of the battery wind and aluminum shell in the parallel direction was assumed infinite. The effect of this assumption should be small considering the cross-sectional area of this contact area was much smaller than the contact area perpendicular to the stack.

The remaining boundary condition was the surface convection, which is modeled using a heat balance on the surface of the battery as follows:

$$-k_{\text{shell}} \left. \frac{\partial T}{\partial x_n} \right|_{\text{wall}} = h_{\text{cool}} \left(T\big|_{\text{wall}} - T_{\text{cool}} \right) \tag{5.29}$$

There were two cooling modes investigated in this study: air and liquid cooling. The liquid in this study is a 30/70 mixture by weight of ethylene glycol and water. The following were the assumptions for this boundary condition:

- Series inter- and parallel intra-module cooling (Figure 5.1)
- Uniform coolant distribution within the pack (same flow rate evenly divided between cells)
- Constant coolant temperature (26.85°C)
- Constant convective heat transfer coefficient over the entire surface (including both straight and curved portions)
- Laminar flow.

To verify that the flow was laminar, the Reynolds number was calculated as follows:

$$Re_{\text{cool}} = \frac{V_{cool} D_{\text{h,gap}}}{\mu / \rho} \tag{5.30}$$

The velocity and hydraulic diameter of the gap between the cells were calculated as follows:

$$V_{\text{cool}} = \frac{\dot{V}_{\text{cool}}}{\left(N_{\text{cell,par}} + 1 \right) \left(gap_{\text{cool}} \cdot H_{\text{cell}} \right)} \tag{5.31}$$

$$D_{\text{h,gap}} = 2 \frac{gap_{\text{cool}} \cdot H_{\text{cell}}}{gap_{\text{cool}} + H_{\text{cell}}} \tag{5.32}$$

The number of cells per module is 75, and the gap width and height are 5 mm and 153 mm, yielding a hydraulic diameter of 9.684 mm. The air and liquid volumetric flow rates were 500 m^3 hr^{-1} and 5 lpm, respectively, which yield velocities of 2.39 m s^{-1} and 0.0014 m s^{-1}, respectively. (These flow rates were chosen because at these values, the fluid temperature rise is less than 5 K and 2 K, respectively, across the entire pack using the nominal heat generation rate for *CF* = 1: 770 W, *i.e*, 20.4 W L^{-1} at a unit cell volume of 37.7 L.) With kinematic viscosities of 1.596×10^{-5} m^2 s^{-1} and 1.728×10^{-6} m^2 s^{-1} for the air and liquid, respectively, the Reynolds numbers are 1450 and 8.03, which are laminar.

The Nusselt number was calculated using the method in Kakac *et al.* (1987) for laminar flow in rectangular ducts:

$$Nu_{\text{cool}} = 8.235\left(\begin{array}{c} 1 - 2.0421\alpha_{\text{gap,cool}} + 3.0853\alpha_{\text{gap,cool}}^2 \\ -2.4765\alpha_{\text{gap,cool}}^3 + 1.5078\alpha_{\text{gap,cool}}^4 - 0.1861\alpha_{\text{gap,cool}}^5 \end{array}\right) \quad (5.33)$$

The aspect ratio ($\alpha_{\text{gap,cool}}$) was calculated from the gap width and height between the channels (5 mm ÷ 153 mm = 0.0327); therefore, the laminar Nusselt number is 7.712

The convective heat transfer coefficient is calculated as follows:

$$h_{\text{cool}} = Nu_{\text{cool}} \frac{k_{\text{cool}}}{D_{\text{h,gap}}} \quad (5.34)$$

The thermal conductivities of air and liquid at 26.85°C and 100 kPa were 0.0264 W m^{-1} K^{-1} and 0.4715 W m^{-1} K^{-1}, respectively. For a hydraulic diameter of 9.684 mm, the heat transfer coefficients for air and liquid cooling are 21.0 W m^{-2} K^{-1} and 375.5 W m^{-2} K^{-1}, respectively.

The only boundary condition required for the electrochemical model was the required cell power. Although the cell potential was assumed to be the same everywhere,

the non-uniformity in temperature, *DOD*, and overpotential caused the local current generation to be spatially non-uniform. Thus, the current generation rate for the battery was determined by integrating the local current generation rate across the entire battery. Therefore, the applied (drawn) power to (from) the battery was calculated as follows:

$$Power = V \cdot H_{\text{cell}} \cdot \int i''' dA_{\text{cell}} \tag{5.35}$$

The integral applied over the entire cross-sectional area of the battery was multiplied by the battery height to calculate the total current generated by the battery.

The dynamic power requirements were the same as those used for the HEV tests on the commercial battery. Assuming that each battery within the pack supplies the same power, the power requirements for a single battery were calculated by dividing the pack requirement power by the number of cells in the pack (375 and 150 cells for the 8 Ah and 20 Ah batteries, respectively) as follows:

$$Power = \frac{Power_{\text{pack}}(t)}{N_{\text{cell,pack}}} \tag{5.36}$$

Using Figure 3.20, Figure 5.8 shows the power requirements for each individual battery within the 9.6 kWh pack. For example, at a required pack charging power of -6.91 kW at 100 s, the individual power requirements for the 8 ah and 20 Ah cells were -18.4 W and -46.1, respectively.

The only required initial condition for the electrochemical model was the normalized *DOD*, which was assumed to be uniform across the battery. Furthermore, it is desirable to reduce the size of the pack in HEV applications. Therefore, a configuration that reduces battery pack size while keeping the power requirements the

same was designed and investigated in this study. This was achieved through a modified dynamic power boundary condition based on a compactness factor defined as follows:

$$Power = CF \frac{Power_{\text{pack}}}{N_{\text{cells,pack}}} \tag{5.37}$$

For the (baseline) nominal energy of the pack, 9.6 kWh, Figure 5.8 represents a compactness factor of 1. Additional simulations for compactness factors ranging from 2 to 5 were also conducted, as well as CF = 10 for the optimized internal cooling system (Section 5.4.3). As the compactness factor increases, each individual battery should be cycled more aggressively. For example, the charge power required by an individual cell at 100 s increased from -18.4 W to -92.1 W as the compactness factor increased from 1 to 5. However, as was the case for the experiments in this study (Section 3.3.1), the battery voltage was limited to within 2.0 V and 4.2 V at the tab. (The manufacturer's limits were 2.0 V and 4.1 V. However, to be consistent with the experiments, the charge limit was increased to 4.2 V.) Hence, the maximum extractable power was limited for charge and

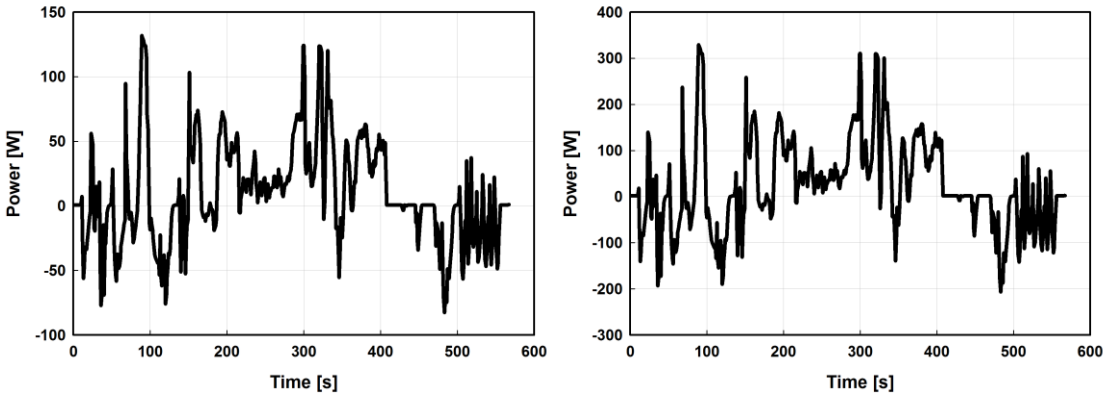

(a) (b)

Figure 5.8: Dynamic Power Requirements for Individual Cells with CF = 1: (a) 8 Ah and (b) 20 Ah

discharge at $CF > 3$ and $CF > 1$, respectively (Table 5-5). For example, at $CF = 5$, the charge and discharge power limits were -240 W and 205 W, respectively. These limits correspond to the power estimated from prescribed limits of 1.94 V and 4.16 V at 24°C. In such cases, despite the prescribed compactness factor, the actually achieved effective compactness was lower than the defined value due to these limitations at the battery tabs. For the dynamic power simulation, the battery was assumed to have initial *DOD*s ranging from 0.20 to 0.45 for compactness factors ranging from 1 to 5 to accommodate both the charge depletion and voltage limitations in this particular application.

For time stepping, the simulation software dynamically determined the appropriate time step using the generalized-alpha method (Chung and Hulbert, 1993; Jansen *et al.*, 2000). However, to ensure that dynamic load was properly simulated, the time steps taken by the solver was set to "strict", which forced at least one time step to occur every 1 s at each prescribed boundary condition. In addition, the *maximum* time step was further limited to only 0.1 s to accommodate this rapidly varying time load. To ensure that the solution was sufficiently accurate, both the relative and absolute tolerance settings in all simulations were set to very tight values (1×10^{-8}), with the latter applied to all scaled variables.

5.3.2. Quasi-Three-Dimensional Model for Edge and Internal Cooling

Ideal current collection was assumed for the domains used to simulate cell performance when cooled by air or liquid. However, concentration of current can increase local heat generation near the tabs due to Ohmic heating (Kim *et al.*, 2008; Kim *et al.*, 2009). This effect was modeled for edge and internally cooled cells. As shown in Figure 5.9, the thermal domain was modeled in two dimensions as an unwound unit cell for these cases. However, as shown in Figure 5.10, the positive and negative collectors

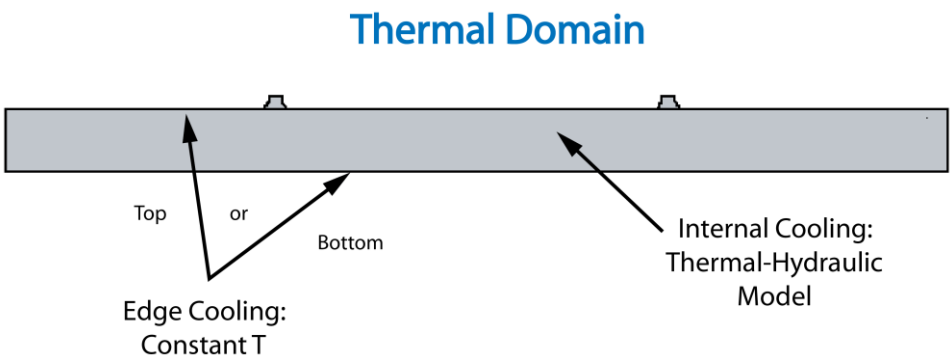

Figure 5.9: Thermal Domain for Edge and Internal Cooling

were modeled separately, which allowed for current to be concentrated at the tabs. The local overpotential was calculated from the local potential difference between the two collector domains. Using the local temperature and *DOD*, this local overpotential was used to calculate the local current generation.

The thermal boundary conditions are summarized in Figure 5.9 and Table 5-5. For edge cooling, it was assumed that the cold plate and battery case had minimal thermal resistance. Therefore, it was assumed that the cooled edge had a fixed temperature equal to its initial temperature (26.85°C). For internal cooling, a surface heat transfer coefficient was applied to the entire surface (except the current collection tabs). The heat transfer coefficient was calculated using the model of Bertsch *et al.* (2009) as a function

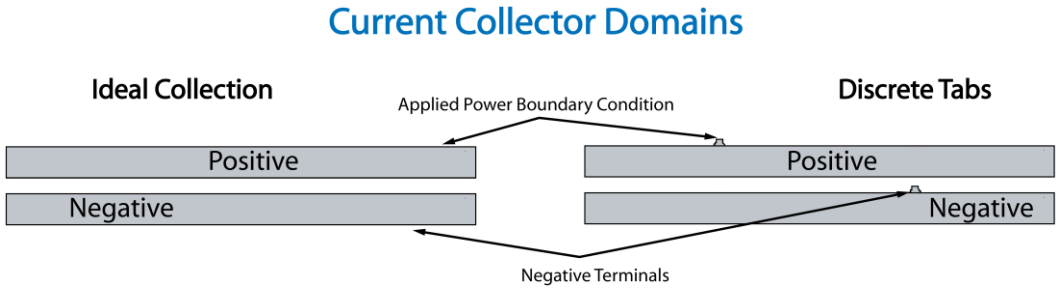

Figure 5.10: Current Collection Domains for Edge and Internal Cooling: Ideal Collection and Discrete Tabs

of the predicted mass flow rate and outlet quality of the passive microchannel evaporator, which was determined from the simplified thermal-hydraulic model detailed in the next section. The thermal properties used in this model were the same as those used in the two-dimensional model, except for the fact that no correction was needed for the anisotropic thermal conductivity because heat was transported through conduction only in the direction parallel to the stack (*i.e.*, $k = 80.3$ W m^{-1} K^{-1}).

For the electrochemical model, the same initial normalized *DOD*s and compactness factors were used as in the two-dimensional model for air and liquid cooling. However, the boundary condition at the positive tab edge needed iterative analyses and was based on the inward current flux as follows (Figure 5.10):

$$i'' = \frac{Power \cdot L_{tab}}{\int V_{tab}\, dL_{tab}} \tag{5.38}$$

The average voltage was calculated at the positive tab, which was either the entire top surface for ideal current collection or the top edge of the discrete tab. As shown in Figure 5.11, the top edge of the discrete tab (which was 30 mm wide) was downstream of the slightly curved edged to avoid the effects of superfluous resistive heating or voltage spikes at sharp corners. Similar to the two-dimensional model, the required power was determined from Figure 5.8 at the specified compactness factor.

In contrast to the two-dimensional model, the time step taken by the solver was *fixed* at 0.05 s to ensure that dynamic load was properly simulated while not prohibitively extending solution time. The relative and absolute tolerance settings in all simulations were set to the same very tight tolerances (1×10^{-8}), with the latter again applied to all scaled variables.

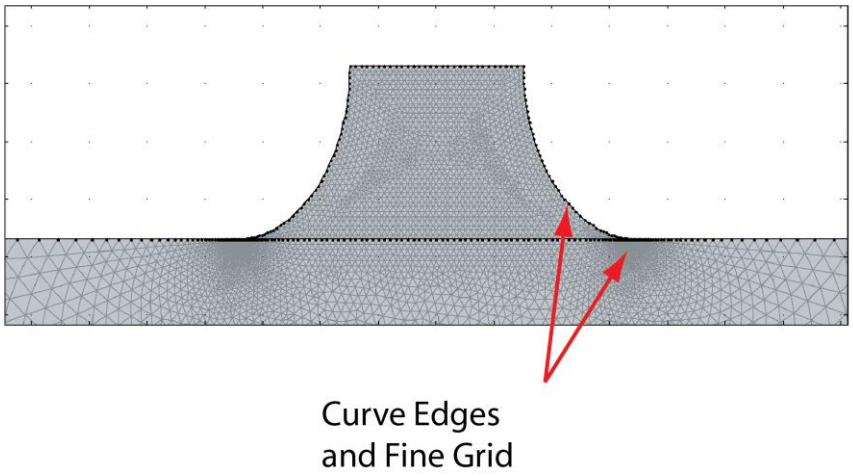

Figure 5.11: Close-up View of Discrete Positive Tab

5.3.3. Simplified Thermal-Hydraulic Model for Internal Cooling

To simulate coupled electrochemical-thermal performance of the battery with internal cooling, a thermal-hydraulic model was developed based on the results of the passive internal cooling system investigation described in Chapter Four. Figure 5.12 shows a schematic of this simplified passive internal cooling system. In this system, it was assumed that the gravity head between the condenser outlet and the evaporator inlet balances only the two-phase frictional pressure drop, which was shown to be the dominant pressure drop in a majority of the cases investigated. The gravity head was calculated in a manner similar to that used in Equation 4.60, without the effects of the outlet header, as follows:

$$\begin{aligned}\Delta P_{\text{head}} = \rho_{\text{l}} g \Delta H - \left[\left(1 - VF_{\text{SF}}\right)\rho_{\text{l}} + VF_{\text{SF}}\rho_{\text{v}}\right] g \left(\Delta H - H_{\text{cell}}\right) \\ - \sum_{i=1}^{20} \left[\left(1 - VF_{\text{HG,i}}\right)\rho_{\text{l}} + VF_{\text{HG,i}}\rho_{\text{v}}\right] g \frac{H_{\text{cell}}}{20}\end{aligned} \tag{5.39}$$

It was assumed that the working fluid (R134a) was a saturated liquid at the inlet of the channels. Therefore, there was no single phase region in the evaporator. As in the

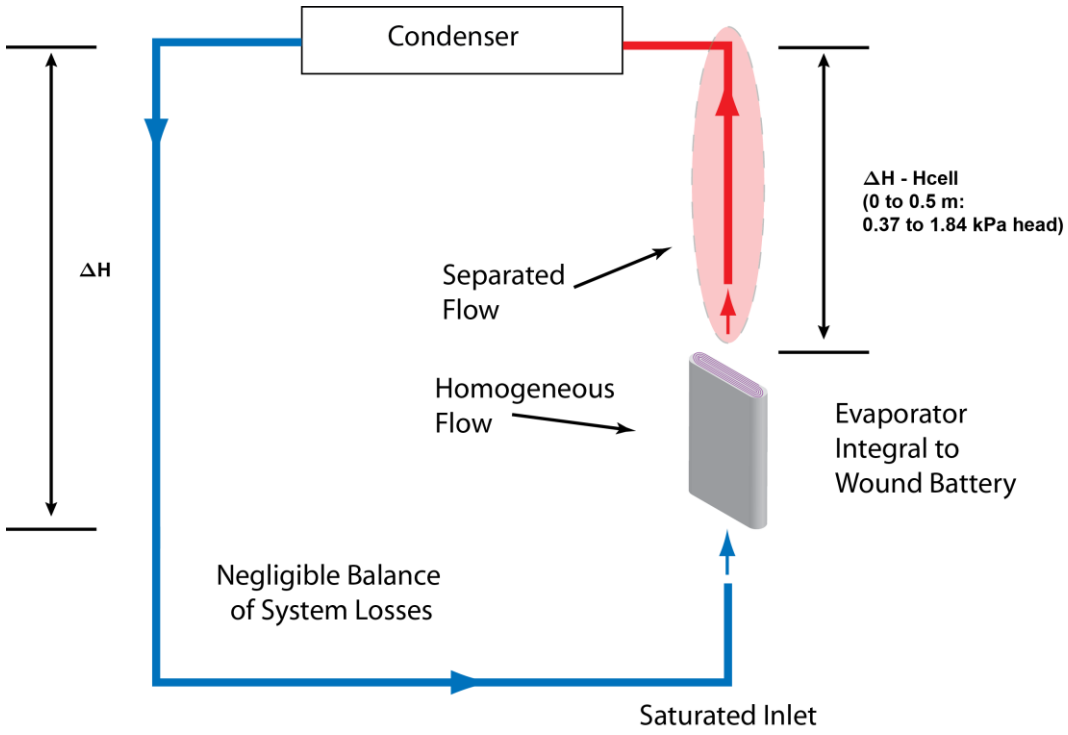

Figure 5.12: Schematic for Simplified Passive Microchannel Phases Model for Coupling with Battery Model

frictional pressure drop calculation in Section 4.4.3, the void fraction was calculated in the evaporator using the homogenous flow assumption, Equation 4.63. Similarly, the Baroczy (1965) void fraction correlation (Equation 4.64) was used in the connection tubing between the outlet of the evaporator and the inlet of the condenser. For example, using the representative point in Table 5-6, the separated flow void fraction at an evaporator outlet quality of 0.017 was 0.256. The homogeneous void fractions in the 20 evaporator sections are given in Table 5-7. The elevation difference between the condenser and the evaporator ($\Delta H - H_{cell}$) is an adjustable design parameter that can add gravity head to increase pumping power for fluid movement, if necessary. As shown in Figure 5.12, for an elevation difference between the evaporator outlet and condenser inlet

of 0.5 m and a cell height of 153 mm, the corresponding pressure head was 1.836 kPa. In contrast, the pressure head that must be supplied by gravity decreases to 0.374 kPa if the distance between the evaporator and condenser is eliminated, because the frictional pressure drop is lower in this case, due to a shorter flow length and a lower refrigerant mass flow rate.

Table 5-6: Sample Data Point for the Simplified Thermal-Hydraulic Passive Internal Cooling Model

Item	Units	Value
Geometry		
N_{ch}		226
W_{ch}	mm	3.175
H_{ch}	μm	160
N_{pitch}	mm	7.046
$t_{unit\ cell}$	μm	284.5
Fluid Flow		
$\dot{m}_r$	g s^{-1}	13.78
G_{ch}	kg m^{-2} s	120.03
$x_{r,e,o}$		0.017
$\dot{Q}'''$	W L^{-1}	400
Properties		
P_{sat}	kPa	703.2
T_{sat}	°C	26.85
ρ_l	kg m^{-3}	1200
μ_l	kg m^{-1} s^{-1}	1.900×10^{-4}
k_l	W m^{-1} K^{-1}	0.082
Pr_l		3.300
ρ_v	kg m^{-3}	34.18
μ_v	kg m^{-1} s^{-1}	1.205×10^{-5}
k_v	W m^{-1} K^{-1}	0.015
Pr_v		0.847
σ	N m^{-1}	0.0078
P_r		0.173
M	g mol^{-1}	103.032

The frictional pressure drop was calculated using the model developed in Chapter

Four (Equations 4.86 through 4.94), and the values for the twenty segments in the sample point are also shown in Table 5-7. The flow in the evaporator was divided into multiple

Table 5-7: Segmental Void Fraction and Gravity Head for the Simplified Thermal-Hydraulic Passive Internal Cooling Model

Segment	$x_{r,e,a}$	VF_{HG}	ΔP_{head}	ϕ_l^2	ΔP_l	ΔP_{tp}
1	0.0004	0.014	0.089	1.034	0.070	0.073
2	0.0012	0.042	0.086	1.078	0.070	0.076
3	0.0021	0.068	0.084	1.115	0.070	0.078
4	0.0029	0.093	0.082	1.148	0.070	0.081
5	0.0037	0.116	0.080	1.179	0.070	0.083
6	0.0046	0.138	0.078	1.208	0.070	0.085
7	0.0054	0.160	0.076	1.236	0.070	0.087
8	0.0062	0.180	0.074	1.263	0.070	0.088
9	0.0070	0.199	0.073	1.289	0.070	0.090
10	0.0079	0.218	0.071	1.315	0.070	0.092
11	0.0087	0.236	0.069	1.340	0.070	0.094
12	0.0095	0.252	0.068	1.364	0.070	0.095
13	0.0104	0.269	0.067	1.388	0.070	0.097
14	0.0112	0.284	0.065	1.411	0.070	0.098
15	0.0120	0.299	0.064	1.434	0.070	0.100
16	0.0128	0.314	0.063	1.457	0.070	0.101
17	0.0137	0.327	0.061	1.479	0.069	0.103
18	0.0145	0.341	0.060	1.501	0.069	0.104
19	0.0153	0.353	0.059	1.523	0.069	0.106
20	0.0162	0.366	0.058	1.544	0.069	0.107
Total			1.427			1.836

parallel passages at the same pitch (10.16 mm), width (3.175 mm), and effective height (160 μm) as in the microchannel test section described in Chapter Four. Accordingly, and because the header friction and the remaining balance of system component losses were neglected in this simplified model, neither the frictional pressure drop nor the gravity head were a function of the total mass flow rate. (In other words, the calculations were essentially performed on the basis of the mass flux in individual channels.) Therefore, this model applied to both the 8 Ah and 20 Ah battery designs.

As mentioned above, the height between the evaporator outlet and condenser inlet was an adjustable parameter. Figure 5.13 shows the calculated mass flux and outlet quality for two different values of ΔH (0.653 m and 0.153 m) as a function of average volumetric heat generation rates ranging from 0 W L^{-1} to 4500 W L^{-1}. It can be seen that the calculated mass flux and evaporator outlet quality differ substantially depending on the height selected. For example, at the smaller height, the mass flux peaks at 41.3 kg m^{-2} s^{-1} near a volumetric heat rate of 820 W L^{-1}, and the outlet quality reaches 0.863 at a volumetric heat generation rate of 4500 W L^{-1}. In contrast, the mass flux peaks at 176.4 kg m^{-2} s^{-1} near a heat rate of 3200 W L^{-1} for ΔH = 0.653 m, and the outlet quality was only 0.129 for a volumetric heat rate of 4500 W L^{-1}.

The mass flow rates and qualities predicted for this model were used to calculate the average two-phase heat transfer coefficient using the model of Bertsch *et al.* (2009). To develop their model, they used a large database of evaporation heat transfer coefficient data from multiple different investigations on different fluids and geometries, which is summarized as follows:

- 160 μm < D < 2.92 mm
- 0.3 < Co < 4.0
- 20 < G < 3000 kg m^{-2} s^{-1}
- 0.4 < $\dot{Q}''$ < 115 W cm^{-2}

The present investigation falls within all of these parameters except the heat flux, which, at a heat input of 1400 W L^{-1}, was a maximum of 0.040 W cm^{-2}.

In their model, the composite heat transfer coefficient was calculated from the combined effects of convective and nucleate boiling as follows:

$$h_{tp,e} = h_{conv,eff} \cdot F + h_{NB} \cdot (1 - x) \tag{5.40}$$

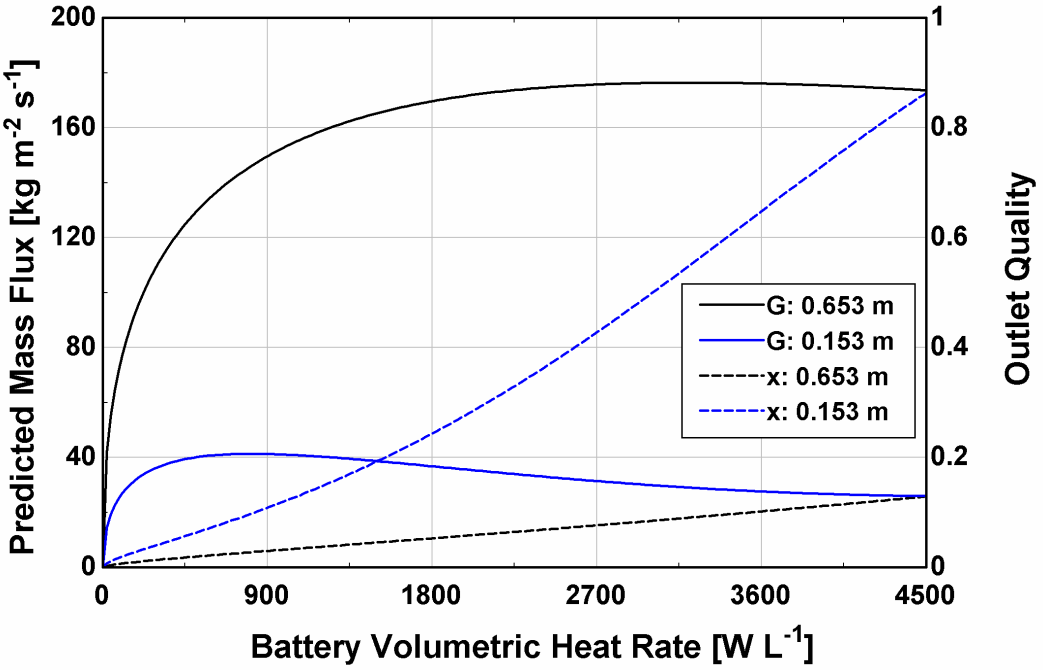

Figure 5.13: Simplified Internal Cooling System Performance at Two Gravity Heads: Mass Flux and Outlet Quality

The effective convective heat transfer coefficient was calculated using the Hausen (1943) developing flow correlation for each phase as follows:

$$h_{conv,eff} = h_{conv,l} \cdot (1 - x) + h_{conv,v} \cdot x \tag{5.41}$$

$$h_{conv} = \left(3.66 + \frac{0.0668 \cdot \frac{D_{ch}}{h_{cell}} \cdot Re \cdot Pr}{1 + 0.04 \cdot \left[\frac{D_{ch}}{H_{cell}} \cdot Re \cdot Pr \right]^{2/3}} \right) \frac{k}{D_{ch}} \tag{5.42}$$

The liquid-only and vapor-only Reynolds numbers were calculated as follows:

$$Re_{lo} = \frac{G \cdot D_{ch}}{\mu_l} \tag{5.43}$$

$$Re_{\mathrm{vo}} = \frac{G \cdot D_{\mathrm{ch}}}{\mu_{\mathrm{v}}} \tag{5.44}$$

For the sample point, these Reynolds numbers were 192.4 and 3033, respectively, which result in average convective coefficients of 1011 W m^{-2} K^{-1} and 192.0 W m^{-2} K^{-1}, respectively. The enhancement factor (*F*) and confinement number (*Co*) were defined by them as follows:

$$F = 1 + 80 \cdot \mathrm{e}^{(-0.6 \cdot Co)} \left(\bar{x}^2 - \bar{x}^6 \right) \tag{5.45}$$

$$Co = \left(\frac{\sigma}{g \left(\rho_{\mathrm{l}} - \rho_{\mathrm{v}} \right) D_{\mathrm{ch}}^2} \right)^{1/2} \tag{5.46}$$

Using the representative data point in Table 5-6, at a mass flux of 120 kg m^{-2} s^{-1}, average quality of 0.008, and a battery height of 153 mm, the convective heat transfer coefficient and enhancement factor were 1005 W m^{-2} K^{-1} and 1.001, respectively, for a confinement number of 2.7. The nucleate boiling heat transfer coefficient was calculated as follows for an unknown surface roughness (Cooper, 1984):

$$h_{\mathrm{NB}} = 55 \cdot P_r^{0.12} \cdot \left(-\log_{10} P_r \right)^{-0.55} \cdot M^{-0.5} \cdot \left(\dot{Q}'' \right)^{0.67} \tag{5.47}$$

For the example data point, the heat flux (113.8 W m^{-2}) was the volumetric heat rate (400 W L^{-1}) multiplied by the unit cell thickness (284 μm). The nucleate boiling heat transfer in this case was 122.3 W m^{-2} K^{-1}, which was moderated at high qualities by a suppression factor equal to $1 - x$. Therefore, the total heat transfer coefficient calculated from Equation 5.40 was 1128 W m^{-2} K^{-1}.

Figure 5.14 shows the instantaneous volumetric heat generation rate as a function of time using the electrochemical model described in Section 5.2.1 and the power

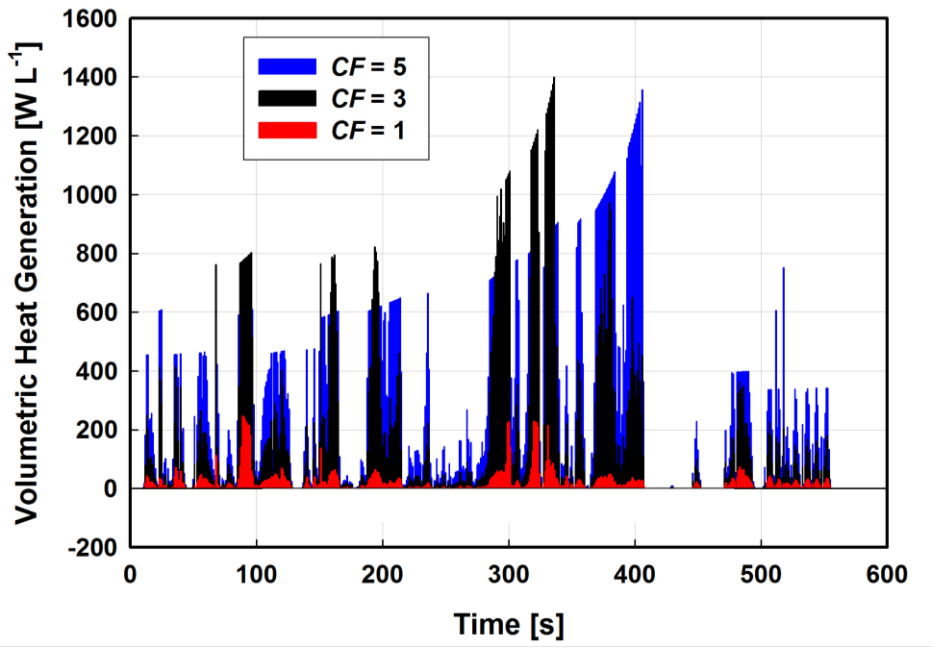

Figure 5.14: Instantaneous Volumetric Heat Generation

simulation inputs shown in Figure 5.8 for compactness factors of 1, 3, and 5 at a temperature of 24°C. The maximum expected heat generation rate was ~1400 W L^{-1}. The shift in the peak as the compactness factor increased is due to the different normalized *DOD*s utilized at different compactness factors (Table 5-5). For example, the peak heat rate for *CF* = 3 occurs at 336 s, where it is discharged at 208 W at a *DOD* of 0.571. In contrast, at this same time, but for a power of 205 W, the *DOD* was lower (0.458) for *CF* = 5, which resulted in a lower heat rate. The predicted two-phase heat transfer coefficients using the average qualities for both assumed condenser-to-evaporator distances are shown in Figure 5.15 for battery volumetric heat rates up to 1500 W L^{-1}. As shown in the figure, there was very little influence of ΔH on the heat transfer coefficient over this range. Therefore, the following curve fit based on the average quality and negligible height between the condenser and the evaporator (ΔH = 0.153) was used to calculate the instantaneous local two-phase heat transfer coefficient in

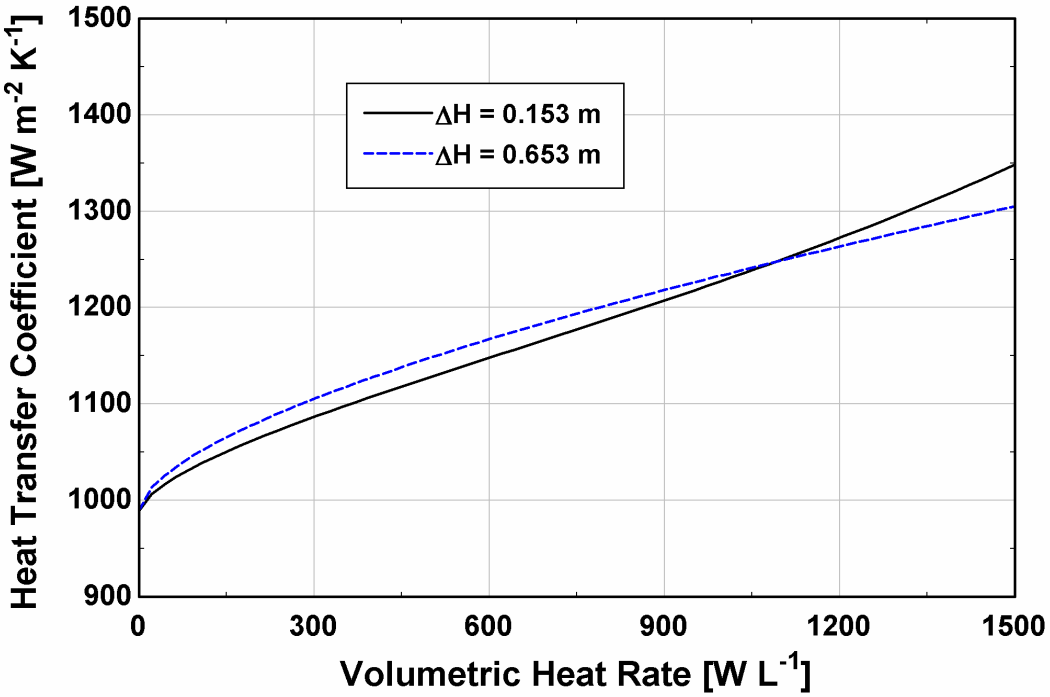

Figure 5.15: Average Evaporator Heat Transfer Coefficient for Two Condenser to Evaporator Heights

the battery model:

$$h_{tp,e} = 1009.2 + 0.3335 \cdot \left|\dot{Q}'''\right|^{0.9425} \tag{5.48}$$

The absolute value of the volumetric heat generation rate was used for instances when the heat generation rate was negative. This rarely occurred, and had a minimal impact on the results due to their small magnitudes (less than -0.34 W L^{-1} for all simulated points at 24°C).

Because the cooling channels do not cover the entire surface of the unit cell, the effective heat transfer coefficient applied to the surface of the battery was less than two-phase heat transfer coefficient (Figure 5.16). The effective heat transfer coefficient

applied to the surface was calculated as follows:

$$h_{\mathrm{e,eff}} = h_{\mathrm{tp,e}} \frac{\eta_{\mathrm{fin}} \left(N_{\mathrm{pitch}} - W_{\mathrm{ch}} \right) + W_{\mathrm{ch}}}{N_{\mathrm{pitch}}} \tag{5.49}$$

The cooling sheet was assumed to be fabricated from a low thermal and electrical conductivity material that isolated it from the cell. Therefore, the effective thermal conductivity and thickness of the uncovered surface between adjacent channels (*i.e.*, the "fins") was assumed to be the same as the parallel thermal conductivity and thickness of the unit cell (80.3 W m^{-1} K^{-1} and 284 μm), with a fin efficiency calculated as follows:

$$\eta_{\mathrm{fin}} = \frac{\tanh\left[\sqrt{\frac{2H_{\mathrm{e,eff}}}{k_{\parallel} t_{\mathrm{unit\ cell}}}} \frac{\left(N_{\mathrm{pitch}} - W_{\mathrm{ch}} \right)}{2} \right]}{\sqrt{\frac{2H_{\mathrm{e,eff}}}{k_{\parallel} t_{\mathrm{unit\ cell}}}} \frac{\left(N_{\mathrm{pitch}} - W_{\mathrm{ch}} \right)}{2}} \tag{5.50}$$

For the sample data point using the heat transfer coefficient calculated from Equation 5.48 (1103 W m^{-2} K^{-1}), the fin efficiency was 0.733, resulting in an effective heat transfer coefficient of 900 W m^{-2} K^{-1}.

Equations 5.48 through 5.50 constitute the parameterized thermal-hydraulic model that was used in a coupled manner with the electrochemical model. This model assumes that the both the battery surface temperature and volumetric heat generation rate are uniform. This was shown to be the case for the internal cooling system, which exhibited minimal temperature rise and difference in the battery even when collection tabs were simulated.

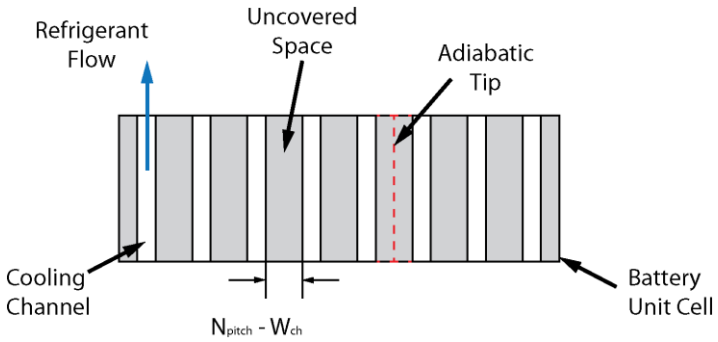

Figure 5.16: Internal Cooling Channel Effective Heat Transfer Conductance Estimation

5.4. Results and Discussion

The model described in this chapter enables coupling of the electrochemical-thermal interaction and current collection within a battery subjected to a dynamic load. As a result, different thermal management strategies can be assessed in a real application. In this section, significant results from the simulations outlined in Table 5-5 are discussed. To show that these solutions are independent of the grid size, a grid sensitivity analysis was conducted first for a sample constant power simulation using the same time-stepping procedure and tolerance settings as were used for the HEV simulations. Thereafter, the results from the external cooling (air, liquid, and edge cooling) simulations are presented. Specific attention is paid to the influence of cell size and compactness factor on performance. These simulations also highlight the performance limitations of external cooling techniques. Finally, the results from the coupled thermal-hydraulic and electrochemical-thermal cell model as a function of compactness factor show that the thermal management system with passive internal cooling can lead to smaller battery packs than for thermally limited externally cooled systems.

5.4.1. Grid Sensitivity Analysis

To verify that the solution was independent of meshing, comparisons were made between two different grid sizes for a constant power boundary condition (150 W and 375 W for the 8 Ah and 20 Ah cells, respectively). Four different combinations that exhibited the largest possible temperature difference were investigated: liquid cooled 8 Ah and 20 Ah cells, and a bottom edge cooled 8 Ah cell with tabs, and another bottom edge cooled 8 Ah cell case with ideal current collection. For the liquid cooled battery, the coarse grid was generated using the "extremely fine" (maximum element size of 0.848 mm) default setting for the automatic triangular mesh generator in COMSOL (2010). The second mesh was generated with the same setting, except that the maximum element size was limited to 317 μm, which increased the number of elements (*e.g.,* from 1.863×10^4 to 4.154×10^4 elements for the 8 Ah battery) and increased the required solution time by a factor of 24, or from 2.86 hours to 68.4 hours, for the liquid-cooled 8 Ah cell. For the edge-cooled battery, different mesh sizes were utilized for the tabs and the remainder of the cell. For the coarse mesh, both the tab and the remainder were meshed using the same extremely fine setting, but with a maximum element size of only 1 mm for the tab (vs. 23.1 mm for the remainder). The fine grid was generated using the same base setting, but with maximum elements sizes of 0.5 mm and 10 mm for the tab and the remainder, respectively.

The solutions generated from the two different meshes were nearly identical in all cases, and the results for the two cases with largest temperature difference are discussed here. For example, Figure 5.17 shows temperature and *DOD* cross sections for the 20 Ah cell after 270 s of discharge when liquid cooled. It can be seen that the magnitude of the maximum temperature difference and *DOD* difference were identical (10.6 K and 0.042,

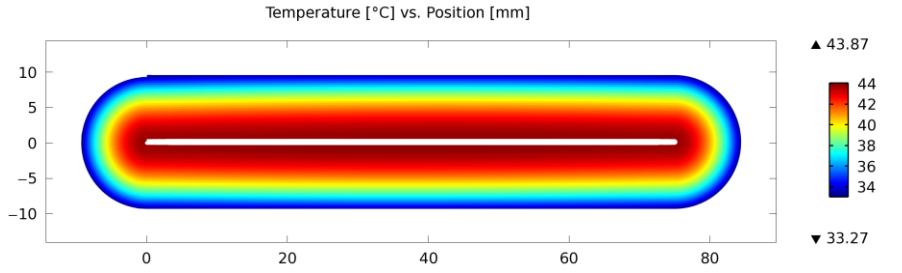

(a)

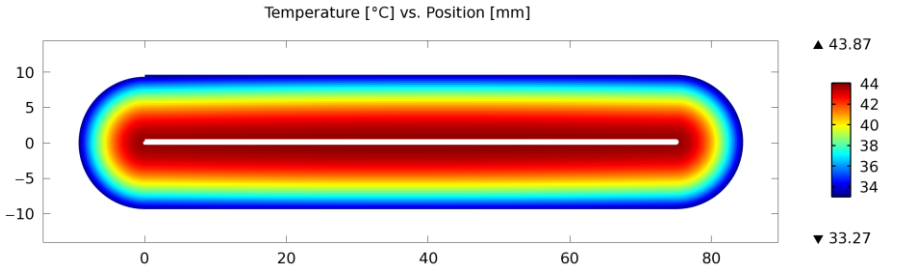

(b)

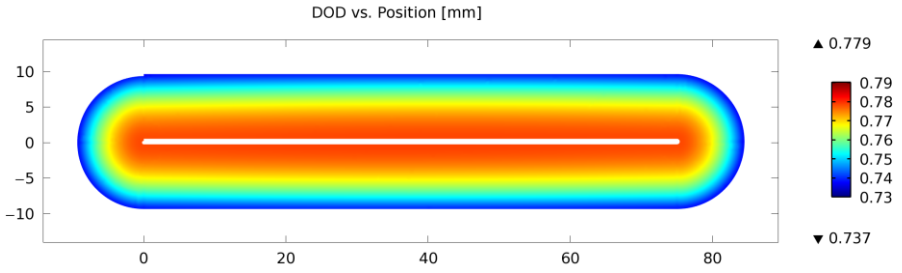

(c)

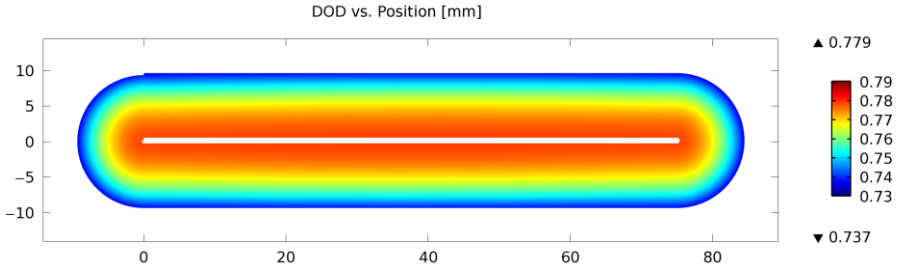

(d)

Figure 5.17: Effect of Grid Size on Temperature and *DOD* after 270 s Discharge of a Liquid-Cooled 20 Ah Cell: (a) *T*, coarse, (b) *DOD*, coarse, (a) *T*, fine, (b) *DOD*, fine

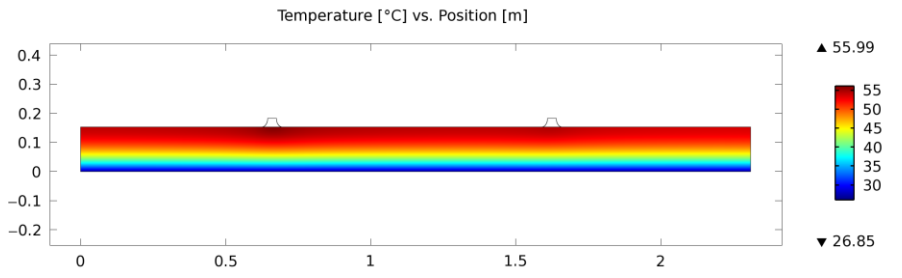

(a)

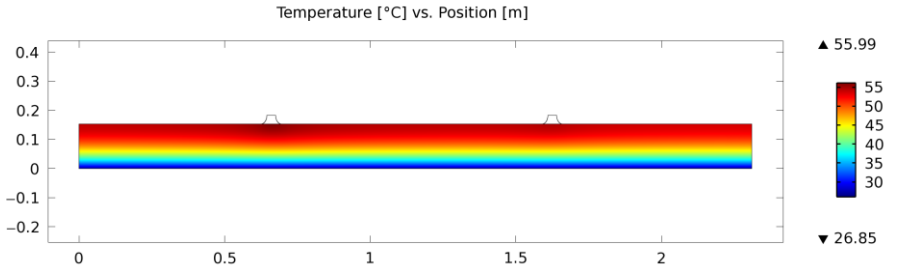

(b)

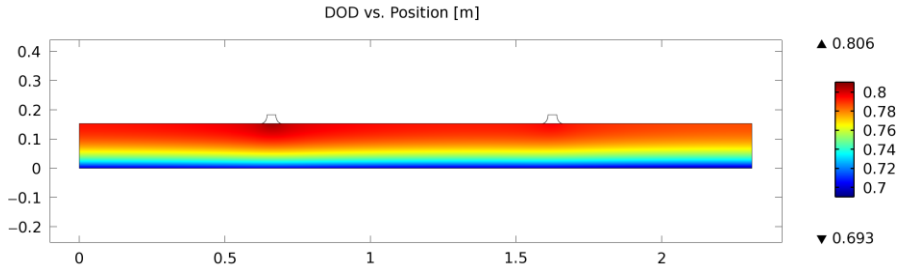

(c)

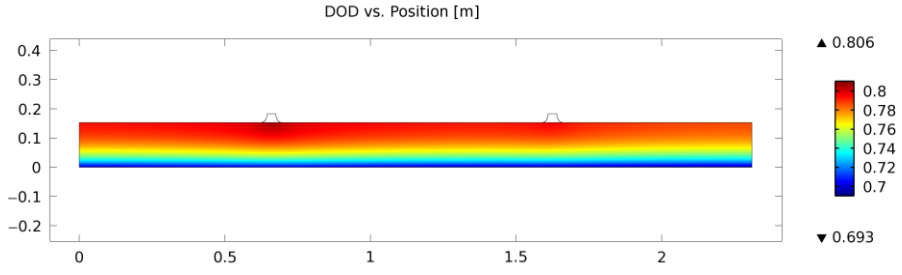

(d)

Figure 5.18: Effect of Grid Size on Temperature and *DOD* after 270 s Discharge of an Edge-Cooled 8 Ah Cell with Tabs: (a) *T*, coarse, (b) *DOD*, coarse, (a) *T*, fine, (b) *DOD*, fine

respectively) for both grid sizes. Furthermore, the graphs show identical spatial distributions, with the hotter and more discharged cells near the center of the battery. Similar results were obtained for the bottom edge-cooled 8 Ah cell with tabs (Figure 5.18), where the coarse grid solved faster by a factor of 3.1 (10.7 hours vs. 33.3 hours). Based on these results, the coarse grid was used for all solutions presented below.

In all grid sensitivity cases, the relative error between the calculated and prescribed power was calculated as follows:

$$Power_{\text{error}} = \frac{I_{\text{calc}} \cdot V_{\text{calc}} - Power}{Power} \tag{5.51}$$

The maximum relative error for the liquid cooled 20 Ah battery in the grid sensitivity study was -8.05×10^{-8}. In contrast, the maximum relative error for the 8 Ah air cooled battery 408 s into the cycle at $CF = 5$ was 0.41. At this point in the cycle, the prescribed discharge power boundary condition changed rapidly from 140.8 W at 407 s to 2.807 W at 408 s. Similar short duration errors with lower magnitudes occur for all other simulations. However, the cumulative impact of these errors on the simulation was minimal. The integrated relative errors for the two-dimensional and quasi three-dimensional simulations were calculated at follows:

$$Power_{\text{error,cumulative}} = \frac{\int \left(V \cdot H_{\text{cell}} \cdot \int i''' dA_{\text{c,cell}} \right) dt - \int \left(Power \right) dt}{\int \left(Power \right) dt} \tag{5.52}$$

$$Power_{\text{error,cumulative}} = \frac{\int \left(V_{\text{tab}} \cdot t_{\text{unit cell}} \cdot \int i''' dA_{\text{cc}} \right) dt - \int \left(Power \right) dt}{\int \left(Power \right) dt} \tag{5.53}$$

For the quasi-three dimensional simulations, the volume-integrated current was used

instead of the integrated current at the tab (Equation 5.38) because it resulted in the maximum error. The maximum cumulative errors for all simulations for the two-dimensional and quasi-three-dimensional domains, respectively, were 7.04×10^{-4} and -4.32×10^{-4}. Therefore, calculated error at instantaneous time steps has minimal impact on the results.

5.4.2. External Cooling Simulations

Figures 5.19 through 5.30 summarize the simulation results for all external cooling simulations. The maximum and minimum temperatures of the unit cell of the 8 Ah cell for a compactness factor of 1 are shown in Figure 5.19 for air, liquid, bottom edge, and top edge cooling. It can be seen that cooling at the bottom edge produced the peak maximum temperature, which occurred near the current collection tabs. For example, after 403 s of operation, Figure 5.20 shows that the hottest portions of the

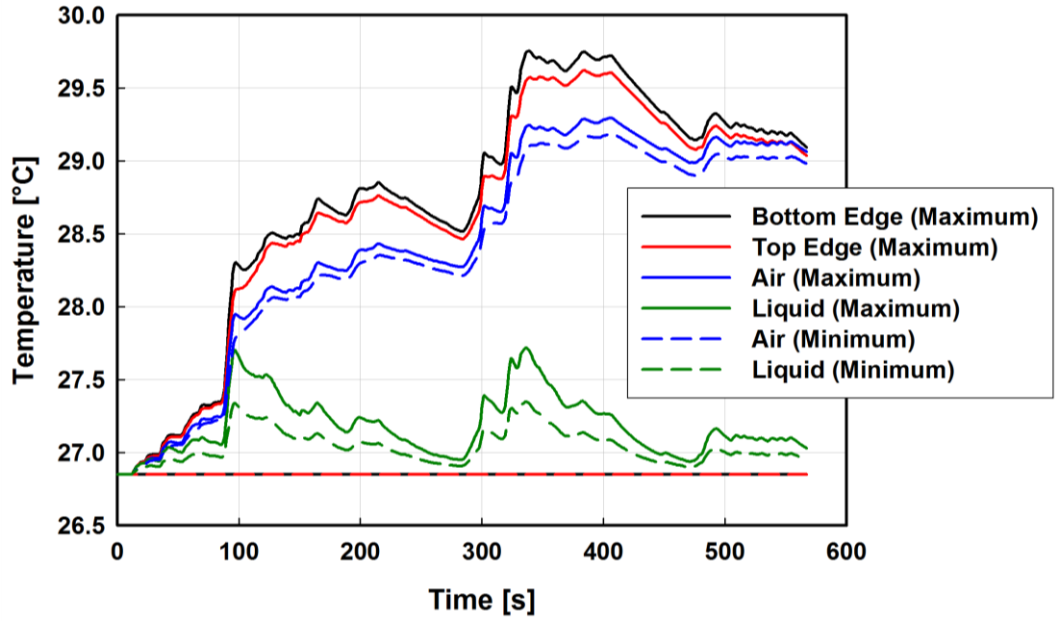

Figure 5.19: Minimum and Maximum Temperatures for External Cooling Strategies at *CF* = 1 for the 8 Ah Cell

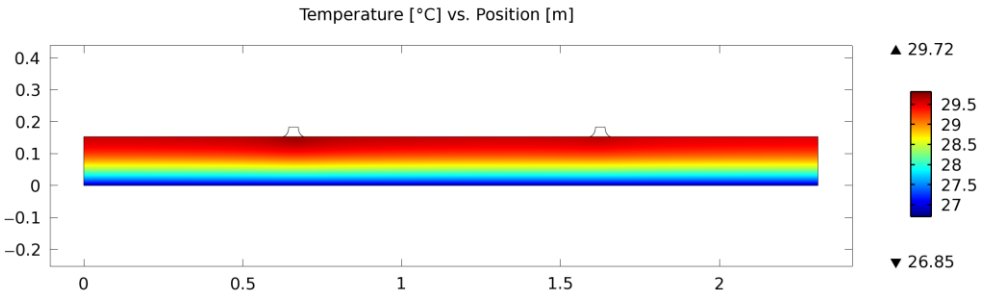

(a)

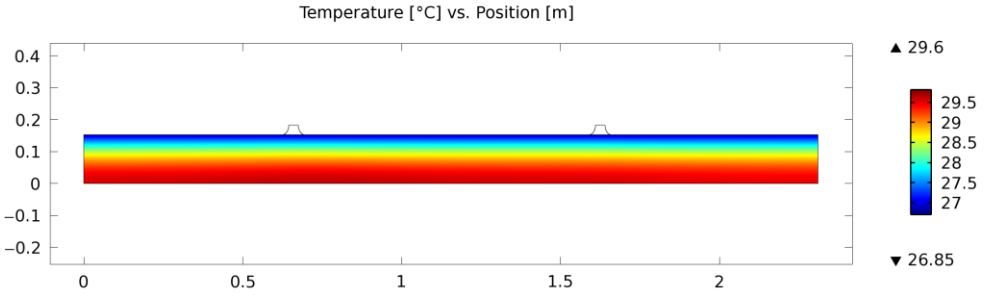

(b)

Figure 5.20: Temperature Contours after 403 s of Cycle Time for Different Edge Cooling Strategies (*CF* = 1) for the 8 Ah Cell: (a) Bottom and (b) Top

battery for edge cooling of the 8 Ah cell were concentrated near the positive tab. Cooling the top edge instead of the bottom edge reduces the peak temperature, but not significantly. For example, after the same duration of discharge, the peak temperature for top-edge cooling was reduced to 29.6°C, a mere 0.12 K lower than bottom-edge cooling. The peak temperature for air cooling was slightly lower throughout the duration of the cycle (29.30°C), but the maximum temperature difference was minimal (*i.e.*, a maximum of 0.20 K) due to the low surface convection. In contrast, the peak temperature of the liquid cooled battery was the lowest (27.72°C), but the maximum temperature difference was slightly larger than that for air cooling. For air and liquid cooling, the maximum temperature and temperature difference was higher for the 20 Ah cell than for the 8 Ah cell. For example, as shown in Figure 5.21, the peak temperature for the air cooled 20

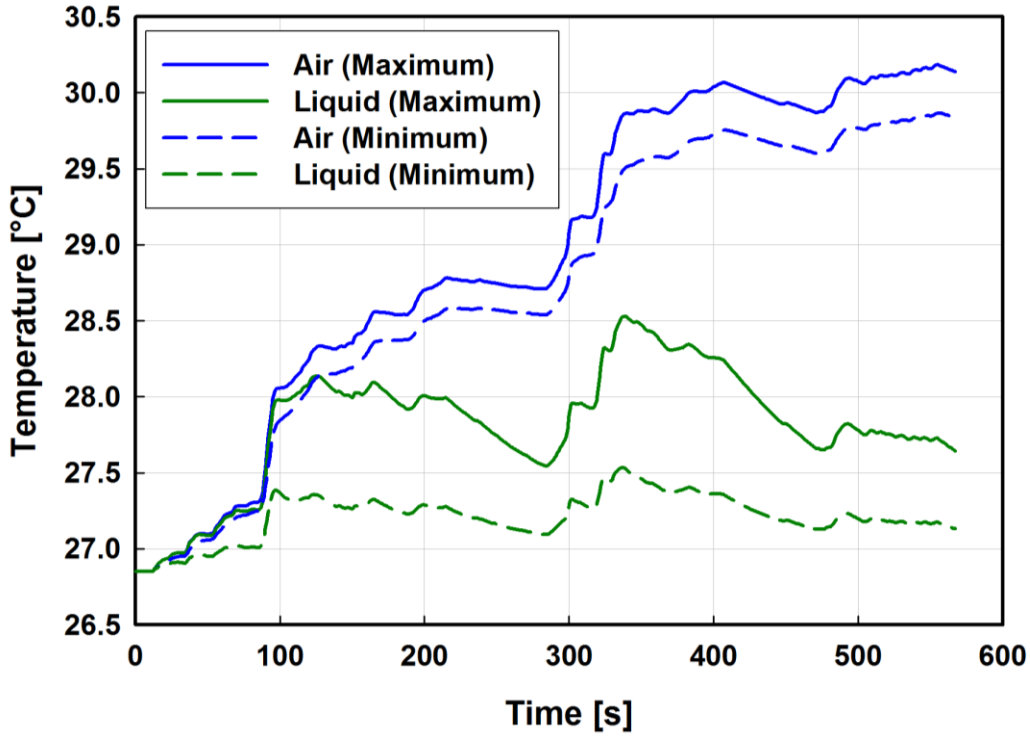

Figure 5.21: Minimum and Maximum Temperatures for Selected External Cooling Strategies at *CF* = 1 for the 20 Ah Cell

Ah battery near the end of the cycle was 30.18°C. The maximum temperature difference for this battery increased to 0.37 K due to the larger thermal resistance experienced for the interior portions of the cell. Similarly, the peak temperature of the liquid cooled battery was 28.53°C, while the maximum temperature difference increased to 1.02°C.

The larger maximum temperature differences for edge cooling lead to non-uniform rates of discharge and charge. Figures 5.22 and 5.23 show the local overpotential and current generation rate at a cycle time of 403 s, which correspond to a required discharge power of 50.5 W, for the top and bottom edge cooled cells, respectively. As shown in these figures, the local temperature has a much greater influence on the current generation than the local overpotential for either edge cooling case. For example, the local overpotentials at positions 1 and 2 in Figure 5.22 were

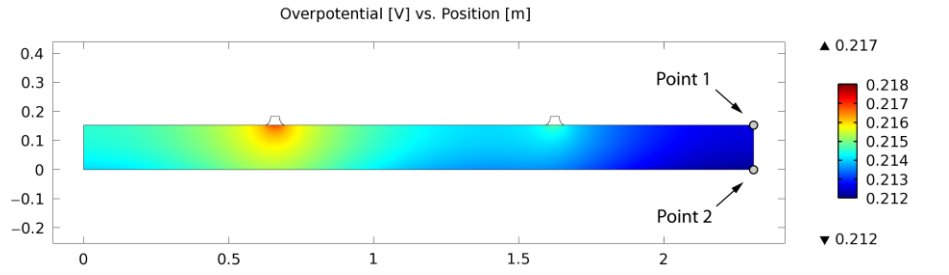

(a)

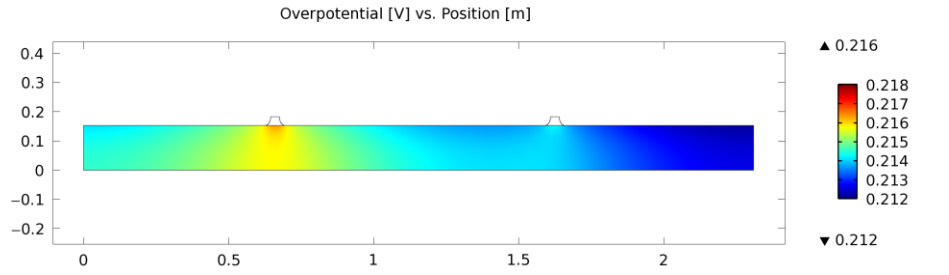

(b)

Figure 5.22: Overpotential Contours after 403 s of Cycle Time for Different Edge Cooling Strategies (*CF* = 1) for the 8 Ah Cell: (a) Bottom and (b) Top

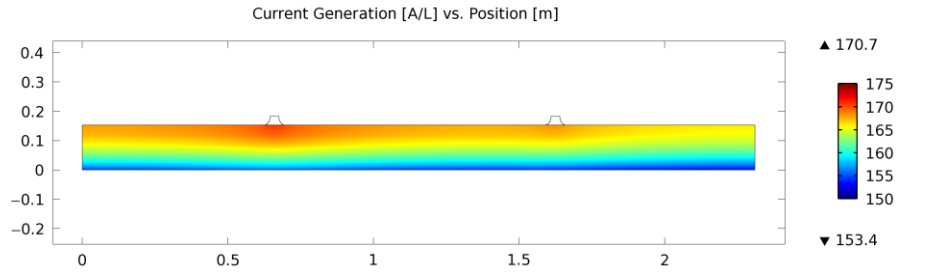

(a)

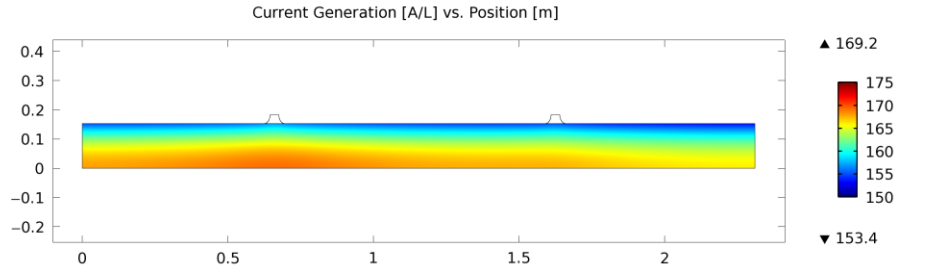

(b)

Figure 5.23: Current Generation Contours after 403 s of Cycle Time for Different Edge Cooling Strategies (*CF* = 1) for the 8 Ah Cell: (a) Bottom and (b) Top

nearly the same (0.2126 V and 0.2121 V, respectively) for bottom edge cooling, but the temperatures (29.48°C and 26.85°C, respectively) and current generation rates (165.9 A L^{-1} and 153.4 A L^{-1}, respectively) were substantially different. Similarly, at these same two locations, the local overpotentials, temperatures, and current generation rates were 0.2122 V and 0.2126 V, 26.85°C and 29.48°C, and 153.4 A L^{-1} and 165.9 A L^{-1}, respectively, for top edge cooling. As a result of this current generation difference, the cells develop a non-uniform *DOD* across the battery that was primarily driven by the difference in temperature. For example, as shown in Figure 5.24, the maximum differences in normalized *DOD* were 0.009 and 0.008 for bottom and top edge cooling, respectively. These were significant because, for example, the changes in *DOD*s from the beginning to the end of this cycle for point 1 were only 0.072 and 0.068 for these two cooling conditions, respectively. Furthermore, these differences in *DOD* after 1 cycle can continue to increase as the battery is subjected to multiple drive cycles. Figures 5.24 and 5.25 show the maximum differences in normalized *DOD* for air and liquid cooling of the 8 Ah and 20 Ah cells, respectively. These differences are substantially smaller than those for edge cooling, with neither producing substantial differences in *DOD* due to their nominally uniform temperature. For example, the 20 Ah liquid cooled cell had maximum temperature and *DOD* differences of 1.016 K and 0.002, respectively. However, it is when the compactness factor is increased in the interest of obtaining small battery packs that these differences assume considerable significance, as discussed below.

The peak temperature rise, maximum temperature difference, and non-uniformity of *DOD* versus the compactness factor are shown in Figures 5.26, 5.27, and 5.28, respectively, for the 8 Ah and 20 Ah cells. At compactness factors of 1, 3, and 5, the

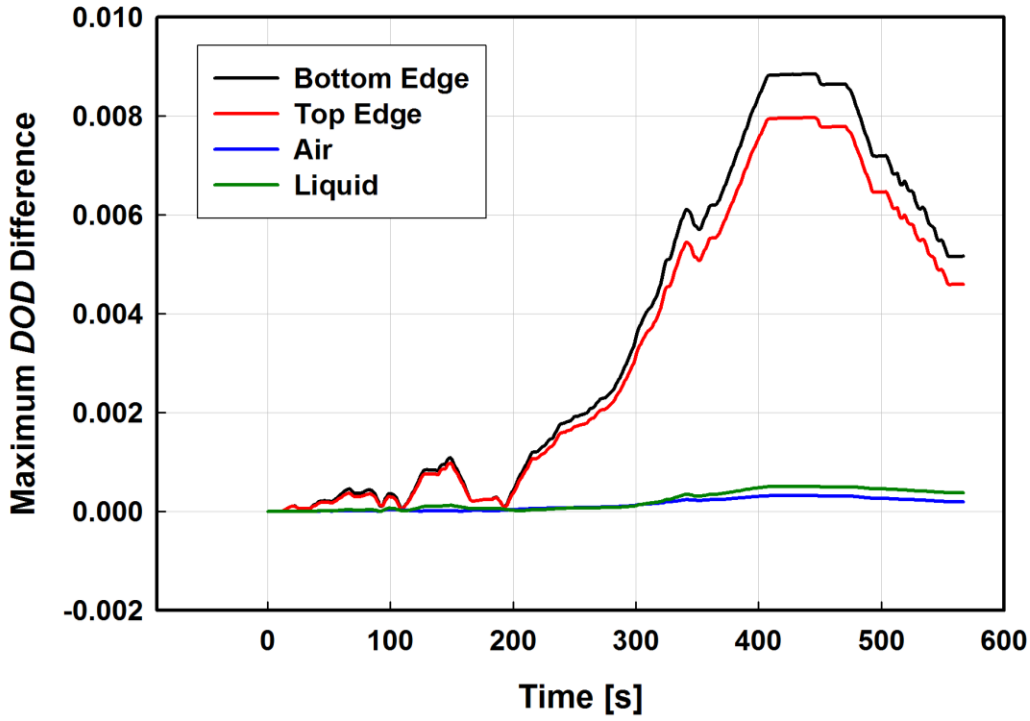

Figure 5.24: Maximum *DOD* Difference for External Cooling Strategies at *CF* = 1 for the 8 Ah Cell

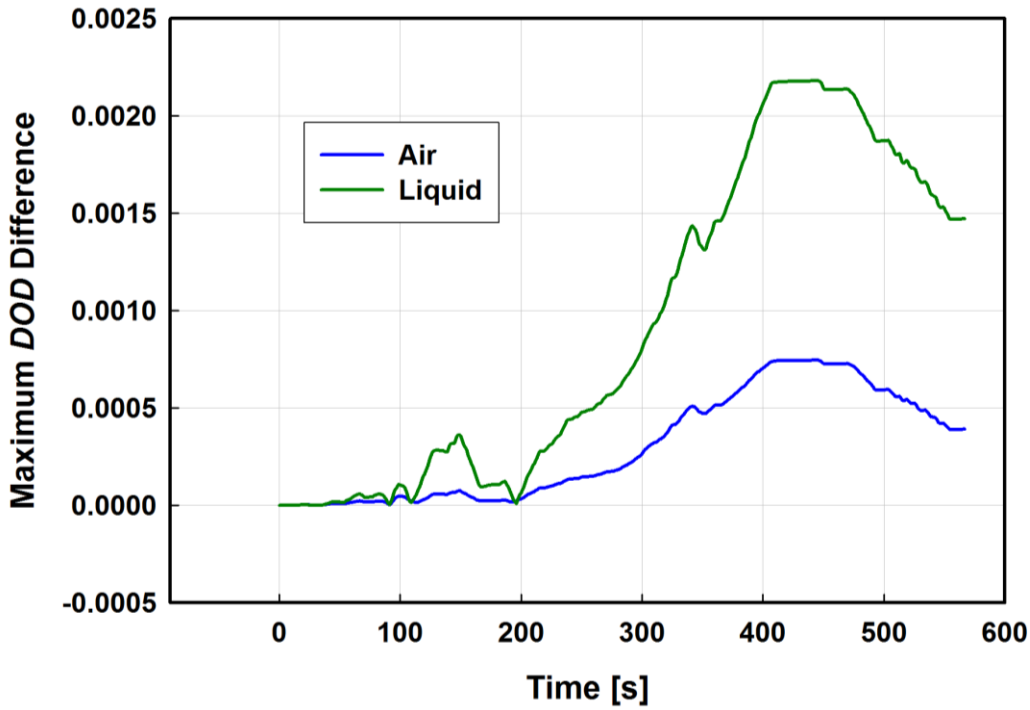

Figure 5.25: Maximum *DOD* Difference for Selected External Cooling Strategies at *CF* = 1 for the 20 Ah Cell

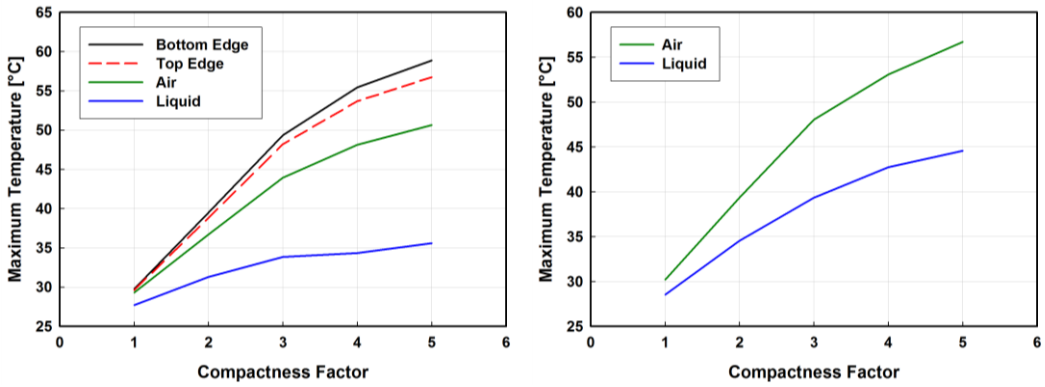

(a) (b)

Figure 5.26: Maximum Temperature versus Compactness Factor for Different Cell Sizes: (a) 8 Ah and (b) 20 Ah

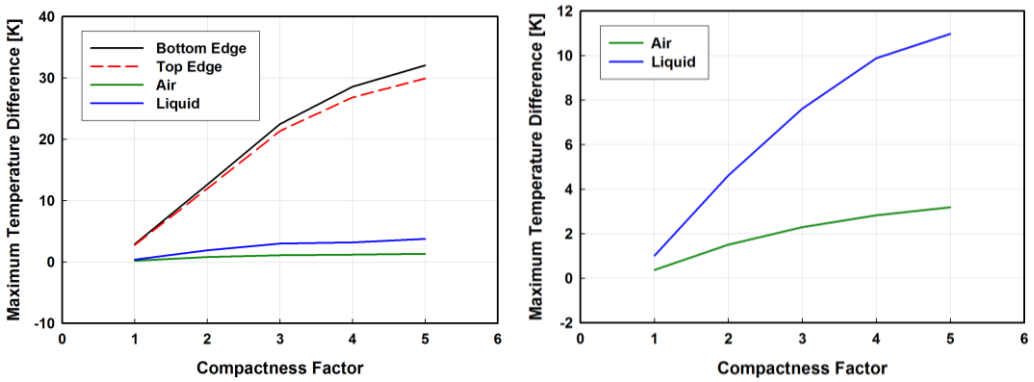

(a) (b)

Figure 5.27: Maximum Temperature Difference versus Compactness Factor for Different Cell Sizes: (a) 8 Ah and (b) 20 Ah

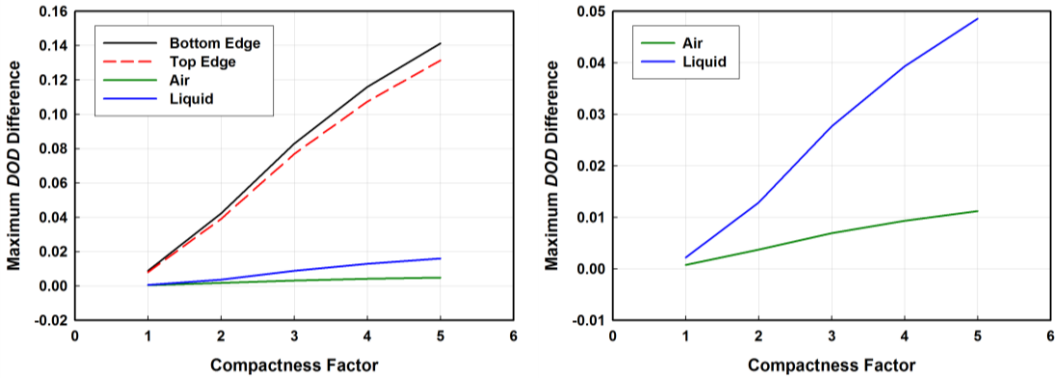

(a) (b)

Figure 5.28: Maximum *DOD* Difference versus Compactness Factor for Different Cell Sizes: (a) 8 Ah and (b) 20 Ah

peak temperatures of the bottom edge cooled cell increased from 29.75°C to 49.32°C to 58.88°C. As a result of the thermally induced maldistribution in current generation, the maximum *DOD* difference increased from 0.009 to 0.083 to 0.141 for these compactness factors. In addition, the maximum *DOD* difference increased much more with increased compactness factor for the 20 Ah liquid cooled cell than for smaller or air cooled cells. For example, the maximum *DOD* difference increased from 0.002 to 0.049 for the liquid cooled 20 Ah cell as the compactness factor increased from 1 to 5, but only from 0.001 to 0.016 for the 8 Ah cell. The air cooled cells also had a maximum difference of only 0.011 for the 20 Ah cell.

In addition to charge imbalance, these increases in temperature and *DOD* non-uniformity can lead to non-uniform cycling of the cell, which could lead to non-uniform rates of aging. For example, as shown in Figures 5.29 and 5.30 for $CF = 3$, the discharge and charge current generation rates varied between 462.6 and 616.2 A L^{-1} and -195.5 and 356.8 A L^{-1}, respectively, for a bottom edge cooled battery at cycle times of 403 s and 449 s, which correspond to required discharge and charge powers of 151.6 W and -102.6 W, respectively. The largest magnitudes of current generation at these cycle times were concentrated near the hottest portion of the cell at the top of the battery. Similarly, these current generation rates varied between 462.9 and 608.6 A L^{-1} and -195.8 and -346.8 A L^{-1}, respectively, for a top edge cooled battery, but with the largest magnitudes concentrated near the bottom of the cell. In addition, the current generation contour plots at these same cycle times are shown in Figures 5.29 and 5.30, respectively, for the liquid cooled 8 Ah and 20 Ah cell, respectively, at the same compactness factor. As shown in these figures, the thermally induced cycling was less for the 8 Ah cell due to its smaller

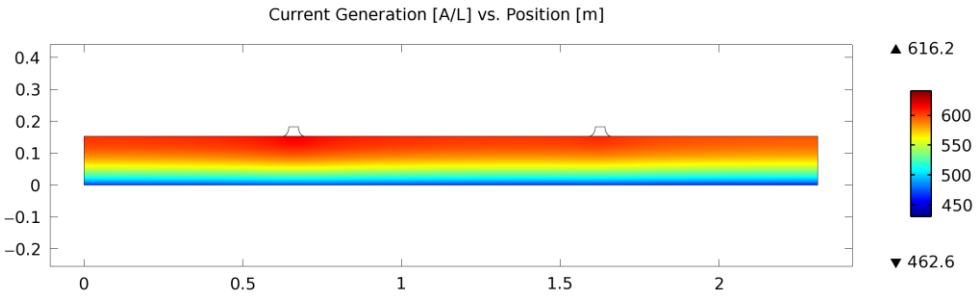

(a)

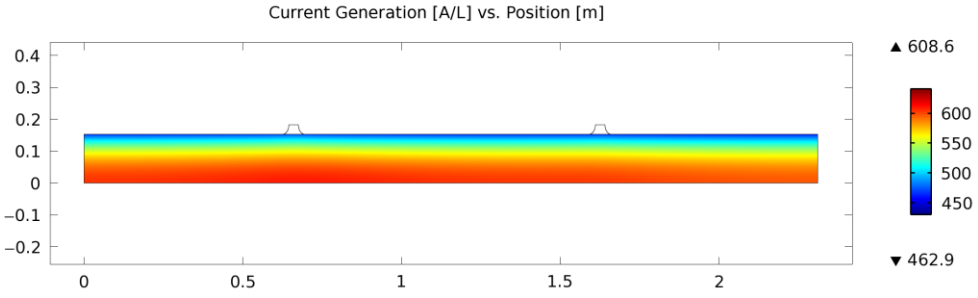

(b)

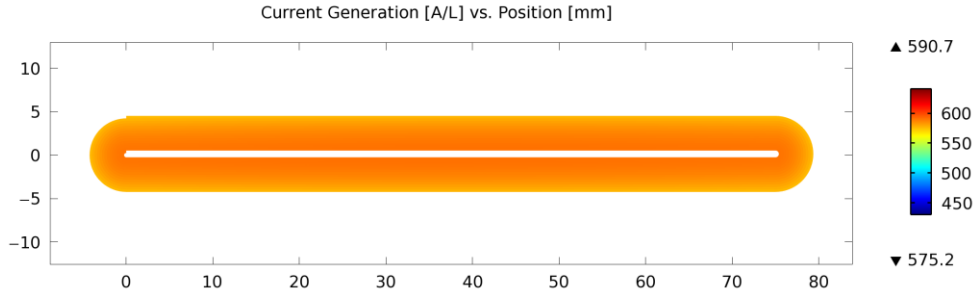

(c)

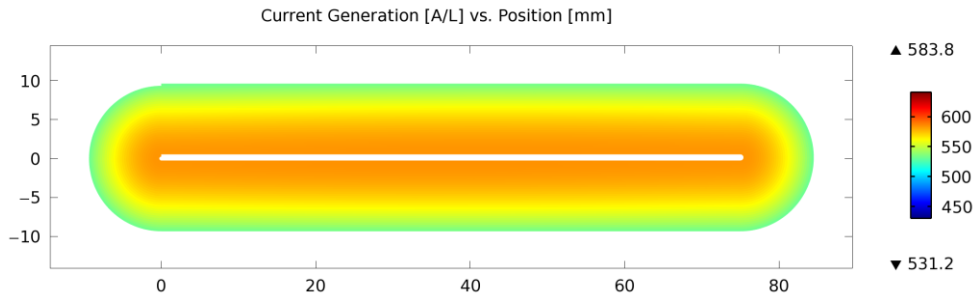

(d)

Figure 5.29: Current Generation Contours after 403 s of Cycle Time for Different Cooling Strategies and Cell Sizes (*CF* = 3): (a) Bottom Edge, 8 Ah, (b) Top Edge, 8 Ah, (c) Liquid, 8 Ah, and (d) Liquid, 20 Ah

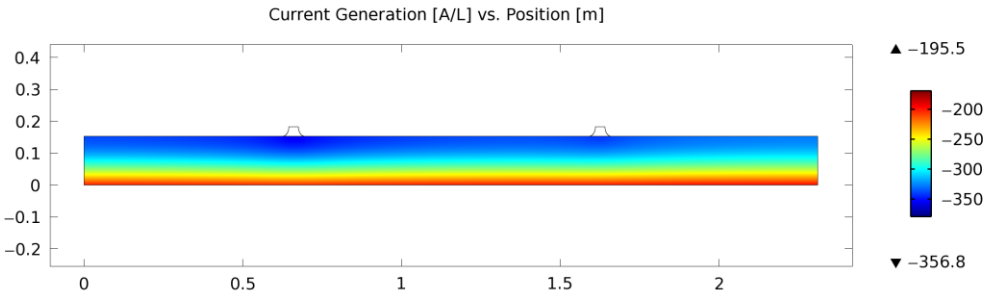

(a)

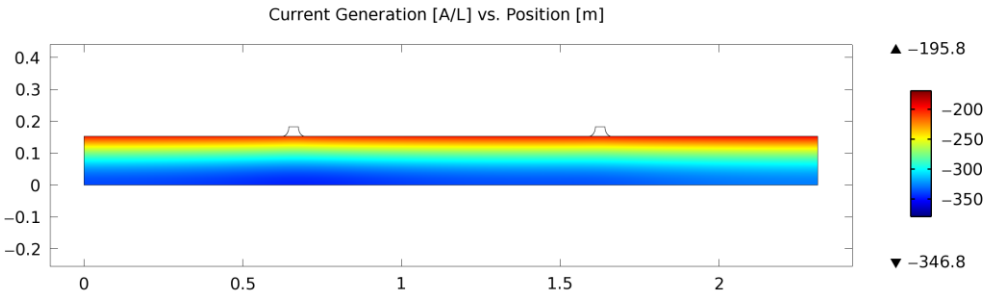

(b)

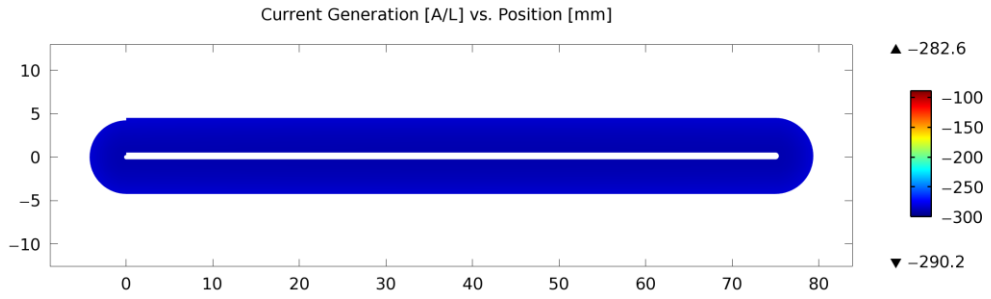

(c)

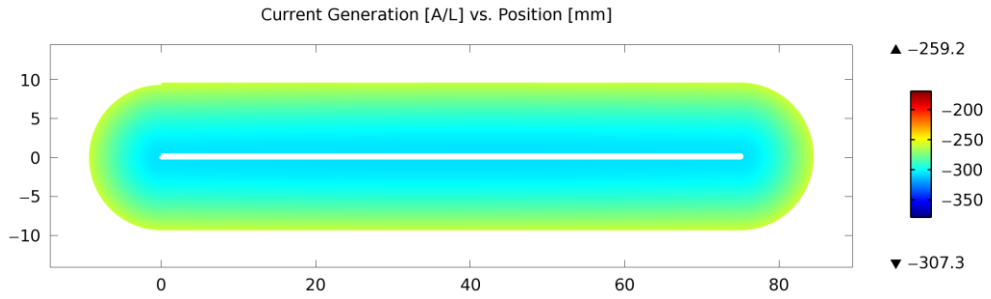

(d)

Figure 5.30: Current Generation Contours after 449 s of Cycle Time for Different Cooling Strategies and Cell Sizes (*CF* = 3): (a) Bottom Edge, 8 Ah, (b) Top Edge, 8 Ah, (c) Liquid, 8 Ah, and (d) Liquid, 20 Ah

temperature difference. For example, the current generation ranged only from 575.5 A L^{-1} to 590.7 A L^{-1} at 403 s for the 8 Ah battery, while it ranged from 531.2 A L^{-1} to 583.8 A L^{-1} at this same time for the 20 Ah battery. Similarly, the current generation ranged from -282.6 A L^{-1} to -290.2 A L^{-1} and from -259.2 A L^{-1} to -307.3 A L^{-1} for these two cells, respectively, at a cycle time of 449 s, leading to the hot center of the 20 Ah cell experiencing increased cycling compared to its edge cells.

The non-uniform cycling experienced in the cell may be offset (or exacerbated) by the existence of a thermal gradient. The open circuit potential changes with temperature, which causes a local potential difference that induces an electrochemical reaction within the cell. This occurs because electrons can flow in the current collectors between cell locations while lithium ions can migrate between these same locations. The following non-dimensional parameter may be used to quantify this driving force for the electrochemical reaction relative to the transport of electrons within the current collector:

$$N_{\text{balance}} = \frac{\Delta U\left(\Delta T\right)}{i'''\left(\Delta U\right)\cdot 2\Delta l_{\text{cc}}^{2}\cdot\left(\frac{1}{\sigma_{+}}+\frac{1}{\sigma_{-}}\right)} \tag{5.54}$$

The numerator is the open circuit potential difference induced between two cell locations that have different temperatures, and the current generation in the denominator is calculated from this potential difference using Equations 5.6 through 5.13. The distance Δl_{cc} is the total length between these two locations along the unit cell, which has positive and negative current collectors of different electrical conductivities. This non-dimensional parameter approximates the ratio of the current movement in the collector to the electrochemical reaction rate induced by the temperature difference in the cell. Therefore, values close to 1 constitute a strong tendency for charge migration in the when

a substantial thermal gradient along the current collector is present. For the side cooled battery investigated in this study, the values are very low due to low thermal gradient in the unit cell direction. For example, the maximum temperature difference observed for the liquid cooled 20 Ah cell at CF = 5 was 11.0 K, which corresponds to a maximum potential difference of 2.27 mV using the maximum observed entropic heat coefficient (0.207 mV K^{-1}). This potential difference will induce a maximum current generation of 1380 A/L at the peak temperature (44.6°C) for DOD = 0.522. Using the unit cell winding length of 5.78 m and the requisite current collector electrical conductivities (3.774×10^7 S m^{-1} and 5.998×10^7 S m^{-1} for aluminum and copper, respectively), the non-dimensional parameter is only 0.0006. In contrast, for the edge cooled cell, the largest temperature difference was 32.0 K across a Δl_{cc} of only 153 mm. Therefore, the non-dimensional parameter is a maximum of 0.671, which means that lithium could migrate due to the presence of a larger thermal gradient (*i.e.*, 209 W m^{-1} for the edge cooled cell versus 1.9 W m^{-1} for the liquid cooled cell). More investigation of this effect in future studies that exhibit large thermal gradients along the unit cell is warranted.

The maximum temperature is a critical parameter for determining the cycle lifetime of batteries. Using 35°C as an upper temperature limit, Figure 5.26 shows that compactness factors above 1 were not feasible for either edge cooling method. Although an 8 Ah air-cooled cell cannot sustain a compactness factor greater than 2, a liquid cooled battery can withstand compactness factors up to 4 for a 35°C limit. However, when the cell sized was increased to 20 Ah, neither the air-cooled nor the liquid-cooled batteries can withstand compactness factors great than 1 or 2, respectively. As shown in the following section, internally cooled batteries overcome these thermal limitations and can

sustain even higher compactness factors due to their improved heat removal capabilities.

5.4.3. Internal Cooling Simulations with Passive Microchannel Phase Change

In this section, the results from the coupling of the thermal-hydraulic model for internal cooling with the electrochemical-thermal model are presented. The two-phase heat transfer coefficient within the evaporator channels was calculated using Equation 5.48. After modification due to fin effects, this was uniformly applied to the surface of the battery, which assumes both little variation in the volumetric heat generation rate across the surface of the cell and minimal impact from heat generation inside the tabs. Figure 5.31 shows the instantaneous cell and tab heat generation rates for an 8 Ah internally cooled cell with a compactness factor of 5 using the following equations:

$$\dot{Q}_{\text{cell}} = t_{\text{unit cell}} \cdot \int \left[\begin{array}{l} i'''\left(U - V - T\dfrac{\partial U}{\partial T} \right) \\ \qquad + \left(\sigma \left| \nabla \phi \right|^2 \right)_{\text{cc,pos}} \dfrac{t_{\text{cc,pos}}}{t_{\text{unit cell}}} + \left(\sigma \left| \nabla \phi \right|^2 \right)_{\text{cc,neg}} \dfrac{t_{\text{cc,neg}}}{t_{\text{unit cell}}} \end{array} \right] dA_{\text{cell}} \tag{5.55}$$

$$\begin{aligned} \dot{Q}_{\text{tab}} = & \int \left[\left(\sigma \left| \nabla \phi \right|^2 \right)_{\text{cc,pos}} \cdot t_{\text{cc,pos}} \right] dA_{\text{tab,pos}} \\ & + \int \left[\left(\sigma \left| \nabla \phi \right|^2 \right)_{\text{cc,neg}} \cdot t_{\text{cc,neg}} \right] dA_{\text{tab,neg}} \end{aligned} \tag{5.56}$$

At this compactness factor, the heat load at the tab was at most 0.68% of the heat rates at 327 s of cycling. The tab heat percentage was smaller than 4.93% for all other time instances for all other compactness factors, except at three time instances when *CF* = 1. At 31 s, 32 s, and 272 s, the total and tab heat rates were 0.432 and 0.127 mW, 0.067 and 0.126 mW, and 0.422 and 0.125 mW, respectively. Although the tab heat is a significant percentage in these cases, the absolute differences were small, and have a minimal impact

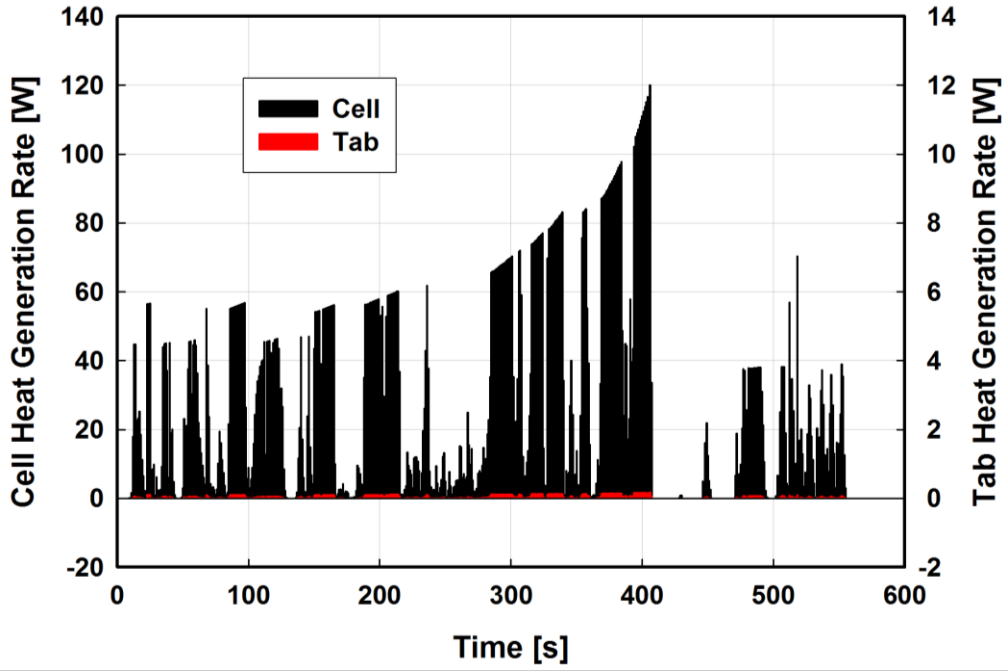

Figure 5.31: Instantaneous Total Cell and Tab Heat for an Internally Cooled 8 Ah Cell at *CF* = 5

on the results. For example, a peak heat rate of 120.0 W occurred at 406 s for *CF* = 5, when the tab heat was only 0.17 W.

Figure 5.32 shows the variation in the local cell heat rate at this time. As shown in this figure, the maximum difference in total cell heat generation was large: from a minimum of 1172 W L^{-1} to a maximum of 1409 W L^{-1}. However, Figure 5.32 also shows that the variation in the effective heat transfer coefficient (Equation 5.49) was only 3.26% of the lowest value (*i.e.*, 1013 W m^{-2} K^{-1} to 1046 W m^{-2} K^{-1}). In addition, for a uniform battery temperature of 26.85°C, Figure 5.33 shows that the instantaneous evaporator outlet vapor quality was always less than 0.16 using the following equation:

$$\dot{Q}_{\text{cell}} + \dot{Q}_{\text{tab}} = \dot{Q}''' \cdot v_{\text{cell}} = \dot{m}_{\text{r}} h_{\text{lv}} \left(x_{\text{r,e,o}} - 0 \right) \tag{5.57}$$

As mentioned in Section 4.5.2, Bertsch *et al.* (2008b) noted that the heat transfer

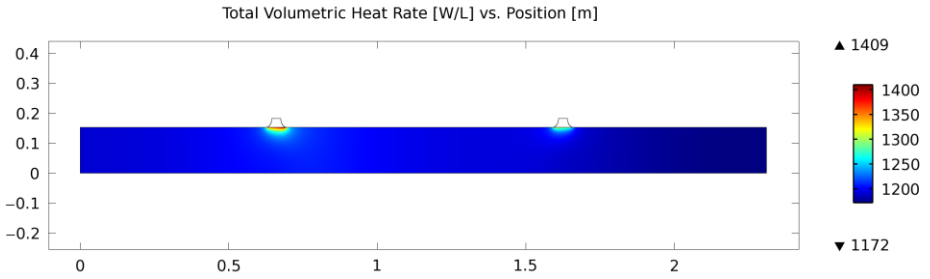

(a)

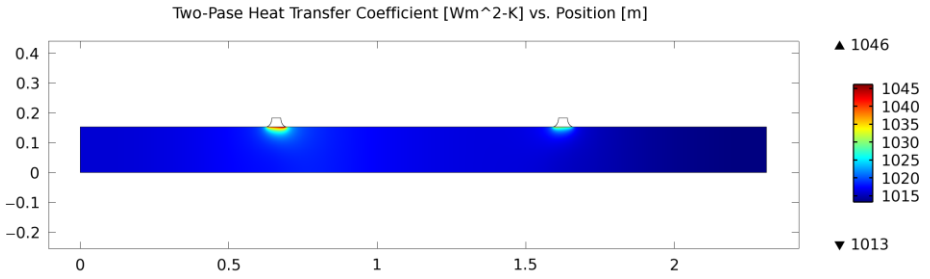

(b)

Figure 5.32: Contour Plots for an Internally Cooled 8 Ah Cell at 406 s (*CF* = 5): (a) Total Volumetric Heat Rate and (b) Local Effective Heat Transfer Coefficient

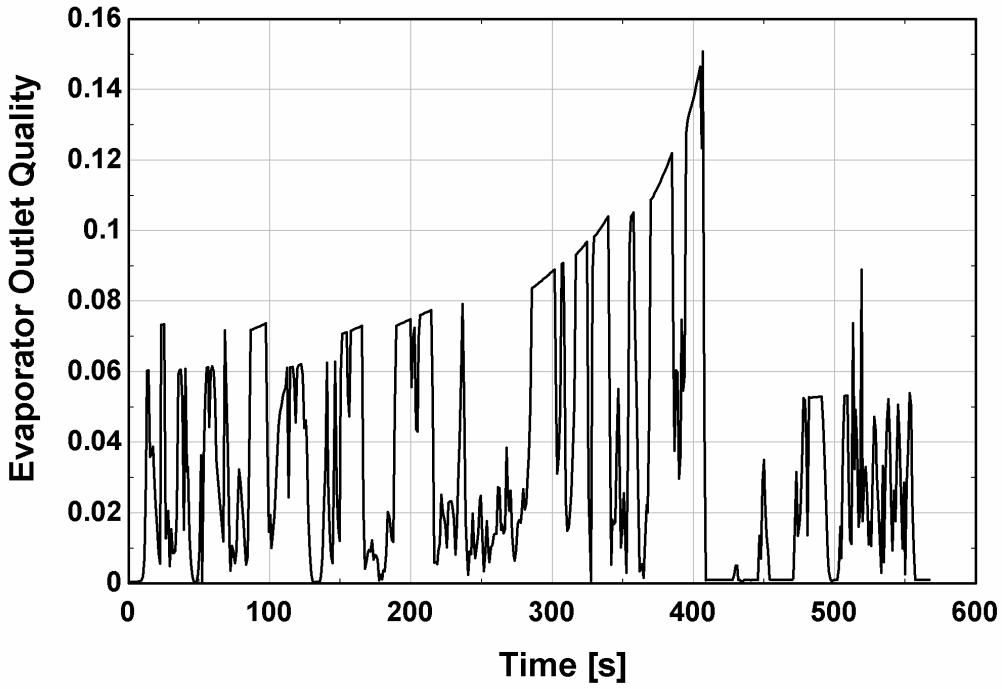

Figure 5.33: Predicted Evaporator Outlet Quality versus Cycle Time for *CF* = 5

coefficient decreases for qualities greater than 0.2. In addition, the experiments

conducted on the representative internal cooling system showed minimal surface temperature differences up to vapor outlet qualities of about 0.2 (Table 4-17). Therefore, because the tab heat was small, and the local variations in heat transfer coefficient and surface temperature are minimal, it was reasonable to couple the battery and simplified internal cooling models by calculating the local heat transfer coefficient based on the local value of volumetric heat generation using Equation 5.48.

Figures 5.34 and 5.35 show the predicted maximum temperature rise and temperature difference observed for the air, liquid, and internal cooling simulations for both cell sizes. It can be seen that there was minimal temperature rise within the internally cooled cell for compactness factors up to 5. As a result, there was minimal differential cycling of the cell. For example, as shown in Figure 5.36, the difference in volumetric current generation was at most 19.1 A L^{-1} and 19.4 A L^{-1} for charge and discharge at 403 s and 449 s, respectively. However, as shown in Figure 5.37, the maximum *DOD* difference for the 8 Ah internally cooled battery with current collection tabs (0.011) was almost the same as it was for external liquid cooling of the same cell (0.016). It should be noted that for the liquid cooled battery, ideal current collection was assumed. To make a consistent comparison with internal cooling, an additional simulation was conducted on the 20 Ah battery with ideal current collection (Figure 5.10), which showed no appreciable *DOD* or temperature difference across the cell. Therefore, the *DOD* difference calculated for the internally cooled 8 Ah battery was attributable primarily to the tab design, and was not thermally induced.

The performance improvement for an internally cooled battery was determined by calculating the total energy extraction density possible for each cooling method. The

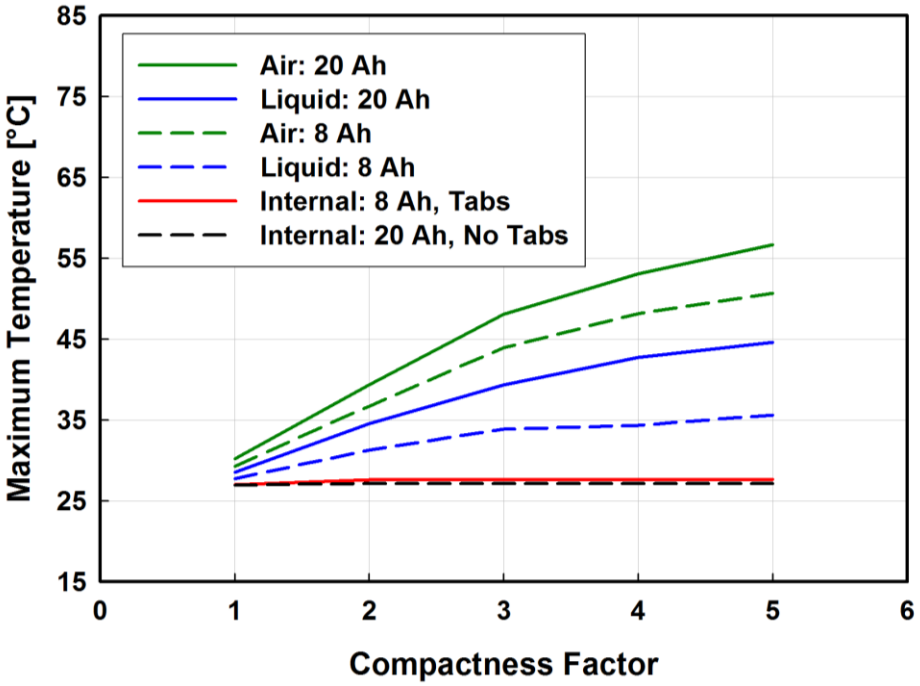

Figure 5.34: Comparison of Internal, Air, and Liquid Cooling Maximum Temperature versus Compactness Factor

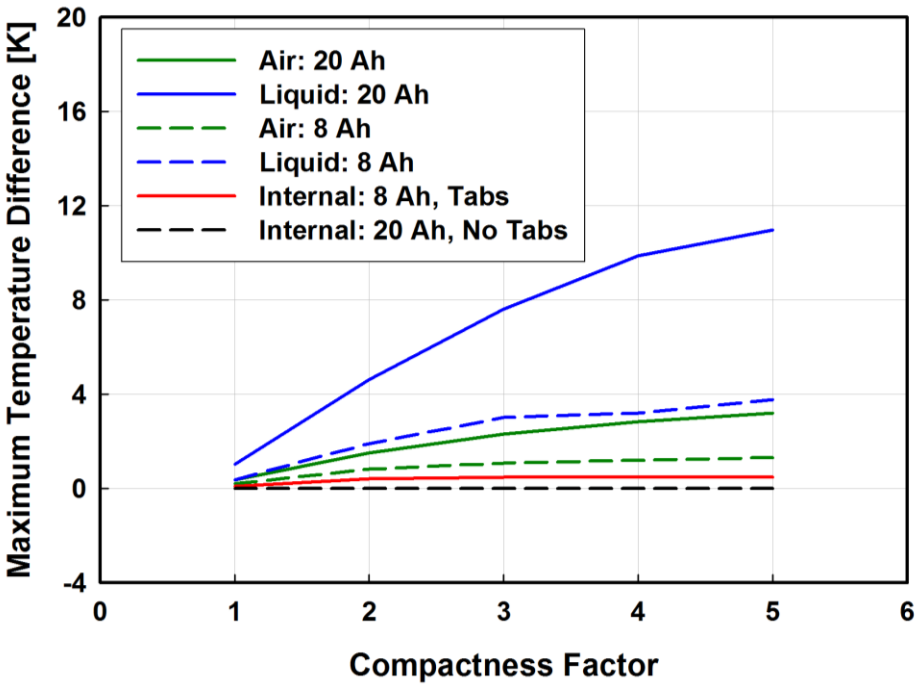

Figure 5.35: Comparison of Internal, Air, and Liquid Cooling Maximum Temperature Difference versus Compactness Factor

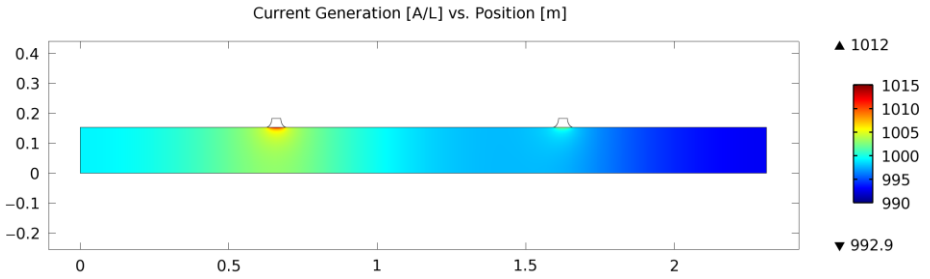

(a)

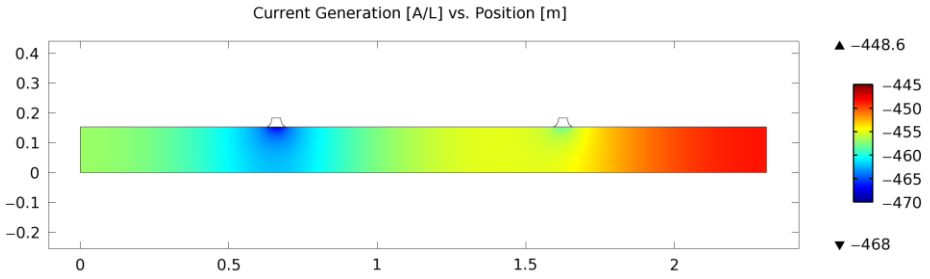

(b)

Figure 5.36: Contour Plots of Local Current Generation for an Internally Cooled 8 Ah Cell at *CF* = 5: (a) 403 s and (b) 449 s

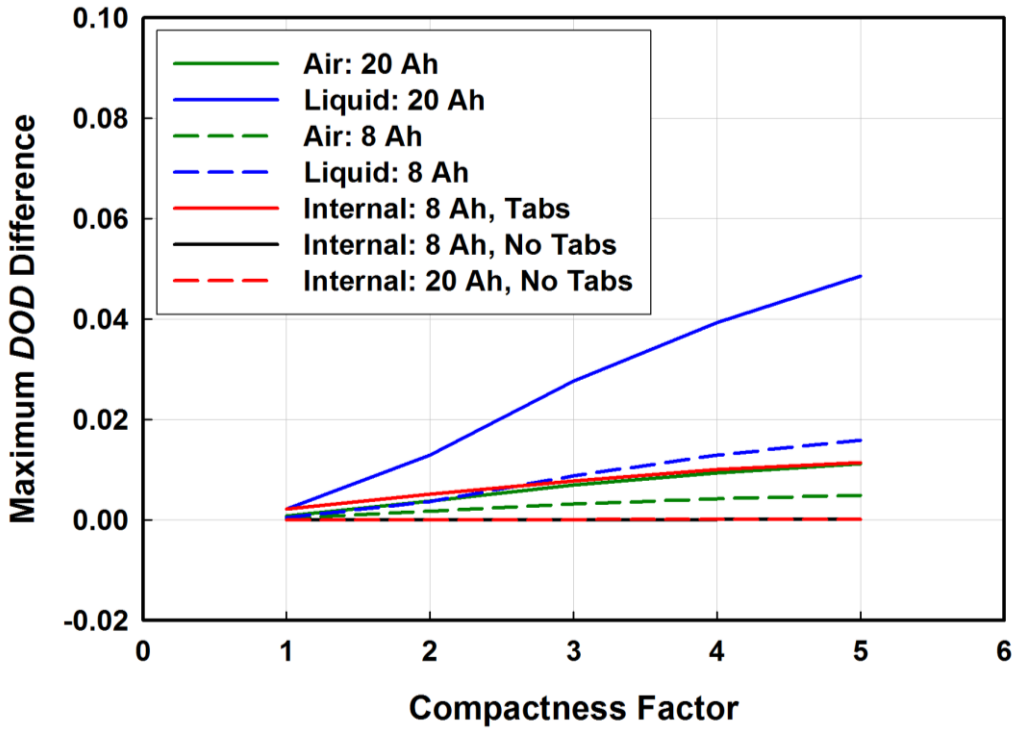

Figure 5.37: Comparison of Internal, Air, and Liquid Cooling Maximum *DOD* Difference versus Compactness Factor

total charge and discharge energy extraction densities were calculated as follows:

$$E'''_{cha} = \frac{\int \left(-Power_{pack,cha}\right) dt}{v_{pack}} \tag{5.58}$$

$$E'''_{dis} = \frac{\int \left(Power_{pack,dis}\right) dt}{v_{pack}} \tag{5.59}$$

For example, the supplied discharge energy to the air-cooled battery for a CF = 2 was 4067 kJ, and its pack volume was 35.3 L, yielding a discharge extraction density of 32.0 Wh L^{-1}. The results for the minimum pack size for an allowable 35°C maximum temperature are summarized in Figure 5.38. For air and liquid cooling, the allowable minimum pack charge and discharge energy extraction densities were 16.8 and 32.0 Wh L^{-1} and 31.3 and 47.04 Wh L^{-1}, respectively, at compactness factors of 2 and 4, respectively, for an 8 Ah cell. In contrast, the internally cooled 20 Ah cell can easily withstand compactness factors of 5, which yields the highest energy density for charge and discharge (40.8 and 61.3 Wh L^{-1}, respectively, 27.5% and 30.3%, respectively, higher than for the liquid cooled pack). The minimum and maximum voltage limits are also shown in Figure 5.38. As shown in Table 5-5, these were set by limiting the peak charge and discharge power corresponding to voltage limits of 1.94 V and 4.16 V for a 24°C cell. As shown in this figure, both the 8 Ah liquid cooled and 20 Ah internally cooled battery have minimum voltages of 2.39 V and 2.16 V, respectively, due to their slightly higher temperatures, which can allow some additional discharge energy extraction. However, the external liquid cooled battery has already reached its thermal limitation of 35°C for CF = 4. Furthermore, the saturation temperature of the internally cooled system can be optimized to balance capacity fade and energy extraction. Therefore, an

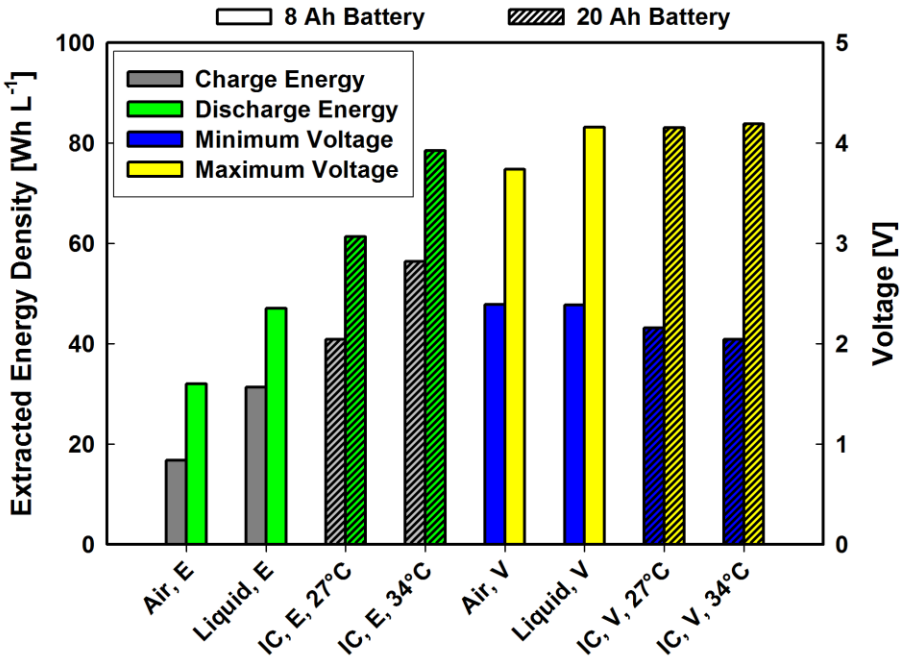

Figure 5.38: Comparison of Discharge and Charge Energy Extraction Densities and Minimum and Maximum Tab Voltages for Largest Pack Size Reduction of each Cooling Method

additional simulation was run for an internally cooled cell without tabs at a 34°C saturation temperature and a compactness factor of 10 with charge and discharge power limits of -240 W and 216 W, respectively. The different thermal properties at this elevated temperature required a new parameterization for the thermal-hydraulic model, which was as follows:

$$h_{\text{tp,e}} = 966.6 + 0.4154 \cdot \left|\dot{Q}'''\right|^{0.9285} \tag{5.60}$$

As shown in Figure 5.38, this optimized system yielded increased charge and discharge energy extraction densities (56.4 Wh L^{-1} and 78.4 Wh L^{-1}, respectively), which were 80.2% and 66.7% improvements over the lowest possible charge and discharge energy extraction densities, respectively, for external cooling.

It is also possible to improve the energy extraction density further for the internal

cooling system by increasing the compactness factor beyond 10. However, due to electrochemical limitations (*i.e.,* 2.0 to 4.2 cell voltage limits), this will not necessarily improve the extraction energy density. One possible remedy for this is to include electrochemical capacitors, which have low energy density but high power density, as buffers between the battery and electric motor. In this system, the power required by the drivetrain can be supplied by capacitors that are continuously charged by the batteries. These capacitors can also absorb power from rapid deceleration before charging the battery pack too. As a result, additional energy could be extracted from the battery. This will increase the thermal load on the pack, for which internal cooling is well suited, but externally cooled batteries are not. Finally, the results presented here assume a channel height of 160 μm, which was 56% of the unit cell thickness. Significant opportunity exists for reducing this channel height, but more fundamental two-phase flow investigations at these small scales are needed to confirm and quantify these potential improvements.

CHAPTER 6. CONCLUSIONS AND RECOMMENDATIONS

The present study is a comprehensive investigation into the coupled electrochemical-thermal transport phenomena in lithium-ion batteries, across the entire range of scales relevant to high energy and power density batteries, *i.e.*, from the particle level electrochemical heat and current generation to the dynamic heat removal and performance at the cell and pack levels. These insights were then used to obtain a comprehensive understanding of the impact of thermal management strategies on large battery and battery pack performance. This work is the first ever study of the coupled electrochemical-thermal phenomena in batteries, from the particle level electrochemical heat generation all the way to the dynamic heat removal in actual HEV drive cycles. The computationally intensive electrochemical-thermal interaction was modeled using battery performance data obtained from a commercially available battery. To address the large internal thermal gradients identified from the electrochemical-thermal modeling, an innovative internal cooling system that utilized passive microchannel liquid-vapor phase change was developed. The performance of this innovative passive cooling system was validated using a representative test section with surrogate heat sources. Data collected on this system were used to develop a thermal-hydraulic model, which was then coupled to the electrochemical-thermal model to demonstrate substantial performance improvement through internal cooling of lithium-ion batteries in HEV applications.

Data were collected on a small (~1 Ah) commercially available lithium-ion

battery designed for high rate applications over a wide range of temperatures (10°C to 60°C), depths of discharge (0.15 Ah to 0.95 Ah), and rates (-5 A to 5 A). Open circuit potential versus temperature data were collected first using a controlled environmental chamber and battery cycler. These data were used to calculate reversible heating over the same range of *DOD*. However, due to the poor battery surface heat removal characteristics of the environmental chamber, it was not possible to maintain constant surface temperature when the battery was charged and discharged at high rates using this test facility. Thus, a specially designed, temperature-controlled wind tunnel was built and used to measure the irreversible electrochemical heat generation rate. In contrast to prior investigations, the surface temperature of the small cell was controlled within ±0.88°C throughout all tests to enable measurement of the effect of temperature on the heat generation rate. The results showed that total electrochemical heat generation was primarily a strong function of charge and discharge rate and *DOD*, and secondarily a function of temperature, over the tested range. In addition, reversible heat was shown to have a strong influence on the measured electrochemical heat generation. For example, the reversible heat was a minimum of 7.5% of the total heat generation at ~5*C* and 15°C. It was also shown to have a strong influence on the total heat generation as a function *DOD* due to its large entropic heat coefficient (~0.2 mV K^{-1}) for $0.35 < DOD < 0.70$. Although significant in these tests, accounting of the observed capacity fade resulted in little variation among samples. Constant current data were also shown to predict dynamic performance well (90% of data predicted to within ±2.5%), which demonstrated the feasibility of using galvanostatic data in HEV simulations.

The heat generation characteristics of this small cell were used to guide the design

and evaluation of a passive internal cooling system. Due to the unknown heat transfer and pressure drop behavior of pure refrigerant liquid-vapor phase change processes at small scales and low mass fluxes, a representative test section with 3.175 mm × 160 μm (effective) channels was investigated in a test facility with a temperature-controlled, liquid-cooled condenser. Flow of the working fluid (R134a) was initiated when heat was applied to the test section using a surrogate heat source that mimics performance in a battery system over a wide range of inputs ($120 < \dot{Q}''' < 6500$ W L^{-1}). The results showed that the mass flow rate and evaporator outlet quality both initially increased as the heat rate increased. However, because the pressure losses (dominated by two-phase test section pressure drop) in the test facility increased at a faster rate than the gravitational potential, the mass flow rate decreased at heat inputs greater than ~1350 W L^{-1}. The system also showed a weak influence of system pressure on performance over the tested saturation temperature range (24°C to 33°C). At increased saturation pressures, two-phase friction losses decreased slightly, which resulted in increased mass flow rates from 24°C to 29°C at a fixed heat input. However, as the system pressure increased further, the driving force due to gravity decreased (caused by decreased liquid density) more than the small decrease in frictional pressure drop, which yielded approximately the same mass flow rate at 29°C and 33°C over the range of heat inputs. Flow maldistribution was also observed under some conditions, and may be attributable to a combination of Ledinegg instability and vapor jetting in the outlet header. These effects may be mitigated by pumping a single-phase fluid through the channels. However, this technique requires an external pump, which adds weight, volume, and complexity. Therefore, more investigation of the observed flow maldistribution during evaporation is warranted in

geometries that more closely represent the intended battery internal cooling system design.

Using the measured mass flow rate and test section outlet quality, the two-phase frictional pressure drop in the test section was calculated accurately (19 of 23 data points within ±22%). Existing two-phase flow models, developed either for larger channels, higher mass flux, or non-condensable gas and water mixtures, were shown to poorly predict the data. Therefore, a new frictional pressure drop correlation was developed by using the work of Saisorn and Wongwises (2009) as a starting point. This model was used to predict the performance of a simplified version of the passive internal microchannel phase-change cooling system, which was then coupled to the battery model.

The electrochemical-thermal model was developed using the temperature-dependent performance data collected on the commercial battery. The improved computational efficiency of the model allowed for comparison of different thermal management strategies on a battery subjected to a representative high-speed aggressive highway driving HEV schedule. The anisotropic thermal conductivity of the battery was incorporated into this model, as well as current movement with induced resistive heating in the collectors. Edge cooling through a low thermal resistance cold plate was shown to induce a large thermal gradient, which led to significant thermally-induced non-uniform cycling. Air cooling resulted in similar temperature increases, while liquid cooling reduced the peak temperature at the expense of inducing a moderate thermal gradient. As the cell size increased from 8 Ah to 20 Ah, liquid cooling exhibited an increased temperature gradient that caused additional non-uniform cycling of the battery. The

effect of charge redistribution was deemed minimal for the side cooled battery, but warrants additional research for battery designs that exhibit large thermal gradients.

The effect of an overall size reduction of the battery pack was also investigated. To reduce pack size, individual cells within the pack were cycled more aggressively, causing cumulative and instantaneous heat generation to increase. Neither edge cooling nor air cooling allowed the pack size to be reduced beyond a factor of 2 for a peak temperature limit of 35°C. Liquid cooling allowed the pack to be reduced by a factor 4, but this reduction could only be applied to a pack based on the 8 Ah cell, which was 25.5% larger than for the pack based on the 20 Ah cell. In contrast, the size of the internally cooled pack can be reduced by at least a factor of 10. As a result, the charge and discharge energy extraction density was highest for the internal cooling system in spite of the volume increase due to 160 μm channels inserted into the 284.5 μm unit cell. Furthermore, the saturation temperature of the phase change fluid can be optimized to balance capacity fade and energy extraction at elevated temperatures. At a saturation temperature of 35°C, the charge and discharge energy extraction densities were 80% and 67% greater than for liquid cooling even when the pack volume increased due to incorporation of the channels.

This research moves towards a more fully integrated understanding of thermal management of large lithium-ion battery packs intended for HEV applications. Internally cooling batteries can lead to improvements in battery performance, safety, and longevity that are unencumbered by thermal limitations.

6.1. Recommendations for Future Work

While this investigation has led to new insights on battery thermal management

and coupled electrochemical-thermal interaction, there are still many new research frontiers that need attention. The most pressing needs for further research are as follows:

- The impact of internally cooling batteries on energy density is strongly dependent on the channel geometry. However, as demonstrated in this investigation, the void fraction and frictional pressure drop characteristics are still poorly understood for pure refrigerants flowing at low mass flow rates (G < 100 kg m^{-2} s^{-1}) inside passages with D_h < ~100 μm. Additional two-phase flow investigations at these conditions are warranted.
- In the present study, metallic channels with surrogate heat sources were utilized to investigate the performance of the internal cooling system. A thermal-hydraulic model based on the data collected on this system was incorporated into the coupled electrochemical-thermal battery model to show that these batteries can be made smaller and cycled more aggressively through improved thermal management. However, the demonstrated performance improvement should be validated using an actual battery with integrated refrigerant channels in the current collectors.
- While the current research has demonstrated the potential for improved performance through internal cooling, there are still some fabrication challenges in incorporating cooling channels into lithium-ion batteries. For a spirally wound configuration, this necessitates a sheet of microchannels with minor dimensions less than 100 μm over a footprint that could extend several meters wide. This problem requires multidisciplinary collaboration among manufacturing specialists, material scientists, electrochemists, and heat transfer experts, but can lead to revolutionary performance, safety, and durability improvements.

- Although the present study focused on the spirally wound configuration, the internal cooling system can be integrated into other cell and pack designs to improve their performance and longevity, and may lead to new designs that minimize cost. For example, the individual cells can have large rectangular cross sections and be stacked upon each other, similar to a bipolar stack. In this arrangement, the edges of the cells are typically cooled, which, as shown in this study, leads to significant temperature differences within the cells. In contrast, a sheet of cooling channels that contain a liquid-vapor phase change fluid can be easily integrated between successive cells for improved heat removal. Furthermore, because the results from the present study show that the maximum temperature difference was significantly smaller for 8 Ah cell than for the thicker 20 Ah cool cell, it may not be necessary to incorporate the cooling channels between every stacked cell. Thus, significant opportunity exists for optimization between energy density, performance, longevity, and cost.
- The results from this study were specific to a C/$LiFePO_4$ cell designed for high rate applications. The electrode thicknesses were thin relative to the unit cell (57% of the total), which led to reduced energy density, irreversibilities and, thus, heat generation relative to other cell designs with thicker electrodes. It is possible that designs previously thought to be impractical for high charge/discharge rates due to the high heat generation rates can be used if internal cooling is utilized. This may lead to packs with simultaneous increases in both energy and power density.
- Capacity fade is a significant problem for lithium-ion batteries operated at elevated temperatures. However, the interaction between thermal management and longevity is not well understood. This is especially critical for external cooling strategies that

use high surface convection and create significant internal temperature gradients and non-uniform cycling. Integrating capacity fade models into the electrochemical-thermal model developed in this study may lead to increased battery lifetime or smaller battery packs due to lower capacity fade safety factors.

- Finally, the study conducted here was for normal operation, and thermal runaway is a significant problem for lithium-ion batteries. The modeling approach used in this investigation is well suited for simulating some abuse scenarios, especially internal and external short circuiting. Incorporation of thermal runaway models into the models developed in this study could lead to a better understanding of the impact of thermal management on preventing or mitigating thermal runaway, which can lead to safer commercial battery packs.

APPENDIX-A. DETAILED UNCERTAINTY CALCULATION

Measurement of the entropic heat coefficient and operation potential required smaller uncertainties in the measured voltage and temperature than stock calibration. Uncertainties in the measurements and the results reported in Chapter Three were estimated using the approach described in Coleman and Steele (1989). Precision error, *i.e.,* the random error about a measured quantity, for the next data point was estimated from statistical analysis of a sample data set assuming a *t*-distribution with N - 1 degrees of freedom as follows:

$$P_X = t \cdot S_X \tag{A.1}$$

The precision error of the sample mean was improved by taking N data points, which is calculated as follows:

$$P_{\bar{X}} = t \frac{S_X}{\sqrt{N}} \tag{A.2}$$

The sample mean ($\bar{X}$) and deviation (S_X) were calculated as follows:

$$\bar{X} = \frac{1}{N} \sum_{i=1}^{N} X_i \tag{A.3}$$

$$S_X = \left[\frac{1}{N-1} \sum_{i=1}^{N} \left(X_i - \bar{X} \right)^2 \right]^{1/2} \tag{A.4}$$

For a 95% confidence interval and 21 sample data points, $N-1 = 20$ and $t = 2.086$ for the

Table A-1: Sample Temperature and Voltage Measurements at 10°C and 0.15 Ah for the Entropic Heat Coefficient Tests

Temperature	Voltage
°C	V
10.169	3.3371
10.126	3.3368
10.242	3.3368
10.095	3.3368
10.242	3.3371
10.064	3.3371
10.095	3.3375
10.095	3.3371
10.200	3.3371
10.242	3.3368
10.126	3.3365
10.169	3.3371
10.200	3.3368
10.200	3.3368
10.126	3.3371
10.157	3.3371
10.157	3.3368
10.126	3.3375
10.157	3.3371
10.200	3.3375
10.157	3.3368

open circuit potential and temperature measurements. Table A-1 summarizes a sample data point used for calculating the precision uncertainty of the measured voltage and temperature. The sample mean and standard deviations for this representative data point were 0.052°C and 0.250 mV, yielding total precision uncertainties of 0.029°C and 0.114 mV for the mean of 21 sample points. The maximum precision uncertainty for the average voltage and temperature of a single thermocouple measured during the OCP tests were 0.159 mV and 0.088°C, respectively. Similarly, assuming $N - 1 = \infty$ and $t = 1.96$, the maximum precision errors for average temperature and current measurements in the operation voltage tests were 1.29°C and 1.71 mA for charging at 0.5 A and 25°C and 3.0 A and 35°C, respectively. Moreover, the operation voltage changes with time; thus, it

was conservatively assumed that the precision error was the same as the maximum precision error reported for the OCP measurements, but for the next measured value instead of the next measured mean value (*i.e.*, 0.729 mV using Equation A.1).

Bias error, *i.e.*, the systematic error between the mean measured value and the true value, does not have an equivalent error that can be estimated from a sample data set. Furthermore, calibration does not remove all sources of uncertainty because measurement error can be inherent in both the calibration standard and the measurement system. For example, the calibration curve fit may not perfectly predict the actual measured data. This bias error was estimated as the standard error of estimate (*SEE*) as follows:

$$SEE^2 = \frac{\sum_{i=1}^{N}\left[Y_i - \left(aX_i + b\right)\right]^2}{N-2} \tag{A.5}$$

The total bias uncertainty (for a 95% confidence interval) was calculated as follows:

$$B_{\bar{V}} = \sqrt{B_{cs}^2 + 4SEE_{\bar{V}}^2} \tag{A.6}$$

The bias uncertainties assumed for this investigation were associated with the calibration standard and the *SEE*. Voltage measurements were calibrated using the Agilent 34401A digital multimeter, which has an uncertainty of 0.0035% of the measured value plus 0.0005% of full scale. The maximum measured value is 4.2 V and the voltage scale is 0 V to 10 V. Thus, the maximum bias error associated with the calibration standard was 0.197 mV, which was conservatively assumed for all average voltage data collected in this investigation. Similarly, for the average temperature, the bias errors arise from the calibration standard (±0.012°C, Hart Scientific Model 1502A with platinum RTD probe) and the error from the calibration curve fit. For measurement calibration, the

Table A-2: Sample Calculation for Standard Error of Estimate of Temperature Measurement

Measured	Corrected	Actual	
10.492	10.330	10.160	0.029
20.210	20.139	20.161	0.000
29.980	30.001	30.158	0.025
39.903	40.017	40.143	0.016
49.903	50.111	50.141	0.001
60.011	60.314	60.149	0.027
		SEE	0.156°C

thermocouples were placed in a temperature-controlled bath (Hart Scientific Model 7340) in close proximity to the tip of the calibration standard RTD to eliminate bias from bath temperature non-uniformity. Tables A-2 and A-3 summarize the calibration results for the voltage and temperature measurements, respectively, which yield *SEE* values of 0.379 mV and 0.156°C, respectively. Hence, the total bias uncertainties for these values measured in the entropic heating tests were 0.427 mV and 0.157°C for these sample data points. The bias error for the instantaneous voltage measurement on both samples was assumed to be the same as for Sample 1 (0.427 mV). Because it was controlled during the tests, current was not calibrated to a standard. Thus, the bias error was assumed to be the published accuracy of the battery cycler: 0.1% of full scale. Two different scales were used during the test: -1 A to 1 A, and -25 A to 25 A. Therefore, for test currents of 0.25 A and 0.5 A, the bias error was 2 mA, while the bias error for test currents 1 A, 2 A, 3 A, and 5 A was 50 mA.

Table A-3: Sample Calculation for Standard Error of Estimate of Voltage Measurement

Measured	Corrected	Actual	
2.5028	2.5033	2.5033	6.08×10^{-9}
3.3560	3.3564	3.3563	2.40×10^{-8}
4.2226	4.2231	4.2232	5.89×10^{-9}
		SEE	0.379 mV

The propagations of bias and precision uncertainties for a function *func* of many variables X_i are calculated as follows:

$$B_{f(X_i)}^2 = \sum_{i=1}^{N}\left[\left(B_{X_i}\frac{\partial func}{\partial X_i}\right)^2 + \sum_{k=1}^{N}\frac{\partial func}{\partial X_i}\frac{\partial func}{\partial X_k}\rho_{ik}B'_{X_i}B'_{X_k}\left(1-\delta_{ik}\right)\right] \tag{A.7}$$

$$P_{f(X_i)} = \left[\sum_{i=1}^{N}\left(P_{X_i}\frac{\partial func}{\partial X_i}\right)^2\right]^{1/2} \tag{A.8}$$

The additional term in the bias uncertainty propagation represents cross-correlation of temperature or voltage measurement, which, in this investigation arose only from the use of the same calibration standards (0.012°C and 0.197 mV). It is assumed here that the correlation coefficient (ρ) across all temperature measurements and across all voltage measurements were equal to 1. The Kronecker delta function was calculated as follows:

$$\delta_{ik} = \begin{cases} 1 & i = k \\ 0 & i \neq k \end{cases} \tag{A.9}$$

Two calculated quantities with propagated uncertainties were used to determine the uncertainty in the entropic heat coefficient: average temperature (two thermocouples) and the slope of OCP with temperature. (The voltage was measured on one channel; therefore, it has only its precision and standard calibration bias uncertainties.) The precision and bias uncertainties on the average of the two thermocouples were calculated as follows:

$$P_{T_{avg}}^2 = \left(\frac{P_{T_1}}{2}\right)^2 + \left(\frac{P_{T_2}}{2}\right)^2 \tag{A.10}$$

$$B_{T_{\text{avg}}}^2 = \left(\frac{B_T}{2}\right)^2 + \left(\frac{B_T}{2}\right)^2 + \frac{1}{2}\frac{1}{2}\cdot 1\cdot\left(0.012^{\circ}\text{C}\right)^2 \tag{A.11}$$

The 0.012°C in the latter equation arises from the calibration standard cross correlation between the two thermocouple measurements. The slope of the average OCP versus temperature at a fixed *DOD* was calculated using Equation 3.4. Therefore, the partial derivatives of the entropic heat coefficient with respect to the average temperature and voltage were calculated as follows:

$$\frac{\partial\left(\frac{\partial U}{\partial T}\right)}{\partial T_{\text{i}}} = \frac{\partial(\lambda)}{\partial T_{\text{i}}} = \frac{\left(U_i - \overline{U}\right)}{\sum_{k=1}^{N}\left(T_k - \overline{T}\right)^2} - \frac{2\left(T_i - \overline{T}\right)\cdot\sum_{k=1}^{N}\left(T_k - \overline{T}\right)\left(U_k - \overline{U}\right)}{\left[\sum_{k=1}^{N}\left(T_k - \overline{T}\right)^2\right]^2} \tag{A.12}$$

$$\frac{\partial\left(\frac{\partial U}{\partial T}\right)}{\partial U_{\text{i}}} = \frac{\partial(\lambda)}{\partial U_{\text{i}}} = \frac{\left(T_i - \overline{T}\right)}{\sum_{k=1}^{N}\left(T_k - \overline{T}\right)^2} \tag{A.13}$$

Finally, the total uncertainty for a given quantity X_i is given by the following equation:

$$UN^2 = B^2 + P^2 \tag{A.14}$$

This equation holds for both measured and calculated quantities. Table A-4 summarizes a sample data point at a *DOD* of 0.15 Ah for the entropic heat coefficient. In this example, total bias and precision uncertainties were 9.309 μV K^{-1} and 2.795 μV K^{-1}, respectively, yielding a total uncertainty of 9.719 μV K^{-1}.

The volumetric heat generation rate was calculated using Equation 3.7, and its partial derivative of volumetric heat generation rate with respect to measured current, voltage, open circuit potential, temperature, and entropic heat coefficient were calculated

Table A-4: Sample Data Point at *DOD* = 0.15 Ah for Calculating Entropic Heat Coefficient Uncertainty

Item	Units	State 1	State 2	State 3	State 4	State 5	State 6
T	°C	10.276	19.921	29.204	38.733	48.840	59.109
U	V	3.337	3.338	3.338	3.338	3.338	3.338
$\partial\lambda/dT$	V K^{-2} × 10^{7}	0.542	3.720	2.029	0.003	-1.722	-4.572
$\partial\lambda/dV$	K^{-1}	-0.015	-0.009	-0.003	0.003	0.009	0.015
B_T	°C	0.136					
B_V	mV	0.427					
P_T	°C × 10^{9}	2.245	11.853	3.581	0.008	4.155	10.828
P_V	V × 10^{6}	1.653	0.991	0.353	0.301	0.995	1.700
Total							
Precision	μV K^{-1}	2.795					
Bias	μV K^{-1}	9.309					
Total	μV K^{-1}	9.719					

as follows:

$$\frac{\partial \dot{Q}}{\partial I} = \frac{1}{v_{\text{nom}}}\left(U - V - T\frac{\partial U}{\partial T}\right) \tag{A.15}$$

$$\frac{\partial \dot{Q}}{\partial V} = -\frac{I}{v_{\text{nom}}} \tag{A.16}$$

$$\frac{\partial \dot{Q}}{\partial U} = \frac{I}{v_{\text{nom}}} \tag{A.17}$$

$$\frac{\partial \dot{Q}}{\partial T} = \frac{I}{v_{\text{nom}}}\left(-\frac{\partial U}{\partial T}\right) \tag{A.18}$$

$$\frac{\partial \dot{Q}}{\partial\left(\frac{\partial U}{\partial T}\right)} = \frac{I}{v_{\text{nom}}}(-T) \tag{A.19}$$

A representative data point at 3.0 A of discharge and 15°C is shown in Table A-5. The cross correlation between the measured voltage and the open circuit potential caused a reduction in the bias uncertainty because Equations A.16 and A.17 had opposite signs

Table A-5: Sample Data Point at 15°C and *DOD* = 0.55 for 3.0 A Discharge for Calculating Total Volumetric Heat Rate Uncertainty

Item	Units	Value
T	°C	15.038
I	A	2.999
U	V	3.294
V	V	2.885
$\partial U/\partial T$	μV K^{-1}	206.2
$\partial \dot{Q}'''/\partial T$	W K^{-1} L^{-1}	-0.047
$\partial \dot{Q}'''/\partial I$	V L^{-1}	26.73
$\partial \dot{Q}'''/\partial U$	A L^{-1}	229.36
$\partial \dot{Q}'''/\partial V$	A L^{-1}	-229.36
$\partial \dot{Q}'''/\partial \lambda$	kA K L^{-1}	66.10
B_T	°C	0.170
B_I	mA	50
B_U	mV	0.427
B_V	mV	0.427
B_λ	μV K^{-1}	9.36
P_T	°C	1.29
P_I	mA	1.71
P_U	mV	0.729
P_V	mV	0.729
P_λ	μV K^{-1}	3.44
Total		
$\dot{Q}'''$	W L^{-1}	80.18
B	W L^{-1}	1.48
P	W L^{-1}	0.337
UN	W L^{-1}	1.52

and their correlation coefficient of bias uncertainty was positive. Therefore, for conservative estimation, this cross-correlation was neglected. Furthermore, because proportional changes in temperature cause a decrease in the entropic heat coefficient (*i.e.*, ρ = -1) and also because both values were positive (Figure 3.6), it was also conservatively assumed that no cross correlation existed between temperature and the entropic heat coefficient for calculating the volumetric heat generation. Finally, the cross correlations due to both U and V with respect to the entropic heat coefficient have equal

and opposite signs, and, therefore, offset each other when calculating the bias uncertainty. Assuming negligible uncertainty in the unit cell volume, and using the maximum precision and bias errors for a single measurement of temperature, voltage, current, and entropic heat coefficient for Sample 1 (1.29°C, 0.729 mV, 1.71 mA, and 3.44 $\mu V\ K^{-1}$ and 0.170°C, 0.427 mV, 50 mA, 9.93 $\mu V\ K^{-1}$, respectively), the total bias and precision uncertainties for the volumetric heat rate in the sample data point shown in Table 3-4 were 0.337 $W\ L^{-1}$ and 1.48 $W\ L^{-1}$, respectively, yielding a total uncertainty of 1.52 $W\ L^{-1}$.

Table 3-4 summarizes maximum propagated uncertainties for relevant calculated quantities in this study. The entropic heat coefficient is known to within a maximum of $\pm 9.93\ \mu V\ K^{-1}$ and $\pm 13.43\ \mu V\ K^{-1}$ for Samples 1 and 2, respectively. Similarly, the maximum uncertainty for the total volumetric heat generation rate varied from ±0.063 $W\ L^{-1}$ at 0.25 A to ±2.85 $W\ L^{-1}$ at 3.0 A.

APPENDIX-B. TWO-PHASE TESTING REPEATABILITY

As mentioned in Section 4.4.2, additional tests were conducted on the representative passive internal cooling system with the inside surface of the environmental chamber completely covered with foil (Figures 4.29 and 4.30). Figure B.1 shows that these tests yielded results consistent with those from the partially covered environmental chamber tests. The heat loss was calculated using the approach described in Section 4.4.2, but all surfaces were assumed to have an emissivity of 0.07.

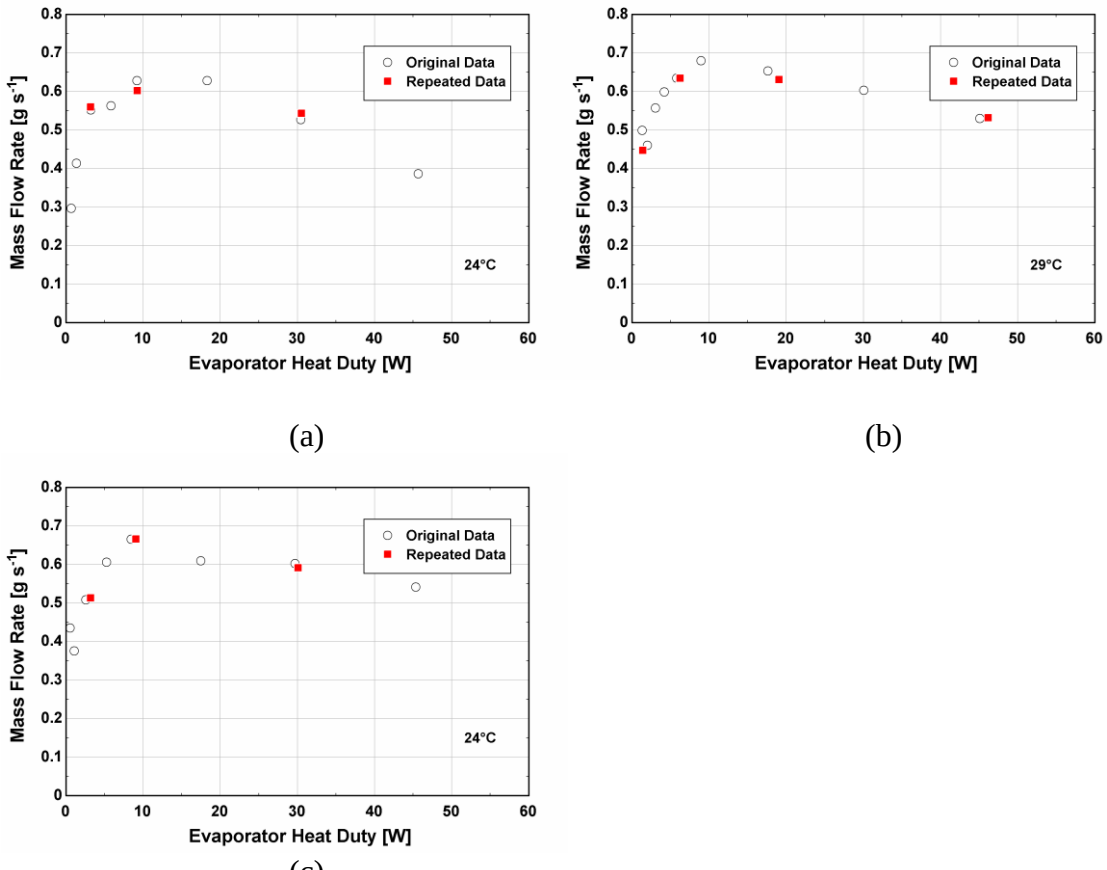

Figure B.1: Data Repeatability Tests: (a) 24°C, (b) 29°C, and (c) 33°C

APPENDIX-C. SAMPLE DATA POINTS

In this section, representative calculations for the two-phase friction pressure drop are provided in Tables C-3 and C-4. These tables use inputs given in Tables C-1 and C-2 for a representative data point. Table C-5 contains representative calculations for the void fraction correlations used in the present investigation.

Table C-1: Sample Data Point for Representative Calculation of Selected Frictional Pressure Drop Models

Item	Units	Value
G	kg m^{-2} s^{-1}	85.25
D_{ch}	mm	0.3046
W_{ch}	mm	3.175
$H_{ch,eff}$	μm	160
L_{tp}	mm	186.13
ΔP_{meas}	kPa	2.867
ε		0
x		0.0261
ρ_l	kg m^{-3}	1208.9
μ_l	kg m^{-1} s^{-1} × 10^4	1.957
ρ_v	kg m^{-3}	31.82
μ_v	kg m^{-1} s^{-1} × 10^4	0.1194
σ	mN m^{-1}	8.153

Table C-2: Common Calculations for Representative Calculation of Selected Frictional Pressure Drop Models

Item	Equation	Results
Re_l	$\frac{G \cdot D_{ch} \cdot (1-x)}{\mu_l}$	129.2
Re_v	$\frac{G \cdot D_{ch} \cdot x}{\mu_v}$	56.76
Re_{lo}	$\frac{G \cdot D_{ch}}{\mu_l}$	132.7

Table C-2: Cont…

Item	Equation	Results
α	$\frac{H_{ch,eff}}{W_{ch}}$	0.0504
$f_{SB,l}$	$f = \frac{96}{Re}\left(1 - 1.3553\cdot\alpha + 1.9467\cdot\alpha^2 - 1.7012\cdot\alpha^3 + 0.9564\cdot\alpha^4 - 0.2537\cdot\alpha^5\right)$	0.6957
$f_{SB,v}$		1.582
$f_{Churchill,lo}$	$\left(\frac{f_{Churchill}}{8}\right)^{12} = \left(\frac{8}{Re}\right)^{12} + \left(\left[-2.547\cdot\ln\left(\left[\frac{7}{Re}\right]^{0.9} + 0.27\frac{\varepsilon}{D}\right)\right]^{16} + \left[\frac{37530}{Re}\right]^{16}\right)^{-1.5}$	0.4823
$dP/dz\|_l$	$\frac{1}{2}\frac{\left[G\cdot(1-x)\right]^2}{\rho_l} f_{SB,l}\frac{1}{D_{ch}}$	6.511 [kPa m^{-1}]
$dP/dz\|_v$	$\frac{1}{2}\frac{\left[G\cdot x\right]^2}{\rho_v} f_{SB,v}\frac{1}{D_{ch}}$	0.4049 [kPa m^{-1}]
$dP/dz\|_{lo}$	$\frac{1}{2}\frac{G^2}{\rho_l} f_{Churchill,lo}\frac{1}{D_{ch}}$	4.759 [kPa m^{-1}]
$X_{Martinelli}$	$\left(\frac{dP/dz\|_l}{dP/dz\|_v}\right)^{0.5}$	4.010
$X_{Martinelli,vv}$	$\left(\frac{\mu_l}{\mu_v}\right)^{0.5}\left(\frac{1-x}{x}\right)^{0.5}\left(\frac{\rho_v}{\rho_l}\right)^{0.5}$	4.012
j_l	$\frac{G\cdot(1-x)}{\rho_l}$	0.0687 [m s^{-1}]
j_v	$\frac{G\cdot x}{\rho_v}$	0.0700 [m s^{-1}]
β_v	$\frac{j_v}{j_l + j_v}$	0.5048
β_l	$\frac{j_l}{j_l + j_v}$	0.4952
Co	$\left[\frac{\sigma}{g\cdot(\rho_l - \rho_v)D_{ch}^2}\right]^{0.5}$	2.759
ψ	$\frac{\mu_l j_l}{\sigma}$	0.00165

Table C-3: Representative Calculation for Selected Frictional Pressure Drop Models based on Two-Phase Multipliers (Listed Alphabetically)

Inputs	Equations	Results
Chung *et al.* (2004)[4]: $X_{\text{Martinelli}} = 4.010$ $dP/dz\|_{\text{l}} = 6.511\ [\text{kPa m}^{-1}]$ $L_{\text{tp}} = 186.13$ [mm]	$\phi_{\text{l}}^2 = 1 + \frac{0.12}{X_{\text{Martinelli}}} + \frac{1}{X_{\text{Martinelli}}^2}$ $\Delta P = \left.\frac{dP}{dz}\right\|_{\text{l}} \cdot \phi_{\text{l}}^2 \cdot L_{\text{tp}}$	$\phi_{\text{l}}^2 = 1.092$ $\Delta P = 1.323$ [kPa]
Cubaud and Ho (2004): $\beta_{\text{l}} = 0.4952$ $dP/dz\|_{\text{l}} = 6.511\ [\text{kPa/m}]$ $L_{\text{tp}} = 186.13$[mm]	$\phi_{\text{l}}^2 = \begin{cases} \beta_{\text{l}}^{-1} & \beta_{\text{l}} < 0.2 \\ \beta_{\text{l}}^{-0.5} & \beta_{\text{l}} \geq 0.2 \end{cases}$ $\Delta P = \left.\frac{dP}{dz}\right\|_{\text{l}} \cdot \phi_{\text{l}}^2 \cdot L_{\text{tp}}$	$\phi_{\text{l}}^2 = 1.421$ $\Delta P = 1.722$ [kPa]
Hwang and Kim (2006): $Re_{\text{lo}} = 132.7$ $X_{\text{Martinelli}} = 4.010$ Co = 2.759 $dP/dz\|_{\text{l}} = 6.511\ [\text{kPa m}^{-1}]$ $L_{\text{tp}} = 186.13$[mm]	$C = 0.227 \cdot Re_{\text{lo}}^{0.452} X_{\text{Martinelli}}^{-0.320} Co^{-0.820}$ $\phi_{\text{l}}^2 = 1 + \frac{C}{X_{\text{Martinelli}}} + \frac{1}{X_{\text{Martinelli}}^2}$ $\Delta P = \left.\frac{dP}{dz}\right\|_{\text{l}} \cdot \phi_{\text{l}}^2 \cdot L_{\text{tp}}$	$C = 0.5771$ $\phi_{\text{l}}^2 = 1.206$ $\Delta P = 1.462$ [kPa]

[4] Constants for the rectangular channels were used in the current investigation.

Table C-3: Cont…

Inputs	Equations	Results
Koyama *et al.* (2003)[5]: D_{ch} = *0*.3046 [mm] $X_{Martinelli}$ = 4.010 $dP/dz\big\|_v = 0.4049$ [kPa m^{-1}] L_{tp} = 186.13[mm]	$C = 21\left[1 - e^{(-0.319 \cdot D_{ch}\,[m])}\right]$ $\phi_v^2 = 1 + C \cdot X_{Martinelli} + X_{Martinelli}^2$ $\Delta P = \left.\frac{dP}{dz}\right\|_v \cdot \phi_v^2 \cdot L_{tp}$	$C = 0.002$ $\phi_v^2 = 17.08$ $\Delta P = 1.287$ [kPa]
Lin *et al.* (1991): $\mu_l = 1.957 \times 10^{-4}$ [kg m^{-1} s^{-1}] $\mu_v = 1.194 \times 10^{-5}$ [kg m^{-1} s^{-1}] $\rho_l = 1208.9$; $\rho_v = 31.82$ [kg m^{-3}] $x = 0.0261$; $G = 85.25$ [kg m^{-2} s^{-1}] D_{ch} = 0.3046 [mm] $Re_{lo} = 132.7$; $\frac{\varepsilon}{D_{ch}} = 0$ $dP/dz\big\|_{lo} = 4.759$ [kPa m^{-1}] L_{tp} = 186.13[mm]	$\mu_{tp} = \frac{\mu_l \cdot \mu_v}{\mu_v + x^{1.4}(\mu_l - \mu_v)}$; $Re_{tp} = \frac{G \cdot D_{ch}}{\mu_{tp}}$ $\phi_{lo}^2 = \left[\frac{\ln\left(\left[\frac{7}{Re_{lo}}\right]^{0.9} + 0.27\frac{\varepsilon}{D_{ch}}\right)}{\ln\left(\left[\frac{7}{Re_{tp}}\right]^{0.9} + 0.27\frac{\varepsilon}{D_{ch}}\right)}\right]^{16}\left[1 + x \cdot \left(\frac{\rho_l}{\rho_v} - 1\right)\right]$ $\Delta P = \left.\frac{dP}{dz}\right\|_{lo} \cdot \phi_{lo}^2 \cdot L_{tp}$	$\mu_{tp} = 1.790 \times 10^{-4}$ [kg m^{-1} s^{-1}] $Re_{tp} = 145.1$ $\phi_{lo}^2 = 1.218$ $\Delta P = 1.079$ [kPa]

[5] Assumed same formulation as Mishima and Hibiki (1996).

Table C-3: Cont…

Inputs	Equations	Results
Lee and Garimella (2008)[6]: $X_{\text{mart,vv}} = 4.012$ G = 85.25 [kg m^{-2} s^{-1}] D_{ch} = 0.3046 [mm] $dP/dz\|_{\text{l}} = 6.511$ [kPa m^{-1}] L_{tp} = 186.13[mm]	$C = 2566 \cdot \left(G[\text{kg m}^{-2}\ \text{s}^{-1}]\right)^{0.5466} \left(D_{\text{ch}}[\text{m}]\right)^{0.8819} \left[1 - e^{(-319 \cdot D_{\text{ch}}[\text{m}])}\right]$ $\phi_{\text{l}}^2 = 1 + \frac{C}{X_{\text{Martinelli,vv}}} + \frac{1}{X_{\text{Martinelli,vv}}^2}$ $\Delta P = \left.\frac{dP}{dz}\right\|_{\text{l}} \cdot \phi_{\text{l}}^2 \cdot L_{\text{tp}}$	$C = 2.139$ $\phi_{\text{l}}^2 = 1.596$ $\Delta P = 1.934$ [kPa]
Lee and Lee (2001)[7]: $\mu_{\text{l}} = 1.957 \times 10^{-4}$ [kg m^{-1} s] $\rho_{\text{l}} = 1208.9$ [kg m^{-3}] $\sigma = 8.153 \times 10^{-3}$ [N m^{-1}] G = 85.25 [kg m^{-2} s^{-1}] D_{ch} = 0.3046 [mm] $\psi = 0.00165$ $Re_{\text{lo}} = 132.7$; $X_{\text{Martinelli}} = 4.010$ $dP/dz\|_{\text{l}} = 6.511$ [kPa m^{-1}] L_{tp} = 186.13[mm]	$\zeta = \frac{\mu_{\text{l}}^2}{\rho_{\text{l}} \sigma D_{\text{ch}}}$ $C = 6.833 \times 10^{-8} \cdot \zeta^{-1.317} \psi^{0.719} Re_{\text{lo}}^{0.557} \qquad Re_{\text{l}}, Re_{\text{v}} < 2000$ $\phi_{\text{l}}^2 = 1 + \frac{C}{X_{\text{Martinelli}}} + \frac{1}{X_{\text{Martinelli}}^2}$ $\Delta P = \left.\frac{dP}{dz}\right\|_{\text{l}} \cdot \phi_{\text{l}}^2 \cdot L_{\text{tp}}$	$\zeta = 1.276 \times 10^{-5}$ $C = 0.0290$ $\phi_{\text{l}}^2 = 1.069$ $\Delta P = 1.296$ [kPa]

[6] Assumed Darcy friction factor for single phase pressure drop calculation.
[7] All data in present investigation had Reynolds numbers of $Re_{\text{v}} < 500$ and $Re_{\text{l}} < 180$.

Table C-3: Cont…

Inputs	Equations	Results
Lee and Mudawar (2005)[7]: ρ_l = 1208.9 [kg m^{-3}] σ = 8.153 × 10^{-3} [N m^{-1}] G = 85.25 [kg m^{-2} s^{-1}] D_{ch} = 0.3046 [mm] Re_{lo} = 132.7; $X_{Martinelli}$ = 4.010 $dP/dz\|_l = 6.511$ [kPa m^{-1}] L_{tp} = 186.13[mm]	$We_{lo} = \frac{G^2 D_{ch}}{\rho_l \sigma}$ $C = 2.16 \cdot Re_{lo}^{0.047} We_{lo}^{0.60}$ Re_l, Re_v laminar $\phi_l^2 = 1 + \frac{C}{X_{Martinelli}} + \frac{1}{X_{Martinelli}^2}$ $\Delta P = \left.\frac{dP}{dz}\right\|_l \cdot \phi_l^2 \cdot L_{tp}$	$We_{lo} = 0.225$ $C = 1.110$ $\phi_l^2 = 1.339$ $\Delta P = 1.622$ [kPa]
Moriyama *et al.* (1992b): μ_l = 1.957 × 10^{-4} [kg m^{-1} s^{-1}] G = 85.25 [kg m^{-2} s] h_{ch} = 0.160 [mm] x = 0.0261 $X_{Martinelli}$ = 4.010 $dP/dz\|_l = 6.511$ [kPa m^{-1}] L_{tp} = 186.13[mm]	$Re_{l,alt} = \frac{2 \cdot G \cdot (1-x) h_{ch,eff}}{\mu_l}$ $C = \begin{cases} 0.9 \cdot Re_{l,alt}^{0.3} & Re_{l,alt} > 1.3 \\ 1 & Re_{l,alt} \le 1.3 \end{cases}$ $\phi_l^2 = 1 + \frac{C}{X_{mart,vv}^2}$ $\Delta P = \left.\frac{dP}{dz}\right\|_l \cdot \phi_l^2 \cdot L_{tp}$	$Re_{l,alt} = 135.8$ $C = 3.927$ $\phi_l^2 = 1.244$ $\Delta P = 1.508$ [kPa]

Table C-3: Cont…

Inputs	Equations	Results
Qu and Mudawar (2003): G = 85.25 [kg m^{-2} s^{-1}] D_{ch} = 0.3046 [mm] $X_{Martinelli,vv}$ = 4.012 $dP/dz\|_l = 6.511$ [kPa m^{-1}] L_{tp} = 186.13[mm]	$C = 21 \cdot \left[1 - e^{(-0.319 \cdot D_{ch}\,[m])}\right] \times \left(0.00418 \cdot G\left[\text{kg m}^{-2}\ \text{s}^{-1}\right] + 0.0613\right)$ $\phi_v^2 = 1 + \frac{C}{X_{Martinelli,vv}} + \frac{1}{X_{Martinelli,vv}^2}$ $\Delta P = \left.\frac{dP}{dz}\right\|_l \cdot \phi_l^2 \cdot L_{tp}$	$C = 8.522 \times 10^{-4}$ $\phi_v^2 = 1.062$ $\Delta P = 1.287$ [kPa]
Revellin and Thome (2007)[8]: μ_l = 1.957 × 10^{-4} [kg m^{-1} s^{-1}] μ_v = 1.194× 10^{-5} [kg m^{-1} s^{-1}] ρ_l = 1208.9 [kg m^{-3}] ρ_v = 31.82 [kg m^{-3}] x = 0.0261 G = 85.25 [kg m^{-2} s^{-1}] D_{ch} = 0.3046 [mm] $dP/dz\|_l = 6.511$ [kPa m^{-1}] L_{tp} = 186.13[mm]	$\mu_{tp} = \left(\frac{x}{\mu_v} + \frac{1-x}{\mu_l}\right)^{-1}$ $\rho_{tp} = \left(\frac{x}{\rho_v} + \frac{1-x}{\rho_l}\right)^{-1}$ $Re_{tp} = \frac{G \cdot D_{ch}}{\mu_{tp}}$ $f_{tp} = 0.08 \cdot Re_{tp}^{-0.2}$ $\Delta P = 2\frac{G^2}{\rho_{tp}} f_{tp} \frac{L_{tp}}{D_{ch}}$	$\mu_{tp} = 1.396 \times 10^{-4}$ [kg m^{-1} s^{-1}] $\rho_{tp} = 614.7$ [kg m^{-3}] $Re_{tp} = 186.0$ $f_{tp} = 0.028$ $\Delta P = 0.406$ [kPa]

[8] Constants used for the 509 μm tube in the present investigation.

Table C-3: Cont…

Inputs	Equations	Results
Saisorn and Wongwises (2008): $X_{Martinelli}$ = 4.010 $dP/dz\|_l = 6.511$ [kPa m^{-1}] L_{tp} = 186.13 [mm]	$\phi_l^2 = 1 + \frac{6.627}{X_{Martinelli}^{0.761}}$ $\Delta P = \left.\frac{dP}{dz}\right\|_l \cdot \phi_l^2 \cdot L_{tp}$	$\phi_l^2 = 3.303$ $\Delta P = 4.003$ [kPa]
Saisorn and Wongwises (2009): $X_{Martinelli}$ = 4.010 $dP/dz\|_l = 6.511$ [kPa m^{-1}] L_{tp} = 186.13 [mm]	$\phi_l^2 = 1 + \frac{2.844}{X_{Martinelli}^{1.666}}$ $\Delta P = \left.\frac{dP}{dz}\right\|_l \cdot \phi_l^2 \cdot L_{tp}$	$\phi_l^2 = 1.281$ $\Delta P = 1.553$ [kPa]
Present Study: $X_{Martinelli}$ = 4.010 $dP/dz\|_l = 6.511$ [kPa m^{-1}] L_{tp} = 186.13 [mm]	$\phi_l^2 = 1 + \frac{6.2729}{X_{Martinelli}^{1.4943}}$ $\Delta P = \left.\frac{dP}{dz}\right\|_l \cdot \phi_l^2 \cdot L_{tp}$	$\phi_l^2 = 1.787$ $\Delta P = 2.166$ [kPa]

Table C-4: Representative Frictional Pressure Drop Calculation using Selected Detailed Flow Models

Inputs	Equations	Results
Garimella *et al.* (2003):	$U_{bubble} = 1.2 \cdot U_{slug}$	$U_{bubble} = 0.1664 [m\ s^{-1}]$
G = 85.25 [kg m^{-2} s^{-1}]	$U_{film} = \frac{U_{slug} - U_{bubble} \cdot \left(\frac{D_{bubble}}{D_{ch}} \right)^2}{1 - \left(\frac{D_{bubble}}{D_{ch}} \right)^2}$	$U_{film} = 0.002$ [m s^{-1}]
x = 0.0261	$U_{interface} = 2 \cdot U_{film}$	$U_{interface} = U_{interface,calc} = 0.004 [m\ s^{-1}]$
D_{ch} = 0.3046 [mm]	$Re_{bubble} = \frac{\rho_V \cdot (U_{bubble} - U_{interface}) D_{bubble}}{\mu_V}$	$Re_{bubble} = 120.2$
L_{tp} = 186.13 [mm]	$\left(\frac{dP}{dz} \right)_{f\text{-}b} = \frac{1}{2} \cdot f_{Churchill,bubble} \times \frac{\rho_V \cdot (U_{bubble} - U_{interface})^2}{D_{bubble}}$	$f_{Churchill,bubble} = 0.5325$
ρ_l = 1208.9 [kg m^{-3}]		$\left(\frac{dP}{dz} \right)_{f\text{-}b} = 0.804 [kPa\ m^{-1}]$
ρ_v = 31.82 [kg m^{-3}]		$f_{Churchill,slug} = 0.2453$
μ_l = 1.957 × 10^{-4} [kg m^{-1} s^{-1}]	$U_{interface,calc} = \frac{(dP/dz)_{f\text{-}b} (D_{ch}^2 - D_{bubble}^2)}{16 \cdot \mu_L}$	$\left(\frac{dP}{dz} \right)_{slug} = 9.359 [kPa\ m^{-1}]$
μ_v = 1.194× 10^{-5} [kg m^{-1} s^{-1}]	$\frac{l_{bubble}}{l_{slug} + l_{bubble}} = \frac{G \cdot x \cdot D_{ch}^2}{U_{bubble} \cdot D_{bubble}^2 \cdot \rho_v}$	$\frac{l_{bubble}}{l_{slug} + l_{bubble}} = 0.506$
$U_{slug} = j_l + j_v$ = 0.1387 [m s^{-1}]	$\left(\frac{dp}{dz} \right)_{slug} = \frac{1}{2} \cdot f_{Churchill,slug} \cdot \frac{\rho_l \cdot U_{slug}^2}{D_{ch}}$	$\Delta P_{trans} = 2.291$ [Pa]
$Re_{slug} = \frac{\rho_l \cdot U_{slug} \cdot D_{ch}}{\mu_l}$ = 261.4	$\Delta P_{trans} = \rho_l \cdot \left(1 - \left(\frac{D_{bubble}}{D_{ch}} \right)^2 \right) \times \frac{(U_{slug} - U_{film})(U_{bubble} - U_{film})}{2}$	$\frac{N_{UC}}{L} = 354.7$ [m^{-1}]
ε = 0	$\frac{N_{UC}}{L} = 2.437 \cdot Re_{slug}^{-0.560} \frac{1}{D_{ch}}$	
$\frac{D_{bubble}}{D_{ch}} = 0.912$	$\frac{\Delta P}{L_{tp}} = \left(\frac{dp}{dz} \right)_{f\text{-}b} \cdot \left(\frac{l_{bubble}}{l_{slug} + l_{bubble}} \right) + \left(\frac{dp}{dz} \right)_{slug} \cdot \left(1 - \frac{l_{bubble}}{l_{slug} + l_{bubble}} \right) + \Delta P_{trans} \frac{N_{UC}}{L}$	$\Delta P = 1.088$ [kPa]

Table C-4: Cont…

Inputs	Equations	Results
Chung and Kawaji (2004)[9]:	$VF = 0.8 \cdot \beta_v$	$VF = 0.4038$
$\beta_v = 0.5048$	$U_{bubble} = \frac{j_v}{VF}$	$U_{bubble} = 0.1734 [m\ s^{-1}]$
$\frac{D_{bubble}}{D_{ch}} = 0.9$	$U_{interface} = \frac{(dP/dx)_{f\text{-}b}}{16 \cdot \mu_L}\left(D_{ch}^2 - D_{bubble}^2\right)$	$U_{interface} = 0.0048 [m\ s^{-1}]$
$G = 85.25$ [kg m^{-2} s^{-1}]	$Re_{bubble} = \frac{\rho_V \cdot \left(U_{bubble} - U_{interface}\right) D_{bubble}}{\mu_V}$	$Re_{bubble} = 123.1$
$D_{ch} = 0.3046$ [mm]	$\left(\frac{dP}{dz}\right)_{f\text{-}b} = \frac{1}{2} \cdot \frac{64}{Re_{bubble}} \times \frac{\rho_V \cdot \left(U_{bubble} - U_{interface}\right)^2}{D_{bubble}}$	$\left(\frac{dP}{dz}\right)_{f\text{-}b} = 0.857 [kPa\ m^{-1}]$
$L_{tp} = 186.13$ [mm]		$U_{slug} = 0.115 [m\ s^{-1}]$
$\rho_l = 1208.9$ [kg m^{-3}]		$Re_{slug} = 216.7$
$\rho_v = 31.82$ [kg m^{-3}]		$\left(\frac{dP}{dz}\right)_{slug} = 7.775 [kPa\ m^{-1}]$
$\mu_l = 1.957 \times 10^{-4}$ [kg m^{-1} s^{-1}]	$\frac{l_{bubble}}{l_{slug} + l_{bubble}} = VF \cdot \left(\frac{D_{ch}}{D_{bubble}}\right)^2$	$\frac{l_{bubble}}{l_{slug} + l_{bubble}} = 0.4985$
$\mu_v = 1.194 \times 10^{-5}$ [kg m^{-1} s^{-1}]	$U_{slug} = \frac{j_l}{1 - VF}$	
$j_v = 0.0700$ [m s^{-1}]	$Re_{slug} = \frac{\rho_l U_{slug} D_{ch}}{\mu_l}$	$\Delta P = 0.805$ [kPa]
$j_l = 0.0687$ [m s^{-1}]	$\left(\frac{dp}{dz}\right)_{slug} = \frac{1}{2} \cdot \frac{64}{Re_{slug}} \cdot \frac{\rho_l \cdot U_{slug}^2}{D_{ch}}$	
	$\frac{\Delta P}{L_{tp}} = \left(\frac{dp}{dz}\right)_{f\text{-}b} \cdot \left(\frac{l_{bubble}}{l_{slug} + l_{bubble}}\right) + \left(\frac{dp}{dz}\right)_{slug} \cdot \left(1 - \frac{l_{bubble}}{l_{slug} + l_{bubble}}\right)$	

[9] The correlation developed for the 250 μm channel was used in the present investigation. In addition, only the laminar friction factor was used here due to $Re_{bubble} < 600$ in the present study.

Table C-5: Representative Void Fraction Calculations (Listed Alphabetically)

Void Fraction Correlation	Equations	Results
Inputs: G = 150 [kg m^{-2} s^{-1}]; D = 2.438 [mm]; x = 0.1; ρ_l = 1208.9 [kg m^{-3}]; ρ_v = 31.81 [kg m^{-3}]; μ_l = 1.958 × 10^{-4} [kg m^{-1} s^{-1}]; μ_v = 1.194× 10^{-5} [kg m^{-1} s^{-1}]; σ = 8.154 × 10^{-3} [N m^{-1}]		
Armand (1946)	$VF = 0.833\beta_v$	VF = 0.674
Baroczy (1965)[10]	$VF = \left[1+\left(\frac{1-x}{x}\right)^{0.74}\left(\frac{\rho_v}{\rho_l}\right)^{0.65}\left(\frac{\mu_l}{\mu_v}\right)^{0.13}\right]^{-1}$	VF = 0.593
El Hajal *et al.*(2003)[11]	$VF = \frac{VF_{Homogeneous} - VF_{Steiner}}{\ln\left(\frac{VF_{Homogeneous}}{VF_{Steiner}}\right)}$	VF = 0.719
Homogeneous[10]	$VF = \beta_v = \left[1+\left(\frac{1-x}{x}\right)\left(\frac{\rho_v}{\rho_l}\right)\right]^{-1}$	VF = 0.809
Lockhart and Martinelli (1949)[10]	$VF = \left[1+0.28\left(\frac{1-x}{x}\right)^{0.64}\left(\frac{\rho_v}{\rho_l}\right)^{0.36}\left(\frac{\mu_l}{\mu_v}\right)^{0.07}\right]^{-1}$	VF = 0.727

[10] These correlations can be found in Carey (1992).
[11] These correlations can be found in Garimella (2006).

Table C-5: Cont…

Void Fraction Correlation	Equations	Results
Premoli *et al.* (1971)[11]	$Re_{lo} = \frac{G \cdot D}{\mu_l}$; $We_{lo} = \frac{G^2 D}{\rho_l \cdot \sigma}$; $y = \frac{VF_{Homogeneous}}{1 - VF_{Homogeneous}}$ $E_1 = 1.578 \cdot Re_{lo}^{-0.19} \left(\frac{\rho_l}{\rho_v} \right)^{0.22}$; $E_2 = 0.0273 \cdot We_{lo} \cdot Re_{lo}^{-0.51} \left(\frac{\rho_l}{\rho_v} \right)^{-0.08}$ $S = 1 + E_1 \cdot \left(\frac{y}{1 + y \cdot E_2} - y \cdot E_2 \right)^{0.5}$; $VF = \frac{x}{x + S \cdot (1 - x) \frac{\rho_v}{\rho_l}}$	Re_{lo} = 1868 We_{lo} = 5.57 y = 4.223 E_1 = 0.8397 E_2 = 0.00244 S = 2.715 VF = 0.609
Smith (1969)[11]	$VF = \left[1 + \left(\frac{1-x}{x} \right) \left(\frac{\rho_v}{\rho_l} \right) \times \left(0.4 + [1 - 0.4] \left[\frac{\left(\frac{\rho_l}{\rho_v} \right) + 0.4 \left(\frac{1-x}{x} \right)}{1 + 0.4 \left(\frac{1-x}{x} \right)} \right]^{0.5} \right) \right]^{-1}$	VF = 0.657

Table C-5: Cont…

Void Fraction Correlation	Equations	Results
Steiner (1993)[11]	$VF = \frac{x}{\rho_v}\left[\begin{array}{l}\left(1+0.12\left[1-x\right]\right)\left(\frac{x}{\rho_v}+\frac{1-x}{\rho_l}\right) \\ +\frac{1.18\left(1-x\right)\left(g\cdot\sigma\cdot\left[\rho_l-\rho_v\right]\right)^{0.25}}{G\cdot\rho_l^{0.5}}\end{array}\right]^{-1}$	VF = 0.636
Tandon *et al.* (1985)[11]	$Re_l = \frac{G\cdot D\left(1-x\right)}{\mu_l}$; $X_{\text{Martinelli,tt}} = \left(\frac{\mu_l}{\mu_v}\right)^{0.1}\left(\frac{1-x}{x}\right)^{0.9}\left(\frac{\rho_v}{\rho_l}\right)^{0.5}$ $FT = 0.15\cdot\left(\frac{1}{X_{\text{Martinelli,tt}}}+\frac{2.85}{X_{\text{Martinelli,tt}}^{0.476}}\right)$ $VF = \begin{cases}1-1.928\frac{Re_l^{-0.315}}{FT}+0.9293\frac{Re_l^{-0.63}}{FT^2} & Re_l < 1125 \\ 1-0.38\frac{Re_l^{-0.088}}{FT}+0.0361\frac{Re_l^{-0.176}}{FT^2} & Re_l \geq 1125\end{cases}$	Re_l = 1681 $X_{\text{Martinelli,tt}}$ = 1.55 FT = 0.444 VF = 0.604
Thom (1964)[10]	$VF = \left[1+\left(\frac{1-x}{x}\right)\left(\frac{\rho_v}{\rho_l}\right)^{0.89}\left(\frac{\mu_l}{\mu_v}\right)^{0.18}\right]^{-1}$	VF = 0.631
Yashar *et al.* (2001)[11]	$Fr_t = \left(\frac{G^2x^3}{\left(1-x\right)\rho_v^2\cdot g\cdot D}\right)^{0.5}$; $X_{\text{Martinelli,tt}} = \left(\frac{\mu_l}{\mu_v}\right)^{0.1}\left(\frac{1-x}{x}\right)^{0.9}\left(\frac{\rho_v}{\rho_l}\right)^{0.5}$ $VF = \left(1+Fr_t^{-1}+X_{\text{Martinelli,tt}}\right)^{-0.321}$	Fr_t = 1.016 $X_{\text{Martinelli,tt}}$ = 1.55 VF = 0.667

Table C-5: Cont…

Void Fraction Correlation	Equations	Results
Zivi (1964)[10]	$VF = \left[1+\left(\frac{1-x}{x}\right)\left(\frac{\rho_v}{\rho_l}\right)^{2/3}\right]^{-1}$	VF = 0.557

REFERENCES

Agarwal, A. (2006), "Heat Transfer and Pressure Drop During Condensation of Refrigerants in Microchannels," Georgia Institute of Technology, *Mechanical Engineering Dept.*, Ph.D. Dissertation, pp. 347.

Al Hallaj, S., H. Maleki, J. S. Hong and J. R. Selman (1999), "Thermal Modeling and Design Considerations of Lithium-Ion Batteries," *Journal of Power Sources*, Vol. 83(1-2), pp. 1-8.

Al Hallaj, S., J. Prakash and J. R. Selman (2000a), "Characterization of Commercial Li-Ion Batteries Using Electrochemical-Calorimetric Measurements," *Journal of Power Sources*, Vol. 87(1-2), pp. 186-194.

Al Hallaj, S. and J. R. Selman (2000), "A Novel Thermal Management System for Electric Vehicle Batteries Using Phase-Change Material," *Journal of the Electrochemical Society*, Vol. 147(9), pp. 3231-3236.

Al Hallaj, S., R. Venkatachalapathy, J. Prakash and J. R. Selman (2000b), "Entropy Changes Due to Structural Transformation in the Graphite Anode and Phase Change of the $LiCoO_2$ Cathode," *Journal of the Electrochemical Society*, Vol. 147(7), pp. 2432-2436.

Ali, M. I., M. Sadatomi and M. Kawaji (1993), "Adiabatic Two-Phase Flow in Narrow Channels between Two Flat Plates," *Canadian Journal of Chemical Engineering*, Vol. 71(Compendex), pp. 657-666.

Armand, A. A. (1946), "The Resistance During the Movement of a Two-Phase System in Horizontal Pipes," *Izv. Vses. Teplotekh. Inst.*, Vol. 1, pp. 16–23 (AERE-Lib/Trans 828).

Baird, J. R., D. F. Fletcher and B. S. Haynes (2003), "Local Condensation Heat Transfer Rates in Fine Passages," *International Journal of Heat and Mass Transfer*, Vol. 46(23), pp. 4453-4466.

Bandhauer, T. M., S. Garimella and T. F. Fuller (2011), "A Critical Review of Thermal Issues in Lithium-Ion Batteries," *Journal of the Electrochemical Society*, Vol. 158(3), pp. R1-R25.

Bang, H., H. Yang, Y. K. Sun and J. Prakash (2005), "In Situ Studies of $Li_xMn_2O_4$ and $Li_xAl_{0.17}Mn_{1.83}O_{3.97}S_{0.03}$ Cathode by Imc," *Journal of the Electrochemical Society*, Vol. 152(2), pp. A421-A428.

Baroczy, C. J. (1965), "Correlation of Liquid Fraction in Two-Phase Flow with Applications to Liquid Metals," *Chemical Engineering Progress Symposium Series*, Vol. 61(57), pp. 179-191.

Bernardi, D., E. Pawlikowski and J. Newman (1985), "A General Energy Balance for Battery Systems," *Journal of the Electrochemical Society*, Vol. 132(1), pp. 5-12.

Bertsch, S. S., E. A. Groll and S. V. Garimella (2008a), "Refrigerant Flow Boiling Heat Transfer in Parallel Microchannels as a Function of Local Vapor Quality," *International Journal of Heat and Mass Transfer*, Vol. 51(19-20), pp. 4775-4787.

Bertsch, S. S., E. A. Groll and S. V. Garimella (2008b), "Review and Comparative Analysis of Studies on Saturated Flow Boiling in Small Channels," *Nanoscale and Microscale Thermophysical Engineering*, Vol. 12(3), pp. 187 - 227.

Bertsch, S. S., E. A. Groll and S. V. Garimella (2009), "A Composite Heat Transfer Correlation for Saturated Flow Boiling in Small Channels," *International Journal of Heat and Mass Transfer*, Vol. 52(7-8), pp. 2110-2118.

Bhatti, M. S. and R. K. Shah (1987). Turbulent and Transition Flow Convective Heat Transfer in Ducts. *Handbook of Single-Phase Convective Heat Transfer*. S. Kakac, R. K. Shah and W. Aung, John Wiley and Sons, Inc. pp 3.1-3.137.

Botte, G. G., B. A. Johnson and R. E. White (1999), "Influence of Some Design Variables on the Thermal Behavior of a Lithium-Ion Cell," *Journal of the Electrochemical Society*, Vol. 146(3), pp. 914-923.

Carey, V. P. (1992). *Liquid-Vapor Phase-Change Phenomena : An Introduction to the Thermophysics of Vaporization and Condensation Processes in Heat Transfer Equipment*. Washington, D.C., Hemisphere Pub. Corp.

Cavallini, A., L. Doretti, M. Matkovic and L. Rossetto (2006), "Update on Condensation Heat Transfer and Pressure Drop inside Minichannels," *Heat Transfer Engineering*, Vol. 27(4), pp. 74 - 87.

Chen, S.-C., Y.-Y. Wang and C.-C. Wan (2006), "Thermal Analysis of Spirally Wound Lithium Batteries," *Journal of the Electrochemical Society*, Vol. 153(4), pp. A637-A648.

Chen, S. C., C. C. Wan and Y. Y. Wang (2005), "Thermal Analysis of Lithium-Ion Batteries," *Journal of Power Sources*, Vol. 140(1), pp. 111-124.

Chen, Y. and J. W. Evans (1993), "Heat Transfer Phenomena in Lithium/Polymer-Electrolyte Batteries for Electric Vehicle Application," *Journal of the Electrochemical Society*, Vol. 140(7), pp. 1833-1838.

Chen, Y. and J. W. Evans (1994a), "Thermal Analysis of Lithium Polymer Electrolyte Batteries by a Two Dimensional Model - Thermal Behaviour and Design Optimization," *Electrochimica Acta*, Vol. 39(4), pp. 517-526.

Chen, Y. and J. W. Evans (1994b), "Three-Dimensional Thermal Modeling of Lithium-Polymer Batteries under Galvanostatic Discharge and Dynamic Power Profile," *Journal of the Electrochemical Society*, Vol. 141(11), pp. 2947-2955.

Chen, Y. and J. W. Evans (1996), "Thermal Analysis of Lithium-Ion Batteries," *Journal of the Electrochemical Society*, Vol. 143(9), pp. 2708-2712.

Choi, C. W., D. I. Yu and M. H. Kim (2011), "Adiabatic Two-Phase Flow in Rectangular Microchannels with Different Aspect Ratios: Part I - Flow Pattern, Pressure Drop and Void Fraction," *International Journal of Heat and Mass Transfer*, Vol. 54(1-3), pp. 616-624.

Choi, K. W. and N. P. Yao (1979), "Heat Transfer in Lead-Acid Batteries Designed for Electric-Vehicle Propulsion," *Journal of the Electrochemical Society*, Vol. 126(8), pp. 1321-1328.

Chung, J. and G. M. Hulbert (1993), "A Time Integration Algorithm for Structural Dynamics with Improved Numerical Dissipation - the Generalized-Alpha Method," *Journal of Applied Mechanics-Transactions of the ASME*, Vol. 60(2), pp. 371-375.

Chung, P. M. Y. and M. Kawaji (2004), "The Effect of Channel Diameter on Adiabatic Two-Phase Flow Characteristics in Microchannels," *International Journal of Multiphase Flow*, Vol. 30(7-8), pp. 735-761.

Chung, P. M. Y., M. Kawaji, A. Kawahara and Y. Shibata (2004), "Two-Phase Flow through Square and Circular Microchannels - Effects of Channel Geometry," *Journal of Fluids Engineering*, Vol. 126(4), pp. 546-552.

Churchill, S. W. (1977), "Friction-Factor Equations Spans All Fluid Flow Regimes," *Chemical Engineering Progress*, Vol. 84(24), pp. 91-92.

Coleman, H. W. and W. G. Steele (1989). *Experimentation and Uncertainty Analysis for Engineers*. New York, Wiley.

Coleman, J. W. and S. Garimella (2000), "Two-Phase Flow Regime Transitions in Microchannel Tubes: The Effect of Hydraulic Diameter," *ASME Heat Transfer Division - 2000*, Orlando, FL, pp. 71-83.

COMSOL (2010), *Comsol Multiphysics*, Ver. 4.0.0.933

Conte, F. V. (2006), "Battery and Battery Management for Hybrid Electric Vehicles: A Review," *Elektrotechnik und Informationstechnik*, Vol. 123(10), pp. 424-431.

Cooper, M. G. (1984), "Heat Flow Rates in Saturated Nucleate Pool Boiling – a Wide-Ranging Examination Using Reduced Properties," *Advances in Heat Transfer*, Vol. 16, pp. 157-239.

Cubaud, T. and C.-M. Ho (2004), "Transport of Bubbles in Square Microchannels," *Physics of Fluids*, Vol. 16(12), pp. 4575-4585.

Doyle, M., T. F. Fuller and J. Newman (1993), "Modeling of Galvanostatic Charge and Discharge of the Lithium/Polymer/Insertion Cell," *Journal of the Electrochemical Society*, Vol. 140(6), pp. 1526-1533.

Doyle, M., J. Newman, A. S. Gozdz, C. N. Schmutz and J. M. Tarascon (1996), "Comparison of Modeling Predictions with Experimental Data from Plastic Lithium Ion Cells," *Journal of the Electrochemical Society*, Vol. 143(6), pp. 1890-1903.

El Hajal, J., J. R. Thome and A. Cavallini (2003), "Condensation in Horizontal Tubes, Part 1: Two-Phase Flow Pattern Map," *International Journal of Heat and Mass Transfer,* Vol. 46(18), pp. 3349-3363.

Friedel, L. (1979), "Improved Friction Pressure Drop Correlations for Horizontal and Vertical Two Phase Pipe Flow," *European Two-Phase Flow Group Meeting*, Ispra, Italy.

Fuller, T. F., M. Doyle and J. Newman (1994), "Simulation and Optimization of the Dual Lithium Ion Insertion Cell," *Journal of the Electrochemical Society*, Vol. 141(1), pp. 1-10.

Garimella, S. (2006). Condensation in Minichannels and Microchannels. *Heat Transfer and Fluid Flow in Minichannels and Microchannels*. S. G. Kandlikar, S. Garimella, D. Li, S. Colin and M. R. King, Elsevier pp xxiii, 450 p.

Garimella, S., A. Agarwal and J. D. Killion (2005), "Condensation Pressure Drop in Circular Microchannels," *Heat Transfer Engineering*, Vol **26**, pp.**:** 28-35.

Garimella, S., J. D. Killion and J. W. Coleman (2003), "An Expermentally Validated Model for Two-Phase Pressure Drop in the Intermittent Flow Regime for Noncircular Microchannels," *Journal of Fluids Engineering*, Vol. 125(5), pp. 887-894.

Gomadam, P. M., J. W. Weidner, R. A. Dougal and R. E. White (2002), "Mathematical Modeling of Lithium-Ion and Nickel Battery Systems," *Journal of Power Sources*, Vol. 110(2), pp. 267-284.

Gu, W. B. and C. Y. Wang (2000), "Thermal-Electrochemical Modeling of Battery Systems," *Journal of the Electrochemical Society*, Vol. 147(8), pp. 2910-2922.

Guo, G., B. Long, B. Cheng, S. Zhou, P. Xu and B. Cao (2010), "Three-Dimensional Thermal Finite Element Modeling of Lithium-Ion Battery in Thermal Abuse Application," *Journal of Power Sources*, Vol. 195(8), pp. 2393-2398.

Hausen, H. (1943), "Darstellung Des Wärmeüberganges in Rohren Durch Verallgemeinerte Potenzbeziehungen," *Z. VDI Beiheft Verfahrenstechnik*, Vol. 4, pp. 91–102.

Hodge, J. D. (2009). *Personal Communication*. K2 Energy Systems, Las Vegas, NV

Hong, J. S., H. Maleki, S. A. Hallaj, L. Redey and J. R. Selman (1998), "Electrochemical-Calorimetric Studies of Lithium-Ion Cells," *Journal of the Electrochemical Society*, Vol. 145(5), pp. 1489-1501.

Hwang, Y. W. and M. S. Kim (2006), "The Pressure Drop in Microtubes and the Correlation Development," *International Journal of Heat and Mass Transfer*, Vol. 49(11-12), pp. 1804-1812.

Ide, H., R. Kimura and M. Kawaji (2008), "Effect of Inlet Geometry on Adiabatic Gas-Liquid Two-Phase Flow in a Microchannel," *Heat Transfer Engineering*, Vol. 30(1-2), pp. 37-42.

Idel′chik, I. E. and M. O. Shteĭnberg (1994). *Handbook of Hydraulic Resistance*. 3rd, Boca Raton, FL, CRC Press.

Incropera, F. P. and D. P. DeWitt. (1996).

Jansen, K. E., C. H. Whiting and G. M. Hulbert (2000), "A Generalized-Alpha Method for Integrating the Filtered Navier-Stokes Equations with a Stabilized Finite Element Method," *Computer Methods in Applied Mechanics and Engineering*, Vol. 190(3-4), pp. 305-319.

Kakaç, S., R. K. Shah and W. Aung (1987). *Handbook of Single-Phase Convective Heat Transfer*. New York, Wiley.

Kelly, K. J., M. Mihalic and M. Zolot (2002), "Battery Usage and Thermal Performance of the Toyota Prius and Honda Insight for Various Chassis Dynamometer Test Procedures," *17th Annual Battery Conference on Applications and Advances*, Long Beach, California.

Khateeb, S. A., S. Amiruddin, M. Farid, J. R. Selman and S. Al-Hallaj (2005), "Thermal Management of Li-Ion Battery with Phase Change Material for Electric Scooters: Experimental Validation," *Journal of Power Sources*, Vol. 142(1-2), pp. 345-353.

Khateeb, S. A., M. M. Farid, J. R. Selman and S. Al-Hallaj (2004), "Design and Simulation of a Lithium-Ion Battery with a Phase Change Material Thermal Management System for an Electric Scooter," *Journal of Power Sources*, Vol.

128(2), pp. 292-307.

Kim, G.-H. and K. Smith (2008), "Multi-Scale Multi-Dimensional Lithium-Ion Battery Model," *ECS Meeting Abstracts*, Vol. 802(12), pp. 1295-1295.

Kim, G.-H. and K. A. Smith (2009), "Large Prismatic Cell Design Evaluation Using Multi-Scale Multi-Dimensional Lithium-Ion Battery Model," *ECS Meeting Abstracts*, Vol. 901(4), pp. 252-252.

Kim, J.-S., J. Prakash and J. R. Selman (2001), "Thermal Characteristics of $Li_xMn_2O_4$ Spinel," *Electrochemical and Solid-State Letters*, Vol. 4(9), pp. A141-A144.

Kim, U. S., C. B. Shin and C.-S. Kim (2008), "Effect of Electrode Configuration on the Thermal Behavior of a Lithium-Polymer Battery," *Journal of Power Sources*, Vol. 180(2), pp. 909-916.

Kim, U. S., C. B. Shin and C.-S. Kim (2009), "Modeling for the Scale-up of a Lithium-Ion Polymer Battery," *Journal of Power Sources*, Vol. 189(1), pp. 841-846.

Klein, S. A. (2010). *Engineering Equation Solver*. F-Chart Software.

Kobayashi, Y., N. Kihira, K. Takei, H. Miyashiro, K. Kumai, N. Terada and R. Ishikawa (1999), "Electrochemical and Calorimetric Approach to Spinel Lithium Manganese Oxide," *Journal of Power Sources*, Vol. 81-82, pp. 463-466.

Kobayashi, Y., H. Miyashiro, K. Kumai, K. Takei, T. Iwahori and I. Uchida (2002), "Precise Electrochemical Calorimetry of $LiCoO_2$/Graphite Lithium-Ion Cell," *Journal of the Electrochemical Society*, Vol. 149(8), pp. A978-A982.

Koyama, S., K. Kuwahara, K. Nakashita and K. Yamamoto (2003), "An Experimental Study on Condensation of Refrigerant R134a in a Multi-Port Extruded Tube," *International Journal of Refrigeration*, Vol. 26(4), pp. 425-432.

Kumaresan, K., G. Sikha and R. E. White (2008), "Thermal Model for a Li-Ion Cell," *Journal of the Electrochemical Society*, Vol. 155(2), pp. A164-A171.

Lee, H. J. and S. Y. Lee (2001), "Pressure Drop Correlations for Two-Phase Flow within Horizontal Rectangular Channels with Small Heights," *International Journal of*

Multiphase Flow, Vol. 27(5), pp. 783-796.

Lee, J. and I. Mudawar (2005), "Two-Phase Flow in High-Heat-Flux Micro-Channel Heat Sink for Refrigeration Cooling Applications: Part I--Pressure Drop Characteristics," *International Journal of Heat and Mass Transfer*, Vol. 48(5), pp. 928-940.

Lee, P.-S. and S. V. Garimella (2008), "Saturated Flow Boiling Heat Transfer and Pressure Drop in Silicon Microchannel Arrays," *International Journal of Heat and Mass Transfer*, Vol. 51(3-4), pp. 789-806.

Lin, S., C. C. K. Kwok, R. Y. Li, Z. H. Chen and Z. Y. Chen (1991), "Local Frictional Pressure Drop During Vaporization of R-12 through Capillary Tubes," *International Journal of Multiphase Flow*, Vol. 17(1), pp. 95-102.

Linden, D. (2002). Basic Concepts. *Handbook of Batteries*. D. Linden and T. B. Reddy, McGraw-Hill pp 1.3-1.18.

Liu, P., J. Wang, J. Hicks-Garner, E. Sherman, S. Soukiazian, M. Verbrugge, H. Tataria, J. Musser and P. Finamore (2010), "Aging Mechanisms of $LiFePO_4$ Batteries Deduced by Electrochemical and Structural Analyses," *Journal of the Electrochemical Society*, Vol. 157(4), pp. A499-A507.

Lockhart, R. W. and R. C. Martinelli (1949), "Proposed Correlation of Data for Isothermal Two-Phase, Two-Component Flow Is Pipes," *Chemical Engineering Progress*, Vol. 45(1), pp. 39-45.

Lu, W., I. Belharouak, S. H. Park, Y. K. Sun and K. Amine (2007), "Isothermal Calorimetry Investigation of $Li_{1+x}Mn_{2-y}Al_zO_4$ Spinel," *Electrochimica Acta*, Vol. 52(19), pp. 5837-5842.

Lu, W., I. Belharouak, D. Vissers and K. Amine (2006a), "In Situ Thermal Study of $Li_{1+x}(Ni_{1/3}Co_{1/3}Mn_{1/3})_{1-x}O_2$ Using Isothermal Micro-Calorimetric Techniques," *Journal of the Electrochemical Society*, Vol. 153(11), pp. A2147-A2151.

Lu, W. and J. Prakash (2003), "In Situ Measurements of Heat Generation in a Li/Mesocarbon Microbead Half-Cell," *Journal of the Electrochemical Society*, Vol. 150(3), pp. A262-A266.

Lu, W., H. Yang and J. Prakash (2006b), "Determination of the Reversible and Irreversible Heats of $LiNi_{0.8}Co_{0.2}O_2$/Mesocarbon Microbead Li-Ion Cell Reactions Using Isothermal Microcalorimetery," *Electrochimica Acta*, Vol. 51(7), pp. 1322-1329.

Melsert, R. (2009). *Personal Communication*.

Mishima, K. and T. Hibiki (1996), "Some Characteristics of Air-Water Two-Phase Flow in Small Diameter Vertical Tubes," *International Journal of Multiphase Flow*, Vol. 22(4), pp. 703-712.

Moriyama, K., A. Inoue and H. Ohira (1992a), "Thermohydraulic Characteristics of Two-Phase Flow in Extremely Narrow Channels (the Frictional Pressure Drop and Heat Transfer of Boiling Two-Phase Flow, Analytical Model)," *Heat Transfer - Japanese Research*, Vol. 21(Compendex), pp. 838-856.

Moriyama, K., A. Inoue and H. Ohira (1992b), "Thermohydraulic Characteristics of Two-Phase Flow in Extremely Narrow Channels (the Frictional Pressure Drop and Void Fraction of Adiabatic Two-Component Two-Phase Flow)," *Heat Transfer - Japanese Research*, Vol. 21(Compendex), pp. 823-837.

Munson, B. R., D. F. Young and T. H. Okiishi (1998). *Fundamentals of Fluid Mechanics*. 3rd, New York, Wiley.

Onda, K., H. Kameyama, T. Hanamoto and K. Ito (2003), "Experimental Study on Heat Generation Behavior of Small Lithium-Ion Secondary Batteries," *Journal of the Electrochemical Society*, Vol. 150(3), pp. A285-A291.

Onda, K., T. Ohshima, M. Nakayama, K. Fukuda and T. Araki (2006), "Thermal Behavior of Small Lithium-Ion Battery During Rapid Charge and Discharge Cycles," *Journal of Power Sources*, Vol. 158(1), pp. 535-542.

Pals, C. R. and J. Newman (1995a), "Thermal Modeling of the Lithium/Polymer Battery," *Journal of the Electrochemical Society*, Vol. 142(10), pp. 3282-3288.

Pals, C. R. and J. Newman (1995b), "Thermal Modeling of the Lithium/Polymer Battery," *Journal of the Electrochemical Society*, Vol. 142(10), pp. 3274-3281.

Parise, R. J. (2000), "Quick Charge Battery with Internal Thermal Management," *Energy*

Conversion Engineering Conference and Exhibit, 2000. (IECEC) 35th Intersociety, pp. 120-127 vol.121.

Premoli, A., D. Francesco and A. Prina (1971), "A Dimensionless Correlation for Determining the Density of Two-Phase Mixtures," *La Termotecnica*, Vol. 25, pp. 17-26.

Qu, W. and I. Mudawar (2003), "Measurement and Prediction of Pressure Drop in Two-Phase Micro-Channel Heat Sinks," *International Journal of Heat and Mass Transfer*, Vol. 46(15), pp. 2737-2753.

Rao, L. and J. Newman (1997), "Heat-Generation Rate and General Energy Balance for Insertion Battery Systems," *Journal of the Electrochemical Society*, Vol. 144(8), pp. 2697-2704.

Revellin, R., V. Dupont, T. Ursenbacher, J. R. Thome and I. Zun (2006), "Characterization of Diabatic Two-Phase Flows in Microchannels: Flow Parameter Results for R-134a in a 0.5 mm Channel," *International Journal of Multiphase Flow*, Vol. 32(7), pp. 755-774.

Revellin, R. and J. R. Thome (2007), "Adiabatic Two-Phase Frictional Pressure Drops in Microchannels," *Experimental Thermal and Fluid Science*, Vol. 31(7), pp. 673-685.

Ribatski, G., L. Wojtan and J. R. Thome (2006), "An Analysis of Experimental Data and Prediction Methods for Two-Phase Frictional Pressure Drop and Flow Boiling Heat Transfer in Micro-Scale Channels," *Experimental Thermal and Fluid Science*, Vol. 31(1), pp. 1-19.

Ribatski, G., W. Zhang, L. Consolini, J. Xu and J. R. Thome (2007), "On the Prediction of Heat Transfer in Micro-Scale Flow Boiling," *Heat Transfer Engineering*, Vol. 28(10), pp. 842 - 851.

Sabbah, R., R. Kizilel, J. R. Selman and S. Al-Hallaj (2008), "Active (Air-Cooled) Vs. Passive (Phase Change Material) Thermal Management of High Power Lithium-Ion Packs: Limitation of Temperature Rise and Uniformity of Temperature Distribution," *Journal of Power Sources*, Vol. 182(2), pp. 630-638.

Saisorn, S. and S. Wongwises (2008), "Flow Pattern, Void Fraction and Pressure Drop of Two-Phase Air-Water Flow in a Horizontal Circular Micro-Channel,"

Experimental Thermal and Fluid Science, Vol. 32(3), pp. 748-760.

Saisorn, S. and S. Wongwises (2009), "An Experimental Investigation of Two-Phase Air-Water Flow through a Horizontal Circular Micro-Channel," *Experimental Thermal and Fluid Science*, Vol. 33(2), pp. 306-315.

Saito, Y., K. Kanari and K. Takano (1997), "Thermal Studies of a Lithium-Ion Battery," *Journal of Power Sources*, Vol. 68(2), pp. 451-454.

Saito, Y., K. Takano, K. Kanari, A. Negishi, K. Nozaki and K. Kato (2001), "Comparative Study of Thermal Behaviors of Various Lithium-Ion Cells," *Journal of Power Sources*, Vol. 97-98, pp. 688-692.

Shah, R. K. and M. S. Bhatti (1987). Laminar Convective Heat Transfer in Ducts. *Handbook of Single-Phase Convective Heat Transfer*. S. Kakac, R. K. Shah and W. Aung, John Wiley and Sons, Inc. pp 3.1-3.137.

Shepherd, C. M. (1965), "Design of Primary and Secondary Cells: 2. An Equation Describing Battery Discharge," *Journal of the Electrochemical Society*, Vol. 112(7), pp. 657.

Sherfey, J. M. and A. Brenner (1958), "Electrochemical Calorimetry," *Journal of the Electrochemical Society*, Vol. 105(11), pp. 665-672.

Smith, K. (2010). *Personal Communication*.

Smith, K. and C. Y. Wang (2006), "Power and Thermal Characterization of a Lithium-Ion Battery Pack for Hybrid-Electric Vehicles," *Journal of Power Sources*, Vol. 160(1), pp. 662-673.

Smith, S. L. (1969), "Void Fractions in Two- Phase Flow: A Correlation Based Upon an Equal Velocity Head Model," *Proceedings of the Institution of Mechanical Engineers, Thermodynamics and Fluid Mechanics Group*, pp. 647-657.

Song, L. and J. W. Evans (2000), "Electrochemical-Thermal Model of Lithium Polymer Batteries," *Journal of the Electrochemical Society*, Vol. 147(6), pp. 2086-2095.

Srinivasan, V. and C. Y. Wang (2003), "Analysis of Electrochemical and Thermal

Behavior of Li-Ion Cells," *Journal of the Electrochemical Society*, Vol. 150(1), pp. A98-A106.

Stanley, R. S., R. F. Barron and T. A. Ameel (1997), "Two-Phase Flow in Microchannels," *Proceedings of the 1997 ASME International Mechanical Engineering Congress and Exposition*, Dallas, TX,pp. 143-152.

Steiner, D. (1993). Heat Transfer to Boiling Saturated Liquids. *Vdi-Wär Meatlas (Vdi Heat Atlas)*, VDI-Gessellschaft Verfahrenstechnik und Chemieingenieurwesen (GCV), (Translator: J.W. Fullarton).

Tandon, T. N., H. K. Varma and C. P. Gupta (1985), "A Void Fraction Model for Annular Two-Phase Flow," *International Journal of Heat and Mass Transfer*, Vol. 28(1), pp. 191-198.

Thom, J. R. S. (1964), "Prediction of Pressure Drop During Forced Circulation Boiling of Water," *International Journal of Heat and Mass Transfer*, Vol. 7(7), pp. 709-724.

Thomas, K. E., C. Bogatu and J. Newman (2001), "Measurement of the Entropy of Reaction as a Function of State of Charge in Doped and Undoped Lithium Manganese Oxide," *Journal of the Electrochemical Society*, Vol. 148(6), pp. A570-A575.

Thomas, K. E. and J. Newman (2003a), "Heats of Mixing and of Entropy in Porous Insertion Electrodes," *Journal of Power Sources*, Vol. 119-121, pp. 844-849.

Thomas, K. E. and J. Newman (2003b), "Thermal Modeling of Porous Insertion Electrodes," *Journal of the Electrochemical Society*, Vol. 150(2), pp. A176-A192.

Triplett, K. A., S. M. Ghiaasiaan, S. I. Abdel-Khalik, A. LeMouel and B. N. McCord (1999), "Gas-Liquid Two-Phase Flow in Microchannels: Part II: Void Fraction and Pressure Drop," *International Journal of Multiphase Flow*, Vol. 25(3), pp. 395-410.

USEPA. (1996), from http://www.epa.gov/OMS/sftp.htm, accessed November, 2011.

Valoen, L. O. and J. N. Reimers (2005), "Transport Properties of $LiPF_6$-Based Li-Ion Battery Electrolytes," *Journal of the Electrochemical Society*, Vol. 152(5), pp. A882-A891.

Verbrugge, M. W. (1995), "Three-Dimensional Temperature and Current Distribution in a Battery Module," *AIChE Journal*, Vol. 41(6), pp. 1550-1562.

Webb, R. L. and K. Ermis (2001), "Effect of Hydraulic Diameter on Condensation of R-134a in Flat, Extruded Aluminum Tubes," *Journal of Enhanced Heat TRansfer*, Vol. 8(2), pp. 77-90.

Yang, H. and J. Prakash (2004), "Determination of the Reversible and Irreversible Heats of a $LiNi_{0.8}Co_{0.15}Al_{0.05}O_2$/Natural Graphite Cell Using Electrochemical-Calorimetric Technique," *Journal of the Electrochemical Society*, Vol. 151(8), pp. A1222-A1229.

Yashar, D. A., D. M. Graham, M. J. Wilson, J. C. Chato, H. R. Kopke and T. A. Newell (2001), "Investigation of Refrigerant Void Fraction in Horizontal, Microfin Tubes," *HVAC and R Research*, Vol. 7(1), pp. 67-82.

Zivi, S. M. (1964), "Estimation of Steady-State Steam Void-Fraction by Means of the Principle of Minimum Entropy Production," *Journal of Heat Transfer*, Vol. 86, pp. 247-252.

Zolot, M., A. A. Pesaran and M. Mihalic (2002), "Thermal Evaluation of Toyota Prius Battery Pack," *Future Car Congress*, Arlington, VA.

Zolot, M. D., K. Kelly, M. Keyser, M. Mihalic, A. Pesaran and A. Hieronymus (2001), "Thermal Evaluation of the Honda Insight Battery Pack," *36th Intersociety Energy Conversion Engineering Conference*, Savannah, GA.